TECHNISCHE UNIVERSITÄT MÜNCHEN

Ingenieurfakultät Bau Geo Umwelt

Lehrstuhl Methodik der Fernerkundung

Oil spill and ship detection using high resolution polarimetric X-band SAR data

Domenico Velotto

Vollständiger Abdruck der von der Ingenieurfakultät Bau Geo Umwelt der Technischen Universität München zur Erlangung des akademischen Grades eines

Doktor-Ingenieurs (Dr.-Ing)

genehmigten Dissertation.

Vorsitzender: Univ.-Prof. Dr.-Ing. Florian Seitz

Prüfer der Dissertation:

1. Univ.-Prof. Dr.-Ing. Richard H. G. Bamler
2. Univ.-Prof. Maurizio Migliaccio
3. Hon.-Prof. Dr. rer. nat. Michael Eineder

Die Dissertation wurde am 15.01.2016 bei der Technischen Universität München eingereicht und durch die Ingenieurfakultät Bau Geo Umwelt am 03.03.2016 angenommen.

Abstract

The understanding of activities associated with the maritime domain that could impact the security, safety and environment are of particular interest and importance for countries bordering on the sea, but not limited to. Due to the different threats the world oceans are subjected to, an ideal surveillance system must be capable of operating independently of weather and sun-light conditions. Moreover, a cost-effective tool that delivers timely information on critical situation at open sea, as reliable as for coastal zones, is an asset. Satellite Synthetic Aperture Radar (SAR) is the only space-borne system that provides non-cooperative surveillance of maritime activities. In particular, the new generation of satellite SAR sensors, such as the Canadian RADARSAT-2, the German TerraSAR-X/TanDEM-X and the Italian COSMO-SkyMed, deliver data in Near Real Time (NRT) in a broad range of imaging modes and specifications. For these reasons, SAR is considered a key instrument to build such integrated maritime surveillance system.

Among the illegal human activities, marine pollution and non-cooperative vessels are considered essential undertaking in the framework of Maritime Security and Safety. To contrast the increasing phenomena of voluntary oil dumping and respond to catastrophic oil spill events (often direct consequences of the high ship traffic) the European Union (EU) has founded the European Maritime Safety Agency (EMSA). CleanSeaNet is the satellite-based oil spill and vessel detection service provided by EMSA to the member states.

SAR imagery, acquired in single polarization, provide information on the sea surface roughness and on the presence of floating metallic targets. Accordingly, SAR imagery is the main input for the service CleanSeaNet. Nevertheless, oil spill and ship detection algorithms, that exploit only the amplitude information of single polarization SAR data, have non-optimal performances.

The topic of this thesis is *oil spill and ship detection using high resolution polarimetric X-band SAR data*. The concern of polarimetry is to analyse the polarization state of the electromagnetic wave to extract physical information from the observed object. Recently its concept has been extended to SAR, hereafter PolSAR. The well-known drawbacks of the actual PolSAR system are the loss in spatial resolution and the cross-track coverage reduction. For these reasons, PolSAR studies in SAR oceanography have been very limited. However, the drawbacks of PolSAR can be mitigated in future missions with new technologies or exploiting complementary SAR satellites, e.g. the ESA Sentinel-1.

This dissertation aims at studying potential benefits of PolSAR techniques to improve the current State-of-the-Art of SAR marine pollution and target detection with an eye to NRT suitability. The algorithms developed to accomplish the main task of this dissertation are among the first to use spaceborne X-band PolSAR data in the maritime domain. A challenging dataset containing field campaign measurements has been analysed to show the novelties found in the research field.

Zusammenfassung

Das Verständnis der maritimen Aktivitäten, die sich auf Sicherheit und Umwelt auswirken könnten, ist besonders, aber nicht nur, für Küstenländer von besonderem Interesse und hoher Bedeutung. Aufgrund der verschiedenen Bedrohungen, denen die Weltmeere ausgesetzt sind, muss ein ideales Überwachungssystem unabhängig von Wetter- und Sonnenlichtbedingungen betrieben werden können. Außerdem ist ein kostengünstiges System, das für kritische Situation auf offener See genauso aktuelle und zuverlässige Informationen liefert wie für Küstengebiete, von großem Vorteil. Satellitengestütztes Synthetische Apertur Radar (SAR) ist der einzige weltraumgestützte Sensor, der die Überwachung der maritimen Vorgänge nicht-kooperativ zur Verfügung stellt. Insbesondere die neue Generation von Satelliten-SAR-Sensoren, wie zum Beispiel der kanadische RADARSAT-2, die deutschen TerraSAR-X/TanDEM-X und der italienische COSMO-SkyMed, liefern Daten in Nahe Echtzeit (NRT) in einer Fülle von Abbildungsmoden und Spezifikationen. Daher wird SAR als Schlüsselinstrument zum Aufbau eines solchen integrierten Überwachungssystems für maritime Sicherheit betrachtet.

Illegale Aktivitäten auf See, wie Meeresverschmutzung und nicht-kooperative Schiffe, sind die Schwerpunktthemen der maritimen Sicherheit. Zur Bekämpfung der zunehmenden Ölverklappung und zur Reaktion auf Ölkatastrophen (oft eine direkte Auswirkung des hohen Schiffsverkehrs) hat die Europäische Union (EU) die European Maritime Safety Agency (EMSA) gegründet. CleanSeaNet ist der satellitengestützte Dienst für Ölverschmutzung und Schiffsdetektion, der den Mitgliedsstaaten von der EMSA zur Verfügung gestellt wird.

SAR-Bilder, aufgenommen in nur einer Polarisation, liefern Informationen über die Rauigkeit der Meeresoberfläche und das Vorhandensein von schwimmenden metallischen Objekten. Daher bilden SAR-Bilder die Hauptdatenquelle für den CleanSeaNet-Dienst. Jedoch erreichen Öl- und Schiffdetektionsalgorithmen, die nur die Amplitudeninformation einzelner Polarisationen von SAR-Daten nutzen, nicht die optimale Leistung.

Diese Arbeit betrachtet die Öl- und Schiffsdetektion mit hochauflösenden polarimetrischen X-Band SAR-Daten. Polarimetrie misst den Polarisationszustand eines elektromagnetischen Wellenfeldes, um daraus physikalische Informationen zu erhalten. In letzter Zeit wurde dieses Konzept auf SAR erweitert, hiernach PolSAR. Die bekannten Nachteile der PolSAR-Methode sind Auflösungsverlust und Abdeckungsreduzierung. Daher gab es nur sehr wenige PolSAR-Studien im Bereich SAR-Ozeanographie. Allerdings können die Nachteile von PolSAR in zukünftigen Missionen mit neuen Technologien oder der Nutzung komplementärer SAR-Satelliten, z.B. der ESA Sentinel-1, gemildert werden.

In dieser Dissertation werden die potenziellen Vorteile von PolSAR-Techniken zur Verbesserung des aktuellen Stands der SAR Öl- und Schiffsdetektion untersucht, wobei auch die NRT-Eignung beachtet werden soll. Die Algorithmen, die zur Erreichung der Hauptaufgabe dieser Arbeit entwickelt wurden, zählen zu den ersten, die weltraumgestützte

X-Band PolSAR-Daten für den maritimen Bereich verwenden. Ein herausfordernder Datensatz mit Feldkampagnen-Messungen wurde analysiert, um die erreichten Fortschritte im Forschungsgebiet zu demonstrieren.

Contents

1. Introduction

Oceans are covering approximately 70% of the Earth's surface. Their monitoring and surveillance has always been not an easy task due to the limitations in coverage and practicality of standard tools like patrol control and similar monitoring means. It is evident that satellite remote sensing is the key factor to accomplish such a demanding task. In this sense the SeaSAT mission, the first satellite equipped with Synthetic Aperture Radar (SAR), planned with the goal of demonstrating the feasibility of studying Earth's ocean on a large scale from space, represents the milestone of the SAR oceanography.

A processing of the Doppler spectrum of the recorded electromagnetic (EM) field by a coherent RADAR (RAdio Detection And Ranging) operating on-board a moving platform, allows to significantly improve the radar spatial resolution along the flight direction. A SAR can be operated either airborne or spaceborne (Cumming and Wong, 2004) (Curlander and McDonough, 1991). The term *synthetic aperture* refers to the fact that a longer than physical antenna length is synthesized. In a nutshell, SAR is an imaging sensor able to produce a bi-dimensional reflectivity map of large areas with very high spatial resolution (Oliver and Quegan, 2004).

SAR developments began in the middle 50s. The following two decades have been ruled by military research and applications due to the ability in man-made target detection (Elachi and Van Zyl, 2006). SAR is, however, more than just a target detector. Thanks to other notable characteristics, its use in civil Earth Observation (EO) applications has increased starting from the early 80s. Satellite carrying SAR sensors, with their: 1) imaging flexibility, i.e. a single system can collect data from wide areas at low resolution (ScanSAR) to small areas at high resolution (SpotLight); 2) coherent phase history record; 3) wide area coverage; 4) data recording independent from day time; have become nowadays essential tools in many fields of Earth monitoring. Nowadays, SAR sensors are being used in many civil applications including Maritime Surveillance and Security.

The topic of this thesis is *oil spill and ship detection using high resolution polarimetric X-band SAR data*. The concern of polarimetry is to analyse the polarization state of a wave field to extract physical information from the observed object (Cloude, 2010) (Lee and Pottier, 2009). Polarimetry is well known in optical science and recently its concept has been extended to radar and SAR, hereafter PolSAR. A great deal of interest in PolSAR data has been dedicated to classify Earth terrain components. The well-known drawbacks of the actual PolSAR system are the loss in spatial resolution and the cross-track coverage reduction. For these reasons, PolSAR studies in SAR oceanography have been very limited. However, the drawbacks of PolSAR can be mitigated in future missions with new technologies and more expensive instrument architecture. Therefore, this dissertation aims at studying potential benefits of PolSAR techniques to improve the current State-of-the-Art of

SAR marine pollution and target detection with an eye to Near Real Time (NRT) suitability.

The algorithms developed to accomplish the main task of this dissertation are among the first to use spaceborne X-band PolSAR data. A challenging dataset containing field campaign measurements has been analysed to show the novelties found in the research field.

This introduction chapter gives the scientific motivation of the thesis, the problem statement and objectives, and finally, the thesis outline.

1.1. Scientific Motivation

The health status of the world's oceans is important for the fact that oceans provide an important means of commerce, transport and source of energy. Oceans are the biggest mass of the hydrosphere and are strongly linked with the rest of Earth's sphere through geophysical processes like evaporation, precipitation, etc. Thus, their constant observation give the opportunity to better understand and predict phenomena like global warming, climate change and to evaluate the health of the entire globe.

Besides the observation of the oceans and their dynamics there are many undesirable maritime activities that exploit ocean's environment and resources in illegal or inappropriate ways. These activities include: dumping of pollutants, illegal fishing, human trafficking and smuggling, pirating, etc. These illegal activities can be grouped in different policy areas and each policy area has a different weight depending on the geographical location, local politics, etc. For example in the Mediterranean Sea human trafficking is a more sensitive matter than in North Sea.

In the recent years the concept of Maritime Surveillance, i.e. monitoring of human activities usually accomplished for security and military reasons, has been exported to civil applications. In 2002 the European Union (EU) has founded the European Maritime Safety Agency (EMSA) to provide technical and scientific advice in the field of maritime safety and prevention of pollution by ships [www.emsa.europa.eu]. Among several of EMSA's operational tasks, CleanSeaNet is the European satellite-based oil spill and vessel detection service covering all European sea areas. CleanSeaNet has been operationally started in 2007 and is by the time of this dissertation almost at the end of the second generation.

1.2. Problem Statement and Objectives

In the last decades a successful series of satellite SAR missions have been accomplished. These include: ERS-1 and -2, ENVISAT-ASAR, RADARSAT-1. The experience gained during these missions has made possible to use the in-orbit SAR satellites, i.e. RADARDSAT-2 (RD-2), TerraSAR-X/TanDEM-X (TS-X/TD-X) and COSMO-SkyMed

(a)

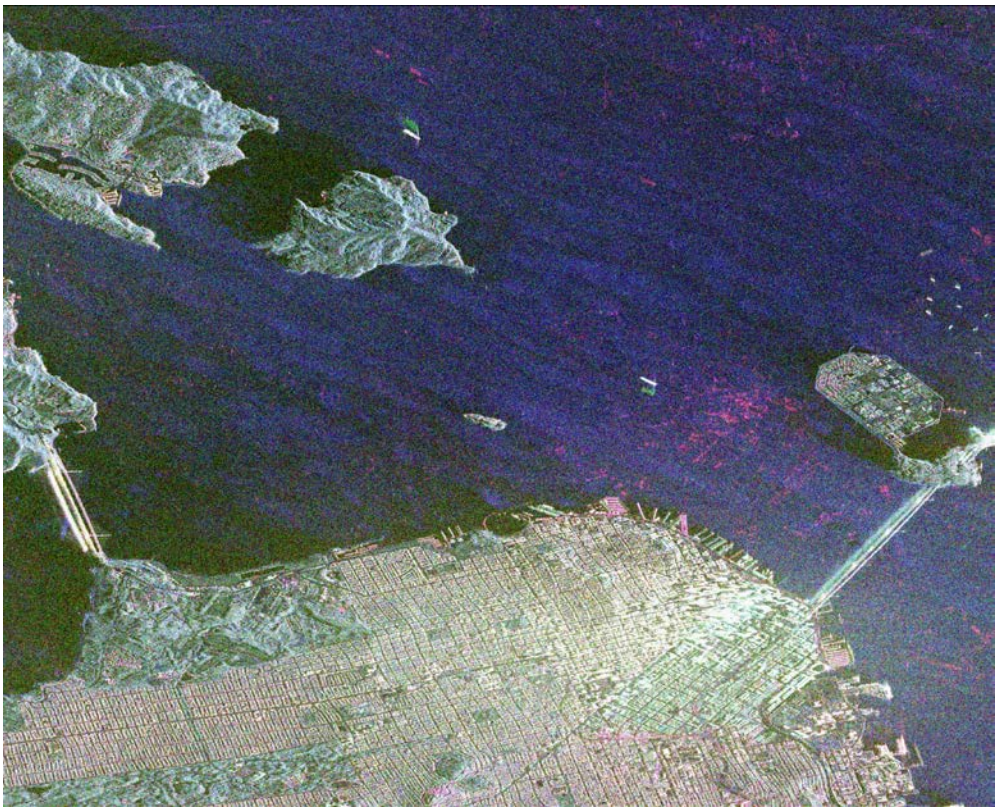

(b)

Figure 1.1 - Sub-scene of a fully polarimetric TS-X data acquired in DRA mode over San Francisco bay in range – azimuth coordinate; (a) shows the amplitude of one single channel (HH); (b) Pauli color-coded composite.

(CSK) constellation, to deliver SAR-based maritime products in NRT (Brusch et al, 2010, Vachon and Quinn, 2012). This has been achieved also thanks to the improvements from both the satellite and ground segment side. Of course running such services involves usually users' feedback. With the help of users' comments and working experiences gathered in several EU projects, the following general needs have been identified (Brekke et al, 2012) (Greidanus et al, 2004) (Greidanus and Kourti, 2006) (Pelizzari, 2012):

- more timely information (less than a day of notice for satellite scene requests, including the delivery of the value-added products to the user);
- the enhancement of situational awareness, and the increase of the reaction capability through the provision of reliable decision support tools;
- more reliable information (lower false alarm rate, better probability of detection and location accuracy).

Although with the new generation of Very High Resolution (VHR) SAR sensors and the technical assistance and support provided by EMSA the first two points have been fulfilled, the third point is still an open matter.

The research activities conducted in this thesis aim at extracting more reliable information from VHR X-band spaceborne PolSAR data to what concerns marine pollution and target detection. Therefore, to improve the current State-of-the-Art, the following objectives must be achieved:

Objective 1: Increase the discrimination capabilities between Oil spill and Look-alike.

Objective 2: Enhance the detectability of marine targets exploiting their physical properties.

Objective 3: Reduce false alarms caused by SAR aliasing of true targets over ocean environment.

Figure 1.1(a) shows a single-polarization (HH channel) amplitude sub-scene of TS-X fully polarimetric Dual Receive Antenna (DRA) mode acquired over San Francisco bay, whereas Figure 1.1(b) shows the four channels (HH, HV, VH, VV) using the Pauli color coding. Comparing Figure 1.1(a) and Figure 1.1(b) it is evident that PolSAR data help in recognizing different land covered classes, e.g. urban area, forest, etc. Nevertheless these benefits are not so evident for maritime related applications, e.g. oil spill and ship detection.

With the development of EO initiatives based on satellite remote sensing, such as the European Copernicus programme, it is obvious to set as last, but not least, objective the following:

Objective 4: Investigation on multi-frequency and synergy between VHR and HR SAR imagery to improve the Maritime Situational Awareness.

1.3. Thesis Outline

This is a *cumulative dissertation* comprising of 5 full peer-reviewed published journal papers (Appendix A) and 1 book chapter (Appendix B). In the framework of Maritime Security and Safety marine pollution and target detection are two topics that are intrinsically related. However, to pursue the aforementioned objectives, they will be treated separately in dedicated chapters. The remainder of this thesis is structured as follows.

Chapter 2 introduces the SAR imaging principles followed by a short overview of wave polarimetry. Polarimetric decomposition and features used to achieve the main goal of the dissertation are presented.

In Chapter 3 the topic of marine pollution is introduced from the physical point of view. The State-of-the-Art in SAR oil detection is reviewed stressing the limitations of such methodology. Afterwards, the use of SAR data acquired in dual-polarization mode is analysed in order to assess the possible benefits in overcoming the limitations of single-polarization mode. Part of this study has been published in (Velotto *et. al.*, 2011).
A.1. Velotto, D., Migliaccio, M., Nunziata, F., Lehner, S., 2011. Dual-polarized TerraSAR-X data for oil-spill observation. IEEE Transactions on Geoscience and Remote Sensing 49 (12): 4751-4762
In addition a review paper that gives the overview of ocean parameters estimated through spaceborne SAR has been published in (Lehner *et. al.*, 2013).
A.2. Lehner, S., Pleskachevsky, A., Velotto, D., Jacobsen, S., 2013. Meteo-marine parameters and their variability observed by high resolution satellite radar images. Oceanography 26 (2): 80–91

Chapter 4 deals with SAR detection of marine targets and it consists of three parts. In the first part detectors and approaches based on single polarization data are presented. In this section the choice of a proper transmitting-receiving antenna polarization combination for ship detection application is addressed. The book chapter on ship surveillance in African waters describes the basic steps executed for the NRT ship detection service using TS-X (Lehner *et. al.*, 2014).
The second part of Chapter 4 gives an overview of available multi-polarization algorithms successfully employed for ship detection. As many of these algorithms require fully polarimetric SAR data and are computationally demanding, an accessible NRT approach that exploits standard TS-X dual-polarization mode has been developed. It makes use of the reflection symmetry properties of man-made marine targets estimated from the combination of co-pol and cross-pol channels. The main outcomes of this algorithm are summarized in (Velotto *et. al.*, 2013) and in this dissertation for the first time the performances are further discussed.
A.3. Velotto, D., Migliaccio, M., Nunziata, F., Lehner, S., 2013. Dual-polarimetric TerraSAR-X SAR data for target at sea observation. IEEE Geoscience and Remote Sensing Letters 10 (5): 1114-1118

The third part of Chapter 4 addresses the discrimination of false positives caused by ghost replicas of real targets displaced in azimuth direction, i.e. azimuth ambiguity. A very fast and robust technique, that is able to discriminate ships from their azimuth ambiguity without loss of resolution and usage of post-processing algorithms, has been published in (Velotto *et. al.*, 2014). The comparison of the proposed technique with other available in literature closes this chapter.

A.4. Velotto, D., Soccorsi, M., Lehner, S., 2014. Azimuth ambiguities removal for ship detection using full polarimetric X-Band SAR data. IEEE Transactions on Geoscience and Remote Sensing 52 (1): 76-88

The increasing number of SAR satellites with different technical characteristics, suggests investigating the synergy between virtual constellations. In the first part of Chapter 5 a virtual C-/X-band constellation formed by Sentinel-1A (S1-A) and TS-X is taken in consideration regarding marine target detection. The outcomes of the multi-frequency analysis and exploitation of the synergy between the two satellites are summarized in (Velotto *et. al.*, 2015a).

A.5. Velotto, D., Bentes, C., Tings, B., Lehner, S., 2015. First comparison of Sentinel-1 and TerraSAR-X data in the framework of maritime targets detection: South Italy case. IEEE Journal of Oceanic Engineering, *accepted for publication***.**

The second part of the Chapter 5 is indeed dedicated to the prospective of the actual constellation TD-X for maritime applications by showing interesting examples which may be the follow-on research line.

The last part of this dissertation, Chapter 6, is dedicated on discussing the results obtained in this thesis. Conclusions and an outlook for future work end the dissertation.

2. SAR Principles and Polarimetry

The objective of this chapter is to give the theoretical background on SAR and polarimetry that are necessary for the following chapters. A brief introduction on SAR imaging principles and signal processing is given in the first part of the chapter. It follows the SAR polarimetry theory and a short description of the X-band SAR mission TS-X.

2.1. SAR Imaging Principles

The mono-static architecture of a SAR system is composed of a transmitter and a receiver that share the same antenna located on a moving platform (i.e., airborne or satellite). Ground-based SAR is also available and used for surface deformation monitoring. If the transmitting and receiving antennas are physically separated, such architecture is called bi-static. In this dissertation mono-static SAR based on pulsed waveform radar is considered.

Figure 2.1 illustrates the SAR principle and its geometry. The illustration and the signal processing principle that follows are limited to the basic SAR imaging mode, known as StripMap. Due to the side looking nature, SAR coordinate system is logically defined as follow:

- The axis x (ground range) is the projection on ground of the axis s (slant range), which gives the distance of a point scatterer on Earth from the radar in the viewing sensor's plane.
- The axis y (azimuth) defines the position of the scatterer along the sensor path.
- The axis z gives the platform height information.
- The angles θ and β represent the elevation and azimuth angle from the antenna pointing direction.

Time reference in range direction τ is known as fast time in opposite to the one in azimuth t, known as slow time. This differentiation comes from the fact that, in range EM waves are travelling at the speed of light c, while, in azimuth the satellite moves at the speed v_{S} (mean TS-X velocity for the reference orbit is 7.6 km/s). Therefore, the range and azimuth scanning processes have time scales that differ from each other by several orders of magnitude, allowing the mutually independent assumption (Curlander and McDonough, 1991; Franceschetti and Lanari, 1999; Schreier, 1993). The swath width gives the scene ground-range extent, while the maximum length depends on the data take duration, on-board memory storage and thermal conditions.

The echo signal formulation retrieved in this context assumes the start-stop approximation, rectilinear flat Earth geometry and EM propagation in vacuum mean. Each of these approximations is source of geometric and radiometric inaccuracies, usually compensated in the SAR processor (Cumming and Wong, 2005; Curlander and McDonough, 1991).

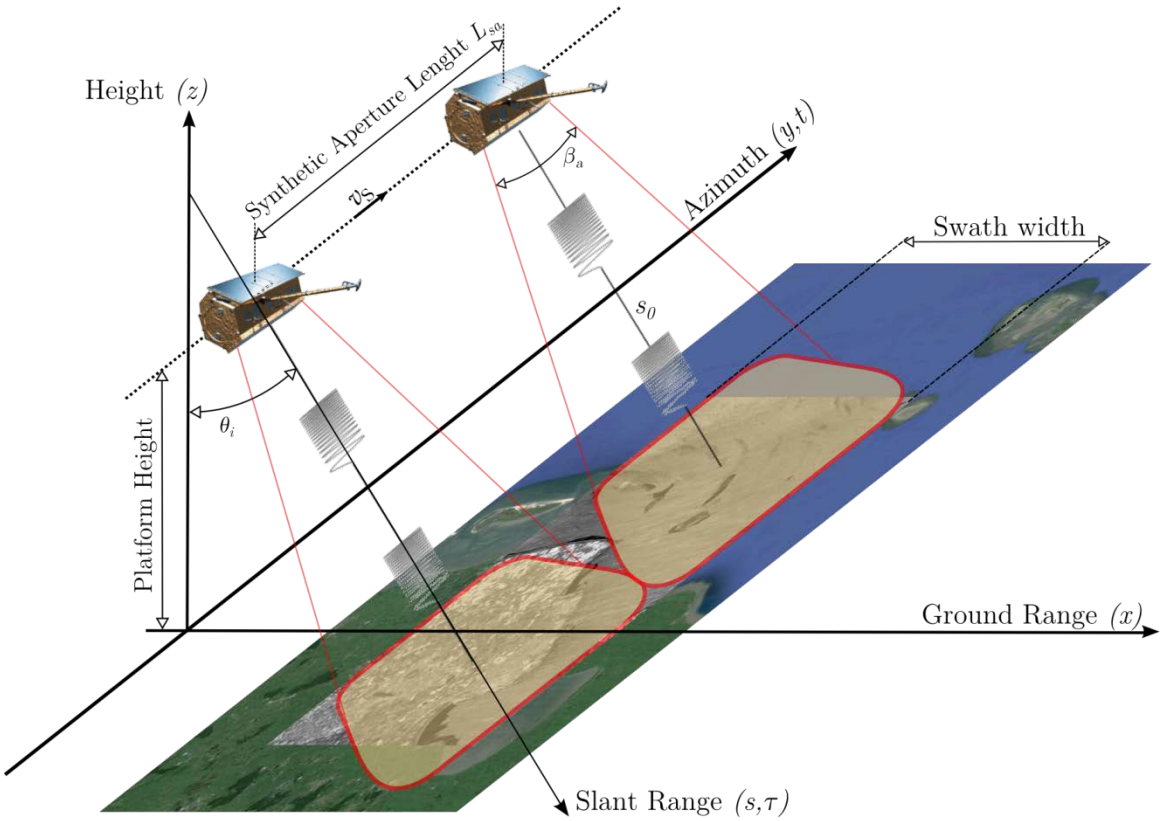

Figure 2.1 - Pictorial description of SAR imaging principle and geometry.

The transmitted signal for a single pulse, for a general antenna transmitting polarization state X, can be written as:

$$s_{\mathrm{Tx}}(\tau) = \; g(\tau) \cdot \exp[i 2\pi f_0 \tau] \tag{2.1}$$

where $g(\tau)$ is the complex envelope of the baseband signal, i the imaginary unit and f_0 the carrier frequency. The demodulated received echo signal, for a general polarization receiving antenna state Y is then:

$$s_{\mathrm{RY}}(\tau) = \; A_w \cdot g\left(\tau - 2\frac{s_p}{c}\right) \cdot \exp\left[-i\frac{4\pi}{\lambda} s_p\right] \tag{2.2}$$

where A_w accounts for the antenna pattern weighting in θ and β directions, $2s_p/c$ is the round-trip time of the EM scattered by a point target P located at s_p. The range time τ represents the first dimension of the final 2D data matrix of complex samples. The second dimension is due to the pulsed nature of SAR, i.e. the radar acquires a range line whenever it travels a distance $v_S \cdot PRI$ (being $PRI = 1/PRF$ the pulse repetition interval)(Curlander and McDonough, 1991; Schreier, 1993). Obviously the distance between the radar and the scatter on the ground varies with time t, according to:

$$s(t) = \sqrt{s_0^2 + (v_S t)^2} \approx s_0 + \frac{(v_S t)^2}{2 s_0} \tag{2.3}$$

being $s_0 = s(t_0)$ the minimum distance and t_0 the time of closest approach. Equation (2.3) is valid for rectilinear orbit usually not sufficient when dealing with VHR SAR data processing (Breit et al., 2014; Prats-Iraola et al., 2012; Raney et al., 1994). The parabolic approximation of the range history shows the well-known range cell migration effect. Finally, the SAR point target response can be written as:

$$s_{\mathrm{R_Y}}(\tau, t) = \; A_w \cdot g\left(\tau - 2\frac{s(t)}{c}\right) \cdot \exp\left[-i\frac{4\pi}{\lambda}s(t)\right] \tag{2.4}$$

The argument of the exponential term in Equation (2.4) is the phase variation with distance. Its instantaneous frequency is given by:

$$f_D = -\frac{1}{2\pi}\frac{\partial}{\partial t}\frac{4\pi}{\lambda}s(t) \approx -\frac{2(v_{\mathrm{S}})^2}{\lambda s_0}t \tag{2.5}$$

that turns out to be a linear frequency modulation and hence referred as azimuth chirp. It is important to mention that the use of continuous variable τ and t in Equation (2.4) is purely for mathematical purposes. In reality, in modern SAR systems, both dimensions are sampled with frequencies higher than the respective Nyquist rate (Moreira et al., 2013; Schreier, 1993; Tomiyasu, 1978). The side-effect of such discretization is one of the main subjects of this thesis and will be discussed later on. Besides a system loss factor and a parameter characterizing the illuminated object, i.e. the radar cross section, Equation (2.4) represents the SAR raw data. Detailed description of SAR focusing, i.e. image formation starting from raw data, is not covered in this thesis since the subject is well described in literature.
Being SAR side-looking imaging radar, it is characterized by resolution in its native coordinate, slant range and azimuth. Similar to real aperture radar (RAR), the SAR slant range resolution is governed by the shape of the pulse envelope $g(\tau)$. As already mentioned, long duration phase coded pulses, e.g. chirp signal, are used, hence (Curlander and McDonough, 1991; Franceschetti and Lanari, 1999; Oliver and Quegan, 2004; Schreier, 1993):

$$\delta_r = c/2W_r \tag{2.6}$$

where δ_r is the slant-range resolution, $W_r = k_r \cdot \tau$ is the range pulse bandwidth and k_r is the frequency rate. In contrary to RAR, where the angular azimuth resolution depends on the 3dB antenna beamwidth, the SAR azimuth resolution is governed by the path length during which the radar receives echo from a point target, i.e. the synthetic aperture (see Figure 2.1). From Figure 2.1, it can be seen that the synthetic aperture length is given by $L_{sa} = \beta_a \cdot s_0$. From antenna theory is known that the azimuth antenna beamwidth (β_a) is well approximated by the ratio between the radar wavelength length $\lambda = c/f_0$ and the antenna size in azimuth L_a. The longer the antenna the narrower the beamwidth. Knowing this, the relation between physical and synthetic antenna size is $L_{sa} = \lambda s_0/L_a$, whereas the beamwidth of the synthetic aperture is $\beta_{sa} = \lambda/2L_{sa}$ (the factor 2 is due to the two-way

path). It is straightforward then the following (Curlander and McDonough, 1991; Franceschetti and Lanari, 1999; Oliver and Quegan, 2004; Schreier, 1993):

$$\delta_a = \beta_{sa} \cdot s_0 = \frac{\lambda s_0}{2L_{sa}} = \frac{L_a}{2} \tag{2.7}$$

which gives the relation between azimuth resolution δ_a and physical antenna size. Although, Equation (2.6) tells that in theory fine azimuth resolution is achievable with short antenna, in practise such antenna will have a low gain (due to the small antenna area) and therefore very high power transmitters are required.

2.1.1. Radar Cross Section and Speckle

For monostatic radar, the received power from a point target P is given by the radar equation (Schreier, 1993; Skolnik, 2001):

$$P_{\mathrm{R}}(\tau) = P_{\mathrm{T}}\left(\tau - 2\frac{s_p}{c}\right) \cdot \sigma \cdot \frac{\lambda^2 A_w^2}{(4\pi)^3 (s_p)^4} \tag{2.8}$$

where P_{T} is the transmitted power, P_{R} is the received power and σ the point target radar cross section (RCS). The RCS is defined in terms of incident ($\vec{E}_i$) and scattered ($\vec{E}_s$) EM fields as (Skolnik, 2001):

$$\sigma = \lim_{r_p \to \infty} 4\pi s_p^2 \frac{\left|\vec{E}_s\right|^2}{\left|\vec{E}_i\right|^2} \tag{2.9}$$

and can be seen as the effective area of an isotropic reflecting object that intercepts the transmitted power and scatter that power back. With these findings Equation (2.4) becomes (Cumming and Wong, 2005):

$$s_{\mathrm{R_Y}}(\tau, t) = A_w \cdot L_c \cdot \sqrt{\sigma} \cdot g\left(\tau - 2\frac{s(t)}{c}\right) \cdot \exp\left[-i\frac{4\pi}{\lambda} s(t)\right] \tag{2.10}$$

where L_c includes propagation losses and system calibration factors. Through signal processing of the SAR point target echo signal is then possible to extract physical information, i.e. σ, of the point target.

When the radar illuminates a natural distributed scene with surface roughness on the scale of the radar wavelength, the returned signal is the result of a constructive/destructive interference of waves reflected by the elementary scatterers within the resolution cell. This process is due to the high sensitivity of the phase term in Equation (2.10) with distance. It is known as speckle and depicted in Figure 2.2 (Oliver and Quegan, 2004). Figure 2.2(a) it refers to a theoretical resolution cell that contains a single scatterer, while Figure 2.2 (b) to a more realistic case where point scatterers are randomly distributed in the cell. Figure 2.2(c) shows the speckle formation in the complex plane. The random location of the elementary scatterers varies their distance from the radar and, therefore a fluctuation of σ from one

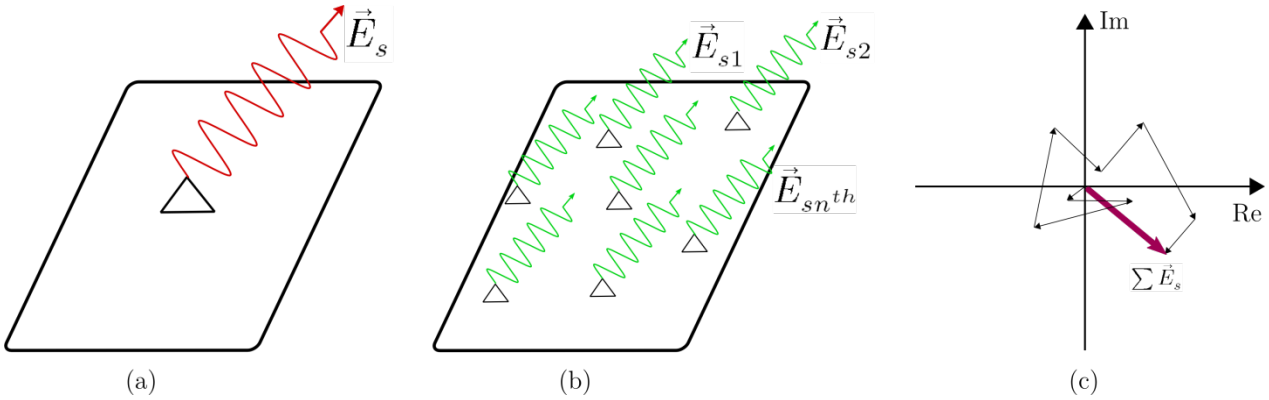

Figure 2.2 - Illustration of the scattering type inside resolution cell. (a) Point scatterer; (b) Randomly distributed scatterers in one resolution cell; (c) Speckle formation.

resolution cell to the next is in place. For distributed scene the normalized radar cross section (NRCS) is used instead (Skolnik, 2001):

$$\sigma_0 = \frac{\langle \sigma \rangle}{A_0} = \frac{4\pi s_p^2}{A_0} \frac{\langle |\vec{E}_s|^2 \rangle}{|\vec{E}_i|^2} \tag{2.11}$$

where A_0 is the illuminated area. It represents the average σ of statistically identical scatterers per unit area. Because speckle hampers the image interpretation and classification, it is mitigated by multilooking processing or spatial averaging. In the first case the standard deviation reduces with the square root of the number of independent looks, while in the second case the amount of speckle reduction depends on filter's kernel and on correlation properties of the single look image (Oliver and Quegan, 2004; Schreier, 1993).

2.1.2. Geometrical Constraints

Typically SAR images are geometrically distorted. The reason for this is that the radar only measures the projection of a three-dimensional scene on the radar coordinates slant range

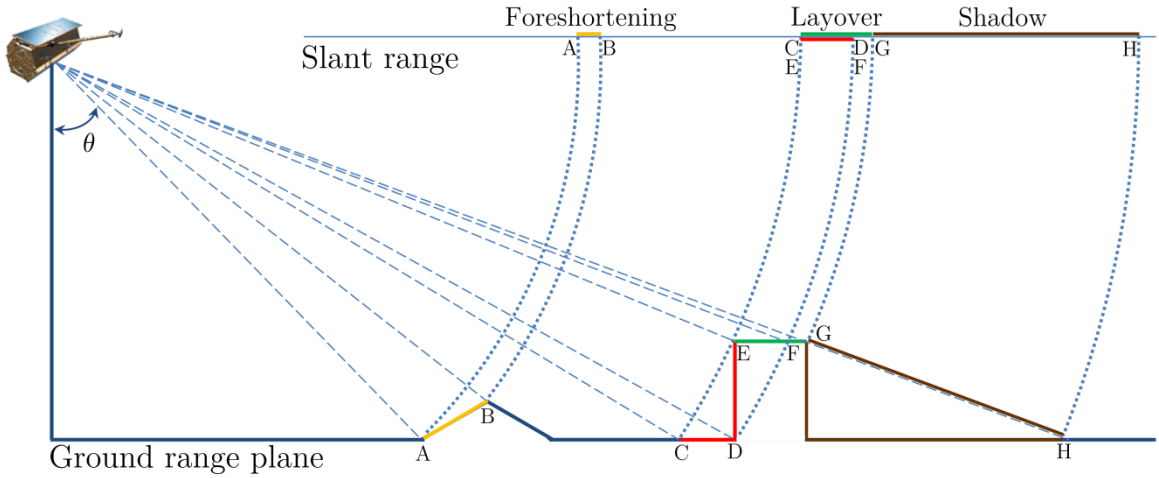

Figure 2.3 - Pictorial explanation of SAR geometrical distortions: foreshortening, layover, shadow.

and azimuth. This causes effects such as shadow for areas hidden from the radar illumination as well as foreshortening and layover manifested by a stretch and compression of sloped terrains.

2.1.3. SAR Artefacts

Although the steady improvements in the SAR processing algorithm and manufacturing, SAR data still suffers of radiometric artefacts, i.e. alteration of the radar brightness properties. Although, giving a detailed list of SAR artefacts and their theoretical explanation is out of the scope of this thesis, it is worth to mention that these may be grouped in due to:

- SAR acquisition geometry
- Focusing algorithm
- Operational imaging mode
- Atmospheric and radio frequency disturbances

Relevant for this dissertation are the artefacts induced by the SAR acquisition geometry, i.e. range and azimuth ambiguity. When designing a conventional SAR system, the analysis of range and azimuth ambiguities play an important role, being among the key system parameters like signal to noise ratio (SNR) and minimum antenna area. For a reason that will be clear in a moment, range and azimuth ambiguity pose a direct constraints on the system PRF value that in turns depends on the geometry (Li and Johnson, 1983; Mehlis, 1980; Tomiyasu, 1978).

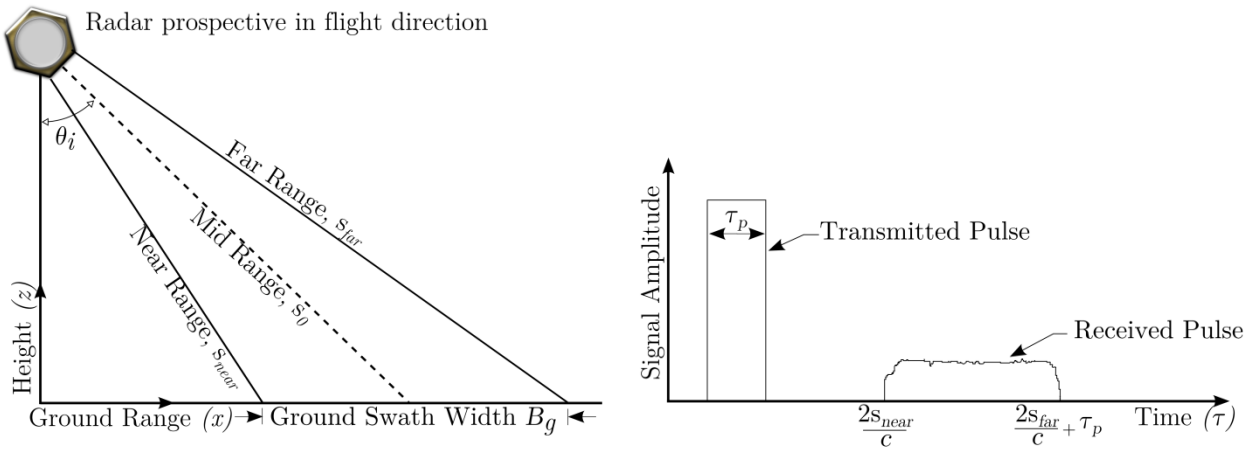

(a) (b)

Figure 2.4 - (a) Viewing prospective of Figure 2.1 in the plane *(x,z)*. (b) Pictorial description of the timing in range direction.

Referring to Figure 2.4(a) it is straightforward that the ground swath width is $B_g = (s_{far} - s_{near})/\sin(\theta_i)$. Figure 2.4(b) is the timing diagram of transmitted and received pulse. Assuming in $\tau = 0$ the start time of the transmitted pulse of length τ_p, the start time of the

received pulse is $2s_{near}/c$ and stop time is $(2s_{far} + c\tau_p)/c$. In order that, the recording of the signal coming from the entire illuminated swath is completed before the transmission of the next pulse, the PRF must obey to following inequality (Tomiyasu, 1978):

$$\mathrm{PRF} < \frac{c}{2[B_g \sin(\theta_i) + \tau_p]} \tag{2.12}$$

Equation (2.12) provides the upper PRF limit and is known as range ambiguity limit because it provides the max unambiguous swath width when the radar operates in StripMap mode. Although the new generation of SAR satellite are designed keeping into account Equation (2.12), there are still particular situations where range ambiguity show up as ghosting replica of real point/distributed targets. This happens when the backscatter of a real target coming from the range antenna pattern side-lobe direction is stronger than backscatter of the target coming from antenna bore-sight direction (see Figure 2.5).

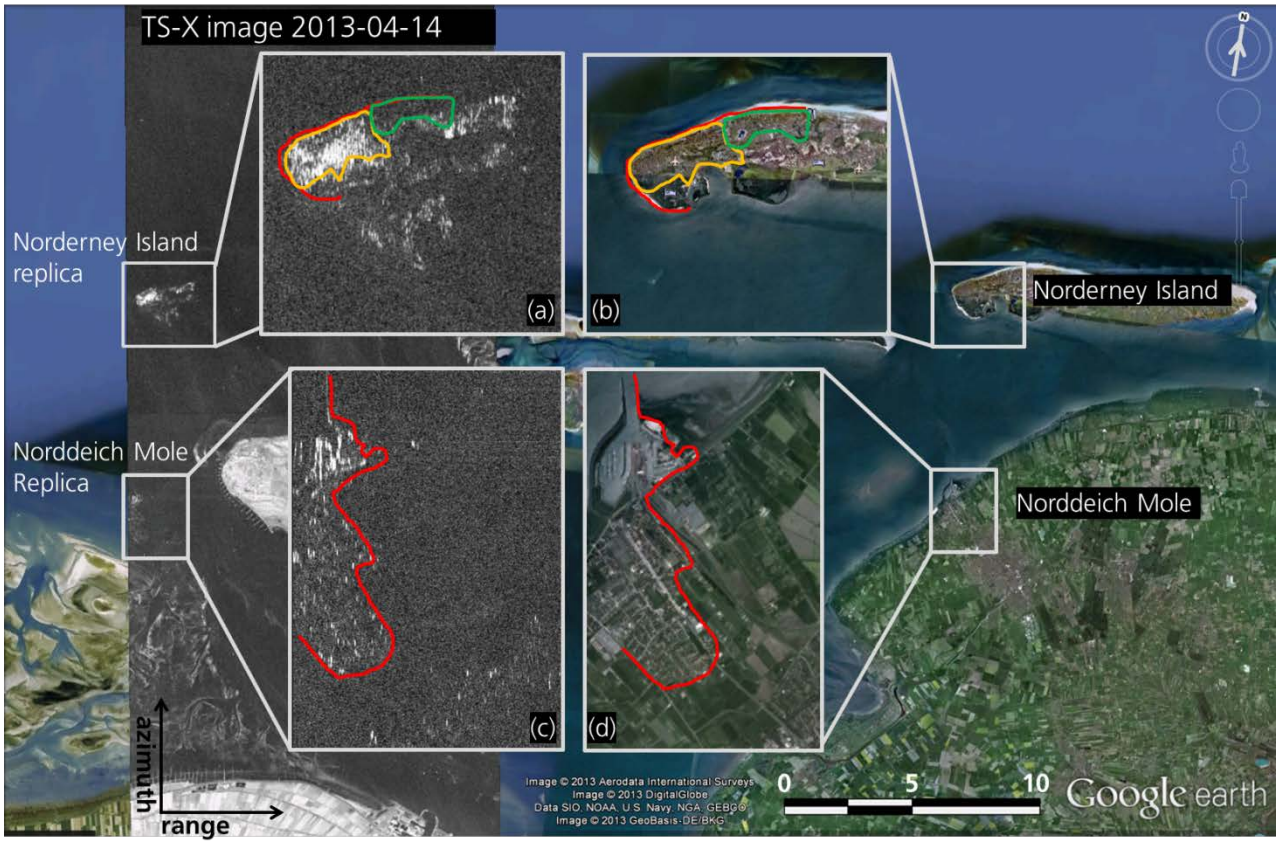

Figure 2.5 - Range ambiguity caused by side-lobe energy coming from distributed target outside the radar ground illuminated area. (a)-(c) ghosting replica of the real distributed targets (b)-(d)

A quality measure parameter often used to define the impact of range ambiguity is the integrated range ambiguity to signal ratio ($RASR$):

$$RASR \approx \frac{\sum_{j \neq 0} \sigma_j^0 G_j^2 / s_j^3 \sin(\theta_j)}{\sigma^0 G^2 / s^3 \sin(\theta)} \tag{2.13}$$

where j is the index of range ambiguity location, σ_j^0 it refers to the given incidence angle θ_j and G is the range antenna pattern (Curlander and McDonough, 1991; Ulaby et al., 1986).

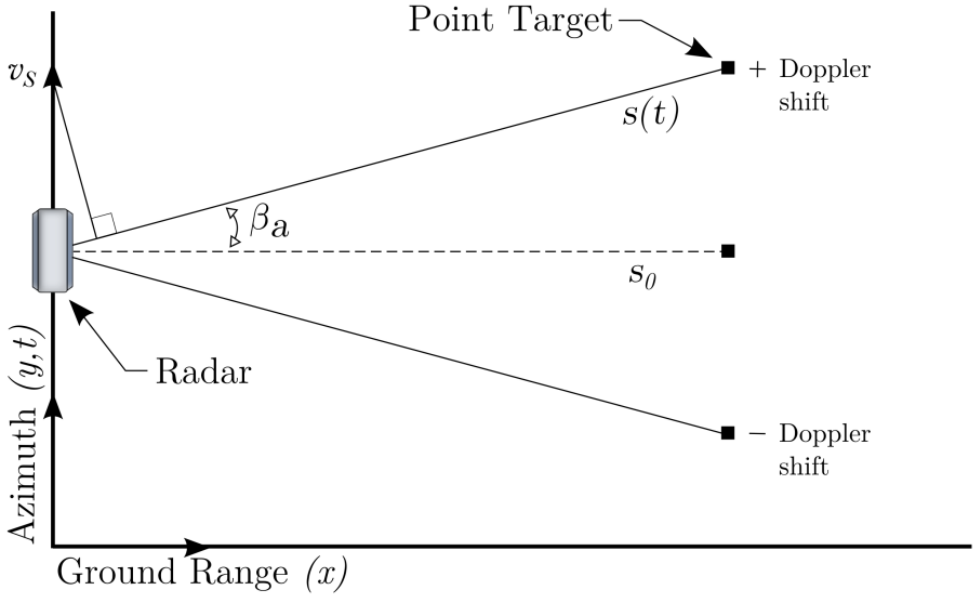

Figure 2.6 - Viewing prospective of Figure 2.1 in the plane *(x,y)*.

Because SAR's pulsed nature also the ambiguous returns in azimuth need to be considered. In (Tomiyasu, 1978), four different approaches are presented to deal with the ambiguous return in azimuth and all conclude to the same limitation of the PRF. For brevity, only the one based on the maximum Doppler shift is reviewed. The ambiguous response in azimuth is caused by a situation where a target illuminated by the radar beam produces a Doppler shift by an amount equal to the PRF. In this situation the receiver will not be able to discriminate between the received signal and the one coming from bore-sight direction. Hence in order to solve this ambiguity the PRF must be higher than the maximum Doppler shift of targets located at beam egde, i.e. Doppler bandwidth:

$$PRF \geq B_D = 2v_r/\lambda \tag{2.14}$$

Referring to the Figure 2.6, the radial velocity can be approximated to $v_r = v_S \sin(\beta_a) \approx v_S \, \beta_a$ that introduced into the Equation (2.14) provides the lower limit of the PRF in terms of antenna length or azimuth resolution (Tomiyasu, 1978):

$$PRF \geq \frac{2v_S\beta_a}{\lambda} = \frac{2v_S}{L_a} = \frac{v_S}{\delta_a} \tag{2.15}$$

Figure 2.7 illustrates the effects of the finite sampling of the azimuth frequency spectrum and the azimuth ambiguity inside the total azimuth processed bandwidth (PBW). It is noticeable the fine agreement between the theoretical AAP and the one annotated in a standard TS-X product. Also for azimuth ambiguity a quality measure is often used and is given by the azimuth ambiguity to signal ratio ($AASR$):

$$AASR \approx \frac{\sum_{m\neq 0} \int_{-B_p/2}^{+B_p/2} G^2(f + mPRF)df}{\int_{-B_p/2}^{+B_p/2} G^2(f)df} \tag{2.16}$$

where B_p is the total azimuth processed bandwidth and G in this case is the AAP. Equation (2.16) suggests that the azimuth ambiguities need only to be evaluated over the azimuth processed bandwidth to achieve the designed azimuth resolution (Tomiyasu, 1978).

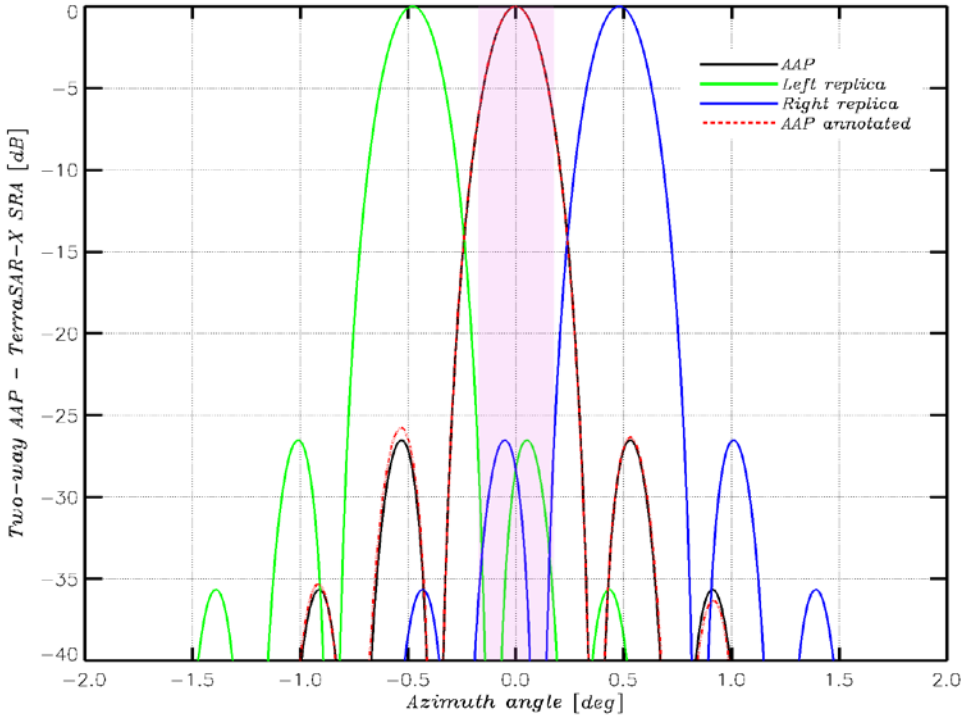

Figure 2.7 - Theoretical and annotated TS-X two-way azimuth antenna pattern (AAP) for the single receive antenna (SRA) mode. First left and right replicas due to the sampling at annotated PRF= 3802 Khz. The pink shaded area is the total processed azimuth bandwidth PBW = 2765 Khz.

It is evident that range and azimuth ambiguity are SAR artefacts related with antenna side-lobe. In order to control side-lobe energy, often windows (i.e. weighting functions also known in antenna design as tapering function) are used during processing to attenuate the spectra towards the edge of the processed frequency band. Generally the introduction of a weighting function further deteriorates the resolutions given by Equations (2.6)-(2.7) and peak signal-to-noise ratio. During the TS-X commissioning phase a trade-off between sharpness and low side-lobes has been found to be a weighting function type Hamming with coefficient ~0.6 (Breit et al., 2010; Mittermayer et al., 2010).

2.2. Polarimetric SAR Principles

A difficult task when dealing with imaging radar data is the interpretation of the measurements' temporal and spatial changes into geophysical information about the

observed target. In general, the backscattered power alone provides partial information that may lead to an inaccurate interpretation. Polarimetry is the science of measuring orientation and object shape through the geometrical properties of EM propagating in space (Cloude, 2009; Elachi et al., 1990; Lee and Pottier, 2009; Mott, 2006). In particular, the shape that the electric field draws with time on the plane transverse to the direction of propagation contains the information on the interaction between the EM with the material bodies and with the propagation medium. For example, two different targets interact with the same polarized EM scattering a wave with different polarimetric signature. Therefore, this can be exploited to discriminate among observed targets.

2.2.1. Wave Polarimetry

Considering an orthogonal basis $(\hat{x}, \hat{y}, \hat{z})$ defined so that the direction of propagation $\hat{k} = \hat{z}$, an EM in the far field zone propagates as a plane wave. The electric field of a plane wave is given by the solution of the wave equation derived from Maxwell's equation assuming loss-free medium. In the time domain and for the established orthogonal basis, the electric field takes the vectorial form (Lee and Pottier, 2009):

$$\vec{E}(z,t) = \begin{bmatrix} E_{0x} cos(\omega t - k_c z + \phi_x) \\ E_{0y} cos(\omega t - k_c z + \phi_y) \\ 0 \end{bmatrix} \tag{2.17}$$

where k_c is the complex wave number and is function of the complex permittivity, complex permeability and angular frequency ω. E_{0x}, E_{0y} are the amplitudes and ϕ_x, ϕ_y are the phases at the origin. Depending of the values of the phases at the origin (ϕ_x, ϕ_y) and the amplitudes (E_{0x}, E_{0y}), three types of polarization can be specified:

- Linear polarization: $\phi_x = \phi_y$
- Circular polarization: $\phi_x = \phi_y + \frac{\pi}{2} + n\pi$ and $E_{0x} = E_{0y}$
- Elliptic polarization: Otherwise

In the general case of elliptic polarization, the tip of the electric field vector draws on the transverse plane an ellipse that can be characterized by three parameters shown in Figure 2.8 (Boerner et al., 1981; Cloude, 2009; Lee and Pottier, 2009):
The amplitude of the ellipse:

$$A_e = \sqrt{E_{0x}^2 + E_{0y}^2} \tag{2.18}$$

The ellipse orientation angle $\phi_e \in [-\pi/2\,, \pi/2]$:

$$\tan(2\phi_e) = 2\frac{E_{0x}E_{0y}}{E_{0x}^2 - E_{0y}^2}\cos(\phi_y - \phi_x) \tag{2.19}$$

The ellipticity $\tau_e \in [-\pi/4\,, \pi/4]$:

$$|\sin(2\phi_e)| = 2\frac{E_{0x}E_{0y}}{E_{0x}^2 + E_{0y}^2}|\cos(\phi_y - \phi_x)| \tag{2.20}$$

The sense of rotation is determined by the sign of the τ_e, while looking in the direction of propagation $\hat{k} = \hat{z}$. A right hand rotation is linked to a negative sign, whereas a positive sign is connected to a left hand rotation (Boerner et al., 1981).

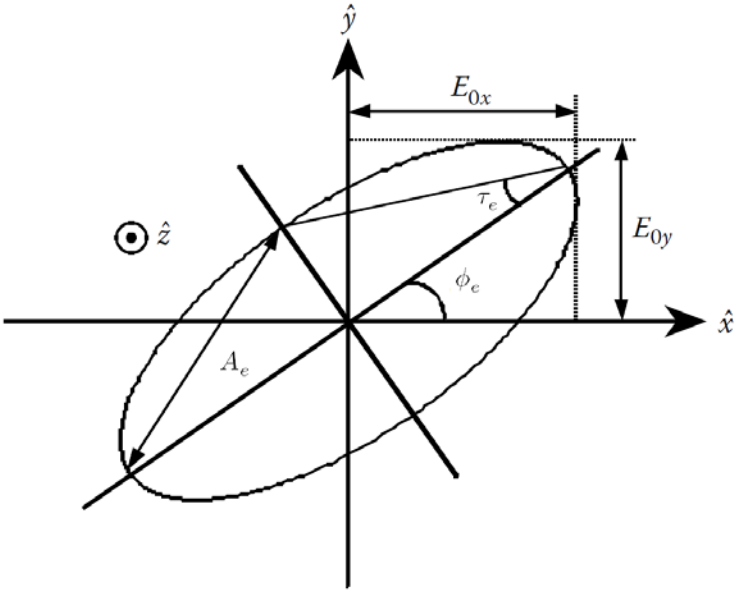

Figure 2.8 – Polarization ellipse.

An alternative and compact way to describe a plane monochromatic wave is given by the *Jones vector*:

$$\underline{E}_{ij} = \begin{bmatrix} E_i \\ E_j \end{bmatrix} \tag{2.21}$$

where E_i and E_j are the complex components of the field in two orthogonal coordinate transverse to the propagation direction. One of the commonly used orthogonal basis is the horizontal (h) and vertical (v) polarizations basis, hence the *Jones vector* is expressed as $\underline{E}_{hv} = [E_h \quad E_v]$ (Lee and Pottier, 2009).

2.2.2. Scattering Matrix and Pauli Vector

The incident and the scattered *Jones vectors* ($\underline{E}^i, \underline{E}^s$ respectively) are related by the complex 2x2 scattering matrix S:

$$\begin{bmatrix} E_h^s \\ E_h^s \end{bmatrix} = F(s) \begin{bmatrix} \dot{S}_{hh} & \dot{S}_{hv} \\ \dot{S}_{vh} & \dot{S}_{vv} \end{bmatrix} \begin{bmatrix} E_h^i \\ E_h^i \end{bmatrix} \tag{2.22}$$

where $F(s)$ is the spherical wave factor of far field zone. The diagonal elements of S describe the changes in the scattered wave depending on the incident wave that has the

same basis as the scattered one, therefore they are called the co-polar channel coefficients. The off-diagonal elements describe the relation of the scattered wave with the incident wave of the orthogonal base, as part of the incident wave with a certain polarisation is transferred to the orthogonal polarisation in the scattering process, therefore the off-diagonal elements are known as the cross-polar channel coefficients. With transmitter and receiver collocated (monostatic radar), the cross-polar channel coefficients are almost identical $\dot{S}_{hv} \approx \dot{S}_{vh}$ (with the exception of noise) under the reciprocity theorem (Cloude, 2009; Lee and Pottier, 2009). As a consequence, S is characterized by 3 rather than 4 complex scattering coefficients. This leads to a vector rather than matrix representation, which is often easier to handle. Two standard basis, *Lexicographic* (indicated with subscript L) and *Pauli* (indicated with subscript P), define the homonym scattering features vectors:

$$k_L = \begin{bmatrix} \dot{S}_{hh} & \sqrt{2}\dot{S}_{hv} & \dot{S}_{vv} \end{bmatrix}^T \tag{2.23}$$

and

$$k_P = \frac{1}{\sqrt{2}} \begin{bmatrix} \dot{S}_{hh} + \dot{S}_{vv} & \dot{S}_{hh} - \dot{S}_{vv} & 2\dot{S}_{hv} \end{bmatrix}^T \tag{2.24}$$

2.2.3. Second Order Statistic

The scattering matrix S describes the scattering from a point target, but it is insufficient to describe the scattering from a distributed target such as natural scenes. Statistically based matrices are required for the full description of such cases.

The outer product of the scattering vector k_L (k_P) and its adjoint vector, together with an averaging operation $\langle \cdot \rangle$, leads to the covariance matrix C_3 (coherency matrix T_3), which is 3x3 as only monostatic case is considered (Cloude, 2009; Elachi et al., 1990; Lee and Pottier, 2009):

$$\mathrm{C}_3 = \langle k_L \cdot k_L^H \rangle = \begin{bmatrix} \langle |\dot{S}_{hh}|^2 \rangle & \sqrt{2}\langle \dot{S}_{hh}\dot{S}_{hv}^* \rangle & \langle \dot{S}_{hh}\dot{S}_{vv}^* \rangle \\ \sqrt{2}\langle \dot{S}_{hv}\dot{S}_{hh}^* \rangle & 2\langle |\dot{S}_{hv}|^2 \rangle & \sqrt{2}\langle \dot{S}_{hv}\dot{S}_{vv}^* \rangle \\ \langle \dot{S}_{vv}\dot{S}_{hh}^* \rangle & \sqrt{2}\langle \dot{S}_{vv}\dot{S}_{hv}^* \rangle & \langle |\dot{S}_{vv}|^2 \rangle \end{bmatrix} \tag{2.25}$$

and

$$\begin{aligned} \mathrm{T}_3 &= \langle k_P \cdot k_P^H \rangle \\ &= \frac{1}{2} \begin{bmatrix} \langle |\dot{S}_{hh} + \dot{S}_{vv}|^2 \rangle & \langle (\dot{S}_{hh} + \dot{S}_{vv})(\dot{S}_{hh} - \dot{S}_{vv})^* \rangle & 2\langle (\dot{S}_{hh} + \dot{S}_{vv})\dot{S}_{hv}^* \rangle \\ \langle (\dot{S}_{hh} - \dot{S}_{vv})(\dot{S}_{hh} + \dot{S}_{vv})^* \rangle & \langle |\dot{S}_{hh} - \dot{S}_{vv}|^2 \rangle & 2\langle (\dot{S}_{hh} - \dot{S}_{vv})\dot{S}_{hv}^* \rangle \\ 2\langle \dot{S}_{hv}(\dot{S}_{hh} + \dot{S}_{vv})^* \rangle & 2\langle \dot{S}_{hv}(\dot{S}_{hh} - \dot{S}_{vv})^* \rangle & 4\langle |\dot{S}_{hv}|^2 \rangle \end{bmatrix} \end{aligned} \tag{2.26}$$

where $(\cdot)^H$ is the adjoint operator and $(\cdot)^*$ is the conjugate operator.

As can be seen in Equation (2.25), the diagonal elements of C_3 correspond to the power of each channel, while the off-diagonal are the correlation coefficient between those channels. Equivalently from Equation (2.26), the diagonal elements of T_3 are the power of the *Pauli* components and the off-diagonal are the correlation between them. An import property of C_3 and T_3 is that both are Hermitian positive semi-definite matrices which implies that they possess only real non-negative eigenvalues with orthogonal eigenvectors. C_3 and T_3 are related to each other by a unique transformation (Cloude, 2009; Elachi et al., 1990; Lee and Pottier, 2009; Mott, 2006).

The received SAR signal of almost any natural media is a mixed response of different scattering processes occurring within the resolution cell. Therefore polarimetric decomposition techniques have been developed and used to separate the different scattering contributions (Cloude and Pottier, 1996). Two different types of incoherent decompositions can be deduced for polarimetric SAR data analyses: eigenvalue decompositions and model-based decompositions.

2.2.4. Eigenvalue decomposition

Eigen decomposition is a technique to decompose the second order statistic matrixes into a maximum of three scattering mechanisms where each can be represented with a single scattering matrix and it is orthogonal to the others. The outputs of the eigenvalue decomposition are the polarimetric parameters *entropy*, *mean alpha angle* and *anisotropy*. These are in turn used to interpret the scattering mechanisms even if they are not completely orthogonal or in case of more than three scattering mechanisms exist within the observed cell. Given the properties of the second order statistic matrixes (coherency and covariance), the eigenvalue decomposition can be applied indifferently to one of them as the eigenvalues are equal. For purely annotation purposes, the formulation is given for the coherency matrix T_3.

The diagonalization of T_3 is described in Equation (2.27):

$$T_3 = [\underline{e}_1 \;\; \underline{e}_2 \;\; \underline{e}_3] \begin{bmatrix} \lambda_1 & 0 & 0 \\ 0 & \lambda_2 & 0 \\ 0 & 0 & \lambda_3 \end{bmatrix} [\underline{e}_1 \;\; \underline{e}_2 \;\; \underline{e}_3]^{-1} = \sum_{j=1}^{3} \lambda_j \, \underline{e}_j \cdot \underline{e}_j{}^H \tag{2.27}$$

where λ_j and e_j is the j-th eigenvalue, eigenvector. The coherency matrix is usually of $rank(T_3) = 3$, which is the extreme case when T_3 is made up of three different scattering mechanisms, i.e., $\lambda_1 = \lambda_2 = \lambda_3 \neq 0$. This is the case of completely de-correlated, non-polarized random scattering behaviour. On the other hand for $rank(T_3) = 1$, i.e., one nonzero eigenvalue, a single scattering mechanism exists within the observed resolution cell. Partially polarized scatterers, i.e., nonzero and nonequal eigenvalues, occur between these two cases (Cloude, 2009; Elachi et al., 1990; Lee and Pottier, 2009; Mott, 2006). The spread of total scattered power across the eigenvalues is evidently a good indicator of

depolarization. By first normalizing the eigenvalues to unit sum, the three probabilities P_j are defined as:

$$P_j = \frac{\lambda_j}{\lambda_1 + \lambda_2 + \lambda_3} \qquad P_j \in [0,1] \tag{2.28}$$

The spread of probabilities can then be represented by a single scalar, the *entropy* defined as:

$$H = -\sum_{j=1}^{3} P_j \log_3 P_j \qquad H \in [0,1] \tag{2.29}$$

which is zero for zero depolarisation, and one for maximum depolarisation. To account for the polarised component, from each eigenvector $\underline{e}_j = [\underline{e}_{1,j} \;\; \underline{e}_{2,j} \;\; \underline{e}_{3,j}]$ a scattering mechanism α_j can be selected as a suitable basic rotation invariant polarised parameter (Cloude, 2009):

$$\underline{e}_j = [\cos\alpha_j \exp(i\phi_{1,j}) \quad \sin\alpha_j \cos\psi_j \exp(i\phi_{2,j}) \quad \sin\alpha_j \sin\psi_j \exp(i\phi_{3,j})]^T \tag{2.30}$$

with $\alpha_j = \cos^{-1}(|e_{1,j}|)$ and $\alpha_j \in [0°, 90°]$. ψ is the rotation angle around the line of sight (LOS) and ϕ is the scattering phase angle which accounts for the phase relations between the elements of the vector. The statistical interpretation suggests forming an average as a sum of the three α_j values, weighted by their probabilities P_j, so it is possible to form the average alpha angle (Cloude, 2009):

$$\overline{\alpha} = P_1\alpha_1 + P_2\alpha_2 + P_3\alpha_3 \tag{2.31}$$

which has the physical interpretation given in Figure 2.9.

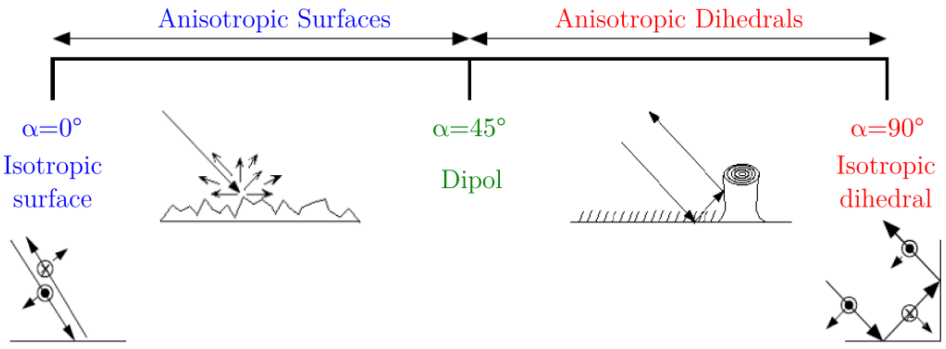

Figure 2.9 – Physical interpretation of the average alpha angle.

An effective method to aid the interpretation of different types of polariser/depolariser, is the bi-dimensional distribution of the two parameters *entropy* and *alpha* derived from T_3. In fact, H rises when the degree of statistical disorder increases and $\overline{\alpha}$ can be used to identify the average underlying scattering mechanism. Such scatterplot is shown in Figure 2.10 and is commonly named $H/\overline{\alpha}$ plane (Cloude and Pottier, 1997).

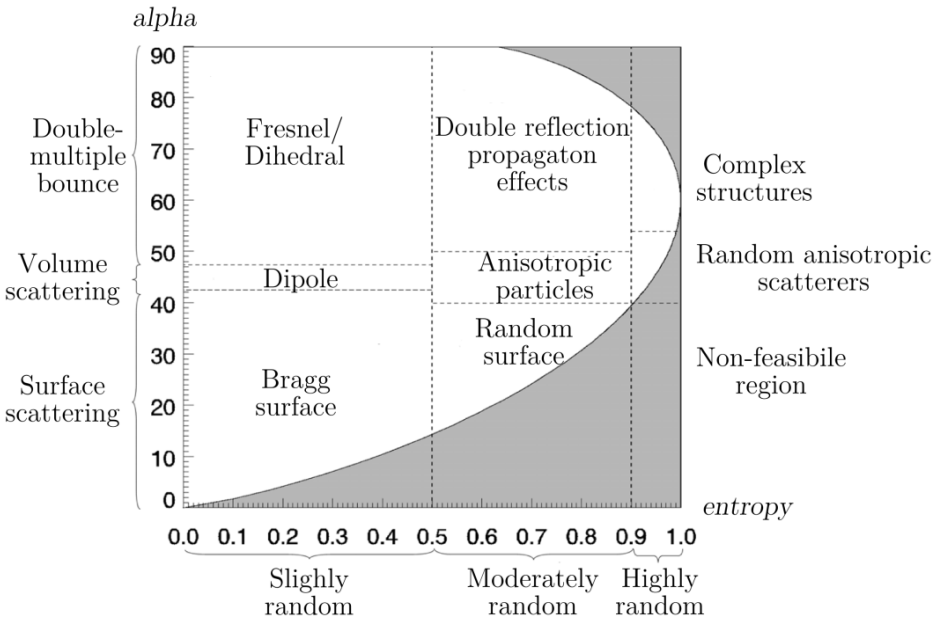

Figure 2.10 – Two-dimensional $H/\overline{\alpha}$ plane for 3x3 coherency (covariance) matrix.

An additional polarimetric parameter, which is derived from the lower order eigenvalues (therefore related to the secondary scattering mechanisms), is the *anisotropy* (Cloude, 2009; Lee and Pottier, 2009):

$$A = \frac{\lambda_2 - \lambda_3}{\lambda_2 + \lambda_3} = \frac{P_2 - P_3}{P_2 + P_3} \tag{2.32}$$

2.2.5. Model based decomposition

For the sake of completeness, model-based decomposition theory is briefly introduced although this approach is not taken into account. This type of decomposition uses predefined physical scattering models to interpret the scattering process. An example is the Freeman-Durden decomposition proposed in (Freeman and Durden, 1998). It considers three simple and primary scattering mechanisms: surface, dihedral and volume. The mechanisms are modelled and incoherently added such that the total coherency matrix is considered to be the accumulation of the three main contributions:

$$\mathrm{T}_3 = [\mathrm{T}_S] + [\mathrm{T}_D] + [\mathrm{T}_V] \tag{2.33}$$

The total power P_t can be retrieved from the trace of the single scattering component matrices (Freeman and Durden, 1998):

$$P_t = Tr([\mathrm{T}_S]) + Tr([\mathrm{T}_D]) + Tr([\mathrm{T}_V]) = P_S + P_D + P_V, \tag{2.34}$$

which is generally used to normalize the power of each scattering component and enables a fair comparison of the strength of the different scattering contributions. In comparison to the

eigenvalue decomposition, scattering mechanisms with a rank higher than one can be included in the modeling.

2.3. New Generation High Resolution SAR: TerraSAR-X

The TS-X mission began on June 15th 2007 with the launch of the first of the 2 satellites that forms the TanDEM-X (TD-X) mission (TerraSAR-X add-on for Digital Elevation Measurements). The TD-X satellite, near identical to the TS-X one, has been launched in June 2010. The two satellites, flying in a close orbit configuration, form a single-pass radar interferometer. The instruments on both satellites are high-resolution X-band SARs based on active phased array technology. The center frequency is $f_0 = 9.65$ GHz with a selectable chirp bandwidth W_r of up to 300 MHz. With a nominal range bandwidth of 150 MHz and an azimuth antenna length of 4.8m, theoretical $\delta_r = 0.89$m and $\delta_a = 2.4$m are achievable for single polarization StripMap acquisitions. In order to improve the *AASR*, *RASR* and the shape of the point target response (*PTR*), the range and azimuth resolutions are degraded to constant 1.2m and 3.3m, respectively, making use of Hamming weighting function.

A TS-X acquisition is a non-coordinated SAR instrument data take by one of satellites of the TD-X constellation (either TS-X or TD-X satellite) that is not in the radar shadow of the other one. All investigations in the context of this thesis are based on TS-X data.

2.3.1. First Spaceborne X-band SAR with coherent polarimetric capabilities

The TS-X mission provides a selection of SAR products, ranging from 10 km swath width at ~1m resolution to 100 km swath width at ~18m resolution, operationally to the scientific and commercial community. The satellite offers 3 different acquisition modes – ScanSAR (SC), StripMap (SM) and Spotlight (SL) – in a full performance incidence angle acquisition range between 20° and 45° (extended to 55° for SL). The High resolution Spotlight (HS) exploits a faster beam steering resulting in an additional gain in azimuth resolution at expenses of azimuth coverage (5 km instead of 10 km). In 2013 the product portfolio has been extended at both edges, adding a 6 beams ~40m resolution Wide-ScanSAR (WSC) mode and the new Staring Spotlight (ST) mode capable to achieve azimuth resolution below 24 cm (Breit et al., 2014; Prats-Iraola et al., 2012).

The SM mode can operate in single or in dual polarization mode, resulting in one or two image layers. Each layer is identified by two letters indicating the transmitted and received polarization (H for horizontal, V for vertical). Dual polarization SM products are selectable between one of the following combination HH-HV, HH-VV and VH-VV. Due to the constraint of the SL imaging mode, the only dual polarization combination possible is HH-VV. SC and WSC products are available only in single polarization mode and selectable as one among the four possible combination HH, HV, VH or VV.

The acquisition of the two image layers with different transmitting/receiving antenna polarization is implemented by toggling transmit and/or receive polarization between consecutive pulses (pulse interleaved). The effective *PRF* in each channel is thus half of the total *PRF*. In order to sample properly the antenna azimuth spectrum in each channel, the total *PRF* should be increased up to the double compared to the one in single polarization mode. Because of an upper total *PRF* limit of 6.5 kHz, the effective *PRF* per channel in SM dual polarization products is decreased. As consequence the effective azimuth resolution is worsened by a factor of 2 (i.e. 6.6m). Moreover, due to the increased total *PRF*, the maximum ground swath width is only half of the single polarization mode in order to keep range and azimuth ambiguities under the design goal.

2.3.2. Experimental Dual Receive Antenna DRA mode

The DRA of the TS-X/TD-X instrument is used for experimental data acquisitions in SM mode only. The whole antenna (4.8 m) is electrically split into two halves (2.4 m each). The preceding and the succeeding halves in flight direction are called the *fore*- and *aft*-channels, respectively. Figure 2.11 depicts the DRA of TS-X, which is used for along track interferometry (ATI, with a spatial baseline of 2.4 m between both channel phase centers) or fully polarized acquisitions (HH-HV-VH-VV, via toggling the two linear polarizations in transmission and receiving both linear polarizations using the redundant receiving chain) (Mittermayer and Runge, 2003).

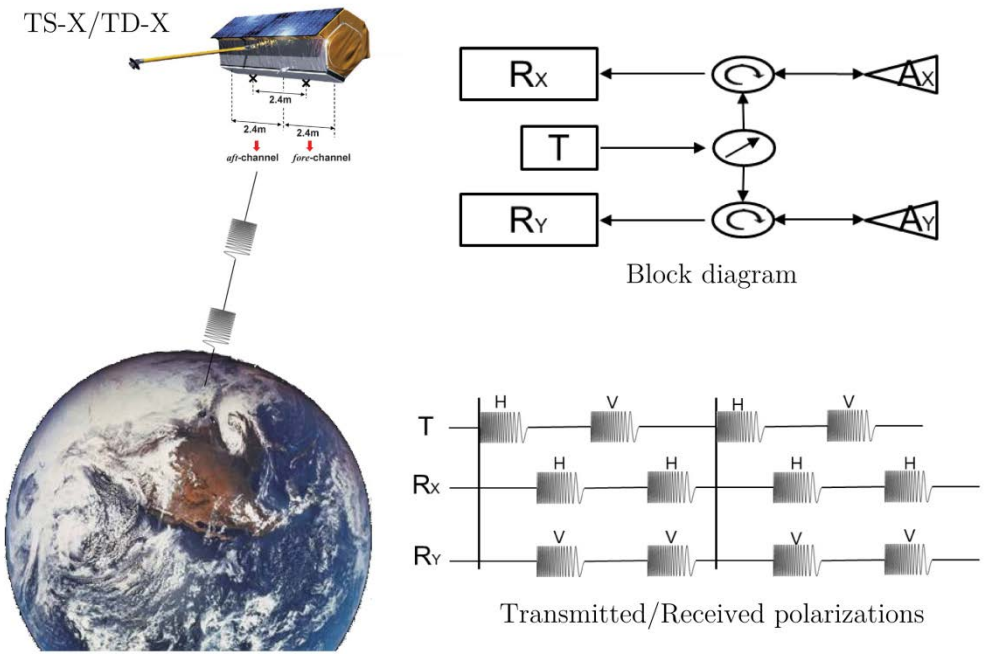

Figure 2.11 – TerraSAR-X DRA realization with block diagram and transmit/receive pulse timing diagram for fully polarized acquisitions.

3. Marine Pollution Detection and Discrimination

Pollution is the term used to indicate the introduction of harmful contaminants that are outside the norm for a given ecosystem. Common man-made contaminants (or pollutants) that reach the oceans include: pesticides, herbicides, chemical fertilizers, detergents, oil, sewage, plastics, and other solids. The dumping of man-made pollutants into ocean ecosystems was legal until 1970's when it became regulated. Nevertheless, the implemented laws by the 1972 Stockholm Conference didn't stop the illegal dumping of waste into the ocean. On this matter, the United Nations (UN) met in London in 1975 to begin the *Convention on the Prevention of Marine Pollution by Dumping of Wastes and Other Matter*. The International Maritime Organization (IMO) was given responsibility for this convention and a protocol for the prevention of pollution from ships (MARPOL 73/78) was adopted as major step in the regulation of sea pollution caused by oil and harmful substances.

As known, petroleum products play an important role in modern society. The term *Oil* is used to indicate any type of hydrocarbon and petroleum products. An oil spill can occur in water, ice or land and may be due to a number of reasons. Marine oil spills can be highly dangerous since wind, waves and currents can scatter a large oil spill over a wide area within a few hours in the open sea (Fingas, 2012). The environmental impacts of an oil spill can be considerable, as it causes a decline in phytoplankton and other aquatic organisms. The livelihood of many coastal people can be impacted by oil spills, particularly those whose livelihood is based on fishing and tourism (Al-Khudhairy, 2002).

In the event of an anthropogenic, natural or accidental oil spill, information about the size and extent of the spill is critical to assist the government and industry in oil spill contingency planning.

3.1. Introduction

Remote sensing is particularly useful to detect and monitor oil spill in the marine environment. Although satellite remote sensing suffers from low temporal (and in same case spatial) resolution, it provides a synoptic view and a cost effective approach compared to traditional monitoring system operated either by airborne or shipborne.

Nowadays, remote sensing sensors used for operational marine oil spill detection and classification include infrared video and photography, thermal infrared imaging, airborne laser fluoro-sensor, optical sensor, microwave radiometer and radar. Table 3.1 summarizes their main technical characteristics in the context of oil spill application (Al-Khudhairy, 2002; Jha et al., 2008; Klemas, 2010).

For oil spill contingency planning the following information must be timely provided (Fingas, 2012; National Research Council, 2003):

- The location and spread of oil spill over a large area;
- The thickness distribution of an oil spill to estimate the quantity of spilled oil;
- A classification of the oil type in order to estimate environmental damage and to take appropriate response activities;
- Any other valuable information to assist the clean-up operations.

Table 3.1 – Characteristics of various types of sensors used for operational oil spill detection in European waters.

	LFS/UV	**Visible**	**Infrared**	**Microwave Radiometer**	**Radar**
Wavelength	0.3 -0.4 μm	0.4 -0.7 μm	0.7 -14 μm	0.2 -0.8 cm	1 -30 cm
Type	Active/Passive	Passive	Passive	Passive	Active
Measure	Fluorescence /Reflectivity	Reflectivity	Emissivity	Emissivity	Reflectivity
Oil appearance	Bright	Bright	Dark/Bright	Bright	Dark
Oil Thickness	Yes <20 μm	No	Yes Relative	Yes <1 mm >50 μm	Not sensible to thin layer
Platform	Aircraft	Aircraft	Aircraft	Aircraft/Satellite	Aircraft/Satellite
Coverage	Small	Medium	Medium	Large	Large/Very Large
Resolution	High 1D	High	High	Low	High/Very High
False alarms	None/Low	High	Medium	Low	High
Operability	24h/7d Clear sky	Daylight Clear sky	24h/7d No cloud and heavy fog	24h/7d No heavy rain	24h/7d(1) Wind speed limited(2)
Cost (K€)	100-2000	0.25-20	1-200	400-2000	1200-8000

(1) Atmospheric blockage phenomenon at high frequencies might hamper sea monitoring reducing the operability.
(2) The lower bound is related to the scattering, while the upper bound is related to the breaking of the oil film, i.e. not a sensor limitation.

It must be noted that these information can't be delivered by a single sensor but only using a combination of them (see Table 3.1). An example of maritime pollution system, that combines several of these sensors, is represented by the Dornier DO 28 D2 aircraft. A fleet composed by 2 aircrafts has been set-up by the German Federal Ministry of Transport to monitor the North and Baltic Sea. Each of them is equipped with Side-Looking Airborne Radar (SLAR), UV/IR scanner and MWR. Since 1991 the Dornier DO 228-212 aircraft substitute the predecessor with an update on the sensors portfolio that includes a LSF (Grüner et al., 1991).

Figure 3.1 shows an example of oil spill accidental disaster observed by MODIS-AQUA optical satellite (left) and TS-X radar satellite (right) within a short time difference.

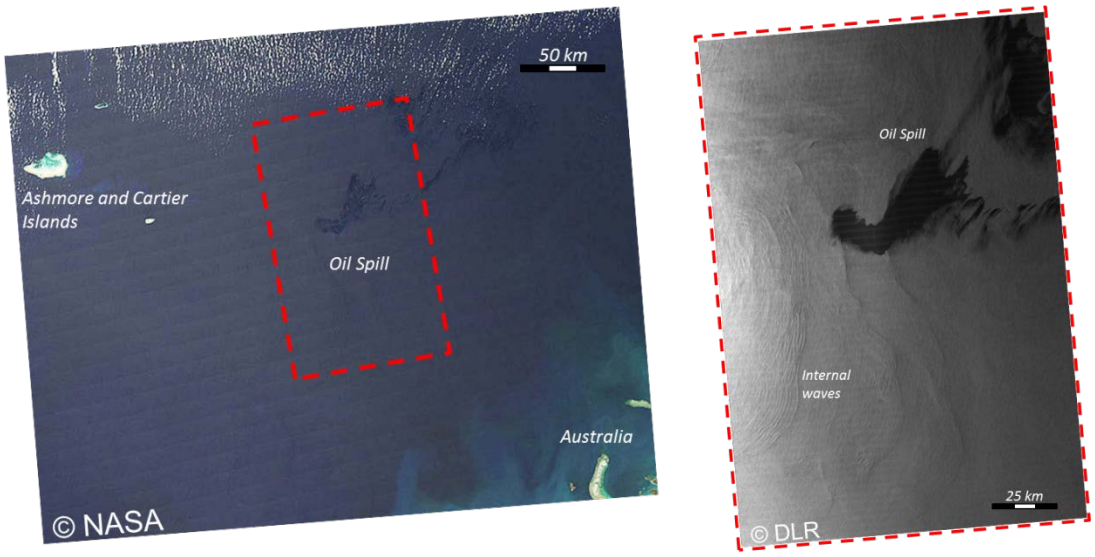

Figure 3.1 – Satellite observations of oil spill disaster in Timor Sea caused by blowout from the Montara wellhead platform on 21 August 2009. [Left] MODIS-AQUA optical image acquired on August 30, 2009 at 05:20UTC. [Right] TS-X radar image acquired on August 30, 2009 at 09:58 UTC.

Last but not least, multi-temporal observations can provide important information required to model oil spill drift and spreading. Oil spill models may be useful for clean-up operations and controlling the oil spill (Baschek et al., 2011).

Among the sensors listed in Table 3.1, satellites equipped with SAR are particularly suitable as early warning detection of oil spills, thanks to the superiority in terms of operability, coverage and resolution compared to other sensors (Table 3.1). On the other hand, the drawbacks are the SAR inability to classify different oil types and the high number of false alarms.

This chapter is dedicated to the **Objective 1**. After a brief theoretical introduction to the scattering of EM wave from rough surfaces and a model for ocean radar backscatter, it follows the State-of-Art of oil spill detection using single-polarized satellite SAR data and a short summary of the methodology proposed in A.1 to exploit dual-polarization VHR TS-X SAR data.

3.1.1. Rough Surface Scattering

The interaction between the transmitted radar EM signals with the Earth's surface is governed by the surface roughness and dielectric properties (assuming negligible atmospheric influence in the microwave spectrum).

The relation between surface roughness and EM scattering is illustrated in Figure 3.2 by 3 meaningful cases: Figure 3.2(a) depicts a smooth surface with specular reflection symmetric to the incident angle and no backscatter; Figure 3.2(b) depicts a slightly rough surface with

a component of specular reflection (also known as coherent component) and a backscatter component (also known as incoherent or diffuse component); Figure 3.2(c) depicts a very rough surface with only diffuse components without any component of specular reflection. Rough surfaces hence produce more radar backscatter (Ulaby et al., 1982).

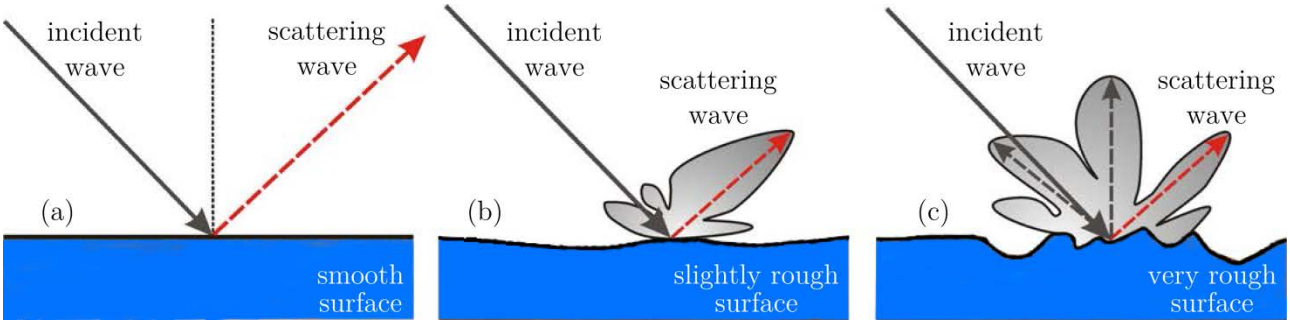

Figure 3.2 - Pictorial interpretations of the relationship between surface roughness and EM scattering pattern

The observable surface roughness depends on the EM incident wavelength, meaning that at decreasing frequencies the surface appears lesser rough. This turns, for instance, a rough surface sensed at X-band ($\lambda = 3cm$) into a smooth surface at L-band ($\lambda = 23cm$). The surface roughness is defined by the Rayleigh or Fraunhofer Criterion. The Rayleigh criterion states that a surface may be considered smooth if the phase difference between two reflected rays is less than $\pi/2$ rad, which leads to:

$$\Delta h < \frac{\lambda}{8 \cos \vartheta} , \tag{3.1}$$

where Δh is the standard deviation of the surface height. When the EM wavelength is in the order of Δh, Fraunhofer criterion is used instead (Ulaby et al., 1982):

$$h < \frac{\lambda}{32 \cos \vartheta} , \tag{3.2}$$

The complex dielectric constant is a measure of the medium response to an EM signal. This response is composed of two parts, and defined in terms of real and the imaginary parts as function of the incident wave frequency f (Hippel, 1954; Stratton, 2007):

$$\epsilon(f) = \epsilon'(f) - j\epsilon''(f), \tag{3.3}$$

where $\epsilon'(f)$ is referred to the permittivity of the material, whereas $\epsilon''(f)$ is referred to the dielectric loss factor of the material. It is common to refer to the relative permittivity ϵ_r, i.e., $\epsilon_r(f) = \epsilon(f)/\epsilon_0$, where ϵ_0 is the permittivity of vacuum. For most natural surfaces $\epsilon''(f) \ll \epsilon'(f)$ (Hippel, 1954). The permittivity of the material $\epsilon(f)$ affects the penetration depth (δ_p) of the EM signal into the medium. δ_p is by definition the distance in the medium over which the intensity of the propagating radiation is attenuated by the exponential factor

e^{-1}. Following this definition, a convenient δ_p expression (known ask skin depth) as function of $\epsilon(f)$ is given by (Ulaby et al., 1982)

$$\delta_p = \frac{\lambda\sqrt{\epsilon'}}{2\pi\epsilon''}, \tag{3.4}$$

3.1.2. Bragg Surface Scattering

Besides surface properties, there are a number of environmental factors (e.g., wind speed and direction relative to the radar beam) and sensor related parameters (e.g., incidence angle, polarization and frequency) that affect the radar backscatter from ocean surface. For example, an increase in wind speed results in a rougher surface and a stronger backscatter signal. Radar backscatter is max if the radar looks in the upwind direction and minimum if the radar looks in the direction normal to the wind direction (Ulaby et al., 1982). The ocean backscatter is known to decrease with increasing incidence angle. Stronger signals are obtained in VV compared to HH and the difference increases with incidence angle and the relative dielectric constant. The cross-polarization backscatter from ocean surface lays around 5 dB below the HH one, and can therefore easily reach the sensor noise floor (noise equivalent sigma naught, NESN) (Holt, 2004; Valenzuela, 1978).

The scattering from sea surfaces is commonly described using the Bragg scattering model (small perturbation model). Ocean wave spectrum contains waves ranging from short ripples of a few millimetres to waves of hundreds of meters long. In the simple case of only short ocean wave components, the ocean backscatter within typical SAR incidence angles (20° - 60°) is dominated by Bragg or resonance scattering. The backscatter arises from the resonance of incident EM wave (in the order of cm) with ocean wave components with similar wavelength, i.e. capillary and short gravity waves (Holt, 2004; Ulaby et al., 1986, 1982; Valenzuela, 1978). When an incoming EM wave with wavelength λ reaches the sea surface, the transmitted signal hits each successive surface crest at a slightly different time. If the excess distance from the radar to each crest is $\lambda/2$ (or a multiple of this), the phase difference between the return signals from each crest is 360°, and the signals add in phase. Otherwise, they add out of phase. The Bragg wavelength, λ_B, of ocean waves resulting in resonance is hence given by

$$\lambda_B = \frac{n\lambda}{2\sin\vartheta}, \tag{3.5}$$

where $n = 1,2,...$ is the order of resonance ($n = 1$ produces the dominant return) (Ulaby et al., 1982; Valenzuela, 1978). From Equation (3.5) it is evident that for a given λ the resonant waves are shorter at more oblique incidence angles, and at a given ϑ, λ_B increases with radar wavelength.

The first order ocean backscatter coefficients σ_0 following Bragg theory model are given by

$$\sigma_0^{XY}(\vartheta) = 4\pi k^4 \cos^4(\vartheta)|g_{XY}(\vartheta)|^2 \, W(2k\sin(\vartheta), 0), \tag{3.6}$$

where $W(\cdot)$ is the two-dimensional wave number spectral density of the surface roughness and the indices X and Y denote the polarization of the incident and backscattered radiation, respectively. The first-order scattering coefficients $g_{XY}(\vartheta)$ for horizontal-horizontal (HH) and vertical-vertical (VV) incident and backscattered polarization are given by

$$g_{HH}(\vartheta) = \frac{(\epsilon_r - 1)}{\left[\cos(\vartheta) + \sqrt{\epsilon_r - \sin^2(\vartheta)}\right]^2}, \tag{3.7}$$

and

$$g_{VV}(\vartheta) = \frac{(\epsilon_r - 1)[\epsilon_r(1 + \sin^2(\vartheta)) - \sin^2(\vartheta)]}{\left[\epsilon_r\cos(\vartheta) + \sqrt{\epsilon_r - \sin^2(\vartheta)}\right]^2}. \tag{3.8}$$

with cross-polarization (HV or VH) returns that are null (Ulaby et al., 1982; Valenzuela, 1978). It is clear from Equation (3.6) that only the coefficient g_{XY} changes depending on the incident/backscattered polarizations, hence $\sigma_0^{VV}/\sigma_0^{HH} = g_{VV}/g_{HH}$. It follows that the ratio of the backscatter coefficients depends only on ϑ and ϵ_r, and is independent of surface roughness. It can hence be used to evaluate the dielectric properties of the illuminated surface. Nevertheless, if second order terms in Equation (3.6) are not negligible, depolarization effects may be introduced with the consequence that the cross-polarization returns are no longer null (Valenzuela, 1967).

3.2. Oil spill monitoring by means of Single polarized SAR data

Anthropogenic inputs of materials to the sea surface microlayer include point sources as coastal industrial activity, agricultural and storm-water run-off, spills of mineral oil from coasts and vessels, natural oil seeps. The lipids molecules of oil (independently of the source it comes from) are characterized by long tails of atoms which forces the substance to stick out of sea water. A combined effect of their low water solubility and high intermolecular attraction results in a high surface viscosity and thus a high short-wave damping effect through an increase in surface tension and a reduction in wind friction (Espedal et al., 1996). Figure 3.3 summarizes the interaction of EM wave emitted by the radar with the ocean surface covered and not-covered by oil following the concepts previously introduced.

Being the EM pulse, emitted by the radar, sensitive to small scale surface roughness, the sea surface smoothed by the oil spill scatter away most of the incident EM energy, in contrast to the surrounding clean sea surface which backscatter is dominated by Bragg scattering. Visualizing the normalized radar cross section (NRCS) in a grayscale picture with low values given to black and high values given to white, the reduction of radar backscatter caused by the presence of an oil spill appears in SAR images as black area (see Figure 3.1 [Right]).

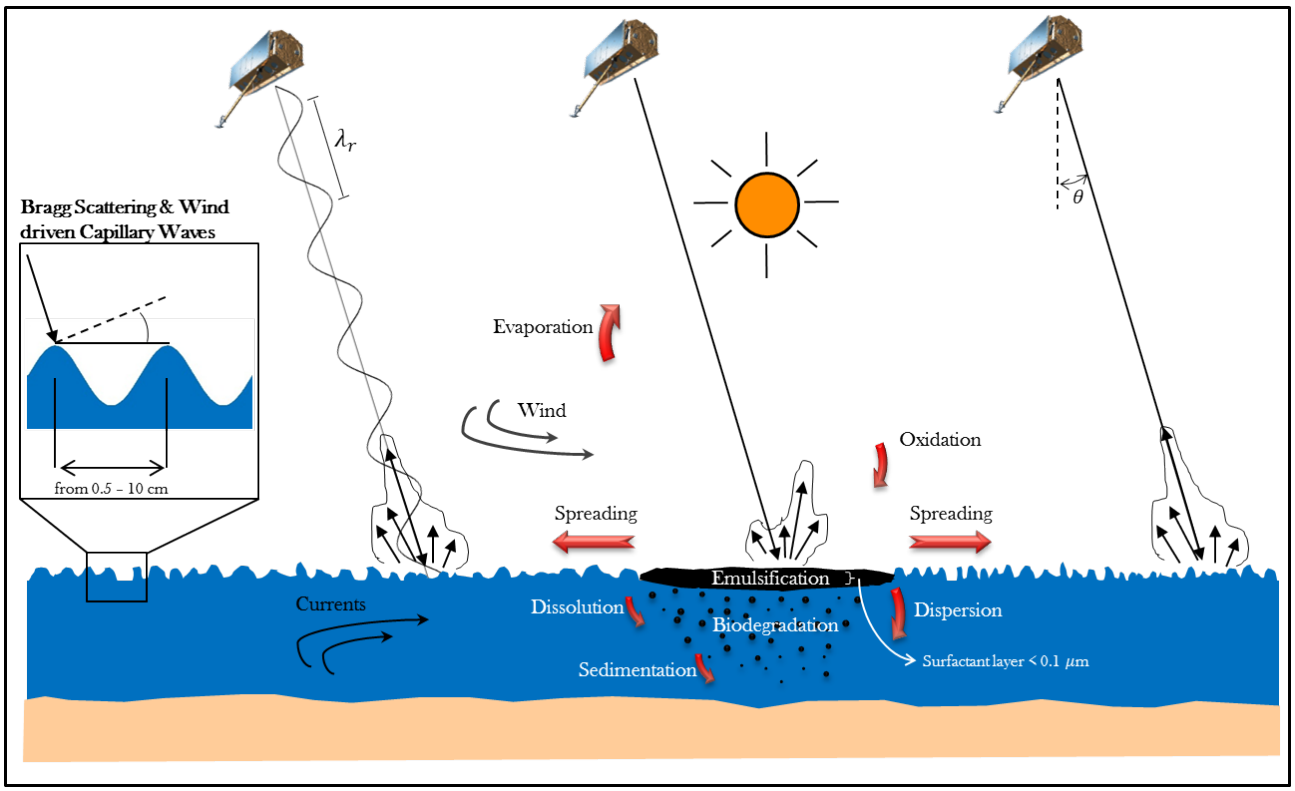

Figure 3.3 - Pictorial interpretations of physical-chemical processes involving oil on the sea surface.

It is however evident that SAR operability for oil spill detection is wind speed limited. A low wind speed will not produce the described contrast as consequence of the absence of wind driven ocean capillary waves. In high wind speed condition, oil surface damping reduces as increase the energy of ocean waves with oil starting to get mixed with waves (no longer smooth). According to the findings in (Gade et al., 2000; Litovchenko et al., 1999) oil spills are visible in the wind speed range 3-12m/s.

Since ocean is non-static water body, the fate of spilled oil in the marine environment depends upon factors such as the quantity of oil, the oil's initial physical and chemical characteristics, the prevailing climatic and sea conditions and whether the oil remains at sea or is washed ashore. The various physical-chemical-oceanographic processes acting on spilled oil are collectively known as *weathering*. Although some of these processes have long time scale (tens of years or more) they influence the detectability in SAR images. Weathering processes are graphically depicted in Figure 3.3 while a brief description of each phenomena is given in the following (ITOPF, 2011).

Spreading: As soon as oil is spilled, it starts immediately to spread over the sea surface. The speed at which this takes place depends to a great extent on the viscosity of the oil and the volume spilled. In open water, wind circulation patterns tend to cause oil to form narrow bands or 'windrows' parallel to the wind direction.

Evaporation: The more volatile components of oil will evaporate to the atmosphere. The rate of evaporation depends on ambient temperatures and wind speed. In general those oil components with a boiling point below 200°C will evaporate within a period of 24 hours in temperate conditions. The initial spreading rate of the oil also affects the rate of evaporation since the larger the surface area, the faster light components will evaporate. Rough seas, high wind speeds and warm temperatures also increase evaporation.

Dispersion: The rate of dispersion is largely dependent upon the nature of the oil and the sea state, proceeding most rapidly with low viscosity oils in the presence of breaking waves. Waves and turbulence at the sea surface can cause all or part of a slick to break up into droplets of varying sizes which become mixed into the upper layers of the water column.

Emulsification: Many oils take up water and form water-in-oil emulsions. This can increase the volume of pollutant by a factor of up to five times. Formation of water-in-oil emulsions reduces the rate of other weathering processes and is the main reason for the persistence of light and medium crude oils on the sea surface and shoreline. Although stable water-in-oil emulsions behave similarly to viscous oils, differences in their compositions have implications for effective response options.

Dissolution: The rate and extent to which an oil spill dissolves depends upon its composition, spreading, the water temperature, turbulence and degree of dispersion. Because only the most volatile oil components are slightly soluble, they evaporate much faster than they dissolve.

Oxidation: It is promoted by sunlight and, although it occurs for the entire duration of the spill, its overall effect on dissipation is minor compared to that of other weathering processes.

Sedimentation: oil droplets can interact with sediment particles and organic matter suspended in the water column so that the droplets become dense enough to sink slowly to the sea bed. Sedimentation is one of the key long term processes leading to the accumulation of spilled oil in the marine environment.

Biodegradation: Sea water contains a range of marine micro-organisms capable of metabolizing oil compounds. Such organisms are more abundant in areas with natural seeps of oil.

Unfortunately, the reduced radar backscatter on the sea surface is not unique to oil. Low winds, biogenic slicks, wind sheltering by land or oceanic structures, grease ice, internal waves, ship wakes, and convergence zones also create areas of reduced radar backscatter. It is evident that a basic processing of searching in SAR images zones of low backscatter signal it is not sufficient as these phenomena might cause false alarms. Among this class of false alarms, biogenic slicks, internal waves and ship wakes are called *look-alikes* as in many cases their shape resemble operational discharges of oil, i.e. vessel discharge of bilge water from

machinery spaces, fuel oil sludge, oily ballast water from fuel tanks. Some examples of look-alikes are shown in Figure 3.4.

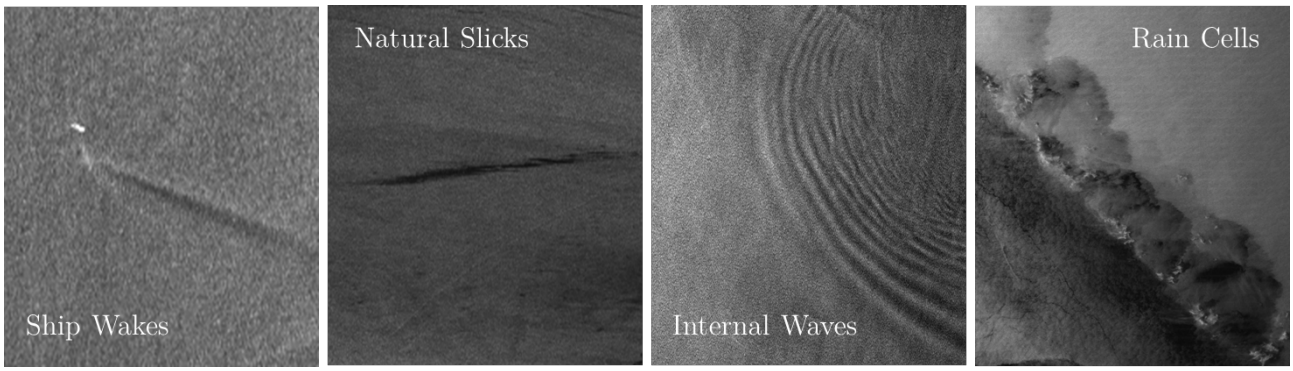

Figure 3.4 - Interpretation of different natural, atmospheric and man-made phenomena causing low backscatter region in SAR image.

The literature on SAR oil spill detection is vast as during the last decades different approaches have been proposed. The investigated methods include: theoretical modelling of the damping ratio (Gade et al., 1998a, 1998b), ocean wave spectrum attenuation by surface films (Alpers and Hühnerfuss, 1989; Lombardini et al., 1989; Trivero et al., 1998), SAR ocean surface simulation and EM models (Franceschetti et al., 2002; Nunziata et al., 2009), statistical and probabilistic classifier (Fiscella et al., 2000; Solberg et al., 2007, 1999), machine learning techniques (Frate et al., 2000; Keramitsoglou et al., 2006; Kubat et al., 1998; Mercier and Girard-Ardhuin, 2005; Topouzelis et al., 2007).

3.2.1. State-of-the-Art in operational pollution monitoring

Through CleanSeaNet, EMSA provides a State-of-the-Art oil spill monitoring service, which can be integrated into national oil spill response chains. Since 2007, CleanSeaNet supplements existing surveillance systems at national or regional level, strengthens member state responses to illegal discharges, and supports response operations to accidental spills. The service is based on radar images obtained from SAR satellites (European Maritime Safety Agency, 2015).

The processing phases commonly performed by a SAR oil spill detection algorithm are composed of the following four steps (Brekke and Solberg, 2005):

1. land masking
2. dark region detection
3. region feature extraction
4. region classification

The land masking procedure is applied in order to speed-up the second step as dark regions needs to be sought only over ocean area. The dark region detection step consists of locating ocean regions which have low radar backscatter and assign them the label of being potential oil spills. This phase can be pursued manually via human operator intervention or automatically via image segmentation processing. Subsequently, meaningful features are extracted (manually or automatically) from each potential oil spill and surrounding area, and used to classify (manually or automatically) the identified low backscatter region in either one of the two classes: oil spill, look-alike.
Depending on the human operator interactions in the processing chain described, it is possible to have full automatic, semi-automatic or manual approach. Detailed description of different approaches can be found in (Frate et al., 2000; Keramitsoglou et al., 2006; Solberg et al., 1999; Trivero et al., 1998) and references therein.
Once a dark region in the satellite radar image has been detected as oil spill, an alert with the confidence level of the detection is generated and sent to the national or local anti-pollution authority for further actions, e.g. identification of oil type, clean-up operation, culprit prosecute, etc. In (Ferraro et al., 2010) some guidelines on how the alert should be generated and which information should contain are given. An overview of different oil spill detection approaches and classification systems adopted by satellite service providers is given in (Ferraro et al., 2012).

3.2.2. The Neural-Network approach developed for TerraSAR-X

Following the initial development, data collection and validation, a NRT TS-X oil spill monitoring service has been established at DLR ground station Neustrelitz. With an elevation of approximately five degree, the ground station Neutrelitz has an acquisition circle that covers most of the European waters (Schwarz et al., 2015). The service is based on the State-of-the-Art in oil pollution monitoring steps described in the previous paragraph. It is a semi-automatic approach with dark spot selection performed via Graphical User Interface (GUI) by a human operator and classifier based on a pre-trained Neural Network (NN). NN is a well-established classifier able to deal with oil spill classification problem (Frate et al., 2000), (Ziemke, 1996), (Topouzelis et al., 2007). The initial development and results are reported in (Avezzano et al., 2011) while the application on the monitoring of offshore platforms in North Sea is demonstrated in (Singha et al., 2014).

In this section we briefly review the NN architecture employed and the results obtained. The NN topology used is an 8-8-8-1 Multi-Layer Perceptron network (MLP) with 8 inputs, 2 hidden layers composed of 8 neurons and one output (Figure 3.5). The feature vector (*area*, *perimeter*, *complexity*, *spreading*, *standard deviation dark object*, *standard deviation background*, *max* and *min contrast*) has been previously used for oil spill detection in C-band SAR data (Frate et al., 2000) and therefore adapted for TS-X data.

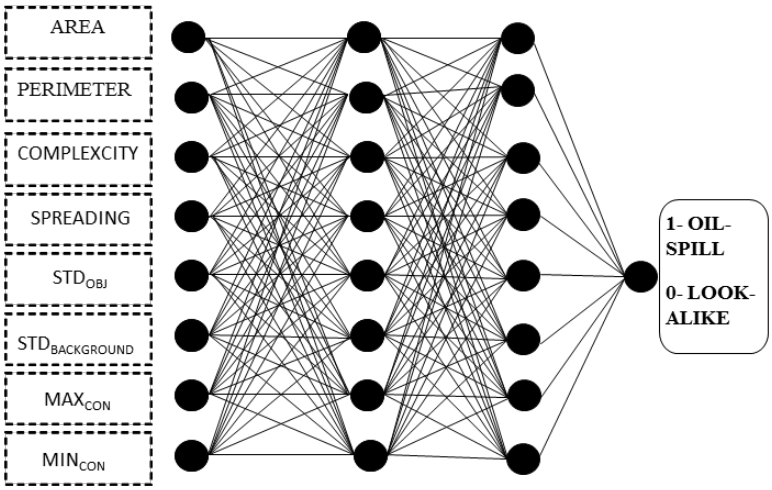

Figure 3.5 - Topology of Neural Network: MLP feed-forward 8-8-8-1 network. The input vector components are the features extracted from the dark spot, the output value represent the actual probability of the object being an oil spill.

The net has been trained using an error backpropagation algorithm, which iteratively adjusts the weights of the neuron's connections to minimize an error function. For the training process, 39 TS-X images (containing 60 oil spills and 58 look-alikes, hence 118 vectors of features) have been collected during known spill accidents and weather conditions. This dataset has been divided in two blocks: one set containing 94 vectors of features used for training and containing equally oil spill and look-alike samples, a second set containing 24 vectors of features used for testing. In addition to the dataset for training purposes, a mutually exclusive set of 11 TS-X images (containing 25 oil spills and 25 look-alikes) has been collected for algorithm validation purpose (Avezzano et al., 2011). The results are summarized by the confusion matrix in Figure 3.6.

		Predicted Class	
		Oil spill	Look-alike
Actual Class	Oil spill	84	16
	Look-alike	80	20

Figure 3.6 - Validation of the Neural Network approach developed for TS-X.

3.3. Observation of Marine Slicks exploiting the Co-Polar channel correlation

This section describes the main research activities conducted to pursue the **Objective 1** defined in Chapter 1. In **A.1** a study exploiting dual-polarimetric X-band SAR data to observe oil at sea is undertaken for the first time.

The polarimetric electromagnetic model proposed in (Migliaccio et al., 2009a, 2009b) for oil slicks observation in L- and C-band PolSAR data predicts a Bragg (non-Bragg) scattering behaviour in accordance with a high (low) inter-channel correlation between the co-polarized channels, i.e. HH and VV. The inter-channel correlation between the co-polarized channels is able to observe oil discharged at sea getting rid of the primary class of look-alikes characterized by weak-damping properties. The extension of the model in X-band PolSAR data it is not direct, as phenomena like white capping and wave breaking, might play a role in this case. Moreover, it is straightforward that, to take full benefit of the model a viable and robust estimator is a key issue.

The estimation of the inter-channel correlation is a non-trivial problem and various methods have been developed (Touzi et al., 1999). In (Migliaccio et al., 2009a, 2009b), the standard deviation of the Co-polarized Phase Difference (CPD) is proposed as estimator of the inter-channel correlation for the observation of oil spills. In (Velotto et al., 2011), first and second moments of the polarimetric parameters CPD and Coherence are investigated for the observation of oil-spill in X-band TS-X data.

3.3.1. Co-Polarized Phase Difference (CPD) and Coherence

As discussed in the section 2.3.1, TS-X provides coherent SAR data in dual polarization SM mode in different combinations. For the observation of marine oil slicks the Co-Polar channels, i.e. HH-VV, are needed.

The *Lexicographic* scattering vector basis, generally defined in Equation (2.23) for fully polarized data, becomes in case of dual polarization (where the subscript $D2$ it refers to the possible dual polarization combination HH-VV):

$$k_{D2} = [\dot{S}_{hh} \quad \dot{S}_{vv}]^T \tag{3.9}$$

which leads to the following covariance matrix (see Equation (2.25)):

$$\mathrm{C}_2 = \langle k_{D2} {k_{D2}}^H \rangle = \begin{bmatrix} \langle |\dot{S}_{hh}|^2 \rangle & \langle \dot{S}_{hh} \dot{S}_{vv}^* \rangle \\ \langle \dot{S}_{vv} \dot{S}_{hh}^* \rangle & \langle |\dot{S}_{vv}|^2 \rangle \end{bmatrix} = \eta \begin{bmatrix} \gamma & \dot{\rho}\sqrt{\gamma} \\ \dot{\rho}^* \sqrt{\gamma} & 1 \end{bmatrix} \tag{3.10}$$

where the elements of C_2 are:

$$\eta = \langle |\dot{S}_{vv}|^2 \rangle \quad \gamma = \frac{\langle |\dot{S}_{hh}|^2 \rangle}{\langle |\dot{S}_{vv}|^2 \rangle} \quad \dot{\rho} = \frac{\langle \dot{S}_{hh} \dot{S}_{vv}^* \rangle}{\sqrt{\langle |\dot{S}_{hh}|^2 \rangle \langle |\dot{S}_{vv}|^2 \rangle}} \tag{3.11}$$

The elements of C_2 defined in Equation (3.11) are knows as: power, polarization ratio and complex coherence. A direct estimator of the co-polar inter-channel correlation is provided by the amplitude of complex coherence: $\dot{\rho} = \rho e^{j\overline{\varphi}}$, where ρ is the amplitude and $\overline{\varphi}$ is the mean phase. Once ergodicity is invoked, the *maximum likelihood estimator* (MLE) of ρ is given by replacing the expectation operator with a spatial averaging window

$$\hat{\rho} = \frac{\left|\sum_{n=1}^{L} \dot{S}_{hh}[n]\dot{S}_{vv}^{*}[n]\right|}{\sqrt{\sum_{n=1}^{L}|\dot{S}_{hh}[n]|^2 \sum_{n=1}^{L}|\dot{S}_{vv}[n]|^2}}, \tag{3.12}$$

Statistical analysis of $\hat{\rho}$ has been described in (Bamler and Hartl, 1998; Touzi et al., 1999) and its first moment $E[\hat{\rho}]$ varying the number of independent samples L is given by:

$$E[\hat{\rho}] = \frac{\Gamma(L)\,\Gamma(1+1/2)}{\Gamma(L+1/2)} \times (1-\rho^2)^L \times {}_3F_2\left(\left[\tfrac{3}{2}, L, L\right]; \left[L+\tfrac{1}{2}\right]; [1]; [\rho^2]\right) \tag{3.13}$$

As pointed out in (Joughin et al., 1994; Touzi et al., 1999), this estimate is biased, i.e. values of low coherence are overestimated. This is clearly shown in Figure 3.7(a) where Equation (3.13) is plotted as function of ρ and L. It must be noted that only using a large numbers of samples L it becomes asymptotically unbiased.

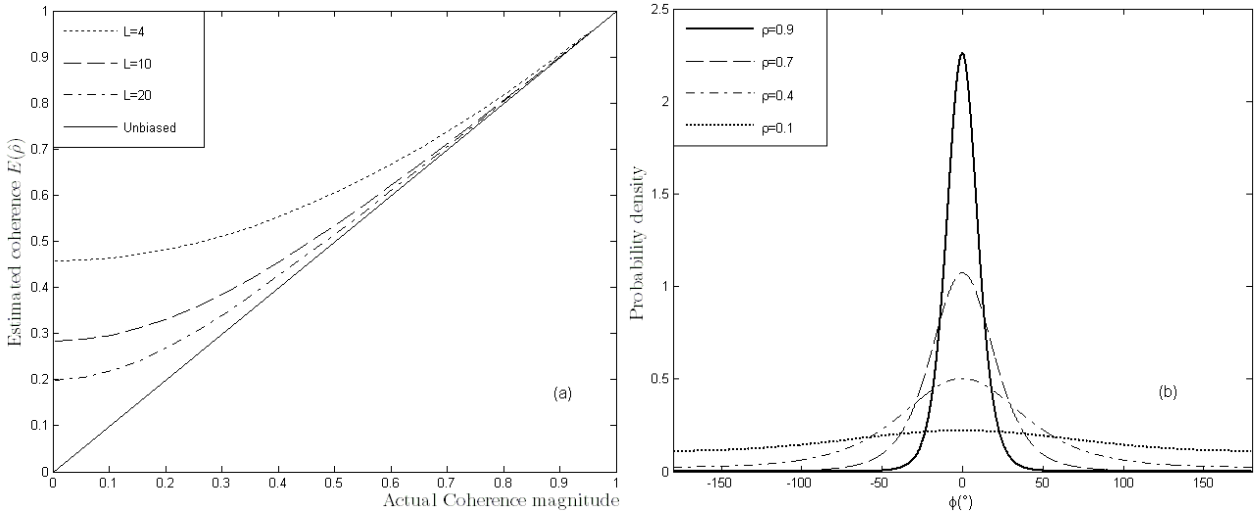

Figure 3.7 - (a) First moment $E[\hat{\rho}]$ of the coherence amplitude as function of true coherence ρ and number of looks L equal to 4, 10 and 20; (b) theoretical CPD pdfs for $\rho \in \{0.9, 0.7, 0.4, 0.1\}$, $\overline{\varphi} = 0°$ and $L = 1$.

An alternative method to estimate the inter-channel correlation is given by the standard deviation of the CPD (Migliaccio et al., 2009b). The CPD is defined as follows:

$$\varphi = \angle \dot{S}_{hh}\dot{S}_{vv}^{*} = \varphi_{hh} - \varphi_{vv} \tag{3.14}$$

The probability density function (pdf) of the CPD is shown in Figure 3.7(b) for $L = 1$, $\overline{\varphi} = 0°$ and varying ρ. The mathematical formulation has been derived in terms of the complex coherence (Joughin et al., 1994; Lee et al., 1994; Sarabandi, 1992):

$$p(\varphi) = \frac{(1-\rho^2)^L\ \Gamma(2L)}{2^{L+1/2}\,\sqrt{\pi}\,\Gamma(L)} \left(\frac{1}{1-\beta^2}\right)^{(L+1/2)/2} P_{L-3/2}^{L-1/2}(-\beta) \tag{3.15}$$

where, $P(\cdot)$ is the Legendre function of the first kind, $\Gamma(\cdot)$ is the Gamma function, and $\beta = \rho\cos(\varphi - \overline{\varphi})$. It is easier to interpret the behaviour of the CPD in regards the inter-

channel correlation as follow: when ρ tends to zero, i.e. HH and VV channels uncorrelated, $p(\varphi)$ tends to a uniform distribution (hence, large standard deviation, see Figure 3.7(b)); when ρ approaches the unity, i.e. HH and VV channels fully correlated, $p(\varphi)$ tends to a Dirac delta function (hence, small standard deviation, see Figure 3.7(b)). It is evident that the standard deviation of the CPD gives information on the inter-channel correlation. Once ergodicity is invoked, the standard deviation of the CPD can be estimated as:

$$\hat{\sigma} = \sqrt{\left(\frac{1}{L}\sum_{n=1}^{L}\left(\angle \dot{S}_{hh}[n]\dot{S}_{vv}^{*}[n]\right)^{2}\right) - \left(\frac{1}{L}\sum_{n=1}^{L}\left(\angle \dot{S}_{hh}[n]\dot{S}_{vv}^{*}[n]\right)\right)^{2}} \tag{3.16}$$

Furthermore, in (Velotto et al., 2011) the Cramer-Rao bounds of the two estimation methods are compared to analyze their effectiveness. It is noted that for low coherence values ($\rho < 0.3$), $\hat{\sigma}$ provides an efficient inter-channel correlation estimation, while for high coherence values ($\rho > 0.5$), the efficient estimator is $\hat{\rho}$.

It is now important to link the polarimetric model, whose based on the inter-channel correlation estimated either via $\hat{\sigma}$ or $\hat{\rho}$, with respect to SAR oil spill application, i.e. discrimination of oil from look-alikes.

Slick-free and weak-damping slicks, e.g. biogenic slicks, ship wakes, calling for a high inter-channel correlation are expected to be characterized by (Migliaccio et al., 2009b; Velotto et al., 2011):

- Narrow CPD pdf $\rightarrow$ low $\hat{\sigma}$ values.
- High $\hat{\rho}$ values.

Oil-covered sea surface, calling for a low inter-channel correlation, is expected to be characterized by (Migliaccio et al., 2009b; Velotto et al., 2011):

- Broaden CPD pdf $\rightarrow$ high $\hat{\sigma}$ values.
- Low $\hat{\rho}$ values.

As a matter of fact, the two proposed estimators are expected to be both able to observe oils and to distinguish them from weak-damping look-alikes. In (Velotto et al., 2011) the proposed model has been tested for the first time in X-band dual-polarized HH-VV coherent SAR data. For the estimation $\hat{\sigma}$ and $\hat{\rho}$, different window sizes are evaluated and the influence of the instrument noise is taken into account.

3.3.2. Case studies

This section is dedicated at verifying the proposed polarimetric model for the observation of oil spill in TS-X data, in which both certified oil slicks and weak damping look-alikes are

present. The results reported in this paragraph are extracted from the paper **A.1**, which constitutes integral part of this dissertation.

Figure 3.8(a) shows the NRCS, η in dB, where a low backscatter area, due to an accidental oil spill, is clearly visible. The Region Of Interest (ROI) displayed in Figure 3.8(a) is a sub-image of approx. 3km x 4km, extracted from a standard TS-X dual-polarized HH-VV data acquired consequently an oil tanker wreck (see (Velotto et al., 2011) for further details). $\hat{\sigma}$ and $\hat{\rho}$ estimated by using $L = 3 \times 3$ moving window are shown in grey tones in Figure 3.8(b)-(c). It is important to note that, due to the high dynamic range of η values, a contrast stretching is needed in Figure 3.8(a). No contrast stretching is indeed performed for Figure 3.8(b)-(c). Figure 3.8(b)-(c) shows that $\hat{\sigma}$ ($\hat{\rho}$) is higher (lower) within the oil covered area. In both cases the oil slick is clearly distinguishable from the surrounding sea. Results confirm the theoretical model which predicts that the Bragg scattering mechanism dominates everywhere but within the oil-covered sea surface. The CPD standard deviation approach ($\hat{\sigma}$) makes the oil brighter than the background, while the sample coherence approach ($\hat{\rho}$) makes it darker.

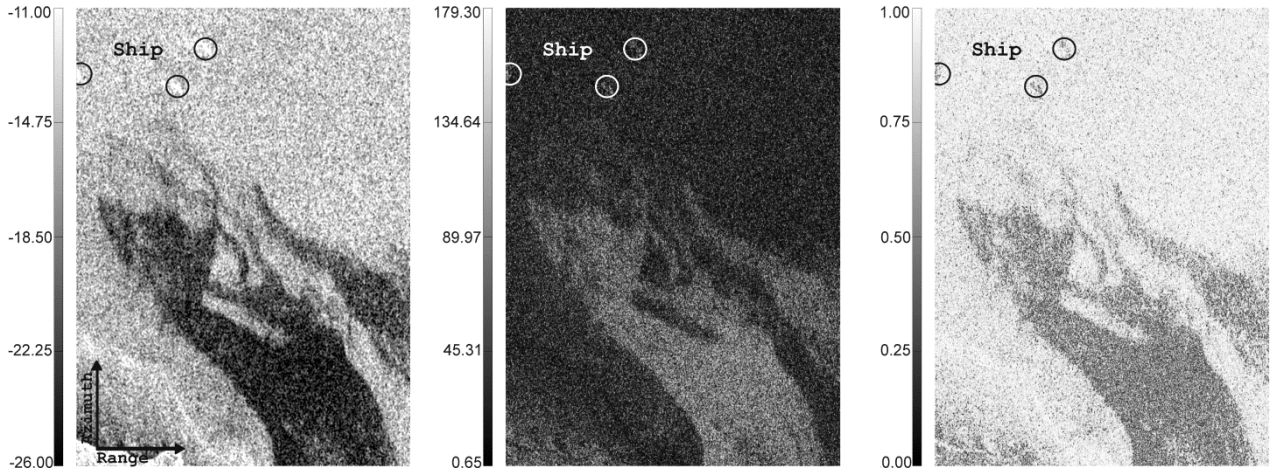

(a) η (dB) (b) $\hat{\sigma}$ for $L = 3 \times 3$ (°) (c) $\hat{\rho}$ for $L = 3 \times 3$

Figure 3.8 - Excerpt of TS-X SAR data in sensor coordinate (slant range and azimuth) showing an ocean area polluted by of an oil spill caused by an oil tanker wreck. (a) NRCS η, (b)-(c) $\hat{\sigma}$ and $\hat{\rho}$ by using $L = 3 \times 3$ moving window.

It is noteworthy that, the interpreted behaviour of $\hat{\sigma}$ and $\hat{\rho}$ over the oil spill is not due to the low NRCS measured over the oil area, but due to a departure from Bragg scattering mechanism. A further confirmation of this interpretation is provided by the signatures in $\hat{\sigma}$ and $\hat{\rho}$ maps of the ships present in Figure 3.8(a). Although ships have higher NRCS compared to oil they appear as well brighter (darker) than surrounding sea in $\hat{\sigma}$ ($\hat{\rho}$) domain as characterized by a complex scattering mechanism that departs from Bragg as well.

Figure 3.9(a) shows the NRCS, η in dB, where a low backscatter area, due to a weak-damping look-alike, is visible in the middle of the image. $\hat{\sigma}$ and $\hat{\rho}$ estimated by using $L = 3 \times 3$ moving window are shown in grey tones in Figure 3.9(b)-(c). The marine feature is not clearly distinguishable from the surrounding sea in the $\hat{\sigma}$ ($\hat{\rho}$) domain, i.e. low (high) $\hat{\sigma}$

($\hat{\rho}$) values following the polarimetric model prediction. As matter of fact, this look-alike is characterized by damping properties such to reduce the measured NRCS but not to be a departure from Bragg mechanism.

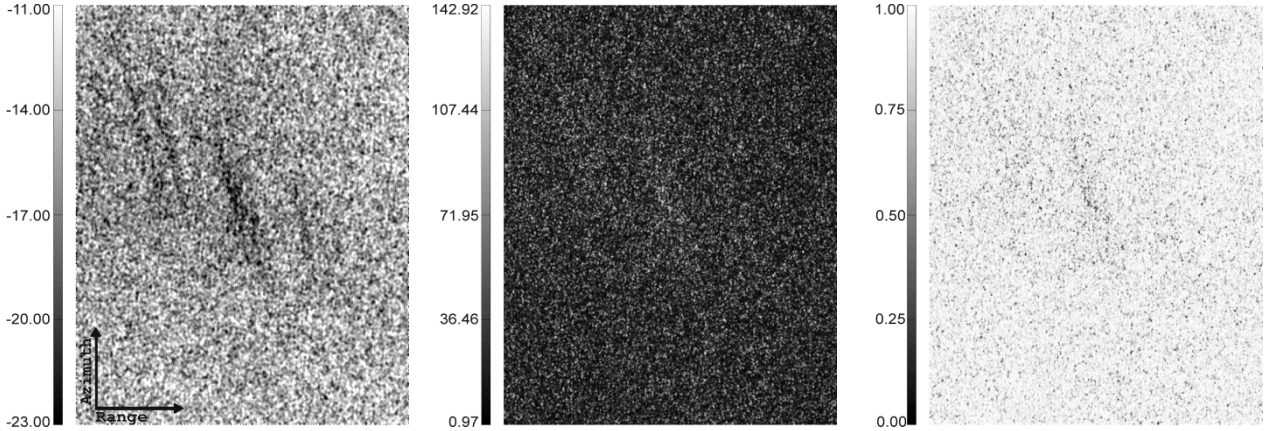

(a) η (dB) (b) $\hat{\sigma}$ for $L = 3 \times 3$ (°) (c) $\hat{\rho}$ for $L = 3 \times 3$

Figure 3.9 - Excerpt of TS-X SAR data in sensor coordinate (slant range and azimuth) showing a low backscatter region caused by weak-damping look-alike. (a) NRCS η, (b)-(c) $\hat{\sigma}$ and $\hat{\rho}$ by using $L = 3 \times 3$ moving window.

To quantitatively validate the previous results, the probability density functions (pdf) of the CPD are compared in Figure 3.10.

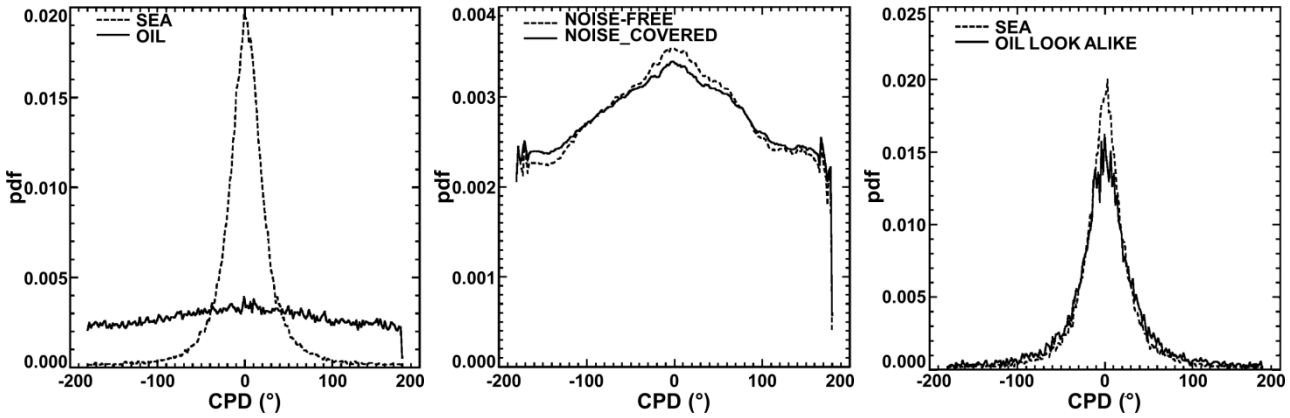

(a) (b) (c)

Figure 3.10 – Qualitative comparison of the CPD densities. (a) Sea and oil CPD densities. (b) Noise influence on the CPD densities. (c) Sea and look-alike CPD densities.

Figure 3.10(a) plots the densities of the CPD for the oil-covered and sea region for the case shown in Figure 3.8. It can be noted that their standard deviation values are completely different, i.e. 85° and 30°. The mean values of $\hat{\rho}$, for both oil-covered and sea surface are equal to 0.53 and 0.91, respectively. To investigate the influence of the instrument noise on the estimation of the inter-channel correlation and of the soundness of the polarimetric model, the CPD densities of noise-free (only data above the NESZ have been considered) and noise-covered data are plotted in Figure 3.10(b). The annotated average NESZ for the SAR data shown in Figure 3.8 is equal to -25dB. Most of the noisy pixels belong to the oil-

covered area. The two densities in Figure 3.10(b) are quite close, with standard deviation values equal to 82° and 85° for noise-free and noise-covered oil area. This result witness that the effect of the instrument noise is negligible in this case, but it must be taken into account. TS-X instrument noise is reported to be between -19dB and -26dB, increasing in this range with increasing incidence angle (Schwerdt et al., 2010). For these reasons it is found not recommendable to use dual-polarization TS-X data acquired with incidence angles above 35° as noise could influence the estimation of the inter-channel correlation even over sea area.

Figure 3.10(c) plots the densities of the CPD for the low backscatter area due to weak-damping look-alike and sea region for the case shown in Figure 3.9. In this case, the CPD density distributions for the look-alike and sea region are almost overlapping with very close standard deviation values, i.e. 38° and 32°. Similarly $\hat{\rho}$ is estimated to be equal to 0.87 and 0.91.
To further compare the performances of $\hat{\sigma}$ and $\hat{\rho}$ using different window sizes the contrast parameters are defined and adapted to the different outputs:

$$c_{\hat{\sigma}} = \frac{\hat{\sigma}_{OIL}}{\hat{\sigma}_{SEA}} \tag{3.17}$$

$$c_{\hat{\rho}} = \frac{\hat{\rho}_{SEA}}{\hat{\rho}_{OIL}} \tag{3.18}$$

Table 3.2 summarizes the results obtained in (Velotto et al., 2011) listing the obtained $c_{\hat{\sigma}}$ and $c_{\hat{\rho}}$ for different oceanic surfactants analysed. These are namely: oil spill caused by ship accident, fresh spill from moving ship, look-alike caused by weak damping surface film, ship wakes. $\hat{\sigma}$ ($\hat{\rho}$) values significantly larger (smaller) than slick-free ones are observed over oil-covered sea surface. $\hat{\sigma}$ and $\hat{\rho}$ values similar to the slick-free ones are observed over areas where a weak damping look-alike is present. It must be noted that no peculiar trend related to the CPD mean value $\overline{\varphi}$ over the oil-covered and slick-free sea surface are revealed in this study even using different window sizes. CPD standard deviation works better than coherence amplitude when smaller windows size is employed. However, despite the fast computation of $\hat{\sigma}$ and $\hat{\rho}$ via boxcar filtering, adaptive solution like the directional filter (Lee et al., 1998) or non-local means filter (NL-means) (Buades et al., 2010) might help the estimation accuracy. Being φ and $\dot{\rho}$ characterized by the same statistical distribution of the interferometric phase and coherence, the NL-means filter applied to interferometric SAR (NL-InSAR filter) recently proposed in (Zhu et al., 2014), is a promising method to avoid the drawbacks of the boxcar implementation.

TABLE 3.2 – Summary of the obtained results.

DATA SET L	Surfactant[1]	Mean $\widehat{\sigma}$ slick [°]	Mean $\widehat{\sigma}$ sea [°]	Mean $\widehat{\rho}$ slick	Mean $\widehat{\rho}$ sea	Mean $\overline{\varphi}$ slick [°]	Mean $\overline{\varphi}$ sea [°]	$c_{\widehat{\sigma}}$	$c_{\widehat{\rho}}$
Kerch Strait [3x3]	Oil 1	85.0	30.2	0.53	0.91	0.17	2.10	2.81	1.72
	Oil 2	61.3	28.9	0.69	0.92	1.53	2.44	2.12	1.33
	Oil 3	45.0	25.0	0.81	0.94	2.22	1.43	1.80	1.16
Kerch Strait [5x5]	Oil 1	93.1	34.5	0.38	0.91	0.18	2.10	2.69	2.39
	Oil 2	67.8	33.2	0.63	0.92	1.51	2.44	2.04	1.46
	Oil 3	50.5	28.8	0.81	0.95	2.21	1.42	1.75	1.17
Kerch Strait [7x7]	Oil 1	95.6	36.1	0.3	0.91	0.20	2.10	2.64	3.03
	Oil 2	70.0	34.7	0.62	0.92	1.50	2.44	2.01	1.48
	Oil 3	52.5	30.4	0.81	0.95	2.21	1.42	1.72	1.17
Black Sea [3x3]	Spill	90.7	60.5	0.50	0.68	3.36	9.21	1.49	1.36
Black Sea [5x5]	Spill	98.5	66.8	0.34	0.62	3.34	9.21	1.47	1.82
Black Sea [7x7]	Spill	100.8	69.0	0.26	0.61	3.30	9.20	1.46	2.34
Kerch Strait [3x3]	LA	38.6	32.3	0.87	0.91	1.08	1.36	1.19	1.05
Kerch Strait [5x5]	LA	43.5	36.8	0.86	0.90	1.07	1.35	1.18	1.05
Kerch Strait [7x7]	LA	45.2	38.4	0.86	0.90	1.04	1.35	1.18	1.05
Ischia wake1 [3x3]	LA	36.0	33.4	0.85	0.90	1.47	1.87	1.08	1.06
Ischia wake1 [5x5]	LA	40.3	37.5	0.88	0.90	1.46	1.86	1.07	1.02
Ischia wake1 [7x7]	LA	41.8	39.0	0.88	0.90	1.45	1.86	1.07	1.02
Ischia wake2 [3x3]	LA	37.6	33.4	0.85	0.88	1.97	1.47	1.12	1.04
Ischia wake2 [5x5]	LA	42.0	37.5	0.86	0.88	1.97	1.47	1.12	1.02
Ischia wake2 [7x7]	LA	43.6	39.0	0.86	0.88	1.98	1.47	1.12	1.02

[1] Oil 1, 2, 3 refers to accidental oil spill; Spill is a fresh spill from ship; LA stands for look-alike

3.3.3. Polarimetric features extracted from the 2x2 Covariance Matrix

This last section is dedicated to a short review of recent studies on the use of PolSAR data for oil spill detection. Of particular interest for this dissertation are the methods based on polarimetric features extracted from the 2x2 covariance matrix (or the equivalent coherency matrix) in case of dual-polarized HH-VV data, i.e. C_2 in Equation (3.10). Algorithms that make use of full-polarized data are not included here but can be found in the reference list therein the bibliography.

The relevance of polarimetric features $H, \overline{\alpha}$ and A to assist oil spill classification has been firstly investigated in (Migliaccio et al., 2007). As outcome of this analysis, H showed to be the main polarimetric feature able to distinguish oil-free with oil-covered area and in some cases to distinguish among biogenic and anthropogenic slicks. One attractive feature of the eigenvalue decomposition approach is that it scales easily to different dimensions. The method described in the section 2.2.4 for the 3x3 case can be applied to the simpler 2x2 case to obtain the polarimetric parameters *entropy* H_2, and *mean alpha angle* $\overline{\alpha_2}$ where the subscripts have been added to indicate the 2x2 case (Cloude, 2007). This has motivated the study in (Velotto et al., 2012) where H_2 has been compared with $\hat{\sigma}$, $\hat{\rho}$ and η. The polarimetric features H_2, $\hat{\sigma}$ and $\hat{\rho}$ gave good results in terms of detecting fresh spillage from offshore platforms as well as floating oil due to oil rig blowout when compared to the intensity based feature η. On the other hand $\hat{\sigma}$ and $\hat{\rho}$ gave better look-alike discrimination power than H_2. (Liu et al., 2011) have indeed proposed a linear combination of $H, \overline{\alpha}$, A and $\hat{\rho}$, as an effective way for oil slick segmentation.

In (Kudryavtsev et al., 2013) the use of only the amplitudes of the co-polar channels HH and VV, has been found to be sufficient in distinguishing between different mechanisms affecting ocean radar backscatter. Dark oceanic patches associated to oil spills have shown a high contribution to the NRCS difference between VV and HH channels, named PD image, while the non-polarized scattering from breaking waves, named NP image, is almost null. Moreover, the polarization ratio, named PR and here indicated with γ, is suggested as a promising parameter to discriminate oil spill from look-alike features caused by low-wind conditions and surface current effects. Similarly (Skrunes et al., 2014) have discarded the cross-polarization channels as found not strong enough for the analysis of oil slick characteristics, i.e. noise corrupted, and focused on polarimetric features from the coherency matrix T_2. A *k*-means classifier based on *geometric intensity* (similar to the *span* of the T_2 but based on the determinat of T_2) and the *magnitude of the real part of the co-polar correlation* (magnitude of the real part of one of the non-diagonal elements of C_2) has been found useful to discriminate simulated biogenic slick and mineral oil.

4. Marine Target Detection and Discrimination

Oceans are exploited in many different ways: transport, fishing, oil and gas extraction, as source for renewable energy, etc. These activities put the world Oceans to face different type of environment threats. The threats include water pollution, climate change, shipping accidents, unsustainable fishing, coastal erosion, etc. Many of the cited threats are often associated with illegal human activities that don't only affect sea wildlife (flora and fauna), but also human life.

In the communication (EU -COM(2009)/538, 2009), the European Commission undertook to "*take steps towards a more interoperable surveillance system to bring together existing monitoring and tracking systems used for maritime safety and security, protection of the marine environment, fisheries control, control of external borders and other law enforcement activities*". The aim of integrated maritime surveillance is to generate a situational awareness of activities at sea, impacting on maritime safety and security, border control, the marine environment, fisheries control, trade and economic interests. Equivalently, the IMO has defined Maritime Situational Awareness (MSA) as the effective understanding of activity associated with the maritime domain that could impact the security, safety, economy, or environment ("International Maritime Organization," 2015). As part of the research in the national masterplan for maritime technologies, DLR is leading the joint project Echtzeitdienste für die Maritime Sicherheit – Security (EMSec) funded by the Federal Ministry of Education and Research (BMBF). EMSec belongs to the DLR programme *research and development for maritime security and related real-time services*, which focus on integrate various sea-, air- and satellite-based data to respond better and more efficiently to critical situations at sea (Figure 4.1).

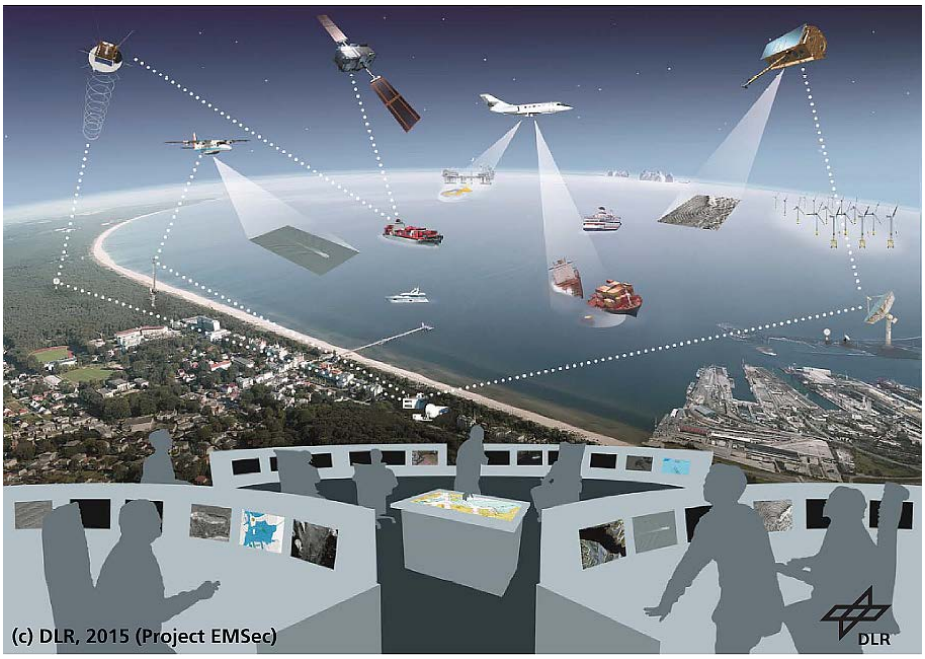

Figure 4.1 – Pictorial description of Maritime Situational Awareness. ©DLR, 2015 (Project EMSec)

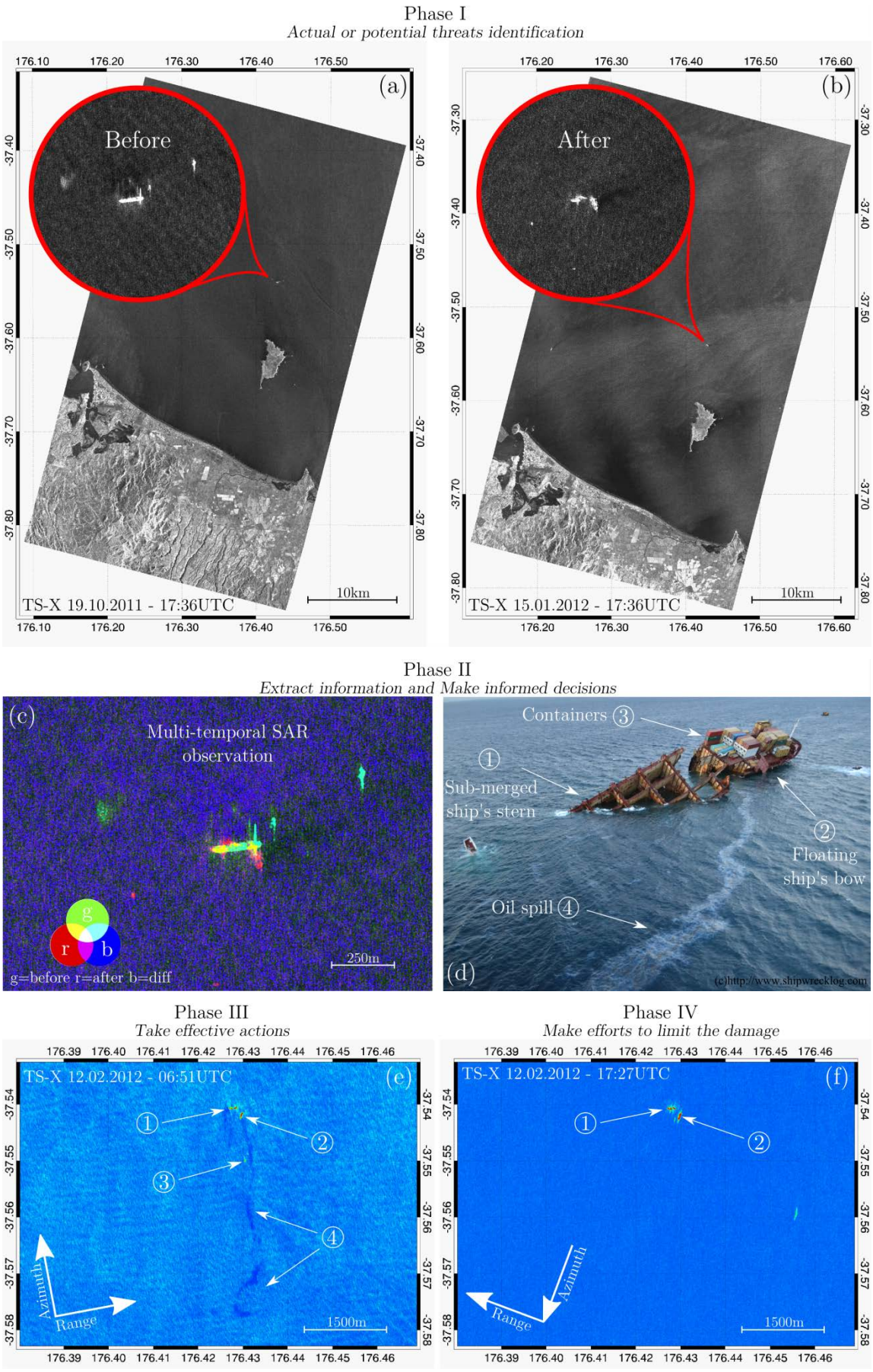

Figure 4.2 – Maritime domain awareness phases. TS-X assisted the rescue of the Rena cargo ship ran aground on coral reef and helped the contingency planning during the accident.

Figure 4.2 shows in a time series of TS-X images, several events following the aground on 5th October, 2011 of the container ship MV Rena on the Astrolabe Reef off the Bay of Plenty, New Zealand. In particular, Figure 4.2(a) shows the location of the ship and the surrounding area, which could be affected by drifting lost containers (some of the containers were carrying hazardous materials) as well as by leakage of the fuel oil. Due to stormy weather, the ship broke in two on 8th January, 2012, as clearly shown by the TS-X image in Figure 4.2(b)-(c), raising the additional potential threat of oil leakage. Figure 4.2(d) is an aerial survey picture showing the status of the shipwreck, while Figure 4.2(e)-(f) are TS-X images acquired after the oil spill event which can be distinctly detected. In this framework, monitoring of maritime metallic targets, i.e. ships, offshore platforms, wind-park, navigation aids, etc., accomplished via space-borne SAR is an essential part of such integrated environment.

4.1. State of the Art

This section is dedicated to briefly summarize the state of the art regarding SAR detection of marine metallic targets, hereafter referred simply as marine targets. Since the vast amount of scientific research papers on this topic, only the techniques that are closely related with the objectives of this dissertation are reviewed. This section starts giving the general concepts, while at the beginning of each sub-section the pertinent literature review is provided.

Marine target detection algorithms are composed of five steps (Crisp, 2004; Lehner et al., 2014):

1. Pre-processing
2. Land masking
3. Pre-screening
4. Discrimination
5. Feature extraction

The pre-processing and land masking procedures are steps which are commonly performed also in SAR oil spill detection and therefore, already motivated in this dissertation.
Pre-screening is the key processing step. The purpose is to find all possible targets with negligible missing and false alarm rates. However, is preferable during pre-screening phase to examine all ocean pixels with a high probability of false alarm in order to avoid missing some targets and set-up more restricting rules during the discrimination phase. Pre-screening algorithms are global thresholding or adaptive thresholding. In the latter one falls the Constant False Alarm Rate (CFAR). The CFAR algorithm consists of three nested sliding windows: the target window w_t, guard window and background window w_b. The intensity of

the target window is compared to a local threshold Thr, which changes according to the statistics of the background window, so that the specified Probability of False Alarm (PFA) remains constant (Crisp, 2004). A comprehensive survey of the different CFAR methods is given in (El-Darymli et al., 2013). Among them, the most common are the two-parameter CFAR (2P-CFAR) and the cell averaging CFAR (CA-CFAR). In the 2P-CFAR, the Thr changes iteratively depending on the mean and the standard deviation of the intensity signal over the background window:

$$Thr = mean(w_b) + t_{cfar} * stddev(w_b) \tag{4.1}$$

whereas, in the CA-CFAR it depends only on the mean:

$$Thr = t_{cfar} * mean(w_b) \tag{4.2}$$

where, t_{cfar} is the design parameter which controls the PFA (Crisp, 2004).
The discrimination stage is thought to make more discerning decisions about the likelihood of a candidate being a target of interest. As matter of fact, the rejection of some false alarms is done by setting empirical rules about target size and electromagnetic properties, as well as oceanographic and meteorological conditions. The pre-screening and discrimination steps form together the detector.
The last stage, feature extraction, is an optional step that is intended to provide some characteristics of the marine target of interest.

It is important to note, that ship detection algorithm differs from the marine target detection procedure described above only in the discrimination and feature extraction steps. If ships are the targets of interest, it is common to use ancillary data, e.g. Automatic Identification System (AIS), fixed object maps, etc., during the discrimination stage to reject all marine targets that are not ships. Features of interest are in this case: length, width, heading and possibly the speed.

4.1.1. Single Polarization Target Detector

Single polarization target detectors are based on the physical fact that man-made marine targets are made up of metallic plates and corners, which are responsible of stronger coherent radar returns than the surrounding ocean surface. For the simplest SAR configuration where only one polarisation is accessible, the linear horizontal co-polar channel in transmission and reception, HH, seems to be the best choice (Crisp, 2004). This is motivated by the fact that most of marine targets develop mainly in the horizontal plane, facilitating direct reflection and double bounce with the ocean surface. In this case the

$$\left\langle \left| \dot{S}_{hh} \right|^2 \right\rangle > Thr \tag{4.3}$$

pre-screening phase is accomplished via Equation (4.3). Speckle reduction is necessary to avoid false alarms due to intensity spikes over the ocean surface. This is accomplished in Equation (4.3) by using a boxcar filter.

For application like ship detection, the linear co-polarisation (HH or VV) is found to be not always the best choice, as the ocean backscatter can be particularly high in certain circumstances, e.g. high wind speed. For radar configurations that are able to acquire the cross-polarisation channel (HV or VH), rough sea condition don't produce high ocean clutter enhancing the presence of ships. (Touzi et al., 2010) suggest the use of the co-polarisation channel HH to detect ship in SAR images with incidence angle larger than 55°, while for steep incidence angle HV is the best choice. In the latter case, the pre-screener becomes:

$$\left\langle |\dot{S}_{hv}|^2 \right\rangle > Thr \tag{4.4}$$

The benefit of adopting a one polarisation approach is the relatively low complexity of the acquisition system. The drawback is that the performance is rather poor in terms of missed detections and false alarms. For example, if the marine targets of interest are offshore platforms and the selected polarisation is HH, the target backscatter is likely to be below the clutter return as offshore platforms are mainly vertical metallic structures. In such situation

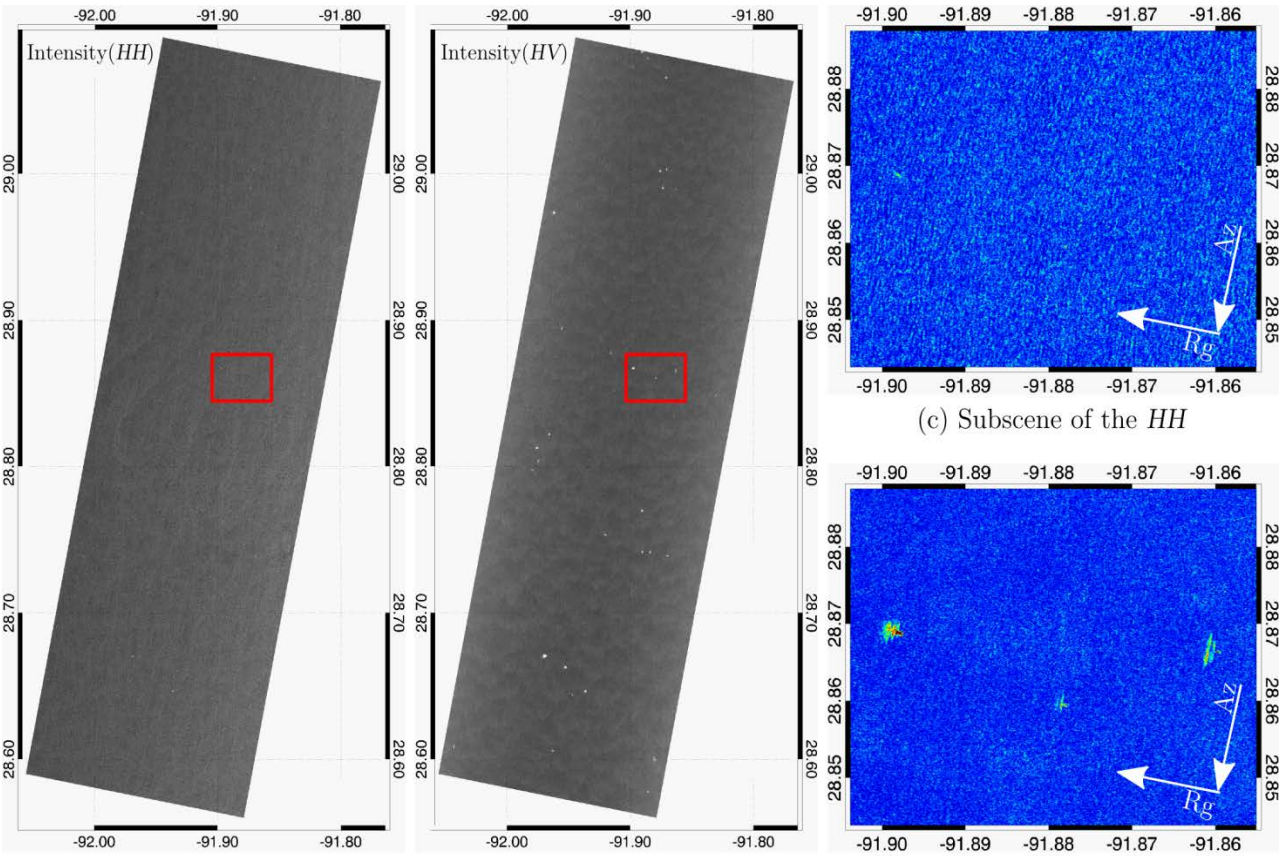

(a) (b) (c) Subscene of the *HH* (d) Subscene of the *HV*

Figure 4.3 – Example of marine metallic targets with co-pol null. (a)-(b) TS-X calibrated intensity of the HH and HV channels. (c)-(d) Zoom-in of the are indicated by the red square.

the missed detection is caused by the so called co-pol null (Boerner et al., 1992; Mott, 2006). An example of such situation is provided in Figure 4.3. TS-X calibrated intensity of HH and HV channel are shown in greyscale in Figure 4.3(a)-(b). The observed area is a known cluster of offshore platforms in Gulf of Mexico. The sub-scenes shown in Figure 4.3(c)-(d) are the color-coded normalized intensities of the two channels (from blue to red), which illustrate that the targets are giving reasonable backscatter in HV but negligible in HH.

The Gaussian GLRT (G-GLRT) is a detector that belongs to the likelihood ratio test in which the decision is made by comparing the likelihood ratio defined in Equation (4.5)

$$\frac{P(x|target)}{P(x|clutter)} > Thr \tag{4.5}$$

where x is the data under test, $P(x|target)$ is the pdf of x given that target is present and $P(x|clutter)$ is the pdf of x given that only background clutter is present. A closed mathematical formulation of the two pdfs is generally unknown but they can be estimated from the target and background window.

In order to avoid the spatial resolution degradation caused by speckle filtering, (Gambardella et al., 2008) propose a simple but very effective ship detector on full-resolution Single Look Complex (SLC) SAR images. The detector is based on a physical approach, which considers ships as dominant scatterers and, therefore, responsible for a strong and coherent backscattered signal. The presence of a non-negligible coherent component in the backscattered sea surface signal can be highlighted by evaluating the Rice Factor, which, according to (Gambardella et al., 2008), follows a log-normal distribution and a CFAR pre-screener could be implemented. The authors did not mention any polarization or incidence angle preference for the dataset analyzed.

The use of discrete wavelet transform for ship detection was firstly investigated in (Tello et al., 2005). The proposed method takes advantage of the difference of statistical behavior among the ships and the surrounding sea, interpreting the information through the wavelet coefficients in order to provide a more reliable detection. Detection performances are evaluated against 2P-CFAR for both real and simulated SAR data. Also in this case, it is not mentioned if the performances of wavelet transform method change with SAR acquisition geometries and polarizations.

4.1.2. Target Detector based on spectral analysis

Sub-aperture processing is an effective technique developed to exploit the information of the phase contained in SAR data. The key point is based on the SAR imaging mechanism that relates the azimuth time with the azimuth frequency content. Figure 4.4 shows the Figure 2.1 in the viewing plane *(y,s)* with the corresponding azimuth time-frequency relation, i.e. positive frequency Doppler shift at early times ($t < t_0$), zero Doppler shift at closest approach (t_0) and negative frequency Doppler shift at late times ($t > t_0$).

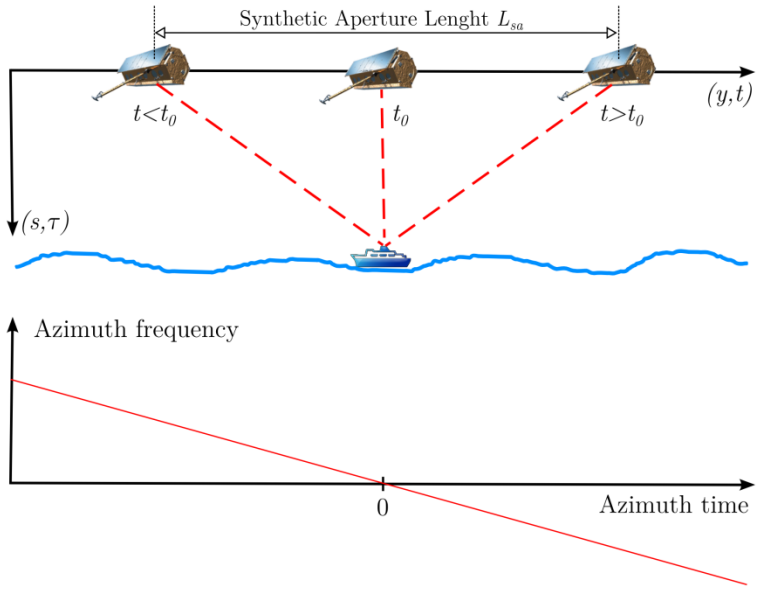

Figure 4.4 – Azimuth time-frequency relation in SAR imaging.

The Doppler shift variation is continuous and approximately linear (assuming low squint angle and stationary targets) within the illumination time, i.e. time equivalent of synthetic aperture length L_{sa}. This property suggests dividing L_{sa} in two (or more) apertures by considering the negative and positive time echoes, independently. This procedure is justified by the linearity between azimuth time and frequency. Each sub-aperture image can be formed by applying the inverse Fourier transform to each azimuth spectrum portion selected. Consequently, each sub-aperture image will have a worse azimuth space resolution, e.g. for two non-overlapping portion of the azimuth spectrum, two sub-aperture images are obtained with half azimuth resolution. Moreover, the sub-aperture technique can be applied to focused SLC data, as the azimuth compression step in raw SAR data processing is a completely linear filter, i.e. the linear relation azimuth time frequency in the raw signal is kept after this step. Sub-aperture processing is, therefore, a useful tool for the spectral analysis of the illuminated target (Ferro-Famil et al., 2003; Souyris et al., 2003). It gives the possibility to analyze the target radar response by slightly different viewing angles in the azimuth footprint of the SAR acquisition, e.g. observations at early times $t < t_0$ and late times $t > t_0$. It must be noted that the sub-aperture processing can be performed also in range or even contemporary in range and azimuth directions. Without loss of generality the analysis and description is limited at the principle of sub-aperture in azimuth.

Figure 4.5 illustrates the processing workflow of the sub-aperture method for the specific case of n=2 sub-apertures with both a synthetic aperture length $L_{sub} = L_{sa}/2$, i.e. no bandwidth overlap. It has been shown that spectral analysis might help in detecting ships (but can be generalized to marine target) which have a poor Target to Clutter Ratio (TCR) (Arnaud, 1999; Ouchi et al., 2004). The principle relies on the assumption that the electromagnetic behavior of the ship, or part of the ship (comers, pillars), is similar to a

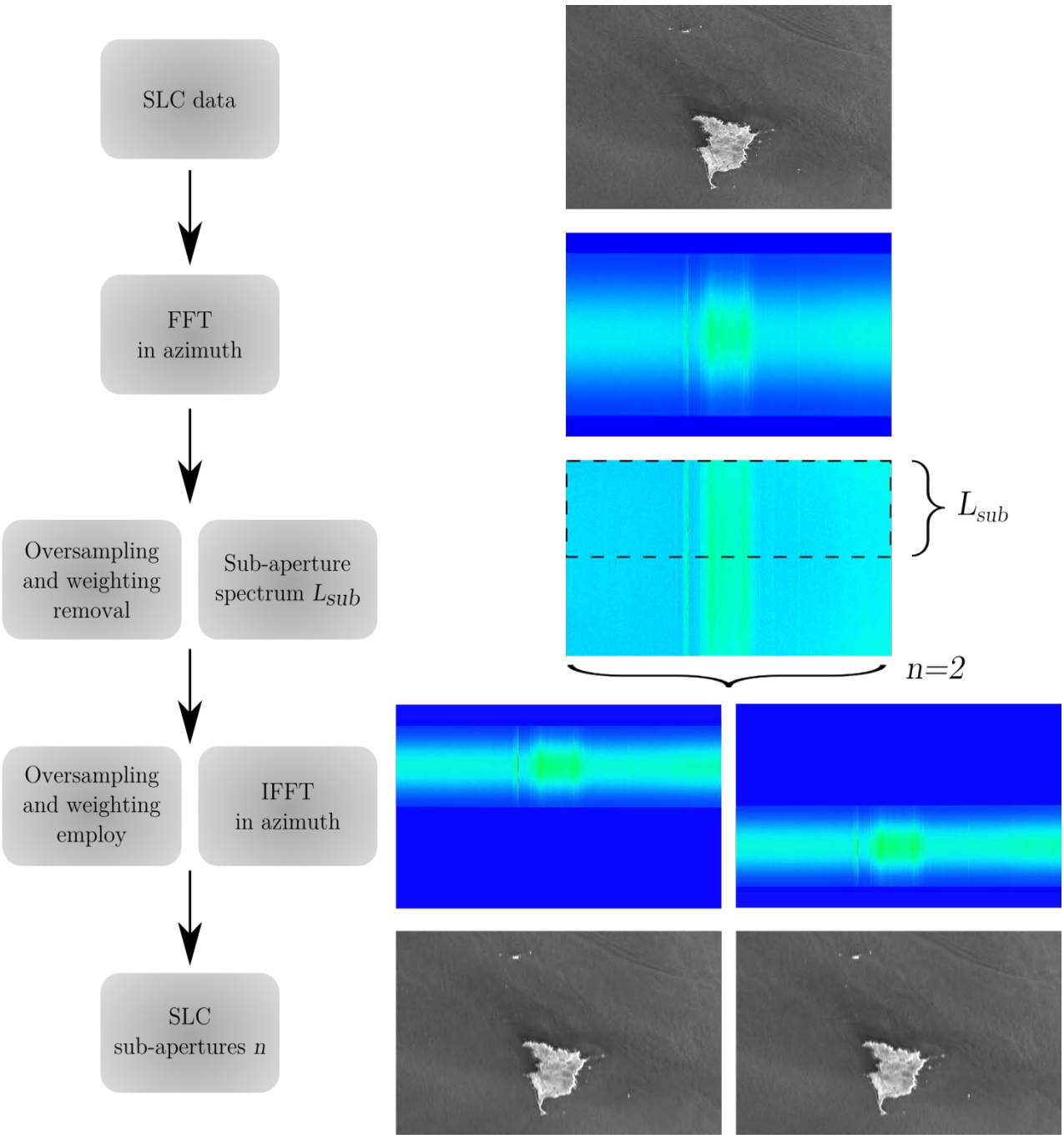

Figure 4.5 – Processing workflow of the sub-aperture method. The example shown refers to the generation of n=2 sub-apertures with non-overlapping bandwidth. The shown SLC data are transformed to amplitude for visualization purposes.

point-like response, i.e. target response isotropic at different viewing angles. While on the other hand, the sea surface is subject to continuous changes during the synthetic aperture, i.e. clutter response dependent on the viewing angle. This peculiarity has led to the development of several approaches for ship detectors by varying the strategy of the sub-aperture method (e.g. number of sub-apertures, direction in range or azimuth, etc.) and the way sub-apertures are employed (e.g. how the resulting apertures are combined).

(Arnaud, 1999; Ouchi et al., 2004) proposed to generate two non-overlapping sub-apertures (as the example shown in Figure 4.5) and used the magnitude of the interferometric coherence:

$$\rho_{sub} = \frac{\left|\langle \dot{sub}_1 \dot{sub}_2^* \rangle\right|}{\sqrt{\langle |\dot{sub}_1|^2 \rangle \langle |\dot{sub}_2|^2 \rangle}} \tag{4.6}$$

where $\dot{sub}_1$ and $\dot{sub}_2$ are the two SLC sub-apertures. In brief, ρ_{sub} assumes values between zero and one, where ships are characterized by high value of coherence in contrast to the low value expected from the sea clutter. Therefore the detector is summarized as

$$\frac{\left|\langle \dot{sub}_1 \dot{sub}_2^* \rangle\right|}{\sqrt{\langle |\dot{sub}_1|^2 \rangle \langle |\dot{sub}_2|^2 \rangle}} > Thr \tag{4.7}$$

However, (Souyris et al., 2003) found the use of ρ_{sub} disappointing for target detection. The main reason is that the normalization factor in Equation (4.6) does not permit to consider radiometry in the detection aspect. To remove this drawback, (Souyris et al., 2003) proposed to use the cross-correlation between the sub-apertures (naming it Internal Hermitian Product, IHP) as it is more suitable to capture both radiometric and phase behaviours, leading to the detector:

$$IHP_{sub} = \left|\langle \dot{sub}_1 \dot{sub}_2^* \rangle\right| > Thr \tag{4.8}$$

(Brekke et al., 2013) pointed their attention to study the effects of L_{sub} and bandwidth overlap using two sub-apertures. Their analysis revealed enhancements in the TCR for large ranges of sub-aperture bandwidths, including cases of partial overlap. (Greidanus, 2006) tested three non-overlapping sub-apertures and several methods to combine them. Based on a limited dataset, it was found that ship targets show a very low correlation between (three non-overlapping) sub-apertures. This has been noticed for small fishing vessels, which are usually subject to azimuth smearing due to sea-state induced motions, and as well for large vessels in the favorable case of low sea state. (Greidanus, 2006) motivated these findings as a possible (but not necessary) combination of the look-to-look fading caused by few dominant scattering centers and azimuth displacements due target rotational motions. In (Marino et al., 2015) an extensive performance analysis of spectral analysis techniques for ship detection has been conducted. The study includes sub-aperture method performed, only in range and only in azimuth, for different polarizations and working frequencies. Besides the detectors based on ρ_{sub} and IHP_{sub}, the sub-aperture entropy

$$H_{sub} = -\sum_{j=1}^{3} P_j \log_3 P_j \tag{4.9}$$

where $P_j = \lambda_j/(\lambda_1 + \lambda_2 + \lambda_3)$, with $j \in \{1,2,3\}$, are the probabilities obtained after diagonalization of the covariance matrix using $n=3$ sub-apertures, and a Generalized Likelihood Ratio Test (GLRT) have been taken into account.

4.2. Multi-Polarization Target Detectors

This section is dedicated to summarize the main research activities carried to pursue the **Objective 2** defined in Chapter 1. The first part is dedicated to an overview of polarimetric detectors. Next to the theoretical part, the proposed approaches developed in the framework of this thesis are discussed showing the obtained results and validation.

4.2.1. Overview of target detection using multi polarization SAR data

In this sub-section, an overview of marine target detection algorithms that make use of multi polarization SAR data is given. The first part introduces algorithms that need a full scattering matrix (quad-pol data), while in the second part are discussed the one that can perform well also for a simpler SAR configuration as for dual-pol acquisitions or that can be adapted to it.

Considering multi polarization SAR data as the contemporaneous availability of different image layers, a very simple strategy is to apply a single-pol pre-screener separately to each polarimetric channel. The final pre-screener has the task to properly combine the individual results. This strategy has been proven to be a solution to reduce the number of false alarms in non-homogeneous ocean clutter in CFAR approaches (Sciotti et al., 2002). On the other hand, fusing the polarimetric channels and then apply a pre-screener algorithm is a strategy that introduces polarimetric knowledge into the detector. One approach is to extract the total backscattered power from the scattering matrix. The detector in this case is provided by

$$Span([S]) = \langle |\dot{S}_{hh}|^2 \rangle + 2\langle |\dot{S}_{hv}|^2 \rangle + \langle |\dot{S}_{vv}|^2 \rangle > Thr \tag{4.10}$$

which should furnish a way to reduce the rate of missed detection due to possible nulls of the target in one polarization. However, the *Span* detector doesn't ensure an increase of detection rate for targets with low backscatter power.

(Novak et al., 1993) firstly demonstrated the Polarimetric Whitening Filtering (PWF) as a technique able to optimally reduce the standard deviation of the backscattering intensity associated with the speckle in PolSAR data. It was mathematically proved that via manipulation of the PolSAR basis, it is possible to have an equally distributed power making the clutter appear as white noise. The new basis is provided by the vector in Equation (4.11)

$$\left[\dot{S}_{hh} \quad \frac{\dot{S}_{hh}}{\sqrt{\varepsilon}} \quad \frac{\dot{S}_{vv} - \dot{\rho}^* \sqrt{\gamma} \dot{S}_{hh}}{\sqrt{\gamma(1-|\dot{\rho}|^2)}}\right]^T \tag{4.11}$$

where γ and $\dot{\rho}$ are the polarization ratio and complex coherence defined in Equation (3.13) and $\varepsilon = \langle |\dot{S}_{hv}|^2 \rangle / \langle |\dot{S}_{hh}|^2 \rangle$. Similarly with the *Lexicographic* basis and the *Span* detector, the PWF detector can be summarized by

$$|i_{PWF}| = |\dot{S}_{hh}|^2 + \frac{|\dot{S}_{hv}|^2}{\varepsilon} + \frac{|\dot{S}_{vv} - \dot{\rho}^* \sqrt{\gamma} \dot{S}_{hh}|^2}{\gamma(1 - |\dot{\rho}|^2)} > Thr \tag{4.12}$$

(Liu et al., 2005) adapted the G-GLRT to PolSAR data, namely PO-LRT. Assuming that the scattering features vector $k_L = [\dot{S}_{hh}\ \dot{S}_{hv}\ \dot{S}_{vh}\ \dot{S}_{vv}]^T$ is characterized by its elements being jointly complex Gaussian variables, k_L is a random vector with pdf

$$P(k_L) = \frac{1}{(2\pi)^2 \sqrt{\det(\mathrm{C}_4)}} exp^{\{-1/2(k_L - \mu)^H \mathrm{C_4}^{-1}(k_L - \mu)\}} \tag{4.13}$$

where μ is the mean vector and C_4 is the 4x4 polarimetric covariance matrix obtained by the outer product of the features vector. (Liu et al., 2005) assumes that both ocean and ship backscatter have zero mean vector ($\mu = 0$), therefore, the detector in the G-GLRT sense given in Equation (4.5) can be written as

$$k_L^H (\mathrm{C}_4^b)^{-1} k_L - k_L^H (\mathrm{C}_4^t)^{-1} k_L > Thr \tag{4.14}$$

where C_4^b and C_4^t are the polarimetric covariance matrix of background and target, respectively. Furthermore, it is typically found that the elements of the covariance matrix for target samples are much larger in magnitude than those of the background samples. Taken this into account the PO-LRT detector can be further simplified with the following approximation

$$k_L^H (\mathrm{C}_4^b)^{-1} k_L > Thr \tag{4.15}$$

In (Marino, 2013) the Geometrical Perturbation-Polarimetric Notch Filter (GP-PNF) is developed and applied to detect ships in PolSAR images. The general idea of the GP-PNF is a filter able to reject sea clutter returns and extract the remaining features. Therefore, it is applied for ship detection but it can be generalized as detector of marine target. Considering the scattering features vector $k_L = [\dot{S}_{hh}\ \dot{S}_{hv}\ \dot{S}_{vv}]^T$ (with $\dot{S}_{hv} \approx \dot{S}_{vh}$) of fully polarimetric SAR data, the features partial scattering vector is introduced as:

$$k = Trace([\mathrm{C}_3]\Psi) = \left[\left\langle|\dot{S}_{hh}|^2\right\rangle\ \left\langle|\dot{S}_{hv}|^2\right\rangle\ \left\langle|\dot{S}_{vv}|^2\right\rangle\ \left\langle\dot{S}_{hh}^H \dot{S}_{hv}\right\rangle\ \left\langle\dot{S}_{hh}^H \dot{S}_{vv}\right\rangle\ \left\langle\dot{S}_{hv}^H \dot{S}_{vv}\right\rangle\right]^T \tag{4.16}$$

where Ψ is a set of 3x3 basis matrices under a Hermitian inner product and therefore the $Trace(\cdot)$ operator is applied to a vector of six matrices. The partial scattering vector $k \in \mathbb{C}^6$ and has the first three elements real positive and the second three complex numbers. The final version of the detector is given by

$$\gamma_n = \frac{1}{\sqrt{1 + \dfrac{RedR}{k^H k - |k^H \hat{k}_b|^2}}} > Thr \tag{4.17}$$

where $RedR$ stands for reduction ratio, as nomenclature inheritance of the Partial Target Detector (PTD) which inspired (Marino et al., 2012). The term $k^H k$ in the Equation (4.17) is the total power, whereas the term $\left|k^H \widehat{k}_b\right|^2$ is the background power (sea clutter). Therefore, $k^H k - \left|k^H \widehat{k}_b\right|^2$ represents the power of marine targets. For sea surface γ_n is proximal to zero, while in the presence of a target it approximates the unity (Marino, 2013).

It is important to note that both approaches proposed by (Liu et al., 2005) and (Marino, 2013) can be adapted for dual-pol SAR data. Both studies agree on the fact that the proposed detectors, PO-LRT and GP-PNF, obtain the best ship detection performances when applied to full polarimetric SAR or for dual-pol configuration when the co-pol channels (HH and VV) are available.

(Shirvany et al., 2012) investigated the complementary of the Degree of Polarization (DoP), thus defined as Degree of Depolarization (DoD), as a potential detector of ships under different linear, hybrid/compact dual-pol SAR configuration. Here we consider the results obtained in (Shirvany et al., 2012) only regarding ship detection using DoD in linear dual-pol SAR. Defined the scattering vectors for dual-pol radar configuration as

$$\begin{aligned} k_{D1} &= [\dot{S}_{hh}\ \dot{S}_{hv}]^T \\ k_{D2} &= [\dot{S}_{hh}\ \dot{S}_{vv}]^T \\ k_{D3} &= [\dot{S}_{vh}\ \dot{S}_{vv}]^T \end{aligned} \tag{4.18}$$

which provides three different combination depending on the transmitted and received linear polarization, the DoD is related to the Stokes vector $[g_0\ g_1\ g_2\ g_3]^T$ by the following relation (Cloude, 2009; Lee and Pottier, 2009)

$$\mathrm{DoD} = 1 - \frac{\sqrt{{g_1}^2 + {g_2}^2 + {g_3}^2}}{g_0} \tag{4.19}$$

The elements of the Stokes vector are called Stokes parameters, which are four real values capable to characterize the polarization state of a wave. If any of the Stokes parameters has a nonzero value, it indicates the presence of a polarized component in the plane wave. Being g_0 equal to the total power (density) of the wave, DoD assumes values between zero and one quantifying the amount of de-polarization in the EM wave. A depolarizing interaction causes totally polarized states to emerge with $\mathrm{DoD} > 0$ and this can be related to presence of a ship or marine target on the ocean surface. Hence, the detector is summarized as

$$1 - \frac{\sqrt{{g_1}^2 + {g_2}^2 + {g_3}^2}}{g_0} > Thr \tag{4.20}$$

Based on their experimental results, (Shirvany et al., 2012) concluded that linear HH-VV dual-pol configuration deliver better detection performance compared to the other two possible combinations.

4.2.2. An approach for target detection using reflection symmetry in Dual-Pol data

The target detector developed for X-band dual-polarimetric co- and cross-pol SAR data has been published in the paper **A.3**, which constitutes integral part of this dissertation.

In (Migliaccio et al., 2011; Nunziata et al., 2012) a physically-based approach to observe man-made marine metallic targets using coherent dual-polarimetric L- and C-band SAR data has been proposed. It is based on the fact that sea surface, being reflection symmetric, calls for a negligible correlation between the co- and cross-polarized channels; whereas the reflection symmetry no longer applies for man-made metallic targets that, hence, results in a larger correlation. In (Nunziata et al., 2012) a meaningful dataset of HH-HV marine images acquired by space-borne L- and C-band SARs, have been processed to show the effectiveness of the proposed approach. The number of targets present in the dataset is quite large and composed of offshore platforms (with available ground-truth) and visually inspected ships (with no available ground-truth). The overall performance of the proposed filter gives a low number of false positives (~1.6%) and false negatives (~2.5%). (Velotto et al., 2013) extended to X-band the physical rational proposed in (Nunziata et al., 2012). It must be noted that X-band SAR observation of man-made metallic targets at sea is more challenging than in L- and C-band. At X-band the probability of occurrence of high coherent returns (and, therefore, false positives) is very high, also at intermediate incidence angles, and it depends on sea state conditions (Migliaccio et al., 2012). Moreover, atmospheric disturbances are more pronounced in X-band than in lower frequencies and a detector not sensible to these disturbances is preferable. The polarimetric background that lies at the basis of symmetry properties and the polarimetric model used for target detection are briefly reviewed.

Symmetry is a property of natural targets that, if satisfied, leads to an easier scattering problem. In (Lee and Pottier, 2009; Nghiem et al., 1992) reflection, rotation and azimuthal symmetry properties have been formulated in terms of the covariance and coherency matrix previously defined by Equation (2.25) and Equation (2.26), respectively. It has been shown that geophysical media that holds symmetry properties can be characterized by a covariance matrix (the explicit formulation is given only for the covariance matrix to save space) with less independent backscattering coefficients. In the context of this thesis, only the reflection symmetry is considered.

The covariance matrix C_3 of a geophysical media under the reflection symmetry, in the plane normal to the Line-of-Sight (LoS), is given by (Nghiem et al., 1992):

$$[\mathrm{C}_3]_{ref} = \begin{bmatrix} \langle|\dot{S}_{hh}|^2\rangle & 0 & \langle\dot{S}_{hh}\dot{S}_{vv}^*\rangle \\ 0 & 2\langle|\dot{S}_{hv}|^2\rangle & 0 \\ \langle\dot{S}_{vv}\dot{S}_{hh}^*\rangle & 0 & \langle|\dot{S}_{vv}|^2\rangle \end{bmatrix} \tag{4.21}$$

This symmetry forces the polarimetric scattering coefficient for the correlation between the co- and cross-polarized scattering amplitudes to be nullified. Hence, the modulus:

$$r = \left|\left\langle \dot{S}_{hh}\dot{S}^{*}_{hv}\right\rangle\right| = \left|\left\langle \dot{S}_{vh}\dot{S}^{*}_{vv}\right\rangle\right| \tag{4.22}$$

is the natural norm to measure the departure from the reflection symmetry case. This means that when r tends to 0, the observed scene is characterized by the symmetry property, while for larger r value departure from reflection symmetry is achieved.
To specialise symmetry properties to the observation of metallic targets at sea in X-band dual-polarization SAR measurements, the following scenarios are expected (Velotto et al., 2013):

- Sea surface is a natural distributed target where reflection symmetry properties are expected, which implies $r \approx 0$.
- Ocean targets are man-made complex structures where reflection symmetry properties are not expected, which implies $r \gg 0$.

It must be noted that, because of the misalignment between radar coordinates and the scene symmetry axis, a slight departure of r from zero for sea surface target is predicted (Nunziata et al., 2012). Last but not least, it is important to remind that coherent co- and cross-pol SAR products are sufficient to apply the Equation (4.22), which is beneficial for SAR configuration which due to the acquisition mode, e.g. TOPSAR in Sentinel-1, or simplicity in the hardware on board, e.g. ENVISAT, are not able to acquire dual-pol channels HH-VV.

In brief, the marine target detector proposed for X-band coherent dual-pol data (depending on the selected combination) is summarized in the Equation (4.23).

$$\left|\left\langle \dot{S}_{hh}\dot{S}^{*}_{hv}\right\rangle\right| > Thr \;;\; \left|\left\langle \dot{S}_{vh}\dot{S}^{*}_{vv}\right\rangle\right| > Thr \tag{4.23}$$

4.2.3. Results and algorithm validation

In this section, the effectiveness of target detection based on the reflection symmetry model is verified using actual TS-X data and ground truth target positions provided by time and space collocated AIS data, static oil rig database, and nautical charts to identify known navigation aids and buoys. This sub-section summarizes the findings published in the paper **A.3** and contains additional material not included in the manuscript.

The dataset analyzed is composed of seven TS-X SM SSC dual polarization HH-HV and VV-VH standard products, which is described in details in Table 4.1. Ancillary external wind information (extracted from model data, buoys, and scatterometer data) is also provided to show the dataset heterogeneity.

Table 4.1 – TS-X dual-polarimetric dataset

ID	Date & Time (UTC)	Location	Polarization	Inc. angle (°)	Wind speed (m/s)	Wind dir.
img-1	2009-07-11; 18:14	Gibraltar	HH-HV	34.73	2.7	SE
img-2	2011-08-30; 14:15	San Francisco	VV-VH	39.69	2.2	SE
img-3	2009-07-15; 06:29	Gibraltar	HH-HV	30.51	5.1	SW
img-4	2009-09-21; 18:06	Spain	VV-VH	20.00	5.5	SE
img-5	2012-03-29; 23:57	Gulf of Mexico	VV-VH	43.00	5.0	SE
img-6	2012-04-12; 16:49	Naples	HH-HV	28.16	3-5	SW
img-7	2011-10-06; 09:28	South Korea	VV-VH	39.68	10-12	NW

Figure 4.6(a) shows the HH-polarized calibrated amplitude image, where land is masked in purple and 19 targets are highlighted by white rectangles (labeled as *T1−T19*). The ROI displayed in Figure 4.6(a) is a sub-image of approx. 7km x 18km, extracted from the TS-X dual-polarized HH-HV data (*img-1* in Table 4.1). According to the AIS information, the targets *T1−T16* are ships whose sizes range from 40m up to 300m. No ground truth is available for targets *T17−T19*, which have been consequently flagged as visually inspected.

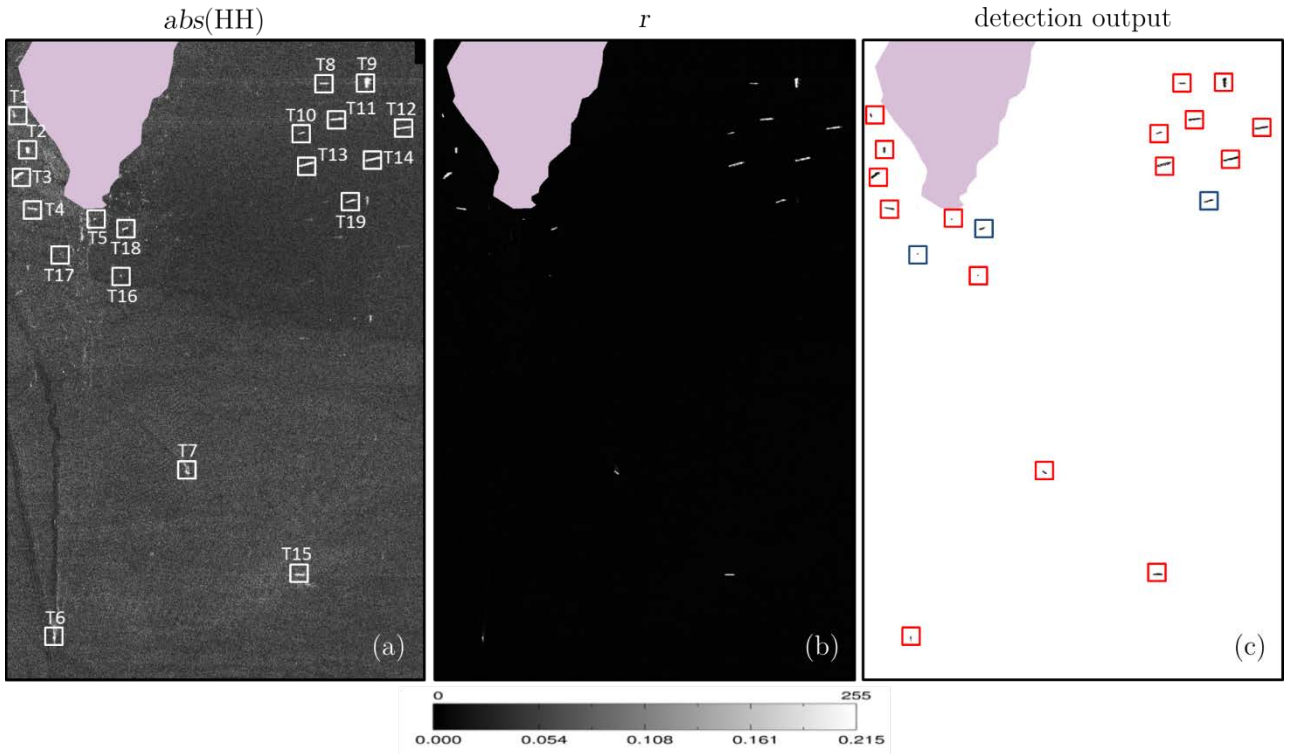

Figure 4.6 – TS-X data collected off the coast of Gibraltar on July 11, 2009, at 18:14 UTC with land masked in purple. (a) Sub-scene of approximately 7km x 18km showing, in radar coordinates, the HH-polarized calibrated amplitude image, where: *T1−T16* are AIS-confirmed ships, *T17−T19* are visually inspected targets. (b) Gray-tone $\boldsymbol{r}$ image estimated using 3x3 window. (c) $\boldsymbol{r}$-based logical true (sea) and false (target) detection output, where targets confirmed by AIS and visually inspected are marked in red and blue, respectively.

Figure 4.6(b) displays the reflection symmetry r parameter using a 3x3 moving window. To visually compare the r image (Figure 4.6(b)) with the calibrated HH amplitude (Figure 4.6(a)) on both data the same histogram stretching procedure has been applied (bottom scale of the colorbar). It can be noted that r is close to 0 everywhere but in correspondence of targets. This confirms the polarimetric model described in the previous section. To discuss the capability of the r-based approach in observing metallic targets at sea, with respect to conventional single-pol ones, mean values of r, HH and HV calibrated amplitudes are evaluated for both targets and their surrounding sea area. The results, obtained for the 19 targets present in Figure 4.6(a), are summarized in the stacked histogram plot in Figure 4.7(a). It is noticeable that the measured mean value of r over sea surface is negligible and always less that both HH and HV. On the other hand, the mean value of r over targets is

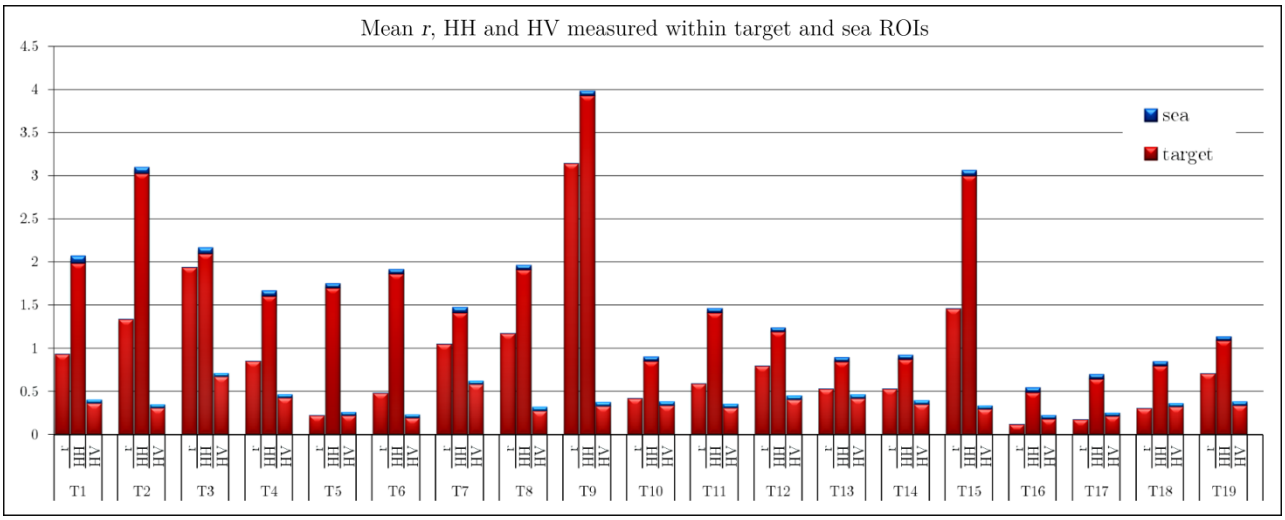

(a)

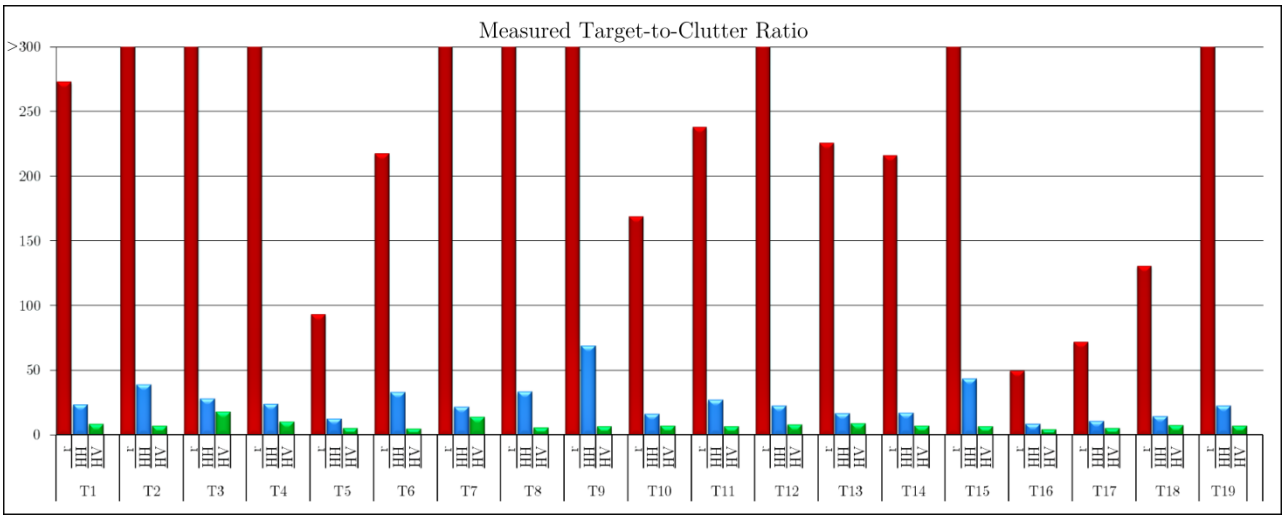

(b)

Figure 4.7 – Qualitative and quantitative comparison of $\boldsymbol{r}$-based approach for target detection, with respect to conventional single-polarization ones. (a) Stacked histogram of mean values of $\boldsymbol{r}$, HH and HV measured over target (red) and surrounding sea surface (blue). (b) Measured TCR for the 3 parameters: $\boldsymbol{r}$ (red), HH (blue) and HV (green).

always less than HH and in the majority of the cases higher than HV. This suggests to quantitatively analysing the TCR. As can be deduced by the TCR histogram plot in Figure 4.7(b), the r_{TCR} is at least one order of magnitude higher than HH_{TCR} and HV_{TCR}. From the trends shown in Figure 4.7(a)-(b) are of particular interest the targets *T5*, *T10* and *T16*. In fact, although the mean r value over these targets is lower than the mean value of the single-pol channel ones, the measured TCR is found to be quite higher. To examine in depth this performance, the normalized HH, HV, and r data that include the ship *T16*, is shown in Figure 4.8. The target *T16* (which happens to be the smallest one) is centred in a 200 x 200 pixel sea area.

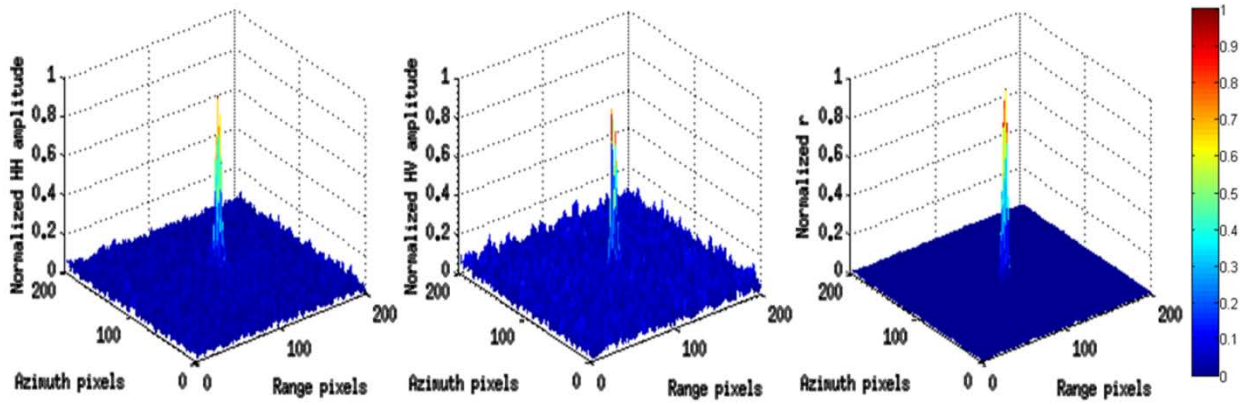

(a) (b) (c)

Figure 4.8 – (a) and (b) Normalized HH and HV calibrated amplitudes and (c) $\boldsymbol{r}$ parameter, measured over a sea surface area that includes the ship labeled as *T16*.

The results shown in Figure 4.8 suggests that the r-based approach acts as a clutter suppression filter while enhancing the target. Accordingly with these findings, a fixed threshold *Thr* can be adopted to conceive an unsupervised filter both robust and effective. Detection output with an empirical threshold $Thr = 0.1$ is shown in Figure 4.6(c), where targets, confirmed by AIS and visually inspected, are marked in red and blue, respectively.

Figure 4.9(a) shows the HH-polarized calibrated amplitude image, where the targets are highlighted by white rectangles. The ROI displayed in Figure 4.9(a) is a sub-image of approx. 15km x 30km, extracted from the TS-X dual-polarized HH-HV data (*img-3* in Table 4.1). All targets present in the ROI were matched with a valid AIS message. In particular these are cargo and tanker ships, whose sizes range from 49m to 274m. A pronounced wavelike pattern (see upper-left side of the image) and atmospheric-related phenomena (see bottom side of the image) make this scene very challenging for conventional SAR-based target detectors (Brusch et al., 2011; Crisp, 2004; Gambardella et al., 2008). Due to the fluctuation in the backscatter caused by these phenomena, some targets are hardly visually distinguishable in the HH amplitude image (e.g., the 49m ship in the middle right of the Figure 4.9(a)). Moreover, the performance of a CFAR detector, based only on backscatter signal of single-pol data, might drop and change between different polarizations. To further investigate this point, the targets in Figure 4.9(a) labeled as *Ship1* and *Ship2*

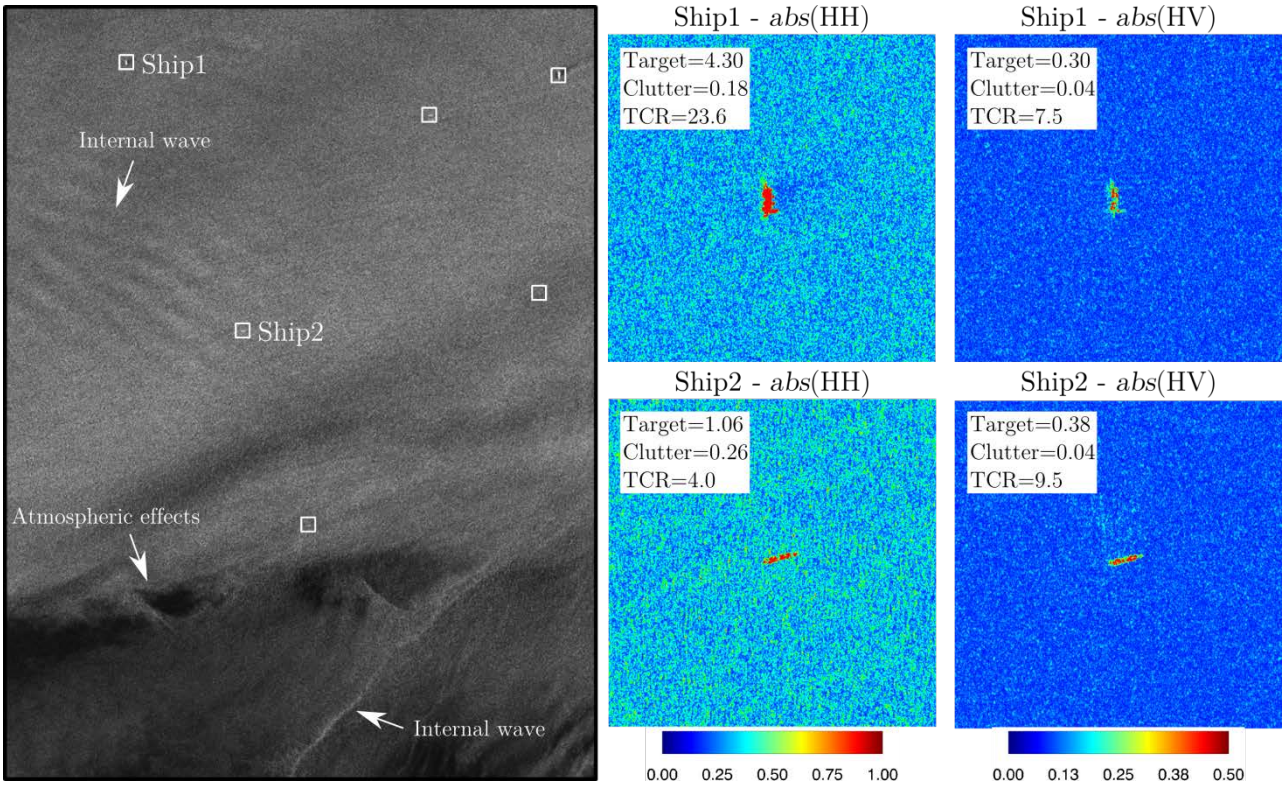

(a) (b)

Figure 4.9 – TS-X data collected off the coast of Gibraltar on July 15, 2009, at 06:29 UTC (indicated as *img-3*). (a) Sub-scene of approximately 15km x 30km showing, in radar coordinates, the HH-polarized calibrated amplitude image. (b) Colour coded radar backscatter of the targets *Ship1* and *Ship2* at different polarizations.

have been used to generate Receiver Operating Characteristic (ROC) curves (Fawcett, 2006). These two targets have been chosen because are two different types of ship with similar length (138m and 128m, respectively) imaged by TS-X with similar angle of incidence, but characterized by different surrounding sea state. This can be qualitatively appreciated in the zoom-in of the two ships shown in Figure 4.9(b), where embedded in the figures are reported the mean values of the radar backscatter (in linear unit) associated with the target and clutter. It can be mainly noted that, based on local measured TCR, HH is the preferable polarization for detecting the target *Ship1*, while for *Ship2* is HV. This behavior is better highlighted by the ROC curves, generated from an ocean region that includes *Ship1* and *Ship2*, shown in Figure 4.10(a)-(b). The detectors' performance based on HH, HV and r can be directly compared. The r-based detector outperforms the ones based on single-pol, independently of the local clutter level. This finding is further confirmed by the ROC curves in Figure 4.10(c), which is obtained considering all targets and clutter variations in Figure 4.9(a).

The detection output for the example in Figure 4.9 can be found in the annex reference paper (Velotto et al., 2013).

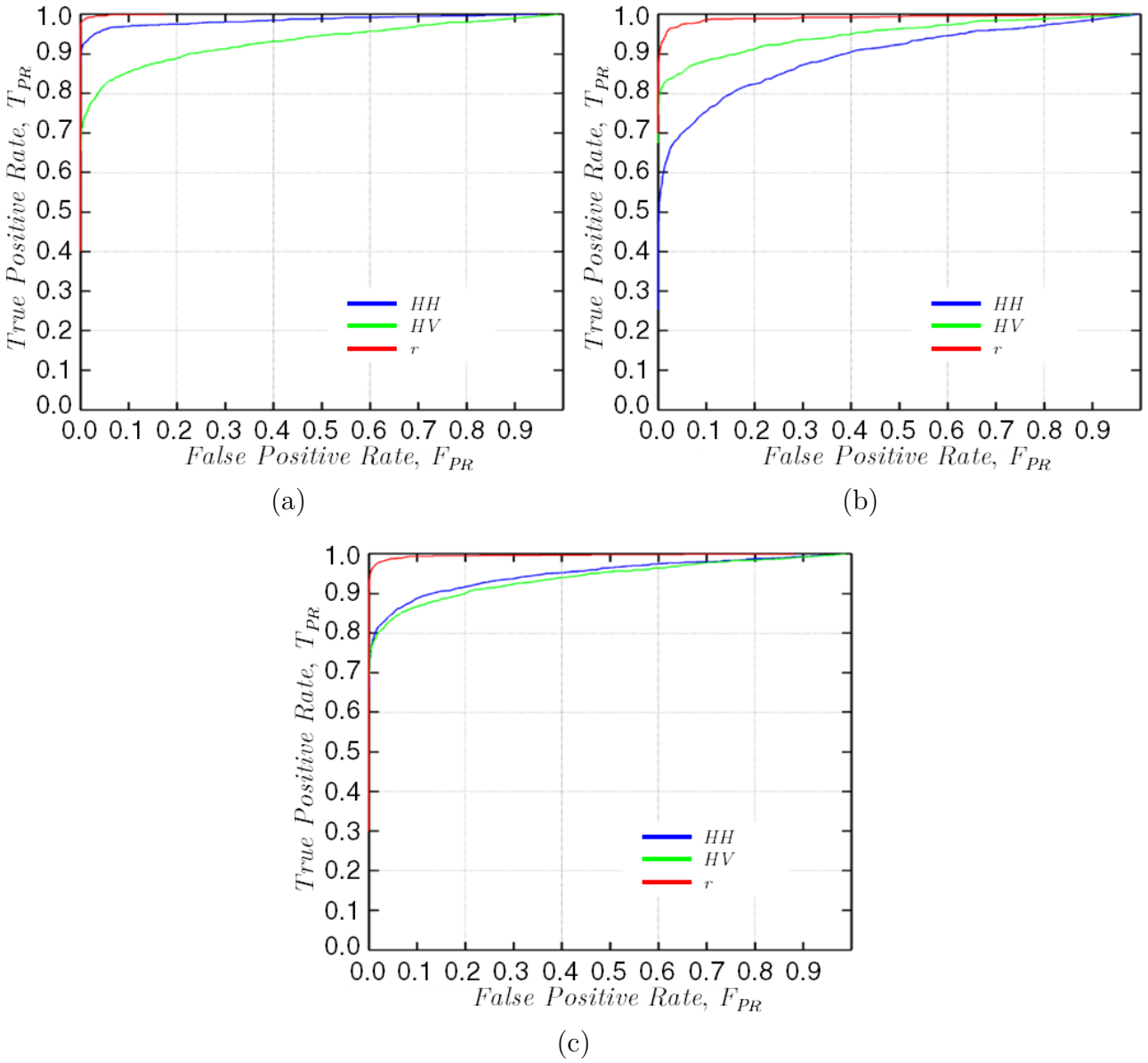

Figure 4.10 – ROC curves, HH in blue, HV in green and $\boldsymbol{r}$ in red. (a) Target labeled *Ship1*. (b) Target labeled *Ship2*. (c) All targets present in Figure 4.9(a).

The experiments conducted on the TS-X dual-pol VV-VH, show that r-based detector is suitable for such case, as further confirmation of robustness and effectiveness (Velotto et al., 2013). This aspect of the r-based detector is important for the new European Space Agency (ESA) SAR mission Sentinel-1, since it provides routinely Interferometric Wide Swath (IWS) dual-pol VV-VH data over European waters.

A preliminary validation of an automatic target detection based on the proposed r filter is given in Table 4.2. It summarizes the results obtained by processing the data set detailed in Table 4.1 with a total number of 191 targets. The proposed filter correctly detects 175 targets with 16 false negatives. The latter are always related to small targets whose sizes are less than 10m.

Table 4.2 – Summary of the target detection results obtained by processing the dataset through the r filter

ID	Targets	Ground truth	Detected targets	False negatives	False positives
img-1	70	57	68	2	0
img-2	50	21	48	2	0
img-3	8	7	8	0	0
img-4	7	5	5	2	0
img-5	14	7	12	2	0
img-6	13	0	12	1	0
img-7	29	4	22	7	0

No false positive is present (excluding a buffer zone from the coastline of ~500m). The minimum sizes of the detected AIS-confirmed and visually inspected targets are 20m and 10m, respectively. Nine lighted buoys, whose sizes are around 2m, are also detected. Note that, even in high-wind conditions (see *img-7* in Table 4.1), no false positive is present (see Table 4.2), while the seven false negatives are due to visually inspected targets whose sizes, estimated by the SAR image, are less than 5 m. Despite these encouraging results, an extensive validation of the automatic approach, which should include also ship parameters estimation, is yet to be done and is planned in the future work.

4.3. Discrimination of False Positives caused by Azimuth Ambiguity

This section is dedicated to summarize the main research activities carried to pursue the **Objective 3** defined in Chapter 1. After giving the motivations of this research and a summary on the theory of the proposed method, the results and an initial validation of the algorithm are discussed. A comparison of the proposed method with other techniques able to remove or reduce azimuth ambiguities in PolSAR data concludes this chapter.

In the Chapter 2, range and azimuth ambiguities have been introduced as SAR artefacts. Although the term *artefact* is not totally appropriate for what is a system limitation, it has been used since azimuth ambiguities are among the main sources of false alarms in marine target detection algorithms. The signal intensity of replicas of point-like targets, e.g. ships, or distributed targets located in coastal area, e.g. harbor metallic structures, can easily exceed the level of radar backscatter recorded over the ocean surface generating ghosts that behave or have shapes similar to marine target. This concept is clarified by two exemplary cases of SAR image given in Figure 4.11. In Figure 4.11(a), the ghost replicas of the Oakland naval supply deposit are clearly visible over the sea surface. These ambiguities make the detection of targets like the ships *T2* and *T3* more challenging, as well as the erroneous

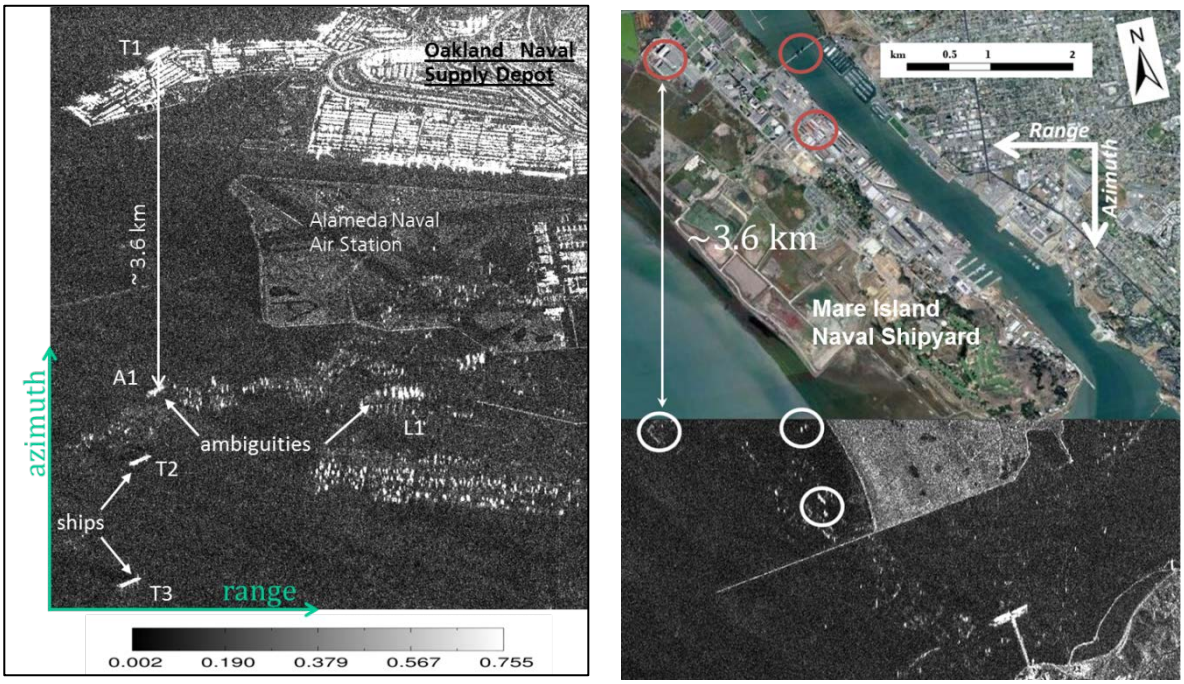

(a) (b)

Figure 4.11 – Examples of possible false alarms caused by azimuth ambiguities. (a) Ships and harbour structures replicas over the ocean. (b) Ship-like ghosts in SAR image due to metallic objects not illuminated by the radar antenna.

detection of the ghosts *A1* and *L1*. The discrimination between real targets and ghosts becomes even harder when the source of the ghost replica is actually not present in the focused SAR image. Figure 4.11(b) depicts this circumstance, where the last patch in azimuth of a SAR acquisition is overlaid to an optical image (© Google Earth) of the same area. What can be visually, because of their shapes similar to ships, misinterpreted in the SAR patch (indicated with white circles) as possible marine targets, are actually ghosts' replica of the structures identified on the optical image (indicated with red circles). It is obvious at this point that the discrimination of real marine targets from false detections caused by ambiguities is not a trivial task.

Azimuth ambiguities in SAR images are spatially displaced in range and azimuth directions at approximate locations:

$$\Delta x_{AZ} \approx \frac{mPRFv_S}{f_{\mathrm{DR}}} \tag{4.24}$$

$$\Delta x_{RG} = \frac{m\lambda PRF}{f_{\mathrm{DR}}}\left(f_{\mathrm{DC}} + \frac{mPRF}{2}\right) \tag{4.25}$$

where m is the ambiguity index, f_{DR} and f_{DC} are the Doppler rate and centroid frequency used in the processor (Curlander and McDonough, 1991). Substituting the equation of the f_{DR} and f_{DC}, the following relation between Δx_{AZ} and Δx_{RG} is obtained:

$$\Delta x_{AZ} \approx m \frac{\lambda PRF}{2v_S} s_0 \tag{4.26}$$

$$\Delta x_{RG} = \frac{(\Delta x_{AZ})^2}{2s_0} \tag{4.27}$$

The azimuth displacement is proportional to the ambiguity index and PRF, while the range displacement is proportional to the square of the azimuth displacement. Because of these displacements, ambiguities appear blurred in the focused image as results of the incorrect range migration correction. (Li and Johnson, 1983) provides the number of range cells that the ambiguity is dispersed, as quantity to measure the blurring effect:

$$N_{RG} \approx \frac{m\lambda^2 PRF}{4v_S \delta_a \delta_r} s_0 \tag{4.28}$$

A large N_{RG} is desirable since the ambiguity will be dispersed in the image. N_{RG} is directly proportional to: - the square of λ, which indicates that ambiguity defocusing is less relevant for high frequency systems, e.g. X-band; - the ambiguity index m, which indicates a linear increase of the dispersed ambiguity energy.

The discrimination of false positives caused by ambiguities proposed in (Brusch et al., 2011) for single-pol TS-X data is based on the rationale that the shifts in position of the ghosts, with respect to the original targets, can be evaluated as a function of the radar system parameters given by Equation (4.28). From a pre-screener point of view, e.g. 2P-CFAR, all possible bright anomalies in the image are detected, only the ones that do not follow at distance of $\pm\Delta x_{AZ}$ from each other are retained as valid targets. Note that, in (Brusch et al., 2011), Δx_{RG} and $m > 1$ have not been considered because the shift in range for $m = 1$ is negligible and higher order ambiguity are considered rare. Although this approach is suitable for NRT ship detection service, it suffers of the following drawbacks:

1) It raises the possibility of missed targets, i.e. a true target is discarded because it is close to the ambiguity of another target (this scenario might happen in harbours with intense ship traffic).

2) It fails to discard ambiguities caused by man-made metallic structures over land, i.e. the ambiguities are caused by distributed targets.

3) It fails to remove false alarms caused by targets that lie outside the focused image, i.e. the replica is not removed if its source is not detected.

The method in (Brusch et al., 2011) tackle the problem of false alarms caused by ambiguity during the discrimination steps adding the mentioned discriminative rule. A different way to deal with the ambiguity issue is in pre-processing, improving the precision of SAR processing (Bamler and Runge, 1991). (Moreira, 1993) proposed a method for suppressing the azimuth

ambiguities in SAR images based on the idea of the ideal filter, i.e. convolution of the sampled azimuth signal with a correction function. However, in order to build the deconvolving function, the phase and amplitude of the ambiguities must be precisely known, which limits its applicability only to the suppression of ambiguities caused by point-like targets. In situations where the source of the ambiguity is a distributed target, i.e. in coastal zone over sea, the concept of selective filter has been found more appropriate (Li and Johnson, 1983; Monti Guarnieri, 2005). The idea is to use only the part of the azimuth spectrum that is less affected by aliasing. This results in an unavoidable resolution loss, but can be used in cases of ambiguity caused by both point and distributed targets. In particular, (Monti Guarnieri, 2005) suggested an adaptive Wiener filter, in order to both minimize the degradation in resolution and limit it to the area affected by the ambiguities. The proposed method is, therefore, composed of two steps: identification of areas affected by ambiguities and local estimation of *AASR*. (Villano and Krieger, 2014) proposed a new technique for the local estimation of the *AASR* in SAR images, based on the spectral properties of the image. The spectral-based method developed in (Villano and Krieger, 2014) doesn't suffer the drawback of the backscatter-based method proposed in (Monti Guarnieri, 2005), which requires that the areas responsible for the ambiguities to be within the focused image. Moreover, by means of Monte Carlo simulations, the spectral-based method has shown to be more accurate than the backscatter-based method, e.g. in case of high values of the local *AASR*. (Di Martino et al., 2014) pointed out that the method proposed in (Monti Guarnieri, 2005) may fail to identify areas affected by ambiguities for the current configurations of the antenna pattern and *PRF* of the in-orbit high-resolution space-borne SARs, e.g. TS-X. In particular, the original Wiener filter is not adequate when the peak of one folded *AAP* sidelobe, e.g. the right one, is close to the null of the other one, i.e. the left one, see Figure 4.12. Starting from this observation (Di Martino et al., 2014) proposed an asymmetric filtering approach, where only the ambiguity due to one folded sidelobe is

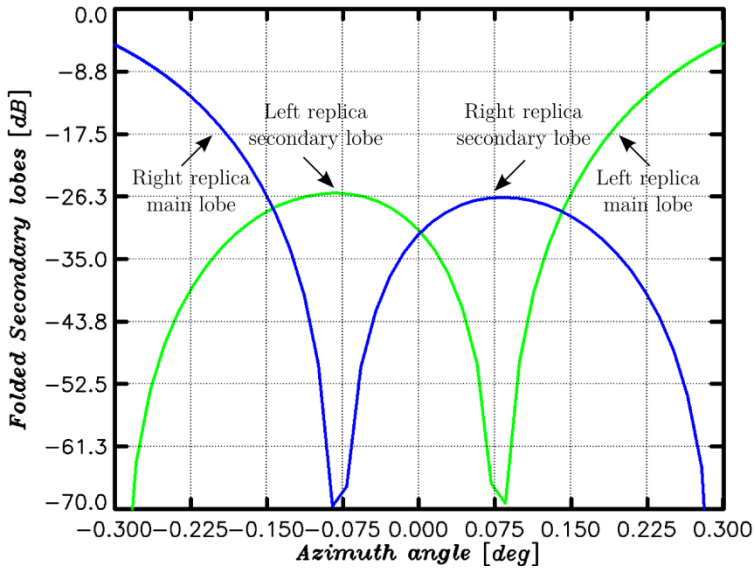

Figure 4.12 – TS-X left and right secondary lobes of the *AAP* folded into the processed azimuth angle for SRA system configuration.

present at time. A noteworthy benefit of the developed approaches in (Di Martino et al., 2014; Villano and Krieger, 2014), over the original idea proposed in (Monti Guarnieri, 2005), is that it can be employed even when sources of ambiguities are not inside the focused image.

4.3.1. Removing Azimuth Ambiguities using Cross-Pol channels

A method to discriminate false positives caused by azimuth ambiguity in marine target detection using X-band quad-polarimetric DRA data acquired by TS-X, has been published in the paper **A.4**, which constitutes integral part of this dissertation.

As discussed in the previous section, azimuth ambiguities are less dispersed at higher frequencies, e.g. X-band, and the ambiguous signal depends on the system configuration, e.g. *AAP* and *PRF*. Before proceeding further, it is important to briefly compare TS-X SRA and DRA system configurations in terms of azimuth ambiguities. Figure 4.13(a)-(b) illustrate the

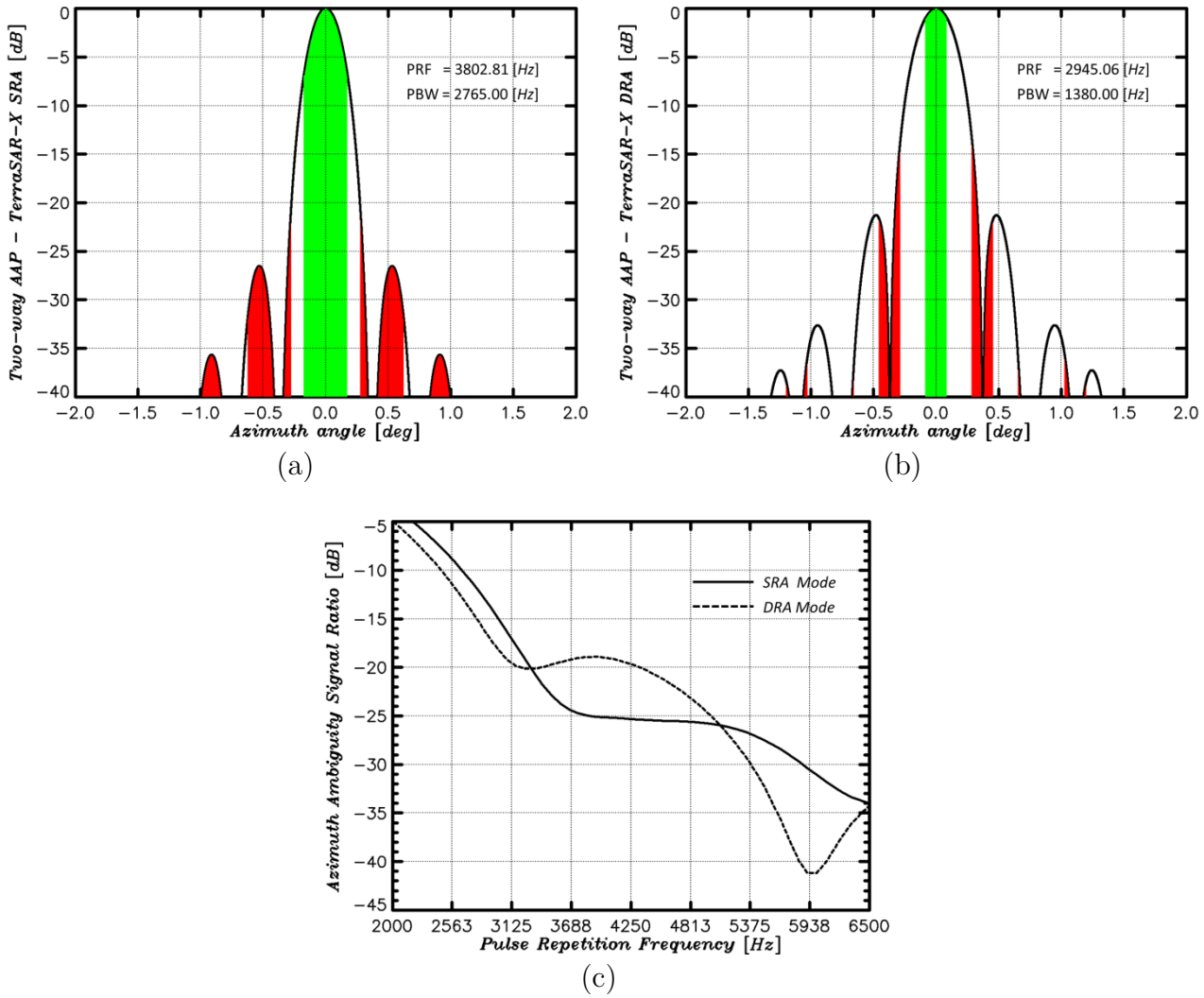

Figure 4.13 – *AASR* for SRA and DRA. (a)-(b) In green the energy of main signal, i.e. unambiguous signal; In red the energy of ambiguous signal. (c) *AASR* at changing the PRF for SRA and DRA system configuration.

un-ambiguous signal (in green) and the ambiguous signal (in red) according to the TS-X SRA ($PRF = 3802$ Hz, $PBW = 2765$ Hz) and DRA system configurations ($PRF = 2945$ Hz, $PBW = 1380$ Hz), respectively. The widen main lobe in the DRA configuration, is due to the reduction of the antenna length in azimuth (see Figure 2.11 for DRA operation) which would provide an enhancement in the geometrical resolution. However, it is also noticeable an increase in the energy of the sidelobes, which would provide a poor $AASR$ with azimuth ambiguities that become too high. (Mittermayer and Runge, 2003) have analysed the performance of TS-X DRA with different configuration and pointed out that, although TS-X was not originally designed to operate in DRA mode, with a reduction of the processed bandwidth, azimuth ambiguity ratio better than 15dB could be obtained for full polarimetric acquisitions. Figure 4.13(c) shows the behaviour of the $AASR$ as function of the PRF for SRA and DRA system configurations (PBW is set equal to 2765 Hz and 1380 Hz for SRA and DRA configurations).

With the reference to TS-X DRA operating mode sketched in Figure 2.11, assuming that the first transmitted pulse is H-polarized, then HH and HV channels are measured at the same time and formed first, whereas the VH and VV channels are measured at the same time and formed with a delay of $PRI/2$. Knowing that the radar acquires a range line whenever it travels the distance $v_S \cdot PRI$, the n-th HV sample has azimuth position $x_n = v_S(n \cdot PRI)$, while the n-th VH sample has azimuth position $x'_n = x_n + (v_S \cdot PRI/2)$. In order to co-register the polarimetric channels a linear interpolation approach is commonly used. Keeping this in mind, recalling the received signal formula given in Equation (2.10), it is specialized for the signals HV and VH as

$$s_{HV}(\tau, x_n) = A_w \cdot L_c \cdot S_{hv} \cdot g\left[\tau - \frac{2}{c}s(x_n)\right] \cdot exp\left[-i\frac{4\pi}{\lambda}s(x_n)\right] \tag{4.29}$$

$$s_{VH}(\tau, x'_n) = A_w \cdot L_c \cdot S_{vh} \cdot g\left[\tau - \frac{2}{c}s(x'_n)\right] \cdot exp\left[-i\frac{4\pi}{\lambda}s(x'_n)\right] \tag{4.30}$$

where the azimuth time variable t has been changed to the azimuth position x_n. S_{hv} and S_{vh} are the RCS coefficients. The signal s_{VH} given in Equation (4.30) at azimuth positions x_n is obtained by linear interpolation

$$s_{VH}(\tau, x_n) \cong \sum_p k_p \cdot s_{VH}\left(\tau, x_n + p\frac{v_S PRI}{2}\right) \tag{4.31}$$

where k_p is the interpolation coefficient and $p \in \{1,3,5,\dots\}$ the odd index (assuming the symmetry in the interpolation process). Approximating the target to sensor distance s in Equation (4.31) with the first two terms of its Taylor series:

$$s\left(x_n + p\frac{v_S PRI}{2}\right) \cong s(x_n) + \frac{\delta}{\delta x_n}s(x_n) \cdot p\frac{v_S PRI}{2} \tag{4.32}$$

it leads to the following approximation of the VH signal:

$$s_{VH}(\tau, x_n) \cong A_w \cdot L_c \cdot S_{vh} \cdot g\left[\tau - \frac{2}{c} s(x_n)\right] \cdot exp\left[-i\frac{4\pi}{\lambda} s(x_n)\right] \cdot \sum_p k_p \; exp\left[-i\frac{2\pi}{\lambda} \cdot pv_S PRI \cdot \frac{\delta}{\delta x_n} s(x_n)\right] \tag{4.33}$$

Making use of the reciprocity property of monostatic radar ($S_{hv} = S_{vh}$) and comparing Equation (4.33) with Equation (4.29), the relationship between HV and VH signals is:

$$s_{VH}(\tau, x_n) \cong s_{HV}(\tau, x_n) F(x_n) \tag{4.34}$$

where:

$$F(x_n) = \sum_p 2k_p cos\left[\frac{2\pi}{\lambda} \cdot pv_S PRI \cdot \frac{\delta}{\delta x_n} s(x_n)\right] \tag{4.35}$$

is the last exponential term in Equation (4.33) expressed in terms of trigonometric function. It follows that to keep the reciprocity property $s_{VH} \cong s_{HV}$ the term $F(x_n) \cong 1$. Assuming that the target position is x_T, such that $\delta r(x_T)/\delta x_T = 0$, and the first ambiguities index positions are $x_A^{\pm}$, such that the phase shift between adjacent samples is $\pm 2\pi$, i.e. the Doppler frequency is $\pm PRF$, the argument of the cosine function:

$$\frac{4\pi}{\lambda} \cdot v_S PRI \cdot \frac{\delta}{\delta x_A} s(x_A) = \pm 2\pi \;\rightarrow\; \frac{2\pi}{\lambda} \cdot v_S PRI \cdot \frac{\delta}{\delta x_A} s(x_A) = \pm \pi \tag{4.36}$$

where due to the cosine symmetry, it is easy to observe that:

$$\begin{matrix} s_{VH}(\tau, x_n) \cong s_{HV}(\tau, x_n) & & x_n = x_T \\ & \text{for} & \\ s_{VH}(\tau, x_n) \cong -s_{HV}(\tau, x_n) & & x_n = x_A^{\pm} \end{matrix} \tag{4.37}$$

which leads to the following theoretical conclusions:

- HV and VH channels are approximately equal in magnitude and phase for targets' pixels.
- HV and VH channels are each other's complex conjugate for azimuth ambiguity pixels.

In other words, due to the acquisition mode of two channels PolSAR systems and the processing applied to the measured received signals, even though reciprocity applies for targets, azimuth ambiguities break the reciprocity law being each other its complex conjugate. It is important to note that the property in Equation (4.37) is valid for any m index. Similar theoretical conclusions have been found in (Liu and Gierull, 2007). This outcome has been used by (Liu and Gierull, 2007) as clutter cancellation approach to highlight moving targets.

In (Velotto et al., 2014) a complete marine target detection processing chain has been developed for VHS X-band PolSAR data. The proposed algorithm performs the discrimination of marine targets from ambiguity first and the target detection after. The sketch of the processing chain is shown in Figure 4.14 and each step will be explained in details in the following.

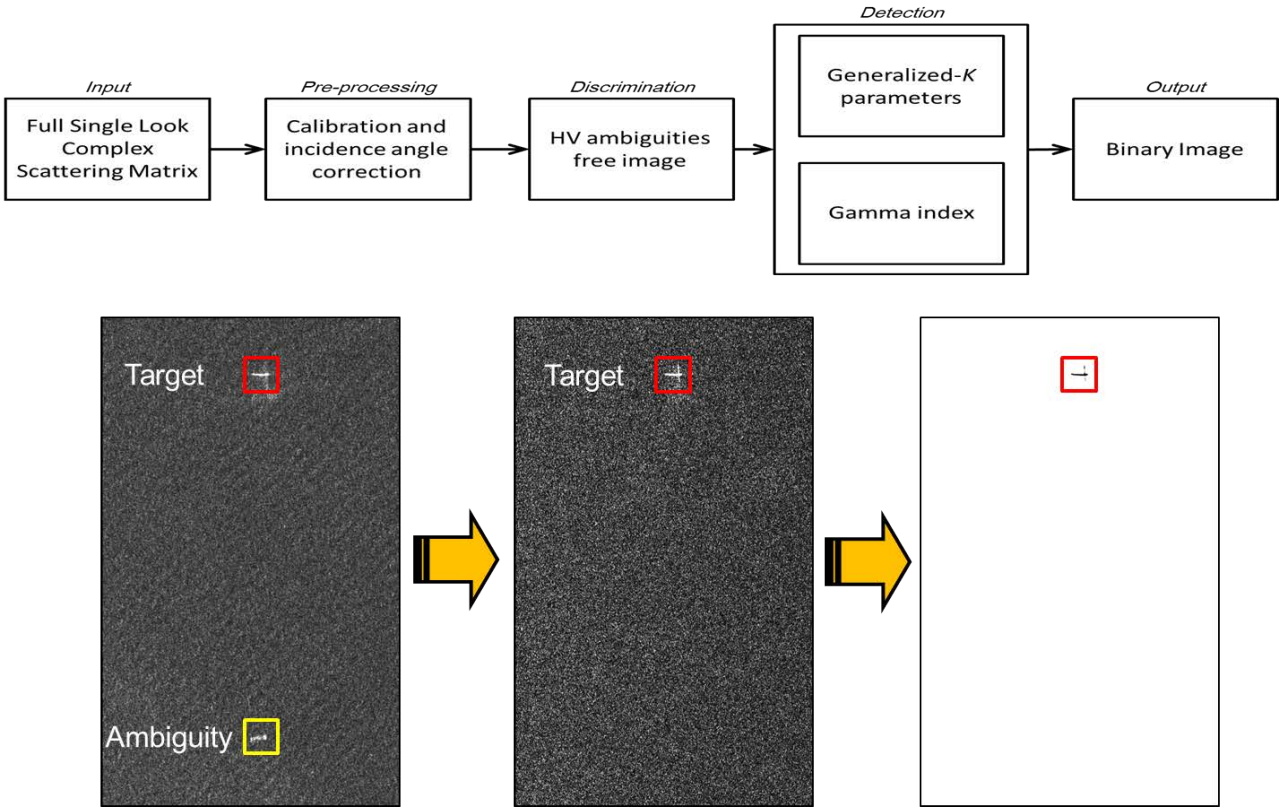

Figure 4.14 – Sketch of the marine target detection processing chain developed for TS-X DRA full polarimetric mode.

The pre-processing step consists in the calibration and incidence angle correction of the SSC full polarimetric X-band SAR data. Both cross-polarized channels, i.e., HV and VH, are then used to create an ambiguity free image, hereafter called HV_{free}. To perform the discrimination step, according to the Equation (4.37), the following combination of the cross-polarized channels is proposed:

$$HV_{free} = \frac{1}{2}\left[(\dot{S}_{hv} + \dot{S}_{vh})(\dot{S}_{hv} + \dot{S}_{vh})^*\right] \tag{4.38}$$

Although, Equation (4.38) is mathematically equivalent to $abs(\dot{S}_{hv} + \dot{S}_{vh})^2$, the formula given for HV_{free} is preferred, because it is of an easier interpretation of the property expressed in Equation (4.37). In addition to an ambiguity free image, merging the complex signals of the cross-pol channels of a time-multiplexed coherent radar, as in Equation (4.38), provides an additional free 3dB in SNR (Raney, 1988).

For the detection of marine targets, the gamma index extracted from the Generalized-K (GK) distribution proposed in (Migliaccio et al., 2007), is adapted here for the HV_{free}. The

GK distribution has been proposed as suitable parametric model of the sea clutter in C-band full-resolution SAR data (Ferrara et al., 2011; Migliaccio et al., 2007; Ward et al., 2006) and for the first time tested on SSC X-band SAR data in (Velotto et al., 2014). The GK expression is given by (Jakeman and Pusey, 1976; Jakeman and Tough, 1987; Maffett and Wackerman, 1991; Ward et al., 2006)

$$P(I) = \frac{2\alpha}{\Gamma(\alpha)\eta^{\alpha+1}} \left(\frac{\alpha}{1+a}\right)^{\frac{\alpha-1}{2}} I^{\frac{\alpha-1}{2}} I_o\left(\frac{\nu}{\eta}\sqrt{I}\right) K_{\alpha-1}\left\{\frac{2}{\eta}[(1+a)\alpha I]^{1/2}\right\} \tag{4.39}$$

Where I is the intensity of the backscattered field, $\Gamma(\cdot)$ is the gamma function, $I_o(\cdot)$ is the first kind zero-order modified Bessel function, $K_{\alpha-1}(\cdot)$ is the second kind $\alpha-1$ order modified Bessel function, and $a = (\nu^2/4\alpha)$. The parameters α, η and ν are shape, slope and departure from the uniform distribution of the phase parameters. It is worth to note that for $\nu = 0$ (strong scattering regime), Equation (4.39) becomes the two parameters K-distribution (Corona et al., 2004). Equation (4.39) for $\alpha \to \infty$ becomes:

$$P(I) = \frac{1}{\eta^2} exp\left(-\frac{\nu^2}{4}\right)\ exp\left(-\frac{I}{\eta^2}\right) I_o\left(\frac{\nu}{\eta}\sqrt{I}\right) \tag{4.40}$$

In (Migliaccio et al., 2007), the Equation (4.40) has been reformulated in terms of the Rice factor, i.e. the coherent to incoherent mean intensity field ratio $R = \bar{I}_c/\bar{I}_i$,

$$P(I) = \frac{1+R}{\bar{I}} exp(-R)\ exp\left(-\frac{I}{\bar{I}}(1+R)\right) I_o\left(2\sqrt{\frac{I}{\bar{I}}R(1+R)}\right) \tag{4.41}$$

Leading to the following expression for the parameters η and ν:

$$\eta = \sqrt{\frac{\bar{I}}{(1+R)}} \tag{4.42}$$

$$\nu = 2\sqrt{R} \tag{4.43}$$

where R is valued employing a suboptimal Rice factor estimator

$$\overline{R} = \frac{[mean(HV_{free})]^2}{2[var(HV_{free})]} \tag{4.44}$$

In (Ferrara et al., 2011), the polarization sensitivity analysis of the parameter η and ν regarding metallic objects observation in C-band, has headed to the following index term

$$\gamma = (\nu/\eta)^2 \tag{4.45}$$

which shows the best performance for the intensity of HV channel (VH is assumed to give the same performance).

4.3.2. Results and algorithm validation

In this section, the effectiveness of the ambiguity discrimination and target detection approach is verified using actual TS-X DRA data. Ground truth target positions provided by AIS and nautical charts have been used as ancillary information in the validation of the algorithm. The results reported in this paragraph are extracted from the paper **A.4**. Additional material and analysis are provided as supplementary to the paper in appendix.

The dataset analyzed is composed of five TS-X SM SSC quad polarization HH-HV-VH-VV products, which is described in details in Table 4.3. Ancillary external wind information, extracted from model, buoys, and scatterometer data, is also provided to show the dataset heterogeneity. The dataset is characterized by medium high radar angle of incidence, as for such geometries the ocean backscatter decreases rapidly and therefore the ambiguous signal targets can easily exceed the un-ambiguous one from the sea surface. However, cases of ambiguity over sea surface have been found also for lower angle of incidence and with moderate to strong wind speed conditions (see Table 4.3 image ID *FI*).

Table 4.3 – TS-X DRA quad-polarimetric dataset

ID	Date & Time (UTC)	Location	Polarization	Inc. angle (°)	Wind speed (m/s)	Wind dir.
NS_1	2010-04-18; 05:50	North Sea	Q	33.04-34.54	3-5	SW
NS_2	2010-04-29; 05:50	North Sea	Q	33.04-34.54	1-3	S
FI	2010-05-04; 05:59	North Sea	Q	27.39-29.10	8-10	NW
SF	2010-04-11; 14:15	San Francisco	Q	39.02-40.37	5-7	SO
SI	2010-05-01; 23:57	Singapore	Q	36.09-37.47	0-2	NO

The discrimination power of real targets from ghost targets on the ocean surface, based on the proposed Equation (4.38), is shown in some explanatory examples in Figure 4.15. It must be pointed out that the proposed ambiguity removal is pixel-based and, therefore, does not involve any local filtering, e.g. Wiener filters. In other words there is no loss of resolution which is beneficial for the detection of small marine targets, e.g. navigation aids. These benefits are deducible from the pure visual analysis of Figure 4.15(a)-(c), where there are two sub-scenes extracted from TS-X DRA data, which show strong ambiguous signals over the ocean area, and the outputs in Figure 4.15(b)-(d), which show that all ghosts are cancelled out. Moreover, in both examples is highlighted the presence of real marine targets (red square), which were hidden or not easily detectable because of the ambiguities.

According with the workflow in Figure 4.14 and the theoretical background introduced in the previous sections, the detector proposed is summarized as:

$$\gamma_{HVfree} = (\nu_{HVfree}/\eta_{HVfree})^2 > Thr \tag{4.46}$$

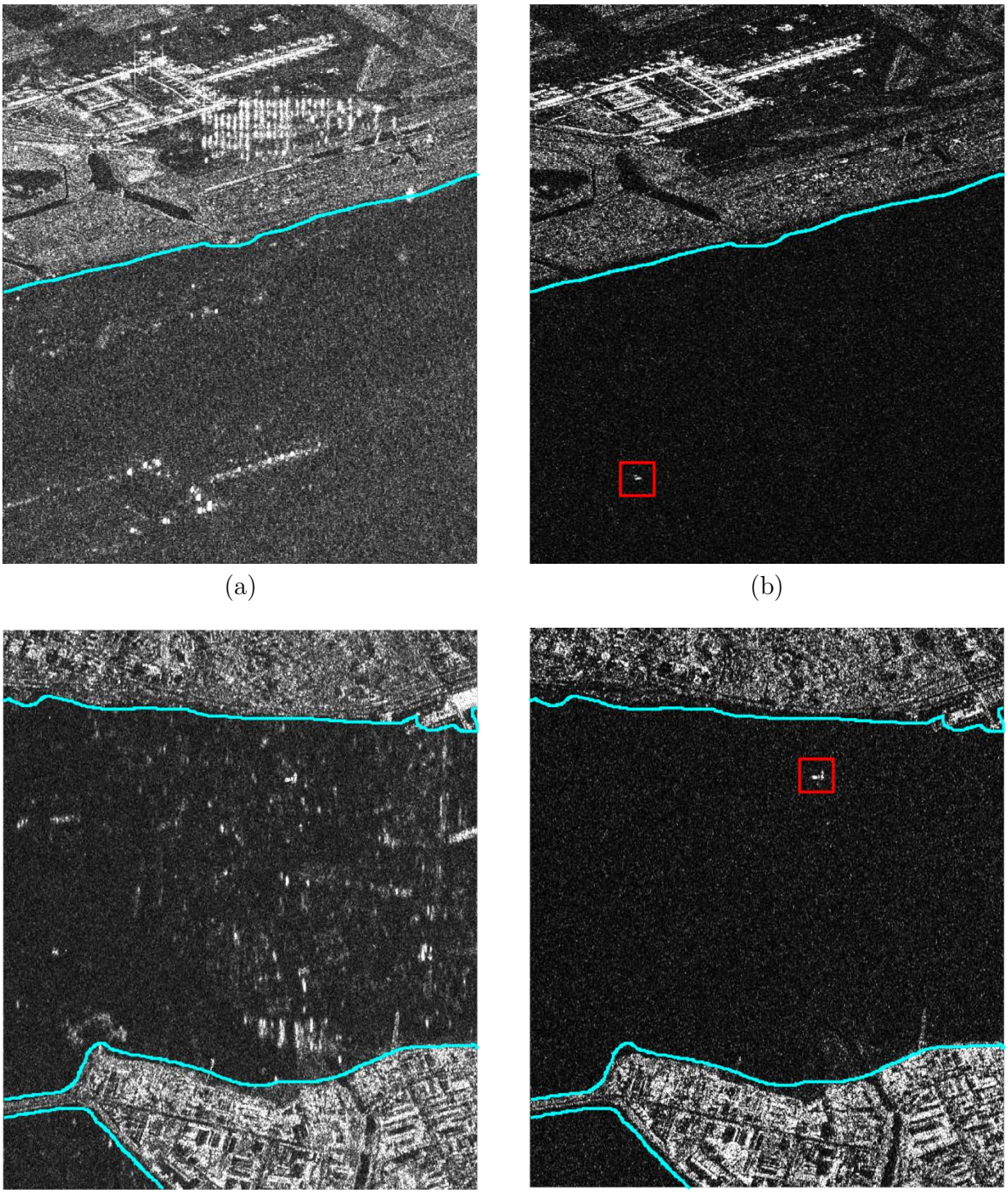

Figure 4.15 – Explanatory examples of the proposed discrimination procedure. (a) and (c) are sub-scenes of TS-X DRA data where ghost targets due to ambiguous signal are clearly visible on the ocean surface (in cyan the coastline). (b) and (d) are the respective $\boldsymbol{HV_{free}}$ images where the red square indicates the presence of a real target.

In (Velotto et al., 2014) a sensitivity study of the γ_{HVfree} for sea surface and targets has been firstly performed on X-band data. In particular, it is observed that detection method

based on GK parameters it is feasible at X-band, and that γ_{HVfree} shows a gain in TCR of factor ~2 compared to the γ_{HV} one.
As outcome of this sensitivity study, the following empirical rule is established to perform target detection

$$\begin{cases} \gamma_{HVfree} < 10 \implies \text{target} \\ \gamma_{HVfree} \geq 10 \implies \text{sea} \end{cases} \tag{4.47}$$

in this way, target and sea pixels are assigned to 0 and 1 in the logical true-false output image, respectively. In order to compute γ_{HVfree}, the estimation of $\overline{R}$ is done using a boxcar filter for both statistical parameters $mean(\cdot)$ and $var(\cdot)$, using a kernel size equal to 3x3, unless otherwise stated.

Figure 4.16(a) shows the HH-polarized calibrated amplitude image, where six ships (red rectangles), with collocated AIS info (cyan rectangles), are visible together with their first order left and right defocused ghost replica (yellow rectangles). Although in this case only the first index replicas of the ambiguous left and right signals are evident, ambiguities with index $m > 1$ have been quite often observed, especially for TS-X acquisitions using the DRA

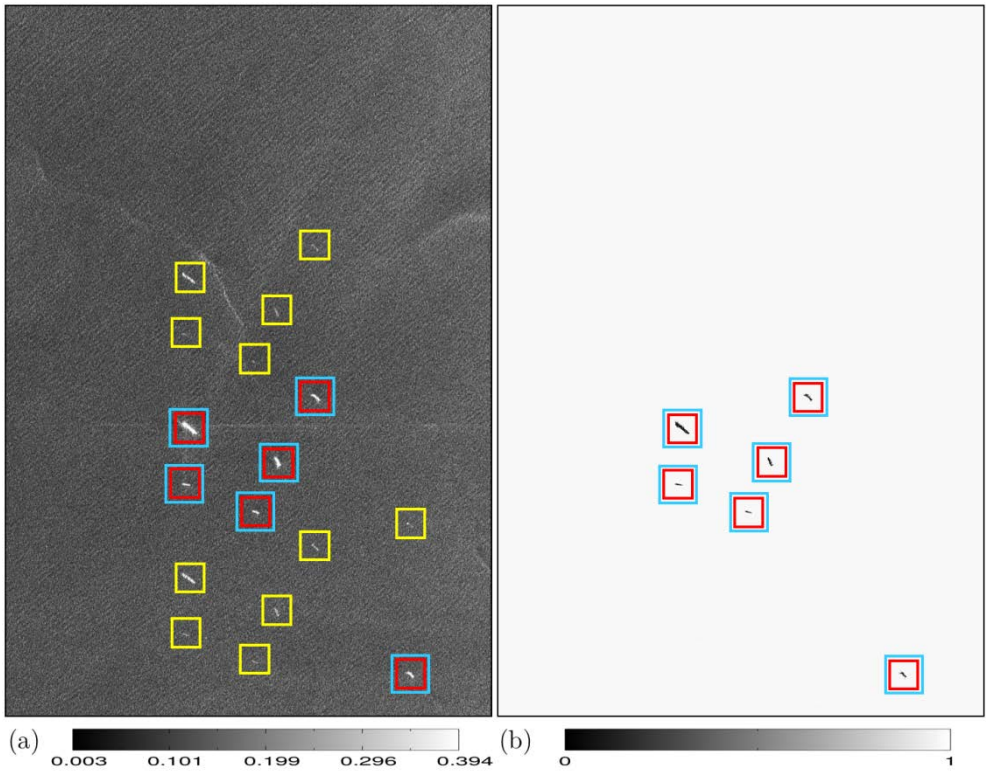

Figure 4.16 – TS-X data collected in North Sea on April 18, 2010, at 05:50 UTC. (a) Sub-scene of approximately 9km x 14km showing, in radar coordinates, the HH-polarized calibrated amplitude image, where ships/targets are indicated with red rectangles, ambiguities caused by ships/targets with yellow rectangles, available AIS data with cyan rectangles. (b) Comparison of available AIS geographical info and logical true-false output according to the proposed target detection algorithm.

configuration and high incidence angle. According to the Equation (4.26), the ghosts are displaced in azimuth by $\pm\Delta x_{AZ}$, where $\Delta x_{AZ} \cong 3.6$ km. The ROI displayed in Figure 4.16(a) is a sub-image of approx. 9km x 14km, extracted from the TS-X DRA data (*NS_1* in Table 4.3). According to the AIS information, the targets are medium to large cargo and tanker ships (length range from 126m up to 347m). Note also the presence of several oceanographic processes along the image (internal waves, breaking waves, and sea currents), which are possible sources of false detection. Available AIS data (cyan rectangle) overlapped on the logical true–false image is shown in Figure 4.16(b). The comparison of ground truth data and detection outputs demonstrate the effectiveness of the proposed methodology to discriminate real targets from azimuth ambiguities. In the framework of ship detection applications, all ground truth targets are correctly detected, and none of the azimuth ambiguities is mistaken as target.

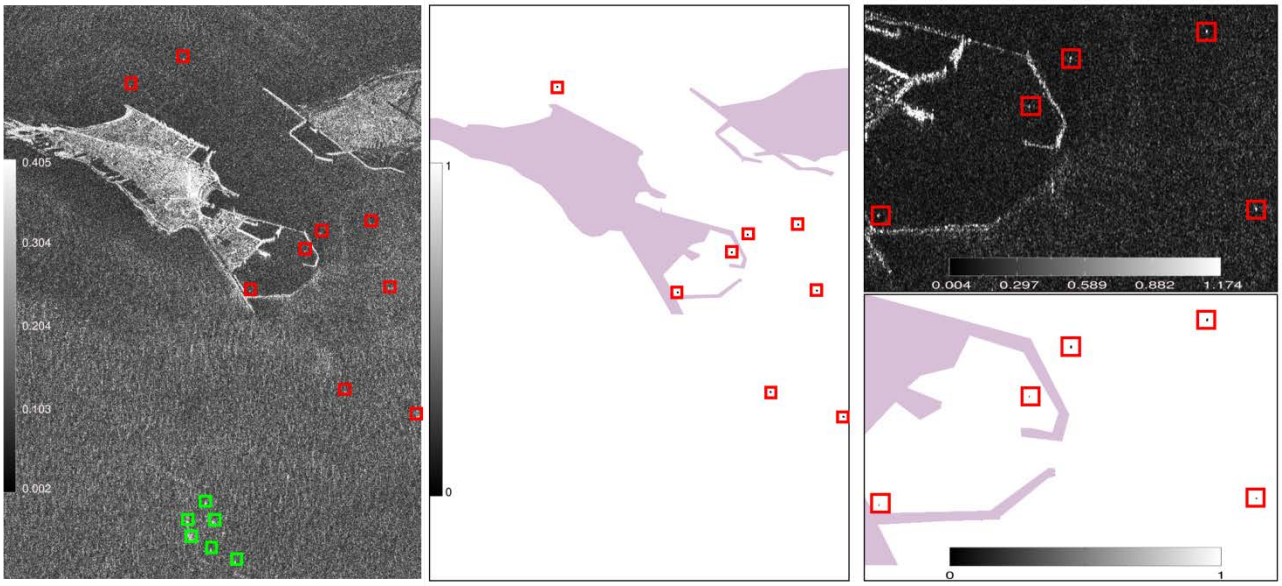

(a) (b) (c)

Figure 4.17 – TS-X data collected in North Sea on April 18, 2010, at 05:50 UTC. (a) Sub-scene of approximately 3km x 5.5km showing, in radar coordinates, the HH-polarized calibrated amplitude image, where targets are indicated with red rectangles, ghosting of Helgoland's city structures on ocean with green rectangles. (b) Logical true-false output according to the proposed target detection algorithm where land is masked in purple. (c) Zoom-in of the Helgoland harbor area showing the positions of known metallic water marks (top) and the detection output (bottom).

The example provided in Figure 4.17 is selected because it yields a challenging case from target detection point of view. In Figure 4.17(a) is displayed the sub-scene of the HH-polarized calibrated amplitude image extracted from the dataset *NS_1*. It is relevant to the surrounding area of Helgoland Island and it shows the SAR signature of small targets (indicated with red rectangles), azimuth ambiguities caused by strong scatterers from Helgoland city (indicated with green rectangles) and breaking waves around the southwest side of Helgoland. The small targets have been identified as buoys and navigation aids via

nautical charts (not shown here). The challenges are represented by the facts that, the ambiguities (green rectangle) have a signature close to the small targets of interest, the source of the ambiguous signal is a distributed target, the targets have sizes (<5m) close to the sensor resolution and last by not least the presence of breaking waves may generate additional false alarms. The corresponding logical true–false output is shown in Figure 4.17(b) where land has been masked in purple and detected targets are indicated with red rectangles. Although the described challenges, only one target is not detected and the absence of false alarms confirms that the proposed methodology is applicable on either ambiguities caused by point and distributed targets. This is a very interesting outcome because such "false" targets are hardly discarded by post-processing ambiguities removal techniques, i.e., the one that looks at $\pm\Delta x_{AZ}$ from detected targets. Helgoland's harbor area and the corresponding detection output are shown in full resolution in Figure 4.17(c) in order to highlight the presence and the detection of small targets.

It is important to note that, the proposed methodology has been successfully tested for the discrimination of ambiguities replica with order $m > 1$, and when the source is not inside the focused image (Velotto et al., 2014).

Table 4.4 – Summary of the target detection results obtained by processing the dataset through the algorithm sketched in Figure 4.14.

ID	No. Targets	Targets with AIS (*detected*)	Visually inspected ships (*detected*)	Visually inspected targets (*detected*)	Total. missed	Ambiguities	False positive caused by Ambiguities
NS_1	18	8(*8*)	0(*0*)	10(*9*)	1	Land&Targets	0
NS_2	19	5(*5*)	6(*6*)	8(*7*)	1	Land&Targets	0
FI	23	14(*14*)	9(*9*)	0(*0*)	0	Targets	0
SF	29	7(*7*)	18(*18*)	4(*4*)	0	Land&Targets	0
SI	147	0(*0*)	120(*118*)	27(*24*)	5	Land&Targets	0

A preliminary validation of the novel target detection algorithm developed for X-band PolSAR full polarimetric TS-X DRA data is given in Table 4.4. The data set consists of five oceanographic scenes that include a total of 236 targets. All 34 ships with valid ground truth AIS message are detected and an overall detection performance of 97% is achieved. The results show that, independently from the nature of the azimuth ambiguities and weather conditions, false alarms caused by ambiguities are reduced to zero without any post-processing step.

4.3.3. Discussion on alternative methodologies

This section is intended to give a short overview of alternative methodologies proposed in literature concerning the removal/filtering of azimuth ambiguities in PolSAR data for ship detection application. Moreover, a direct comparison is here provided to show the achieved

improvement with the respect to the state of the art in this matter (Velotto and Lehner, 2014).

Figure 4.18(a) shows the color composite, using the lexicographic scattering features vector base, of a TS-X DRA PolSAR acquisition over the Strait of Gibraltar. The inserts on the top left of Figure 4.18(a) are showing the intensity signatures of a ship and its first order left and right ambiguities. Moreover, in order to emphasize the challenges of marine target detection

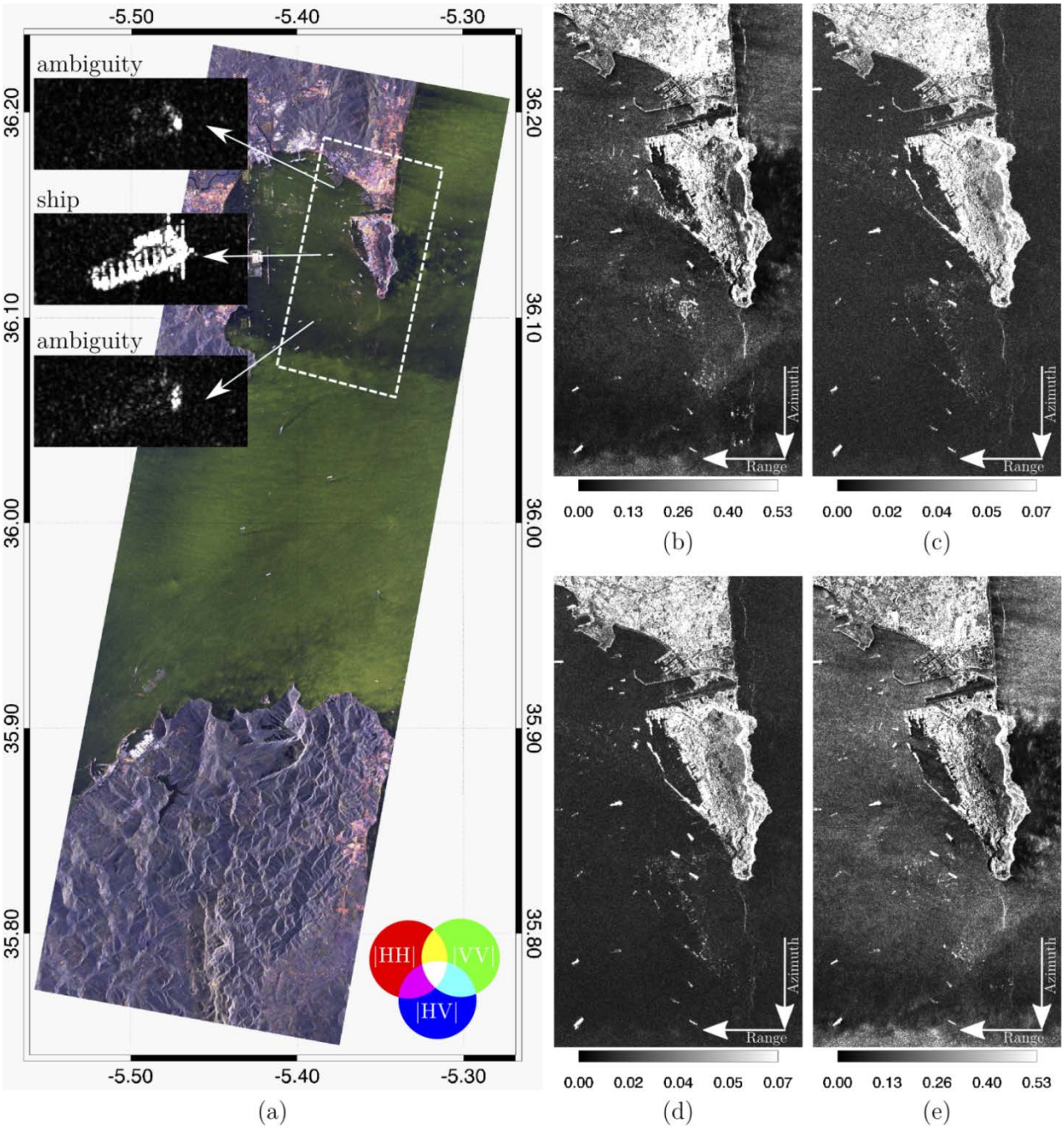

Figure 4.18 – TS-X DRA PolSAR data acquired over the Strait of Gibraltar. (a) Lexicographic color-coded representation (background) with magnified chip of a ship and its ambiguities (top left). (b)-(e) Slant-range calibrated intensities of the HH, HV, VH and VV channels, respectively, showing ships and ambiguities near Gibraltar's harbour.

in coastal and harbor area, a magnified version of the region indicated with a dashed white rectangle is shown on the right hand side of Figure 4.18. In particular, Figure 4.18(b)-(e) are the calibrated intensities of the HH, HV, VH and VV channels, respectively. Strong ambiguities are clearly present in all channels.

Based on the property of the cross-polarized channels expressed by the Equation (4.37), (Liu and Gierull, 2007) proposed to use the phase difference between HV and VH channels to discriminate targets from their ambiguities. However, it is pointed out that the phase difference can only be seen reliably if the target-to-clutter ratio is high. Therefore, the correlation coefficient between HV and VH averaged over a small area is also investigated and found to agree very well with the phase analysis (Liu and Gierull, 2007). Hence, for the objectives of this paragraph the correlation coefficient:

$$\hat{\rho}_c = \frac{\left|\sum_{n=1}^{L} \dot{S}_{hv}[n]\dot{S}_{vh}^{*}[n]\right|}{\sqrt{\sum_{n=1}^{L}|\dot{S}_{hv}[n]|^2 \sum_{n=1}^{L}|\dot{S}_{vh}[n]|^2}}, \tag{4.48}$$

is investigated for the discrimination of ambiguities in X-band PolSAR data. In (Wang et al., 2012) the eigenvalues/eigenvectors decomposition of the T_3 coherency matrix is used to perform ship detection and azimuth ambiguity removal on C-band airborne PolSAR data. (Wang et al., 2012) propose the third eigenvalue λ_3 for the discrimination and Gray-Level Co-Occurrence Matrix (GLCM) to perform the detection. The eigenvalue decomposition theory has been introduced in the section 2.2.4 of this dissertation.

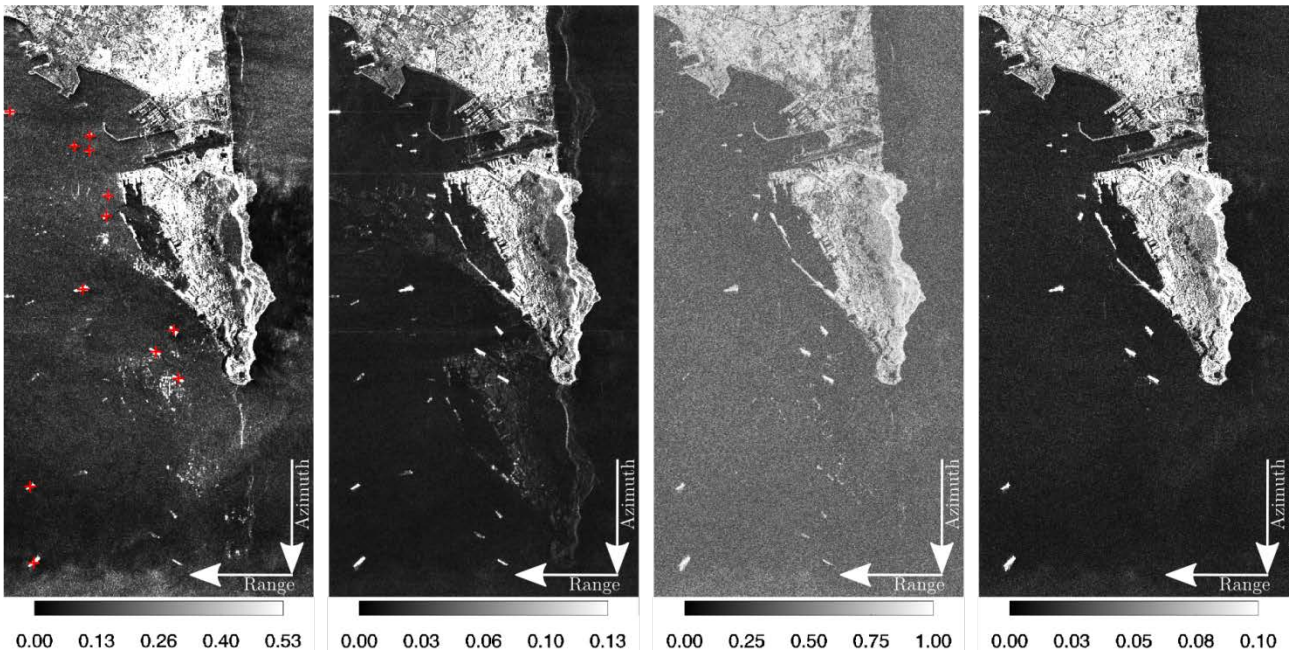

(a) 5x3 (b) 5x3 (c) 5x3 (d) 1x1

Figure 4.19 – Visual comparison of different PolSAR techniques for azimuth ambiguity removal/filtering with reference to the sub-scene shown in Figure 4.18. (a) Sub-scene of the HH-polarized channel, where ships identified with AIS data are marked with a red cross. (b) $\boldsymbol{\lambda_3}$ using a 5x3 boxcar filter. (c) $\hat{\boldsymbol{\rho}}_{\boldsymbol{c}}$ using a 5x3 boxcar filter. (d) $\boldsymbol{HV_{free}}$ without filtering.

The results of the proposed technique, namely HV_{free}, and the previous discussed methods proposed in (Liu and Gierull, 2007; Wang et al., 2012), namely $\hat{\rho}_c$ and λ_3 are shown in Figure 4.19. As visual reference, Figure 4.19(a) shows the calibrated intensity of the HH-polarized channel, where, for an easier interpretation, known marine targets (identified with AIS) are marked with red crosses. Thus, bright pixels over the sea area not identified as targets are possible source of false alarms. The azimuth ambiguity removal/filtering obtained using λ_3, $\hat{\rho}_c$ and HV_{free} are shown in Figure 4.19(b)-(d), respectively. It must be point out that, λ_3 and $\hat{\rho}_c$ are estimated using a boxcar filter of a 5x3 pixels (range and azimuth), while HV_{free} acts pixel-based with no need of multilooking. The choice of a rectangular boxcar filter is justified by the higher resolution in range than azimuth and hence less resolution loss (beneficial for small targets).

The results shown in Figure 4.19 suggest, moreover, investigating the detection performances of the three PolSAR features, (λ_3, $\hat{\rho}_c$ and HV_{free}) and compare them with standard single polarization and multi polarization detectors. This is accomplished by evaluating the ROC curves over a sea area where a real target (e.g. a ship) and its ambiguities are present. In this way, the estimated false positive rate (F_{PR}) includes both, false alarms over sea surface and caused by ambiguities. The ROI used for the ROC curves estimation is displayed in

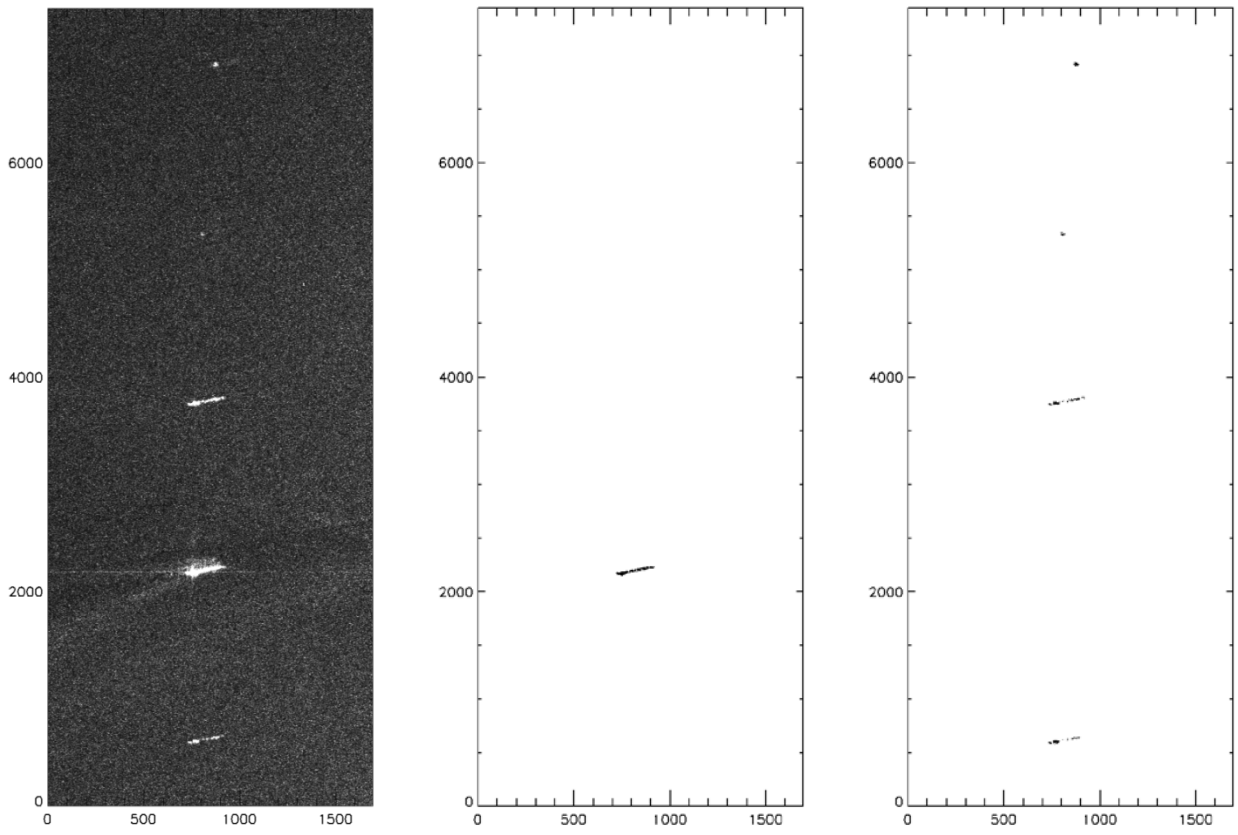

(a) (b) (c)

Figure 4.20 – ROI of X-band SAR data showing a known marine target identified with AIS data and its ambiguity. (a) Extracted HH-polarized calibrated intensity. (b) Target mask. (c) Ambiguity mask.

Figure 4.20(a), which includes an ocean region composed of ~10^7 pixels. The target mask shown in the logical true-false (true=ocean, false=target) output in Figure 4.20(b) is extracted from the results of the detector in Equation (4.3). Similarly for the ambiguity mask, shown in the logical true-false (true=ocean, false=ambiguity) output in Figure 4.20(c). Furthermore, the performance analysis is conducted for different boxcar filter sizes, namely 3x1, 5x3, 7x5 and 9x7 (range and azimuth), as shown by the Figure 4.21(a)-(d). Even though HV_{free} doesn't require any averaging process, it has been applied during the processing to generate the Figure 4.21(a)-(d) in order to have a fair comparison. In general, the averaging process doesn't improve the detection performances of single-pol and PolSAR detectors under analysis (except $\hat{\rho}_c$ which is known to be strongly biased). HV_{free} seems to

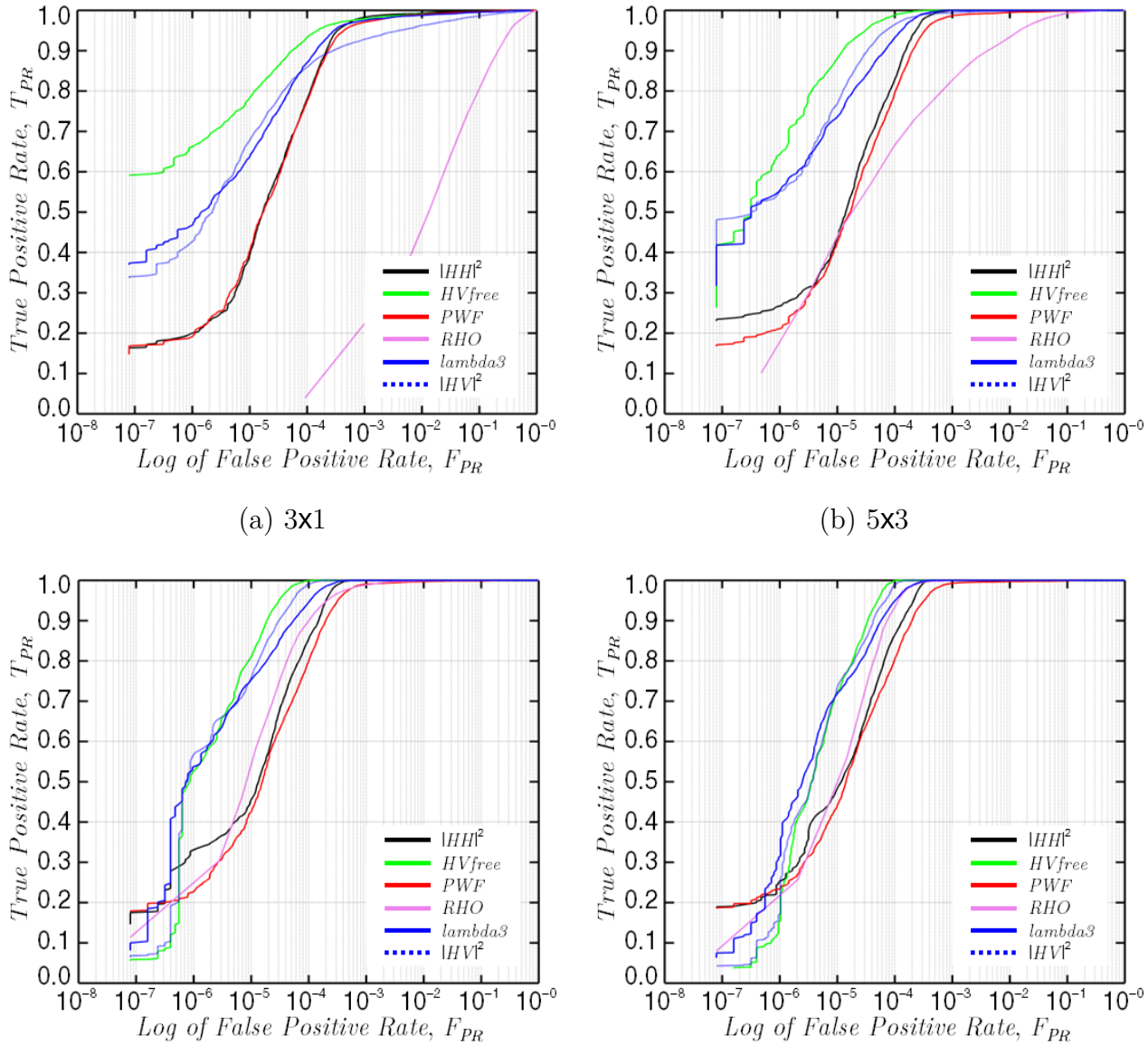

(a) 3x1

(b) 5x3

(c) 7x5

(d) 9x7

Figure 4.21 – ROC curves comparison for different PolSAR detectors and ambiguities discriminators with standard single-pol detectors. 3x1, 5x3, 7x5 and 9x7 (range, azimuth) boxcar filtering results (a)-(d), respectively.

have the best performance for small window size (which it is beneficial for detection of targets with sizes close to the radar resolution).

The last analysis concerns the estimation of the ambiguity filtering efficiency of the different methods discussed. This is accomplished evaluating the First Ambiguity to Target Ratio (FATR) with the help of the target and ambiguity mask shown in Figure 4.20(b)-(c). Once again different boxcar filter sizes are evaluated and the results summarized in Table 4.5.

Table 4.5 – Estimated $FATR$ in dB for the example in Figure 4.20.

Detector	3x1	5x3	7x5	9x7
$\left\langle \lvert \dot{S}_{hh} \rvert^2 \right\rangle$	-15.77	-15.89	-16.02	-16.12
$\left\langle \lvert \dot{S}_{hv} \rvert^2 \right\rangle$	-14.14	-14.17	-14.17	-14.14
PWF	-5.11	-6.60	-7.45	-8.03
λ_3	-14.92	-14.30	-14.07	-14.05
$\widehat{\rho}_c$	-1.11	-1.98	-2.44	-2.69
HV_{free}	-22.21	-22.18	-22.12	-22.00

5. Synergy between SAR platforms for Maritime Surveillance

It is well known that SAR maritime added value products, such as wind speed, sea state, ocean current, wake detection etc., are necessary information when dealing with critical situations at sea caused by ship activities. The extraction of each maritime added value information from SAR data is subject to different needs in terms of coverage, spatial resolution, noise floor and radar polarization. Nevertheless, SAR is a flexible sensor able to fulfil users/applications requirements with a single instrument, thanks to the possibility of implementing different imaging modes. The instrument can operate, therefore, accordingly to the restrictions imposed by the specific application. With the availability of commercial VHS X-band SAR sensors like TanDEM-X constellation (TS-X add-on for Digital Elevation Measurement, TD-X) and the Italian's COSMO-SkyMed (CSK) 4 satellites constellation, the European Space Agency (ESA) C-band SAR satellites, Senitnel-1A (S1-A) and Sentinel-1B (S1-B), have been designed to achieve medium- to high-resolution imaging capabilities and wide coverage. In fact, even though the aforementioned SAR flexibility, wide coverage and very high resolution imagery at the same time is not possible with the actual SAR design technology.

S1-A is the first satellite built with Interferometric Wide Swath (IWS) mode exploiting the Terrain Observation with Progressive Scan (TOPS) technique. IWS is the standard acquisition mode over European waters and land masses for both interferometric applications, e.g. Digital Elevation Model (DEM), and maritime surveillance applications, e.g. pollution and vessel monitoring. IWS in dual-polarization (VV-VH) combination offers 250 km swath at 5m x 20m (range x azimuth) spatial resolution in single look. These imagery characteristics are in line with the needs of the SAR based oil pollution and ship detection CleanSeaNet service run by EMSA. As a matter of fact, when a single SAR polarization is available, VV polarization is the preferred choice for oil spill detection algorithms and HH polarization is preferred for ship detection algorithms (Lehner et al., 2014). On the other hand, while spatial resolution is generally less important than coverage for SAR oil spill detection, it is a critical parameter for both ship detection (regarding small vessel as fishing boats) and classification. Hence, taking into account complementary VHS X-band satellite SAR data as support for specific application needs, the choice of medium- to high resolution C-band dual-polarization VV/VH as default product mode over European's water seems a good trade-off among SAR maritime services prerequisites.

Due to the fact that S1-A and TS-X have different orbit characteristics (the first has a mean height of 693km with a repeat cycle of 12 days; the second has a mean height of 515 km with a repeat cycle of 11 days), an area on Earth can be monitored from space at different times, with different geometries, resolution and coverage. Despite S1-A fixed acquisition plan over European waters, TS-X acquires data on-demand and has a fast satellite commanding (e.g.,

emergencies cases). Thanks to these properties and the aforementioned complement between the two satellites, S1-A and TS-X form an interesting tandem for maritime surveillance applications.

5.1. C-/X-band analysis and synergy

This section is dedicated to the research activities conducted in line with the **Objective 4** previously establish in Chapter 1. The results presented in this section are partially extracted from the annex paper **A.5**.

In the framework of MSA, monitoring of harbour area, detection of small boats without AIS (or similar means of anti-collision network), Moving Target Indication (MTI) and ship speed measurement, are few examples of applications in the radar surveillance domain, which could greatly benefit from the complementary characteristics between S1-A and TS-X. Aiming at this investigation, few months after S1-A concluded the commissioning phase, there was an opportunity to command TS-X acquisitions very close in time to the planned S1-A. During these controlled experiments, ground truth data provided by AIS vessel reports have been recorded approximately 1h before and 0.5h after SAR acquisitions (see Figure 5.1). SAR dataset details can be reviewed in Table 5.1. It is worth noticing that TS-X imagery have been planned in HH (Gulf of Naples) and VV-VH (English Channel) polarization, since it was known that S1-A would provide the combination VV-VH. Hence, cross-checking between different polarizations could also be accomplished. Moreover, the first dataset (Figure 5.1(a)) has been planned in relation to the monitoring of harbour area, while the second dataset (Figure 5.1(b)) in relation with MTI and ship speed measurement. Further analysis on ship wake signature and monitoring of small boats exploiting the synergy between the two platforms can be found in (Velotto et al., 2015a).

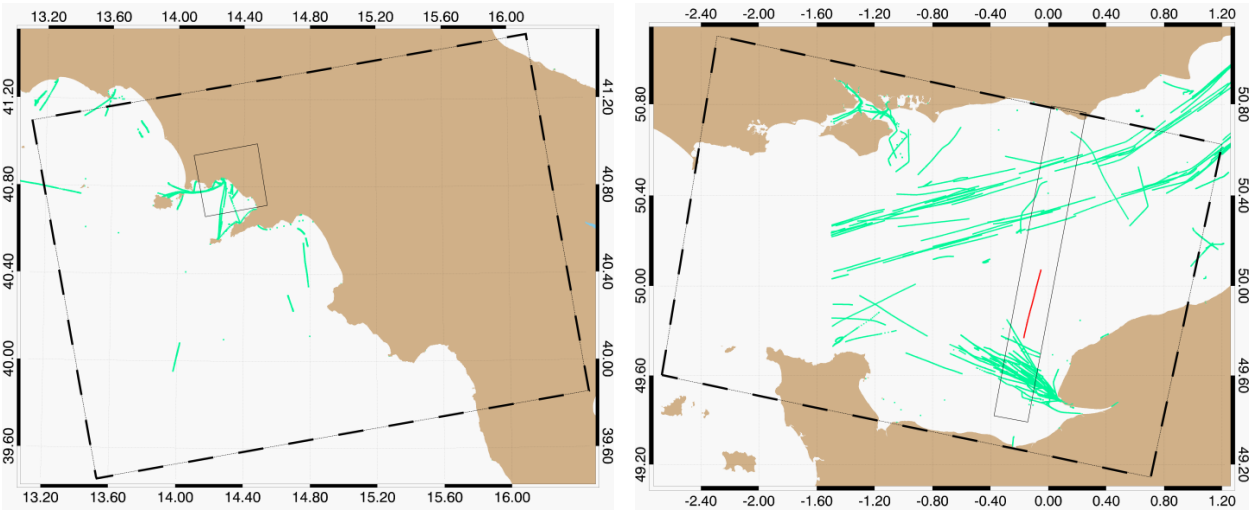

(a) (b)

Figure 5.1 – Collected AIS messages (green dots) inside the boundary box given by the acquired S1-A (dashed black line) and TS-X (continuous black line) SAR data. (a) Gulf of Naples case study. (b) English channel case study.

Table 5.1 – Multi-platform SAR data description

Dataset *Name*	Data *Time*	Resolution (m) *Rg* x *Az*	Inc. angle (°) *Nr* – *Fr*	Swath width *km*	Frequency *Band*	Polarization
Gulf of Naples	2014-11-25 *16:50* UTC	1.2 x 3.3	27.2 – 30.3	32.1	X	HH
	2014-11-25 *16:57* UTC	2.7-3.5 x 21.7	30.0 – 46.0	251.8	C	VV-VH
English Channel	2015-05-03 *06:18* UTC	1.2 x 6.6	34.1 – 35.5	17.0	X	VV-VH
	2015-05-03 *06:15* UTC	2.7-3.5 x 21.7	30.0 – 46.0	251.8	C	VV-VH

Monitoring of harbours from space can be quite a challenging task. VHR imageries are usually preferred for this kind of application. Nevertheless, the VHR SAR data have a limited coverage and the contextual surrounding information is unknown by this means. Hence, the tandem S1-A/TS-X provides complementing information on: the observation of large scale phenomena (like ocean swell, weather fronts, internal waves etc.) that are important for the planning and maintenance of harbour and coastal protection, and fine scale details (like detection of port watermarks, pilot vessels, buoys, etc.) that are necessary for the surveillance of harbour's activities.

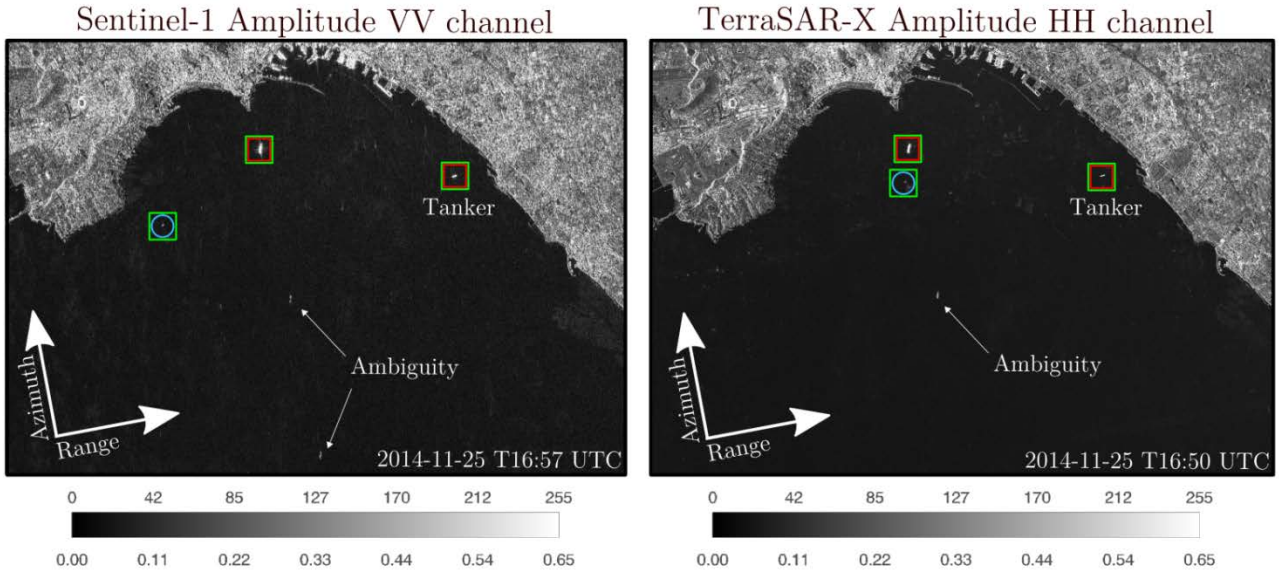

(a) (b)

Figure 5.2 – Naples's harbour area where red rectangles indicate non-moving marine targets, blue circles indicate moving marine targets and green rectangles are targets identified by valid AIS message. (a) S1-A acquired on 25th Nov., 2014 at 16:57 UTC time, VV polarization calibrated amplitude; (b) TS-X acquired on 25th Nov., 2014 at 16:50 UTC time, HH polarization calibrated amplitude.

In Figure 5.2(a)-(b), Naples's harbour imaged by S1-A and TS-X, respectively. Both sub-scenes are ground projected and oriented to North, showing the calibrated amplitude of the

respective co-pol channels (VV for S1-A and HH for TS-X, see Table 5.1). The same histogram scaling is applied in order to have equal visual information content. Speckle is mitigated using a boxcar filter with kernel dimensions adapted to the different resolutions in range and azimuth direction (5x3 in range x azimuth). Three marine targets are identified as ships by co-located AIS messages (green rectangles); two of them are non-moving (red rectangles) and one is moving (blue circle). Due to the low ocean clutter both sub-scenes are affected by azimuth ambiguities.

In the framework of target reconnaissance using multi-frequencies radar, the C-/X-band analysis of the ship radar signature is conducted taking as example the tanker in Figure 5.2. It is an oil/chemical tanker which sizes are: 144m length and 23m breadth. This target has been selected because it is almost perfectly aligned in its length axis with the radar range direction. Furthermore, being the target at anchor, it is assumed that the influence caused by different viewing geometry between the C-/X-band acquisitions is negligible. A pictorial profile of a typical oil/chemical tanker is illustrated in Figure 5.3(a), where the main structures are indicated with letters from A to E. Figure 5.3(b)-(c) show the color-coded C-band radar signature acquired by S1-A in the VV and VH polarizations, respectively. On the other hand, Figure 5.3(d) shows the color-coded X-band radar signature acquired by TS-X in the HH polarization. A common byte scaling is applied to the amplitude measurements across the dataset to facilitate the analysis. It is easy to recognize in Figure 5.3(b) five strong backscattering points along the Tanker length axis, which distribution fits reasonably well with the main structures A-E indicated in Figure 5.3 (a). These signatures are due to a mixture of direct reflections from the metallic constructions, e.g. crane, bridge, etc., and double-bounce between them and the deck. This is further confirmed by the VH polarization signature in Figure 5.3(c) which is more an indication of volume scattering rather than direct or double bounce. The X-band co-pol (HH) radar signature in Figure 5.3(d) is different from the C-band co-pol (VV) in Figure 5.3(b). Unlike what has been highlighted for C-band VV polarization, a diffuse distribution of strong backscattering points along the tanker length axis is in place at X-band (Figure 5.3(d)). The factors that might produce such behaviour in the target signatures at C- and X-band are: 1) different radar illumination geometry; 2) different polarization; 3) different resolution; 4) different frequency. The first factor is excluded a priori since the target is at anchor (according to the AIS message received) in harbour area and imaged by the two satellites with similar orbit heading in a short time difference (hence possible target's pitch, roll and yaw are assumed negligible). Regarding the polarization's influence, having the target a width of 23m, it is reasonable to assume that the dihedrals responsible for the double-bounce (usually the stronger contribution) have a comparable vertical and horizontal size making the radar response quasi polarization independent. In (Velotto et al., 2015b) the influence of the factors 1) and 2) have been further analysed for different types of ships (tanker and cargo) using the dataset English Channel (see Table 5.1), where S1-A and TS-X data have the same polarization and illumination geometry. The conclusions in (Velotto et al., 2015b) confirm the assumptions made here. Concerning the resolution influence, being the marine target oriented with the major and minor axes in SAR range-azimuth directions (see Figure 5.3(b)-(d)), it can be

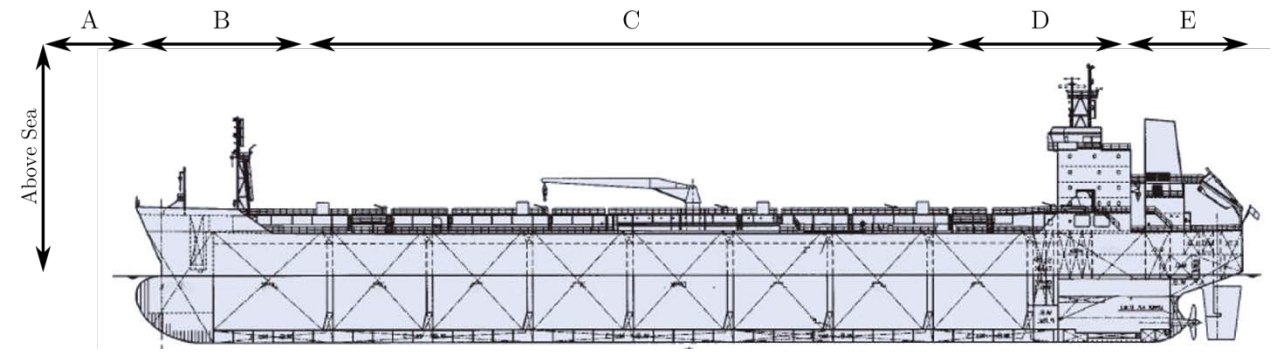

(a)

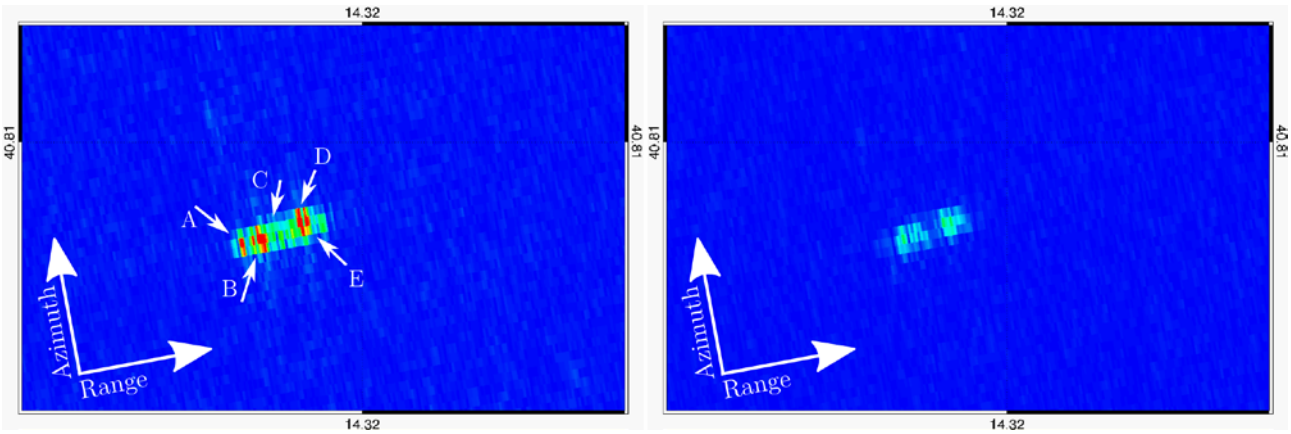

(b) C-band VV-polarization

(c) C-band VH-polarization

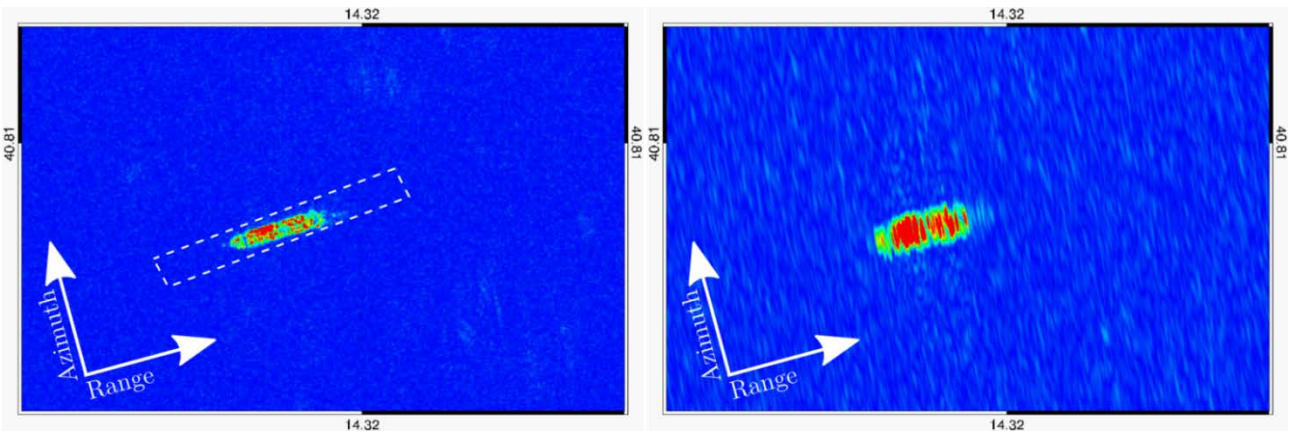

(d) X-band HH-polarization

(e) X-band HH-polarization reduced azimuth resolution

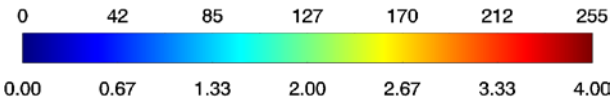

Figure 5.3 – Multi-frequency radar signature of a *Tanker* ship at anchor in Gulf of Naples (see Figure 5.2). All SAR images are ground projected with pixel spacing according to the sensor's resolution (see Table 5.1). (a) Typical Tanker's profile of the type analysed here; (b) S1-A VV-polarization; (c) S1-A VH-polarization; (d) TS-X HH-polarization; (e) TS-X HH-polarization with azimuth resolution reduced to match the one of the S1-A.

discussed individually along these directions. The strong azimuth resolution difference between the C- and X-band SAR data (~21m and ~3m, respectively) is evident comparing Figure 5.3(b) and Figure 5.3(d). The tanker's width signature appears in C-band just in few pixels in azimuth direction while in X-band much more details are provided. On the other hand, the comparable resolution in range of the C- and X band SAR data (~3m and ~1.5m, respectively) does not fully justify the different texture in the radar signature along range direction (along the major axis of the tanker). To further investigate this point, an X-band dataset with reduced azimuth resolution (down to ~21m as for the C-band dataset) has been generated from the original X-band TS-X product by extracting a sub-look with reduced azimuth processed bandwidth, i.e. 1-look with smaller illumination time, via Time-Frequency analysis. The output of this process is shown in Figure 5.3(e), which can be directly compared with Figure 5.3(b). Even though range and azimuth resolutions are in this case similar, the different radar signature in range persists. To compare the radar range signatures at different frequency and resolution, the data extracted from the region given by the dashed white frame in Figure 5.3(d) is plotted (after being averaged in azimuth direction) in Figure 5.4 for the case of Figure 5.3 (b)-(e). Comparing the target range profiles in Figure 5.4, it can be observed that resolution does not play a major role. Considering, for example the main deck of the target under analysis (which corresponds to the area around the 243m of the transect ground range size in Figure 5.4). The radar response in C-band (blue curve) is quite low with no significant texture, i.e. mostly specular reflection, while both original and reduced resolution X-band dataset (red and black curve) show noticeable texture in the radar response.

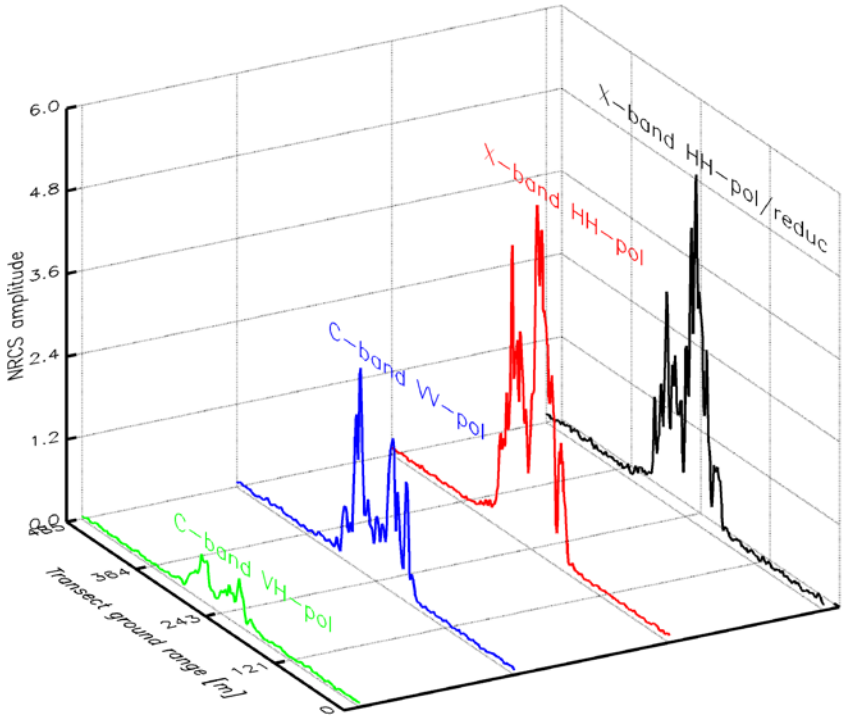

Figure 5.4 – Tanker ship profiles along radar viewing direction for different frequency and polarization.

As outcome of this analysis, it is possible to conclude that among the four factors listed, the different working frequencies plays the major role in the diverse radar backscatter signatures of the tanker ship observed in S1-A and TS-X. Hence, the different information provided by the S1-A and TS-X satellite can be exploited to help marine targets classification. An applicative example is provided in (Velotto et al., 2015b) where a ship located in coastal zone close to a harbour (non-reporting its status via AIS) could be analysed at C- and X-band frequency and conclude that is probably a cargo at anchor.

It must be noted that previous works in literature, have shown the potential improvements for ship detection application when combining satellite meter-resolution X-band SAR data with, optical images (Saur et al., 2011) or airborne centimetre-resolution X-band data (Knapskog et al., 2010). Monitoring of harbour area making use of multiple SAR satellite operating at different frequencies is therefore here firstly investigated. The findings in the C-/X-band analysis of the tanker ship, are in partial agreement with the multi-frequency vessel scattering simulations provided in (Margarit et al., 2009) for two fishing vessels and a passenger ferry. From these simulations, a stable radar backscatter along the frequency span (including C- and X-band) has been observed. Such stability has not been encountered in this study when analysing the backscatter of a tanker in real C- and X-band SAR data. This is probably due to the fact that oil/chemical tankers usually carry complex metallic structures on their deck, formed by pipelines and cranes, which are normally not present in fishing and ferry vessels. Furthermore, it was observed that the backscatter of a tanker ship in the original and reduced resolution X-band data doesn't change the fundamental properties characterizing the scattering map of the ship. This observation is in agreement with the outcomes of the downscaling procedure applied at high frequency to the ships model (which is equivalent to reducing the sensor's resolution) for the simulations of the vessels scattering maps in (Margarit et al., 2009).

Ship parameters like heading, Course over Ground (CoG) and speed, are not easy to extract from single channel SAR imagery or even not possible. Heading extracted from detected ship suffers of the 180° ambiguity. Several methods have been proposed to estimate the speed. These include: the exploitation of the Doppler shift effect (if the ship's wake is detectable with a contemporary target's velocity radial component) (Radius and Marques, 2008; Tunaley, 2003); target's azimuth shift when observed at two azimuth times (if radar illumination time is sufficient to extract two sub-aperture images able to highlight the different position) (Brusch et al., 2011; Kirscht, 1996); Along Track Interferometry (ATI) which is, however, sensitive to the SCR (Suchandt et al., 2010). All these methods have been proven to be efficient under the circumstances described. Alternatively, multiple satellite observations could be used, when none of the previous methods is accessible. Two exemplary cases are of moving ships are selected to show the benefits of the synergy given by the tandem TS-X/S1-A.

As first example, the moving ship (identified as passenger vessel by AIS) in Figure 5.2 is selected because travelling with almost constant radial velocity component towards radars

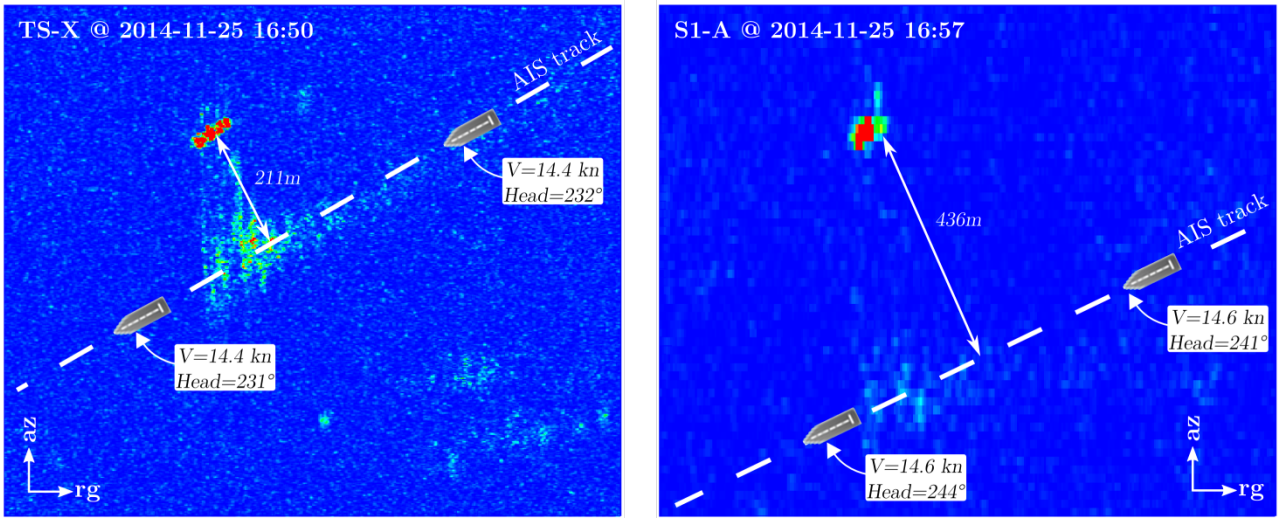

(a) (b)

Figure 5.5 – Moving target in Naples's harbour identified via valid AIS message as passenger ship. The AIS track is given as dashed white line, where have been indicated also velocity and heading. (a) TS-X and (b) S1-A sub-scenes (in radar coordinates) of the passenger ship at respective observation times.

look direction, i.e. range. The Figure 5.5(a)-(b) are the TS-X and S1-A sub-scenes of the passenger ship (at respective observation times), that have been augmented by adding the available AIS info and predicted track. Although the target is moving with approximately constant speed and heading (assumed to be equivalent to the CoG in absence of strong current) during the time gap of the two satellite observations, it is remarkable the different *ship off the wake* distance Δz caused by Doppler shift. The higher ratio s/v_S, due to the different S1-A orbit characteristics compared to TS-X, produces a larger offset Δz, which becomes easier to measure when targets have lower speed, i.e. smaller radial component. Nevertheless, Figure 5.5(b) also shows the difficulties in determine the heading of the ship (that is used to retrieve the 2D speed vector once the radial component is measured) from the radar signature (due to the low S1-A azimuth resolution) which in turns can be estimate with high accuracy (due to high TS-X azimuth resolution) as can be seen in Figure 5.5(a).

A second example is given by a tanker ship moving parallel to satellites' flight directions, i.e. azimuth. The AIS track of this ship is marked in red in Figure 5.1(b), where it is possible to deduce that a linear trajectory is kept during the SAR overpasses. Figure 5.6 is the color composite obtained combining the radar backscatter of the co-polarized channels available in the C- and X-band datasets (50-50 resampled at common pixel spacing). The azimuth time difference between the two images at target positions is about 160 seconds while the distance travelled is about 1200 m. This gives an average speed of 14.7 knots that well compare with the 12.9 knots reported via AIS. Moreover, the measured CoG of 12° (AIS reported CoG equal to 13°) estimated using the two observations permits to eliminated the 180° ambiguity in the heading estimation from the individual SAR ship signature (estimated heading is close to 10°/190° for both SAR dataset, AIS reported heading is 8°) (Velotto et al., 2015b).

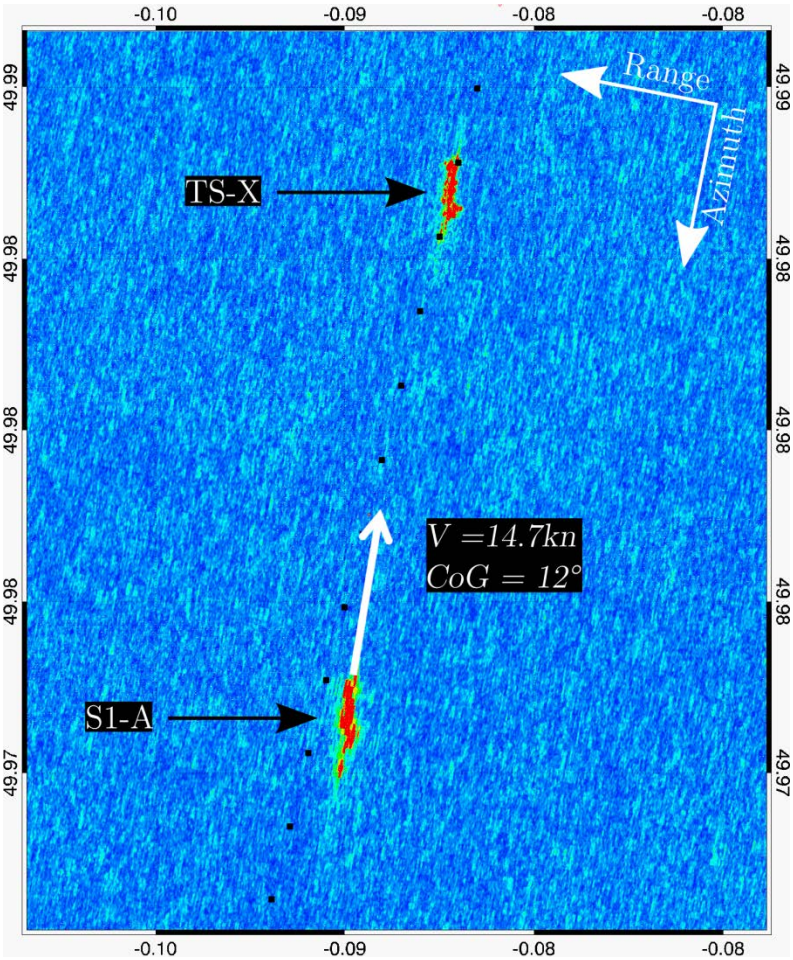

Figure 5.6 – Tanker ship moving parallel to satellites' flight directions as imaged by S1-A and TS-X. Composite of the co-polarized C- and X-band channels (50-50 resampled at common pixel spacing). AIS (black dots) speed reported is 12.9 knot.

5.2. TanDEM-X constellation prospective for maritime applications

The TD-X constellation is the first bistatic SAR mission, formed by adding a second, almost identical spacecraft, to TS-X and flying in a closely controlled formation. Primary mission objective is the generation a global DEM. Once the primary objective has been accomplished, the high configuration flexibility of the two TD-X satellites can be exploited to demonstrate new SAR techniques and applications. In this sense, from October 2014 DLR has opened the TD-X science phase, which is fully supported with data acquisition till December 2015. The TD-X science phase is split in two periods that are relevant to the two main TD-X acquisition configurations, i.e. pursuit monostatic (functioning from October 2014 to March 2015) and bistatic (functioning from April 2015 to December 2015). In addition to that, the experimental DRA mode is activated on both satellites (Hajnsek et al., 2014). Different image acquisitions scenarios have been proposed in literature to meet the needs of applications from different branches. Most of these proposals are specific for the

pursuit monostatic configurations. With the pursuit monostatic configuration, the TD-X satellites operate independently having an along track baseline of approximately 76 km (corresponding to a temporal baseline of ~10 seconds). The most attractive proposals for maritime applications are single look improved resolution, bidirectional SAR (BiDi SAR), Ultra Wide, Interferometric traffic monitoring and Zooming. The details of these imaging modes are not given here, but can be found in (Lumsdon et al., 2015; Prats et al., 2012). According to the results presented in the previous chapters of this dissertation, is indeed advisable to exploit TD-X pursuit monostatic configuration combining single and multi-polarization acquisitions. In this way the drawbacks in coverage and resolution of PolSAR acquisitions can be compensated gaining polarimetric information that are useful for oil spill and marine targets monitoring. Artist view of this concept is shown in Figure 5.7, where an actual oil spill and several marine targets were imaged.

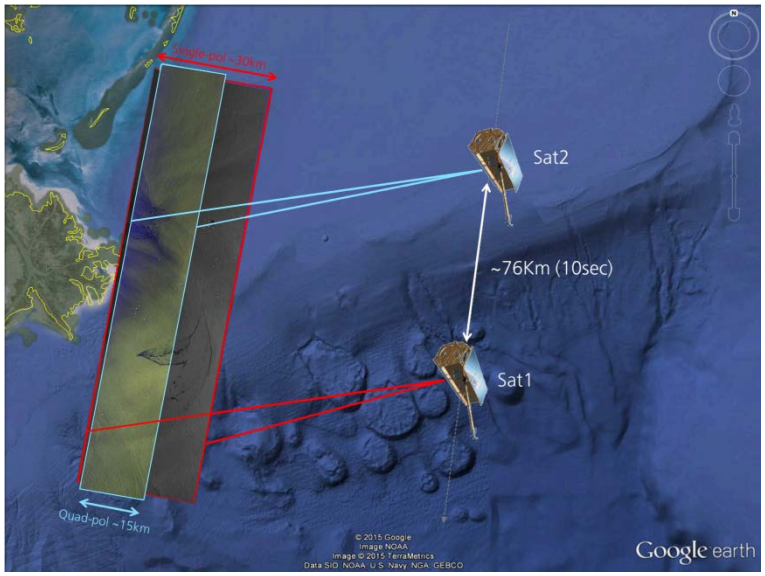

Figure 5.7 – Artists view of the TD-X pursuit monostatic configuration combined with SRA single-pol (fore platform Sat1, in red the swath coverage) and DRA PolSAR (aft platform Sat2, in cyan the swath coverage) SM imaging modes.

In order to evaluate the performances and benefits of this new imaging and polarimetric arrangement, several data-take orders have been planned and successfully acquired during the TD-X pursuit monostatic period.

The first example is given in Figure 5.8, where the fore platform TS-X has acquired data in SM single-pol VV (1.2 x 3.3m nominal resolution) and the aft platform TD-X in SM dual-pol HH-VV (1.2 x 6.6m nominal resolution). Figure 5.8(a)-(c) show the details of a moving cargo ship (reported AIS info are: length 177m, breadth 29m and speed 7.4kn) at different polarization and resolution. Figure 5.8(d) shows the composite of the fore platform (TS-X) and aft platform (TD-X) data-takes in VV polarization. The loss in azimuth resolution, due to the dual-pol acquisition, does not change considerably the radar signal received from the ship structures. This is further shown by the ship signature profiles (along the main axis) in Figure 5.8(e). The one dimensional cross-correlation analysis between the retrieved ship's

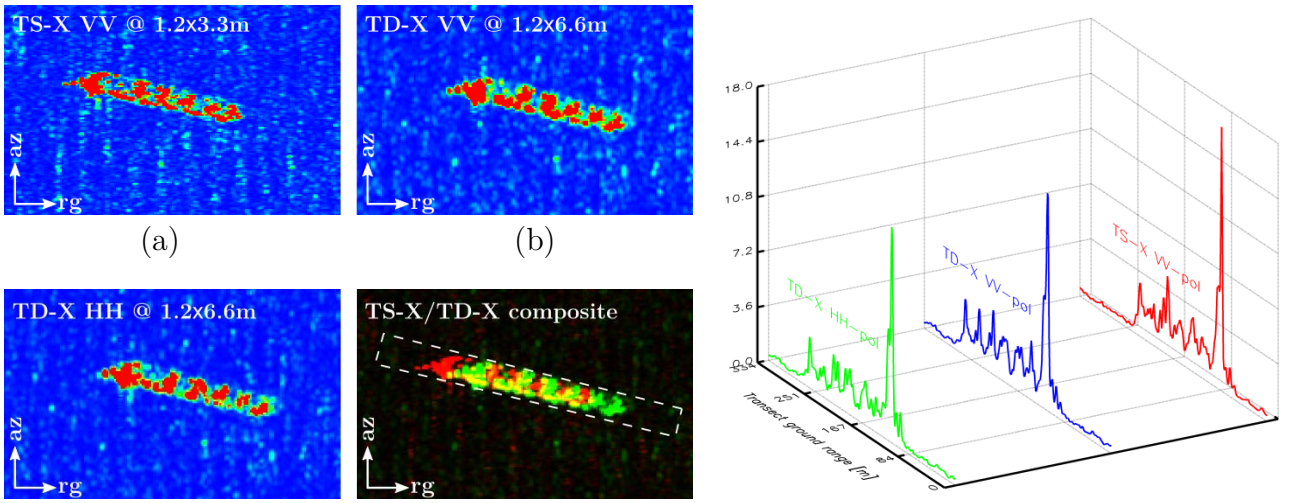

Figure 5.8 – Cargo ship imaged by TD-X satellites in pursuit monostatic configuration: (a) color-coded calibrated amplitude sub-scene extracted from TS-X data-take (fore platform) acquired in VV polarization with 1.2 x 3.3m nominal resolution; (b)-(c) color-coded calibrated amplitude sub-scenes extracted from TD-X data-take (aft platform) acquired in VV and HH polarizations, respectively, with 1.2 x 6.6m nominal resolution; (d) VV polarization composite of the fore platform (TS-X) and aft platform (TD-X) data-takes; (e) ship signal profile along the main target's axis for different resolution and polarization.

profiles, leads to a travelled distance of 39m, which corresponds to an average speed of 7.6kn (temporal baseline 10 seconds). This very preliminary ship speed accuracy analysis of the proposed imaging arrangement, is in line with the performances of the classic TD-X dual-platform SAR-GMTI demonstrated in (Baumgartner and Krieger, 2011). Additional analysis on the accuracy of the target true geographical position and heading is left for future work.

The second example is selected to show the improved capabilities in detecting marine targets, when TD-X constellation is employed with the suggested configuration. An extreme challenging case is the monitoring of fish farm structures in open water. A model of fish farm structure, typically used in the Mediterranean Sea, is shown in Figure 5.9(a). The fish farm considered, whose optical picture is given in Figure 5.9(a), is located in the Gulf of Trieste and is made of circular cages of two different diameters 12m and 8m (the size of the ring is unknown and estimated to be <1m). Monitoring these structures from space is an asset, considering their remote locations and that are subject to extreme weather conditions. Geocoded and color-coded calibrated amplitudes extracted from the aft platform data-take (TD-X dual-pol HH-VV with 1.2 x 6.6m nominal resolution) and fore platform data-take (TS-X dual-pol VV with 1.2 x 3.3m nominal resolution) are shown in Figure 5.9(b)-(d), respectively. Comparing the Figure 5.9(b)-(d) with the reference picture Figure 5.9(a), it is easy to recognize that even the data-take at higher resolution (Figure 5.9(d)) is not able to

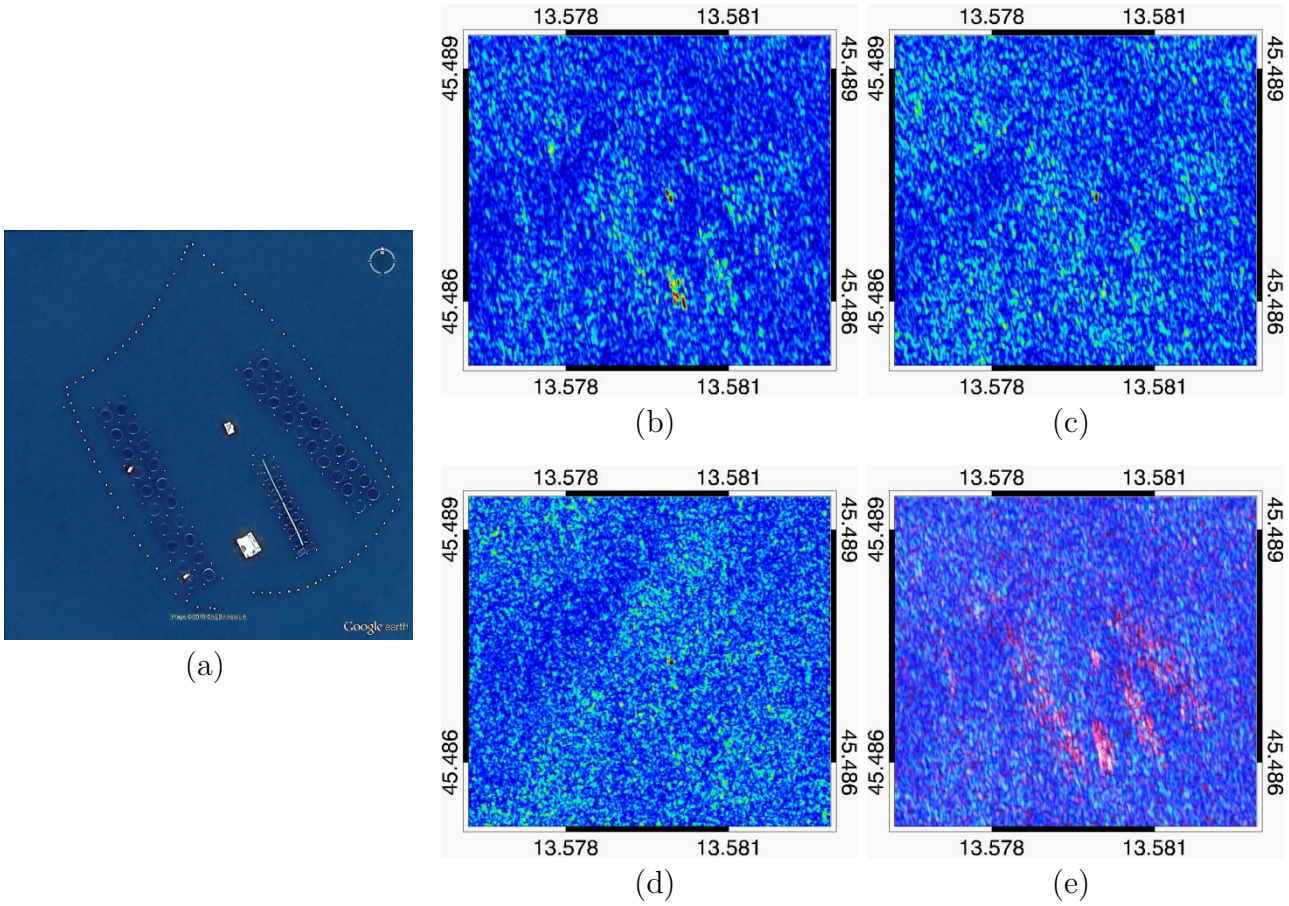

Figure 5.9 – Fish farm structure in the Gulf of Trieste composed of circular cages of two different diameters: 12m and 8m. (a) Reference optical image extracted from Google earth©; (b)-(c) HH and VV color-coded ground projected calibrated amplitude sub-scenes extracted from TD-X dual-pol data-take with 1.2 x 6.6m nominal resolution; (d) VV color-coded ground projected calibrated amplitude sub-scenes extracted from TS-X single-pol data-take with 1.2 x 3.3m nominal resolution; (e) $\boldsymbol{rgb}$ composite of the TD-X dual-pol data-take with $\boldsymbol{r} = |\dot{\boldsymbol{S}}_{\boldsymbol{hh}} + \dot{\boldsymbol{S}}_{\boldsymbol{vv}}|$, $\boldsymbol{g} = |\dot{\boldsymbol{S}}_{\boldsymbol{hh}} - \dot{\boldsymbol{S}}_{\boldsymbol{vv}}|$, and $\boldsymbol{b} = |\dot{\boldsymbol{S}}_{\boldsymbol{hh}}\ \dot{\boldsymbol{S}}^{*}_{\boldsymbol{vv}}|$.

clearly detect the cages of the fish farm and only one of the support platform (the white target in the middle of Figure 5.9(a)) has a higher signal response compared to sea clutter.

Better results are obtained from dual-pol HH channel, where also the second support platform (the white target in the bottom center of Figure 5.9(a)) appears as strong signal above surrounding clutter. In conclusion, making use of the polarimetric phase information between the two co-polar channels (as shown in the *rgb* color-composite in Figure 5.9(e)) it is possible (due to the stronger double bounce returns) in fact to completely recognize the all fish farm structure, including the cages.

The applicative examples shown are just few advantages of the TD-X constellation with the suggested imaging modes. More consistent research in the field of oil pollution and target detection is yet to be completed.

6. Summary

In this dissertation, the capabilities of SAR polarimetry for maritime surveillance are investigated for two key applications of this domain, i.e. marine pollution and target detection. This chapter starts summarizing the research done in the thesis to accomplish the objectives set and the obtained achievements, followed by an outlook about the future works.

6.1. Discussion and Conclusion

This thesis has been set out with the goal of improving the State-of-the-Art in SAR oil spill and ship detection by exploiting VHS X-band spaceborne PolSAR mission such as TS-X. Thanks to the technical progress, from both satellite and ground segment side of the current spaceborne SAR missions, is possible to deliver in NRT information to prevent or assist accidental events at sea. However, for the fulfilment of the user needs, e.g. EMSA, the information reliability of SAR-based marine pollution and target detection products needed to be increased. Taking this into account, this dissertation aimed at research, develop and test advanced PolSAR techniques and algorithms able to overcome known issues of oil spill and ship detection using single-pol SAR data. Furthermore, the intention was also to develop algorithms computationally performant in order to meet NRT requirements, i.e. delivery within 30 minutes from data record. Discussion and conclusions, drawn separately for the different aspects that have been accounted for, are as follow.

A polarimetric model to read the X-band polarimetric sea surface scattering with and without surface slicks has been proposed. The key results emerging from this study can be listed as follows.

- X-band dual-polarimetric SAR data are useful for oil-spill observation purposes. The unique capability of TS-X to acquire coherent dual-pol co-pol channels, HH and VV, is an advantage.
- The polarimetric model investigated is based on the inter-channel correlation. This feature is sensitive to the departures from the Bragg scattering mechanism, which is assumed not to be in place for oil-covered sea surface. On the other hand, because of the physical-chemical weak-damping properties of some oil look-alike, the departure from Bragg become negligible, hence enabling their discrimination.
- For the estimation of the inter-channel correlation, two different approaches have been investigated, namely the standard deviation of the CPD and coherence amplitude. The effectiveness of the two estimators is analysed theoretically and by experiments by using different sizes of the estimation window.
- The system noise (NESZ) influence on the CPD is shown not to play a major role for the case studies. This is simply owed to the very high resolution of TS-X and the large amount of pixels certainly above the noise even within the oil-covered area. However, in simultaneous conditions of low wind regime (low ocean backscatter) and

high incidence angle (higher NESZ), the system noise might come to play a role. No sensitivity of mean value of the CPD with respect to oil slick has been found.
- The standard deviation of the CPD works better than coherence amplitude when smaller window size is employed. This makes the former approach to be preferred for observing illicit oil spills.
- Beyond all scientific aspects, the general value is even more in operational terms since one may think to integrate L-, C-, and X-band spaceborne SAR measurements ensuring much more dense spatial/temporal coverage and resolution.

A dual-polarimetric model to detect metallic targets at sea in dual-polarimetric coherent HH-HV/VV-VH X-band SAR data has been proposed and verified against actual TS-X imagery and ground truth information. The obtained results are

- Metallic targets can be efficiently distinguished from the surrounding sea using VHS X-band dual-polarimetric SAR data. Both the HH–HV and the VV–VH polarimetric combinations can be used.
- The approach exploits the different symmetry properties that characterize sea surface with and without metallic targets. Following this rationale, an operational marine target detector filter has been developed. A typical TS-X scene is processed in seconds by a standard PC processor.
- The proposed detector allows obtaining binary outputs using a fixed threshold. It is proved by experiments that the filter works correctly over a broad range of incidence angles and sea state conditions, including high wind.
- The performances of the proposed detector are evaluated and compared with standard single-pol channels detectors by measuring the obtained TCR and evaluating ROC curves.
- According to a preliminary validation, no false positive is obtained, while false negatives are always due to small targets ($<$ 15 m). The minimum size of the detected ground-truth-verified (visually inspected) target is 2 m (8–10 m).
- The proposed approach, being able to work on L-, C-, and X-band dual-polarimetric SAR data, allows interoperating all the operational/planned dual-polarimetric SAR missions and in particular the newly Sentinel-1A with large coverage IWS VV-VH standard acquisition mode over European waters.

An important aspect in SAR marine target detection is the discrimination of real targets from azimuth ambiguities. A complete processing chain is developed and tested for fully polarimetric TS-X DRA data. In summary, the key results emerging from this study can be listed as follow:

- In the pre-processing step, both cross-polarization channels can be used to generate an ambiguity free image. It is proved theoretically and by experiments the fact that, for targets, HV and VH channels are approximately equal in magnitude and phase, i.e., the reciprocity theorem applies, but opposed in phase for azimuth ambiguities.

- False alarms caused by targets or land azimuth ambiguities over the ocean surface can be reduced to zero exploiting PolSAR data, hence improving the reliability of the extracted information.
- The proposed detection methodology shows a good consistency when compared to ground truth data, i.e., none of the ambiguities is misguided as target.
- Small targets are observed and efficiently detected. Moreover, the results obtained strongly support the use of X-band PolSAR data for marine target detection purposes, particularly where the problem of ambiguities might be critical, i.e., harbours and coastal areas.
- The method proposed requires full polarimetric SAR data. A preliminary comparison with other ambiguity filtering/removal techniques published in recent literature shows that the method proposed is preferable in terms of detection and discrimination capabilities.

Last, synergetic use of multi-frequency and multi-polarization satellite SAR data in the framework of maritime target detection has also been conducted. This research has led to the following conclusions:

- Monitoring of harbours from space can be quite a challenging task. VHS imageries are usually preferred for this kind of application. Nevertheless, the VHS SAR data have a limited coverage and the contextual surrounding information is unknown by this means. The possibility to gather large-scale meteo-ocean information by means of complementary wide swath satellite SAR imagery, e.g. S1-A, is highly desired.
- The joint use of virtual SAR satellites constellation working at different frequencies, e.g. TS-X and S1-A, is proved to improve the maritime surveillance capabilities and target reconnaissance since they carry different information regarding the target and ocean.
- Ship parameters like heading, Course over Ground (CoG) and speed, are not easy to extract from single channel SAR imagery or even not possible. Hence, under certain restrictions the tandem S1-A/TS-X can operate as dual-platform Moving Target Indicator (MTI).

Taking into account these final findings, the vision of this thesis is to encourage the geo-user community in using PolSAR VHR X-band SAR data for maritime application as the benefits overcome the drawbacks which can be easily eliminated making use of other SAR missions planned to achieve large coverage.

6.2. Outlook

The recommendations for future research that have been already provided in the dissertation are here recalled and extended:

A larger scale analysis of detection and discrimination of oil spill by using inter-channel correlation at varying meteo-ocean conditions and SAR system parameters is recommended. The use of Non-Local filter to improve the estimation of phase difference and coherence is promising together with the evaluation of computational time for NRT applications.

X-band quad-pol analysis for oil spill type estimation using VHR TS-X DRA mode.

Large validation of marine target detection based on the r filter is still to be done. In particular the extraction of ship parameters, i.e. length, width, heading, might be more accurate when compared to standard extraction methods based only on intensity signatures. Moreover, the different signature of the ship's wake on co- and cross-pol channel is worth to investigate for ship speed retrieval.

Currently the landmasking step of marine target detection is performed using auxiliary low resolution (~90m spatial resolution) water-body dataset. As consequence of the much higher spatial resolution (~3m) of TS-X, a coastal buffer zone is adapted to avoid false alarms on coastal area. This drawback can be removed by extracting directly the coastline from the VHR SAR data. On this matter, the clutter suppression efficacy of the r-based filter could lead to a robust coastline detector.

Automatic rejection of non-ship marine target (including false detection caused by costal structures not present in the static land-mask) via target classification by using VHR single-pol and multi-pol SAR data would improve the ship detection service. Identification of static marine targets, e.g. platforms, windmill, etc., by multi-temporal medium-high resolution SAR acquisitions is an asset.

The detection of ghost targets over the ocean surface caused by range ambiguity are an issue left for further research.

A. Relevant publications as part of the thesis

A.1. Velotto, D., Migliaccio, M., Nunziata, F., Lehner, S., 2011. Dual-polarized TerraSAR-X data for oil-spill observation. IEEE Transactions on Geoscience and Remote Sensing 49 (12): 4751-4762

Dual-Polarized TerraSAR-X Data for Oil-Spill Observation

Domenico Velotto, *Student Member, IEEE*, Maurizio Migliaccio, *Senior Member, IEEE*, Ferdinando Nunziata, *Student Member, IEEE*, and Susanne Lehner

***Abstract*—A study exploiting dual-polarimetric X-band synthetic aperture radar (SAR) data to observe oil at sea is undertaken for the first time. The polarimetric model exploits the interchannel correlation between the like polarized channels. Accordingly, two parameters related to the interchannel correlation, namely, the amplitude coherence and the copolarized phase difference (CPD) standard deviation, are accounted for, and their performances, with respect to sea oil slick observation, are carefully discussed. Single-look Slant range Complex dual-polarized TerraSAR-X SAR data, in which both certified oil slicks and weak-damping look-alikes are present, are used to verify the efficiency of the proposed approaches. Results show the advantage of the CPD approach and the effectiveness of TerraSAR-X dual-polarized products for such application.**

***Index Terms*—Coherence, copolarized phase difference (CPD), sea oil slicks, synthetic aperture radar (SAR), TerraSAR-X.**

I. Introduction

SYNTHETIC aperture radar (SAR) is the key sensor to observe oil at sea, therefore to observe illicit vessel discharges, to support an early warning system, and to support law enforcement [1]–[3].

In simple terms, oil at sea damps the Bragg waves and reduces the friction velocity, generating a low backscatter area which, in the SAR image plane, appears as a dark area. However, there are other natural phenomena (e.g., biogenic slicks, ship wakes, low wind areas, etc.) which, producing dark areas in SAR images [2], make SAR oil slick observation a very nontrivial task [2], [3]. In fact, although low wind areas can be easily sorted out by employing external or SAR-based wind information, natural look-alikes (LAs) (e.g., biogenic slicks, ship wakes, etc.) are more difficult to be distinguished from oils and cause the primary source of false alarms.

With this respect, the extra information provided by SAR polarimetry (PolSAR) has been recognized to be of special interest in the case [4]. A full-polarimetric SAR transmits and receives both horizontal (H) and vertical (V) linear polarized electromagnetic fields, and therefore, at each resolution cell, the 2×2 complex scattering matrix is measured. Although full-polarimetric SARs are advisable in many geophysical applications, there are hardware and budget considerations that sometimes lead to design a simpler SAR: the dual-polarimetric SAR. In this case, only two elements of the scattering matrix are measured. Typically, they are the two copolarized channels, i.e., the VV and HH ones.

The suggestion to exploit PolSAR for oil slick observation was demonstrated to be true in [5]–[15]. In particular, in [5] and [6], a new physically based approach was first proposed and tested to exploit dual-polarimetric SAR data. It is physically based on the different backscattering behavior of the oil and natural slicks which call for different correlation between the copolarized channels. In fact, oil discharged at sea has strong damping properties, while natural slicks typically have light damping properties. Accordingly, the copolarized phase difference (CPD) procedure [5], [6] was implemented to exploit the correlation between copolarized channels and successfully tested over a large data set of C-band [5], [6] and L-band [7] SAR data. Preliminary encouraging results have been obtained at X-band [8].

It is important to underline that the extension of the procedure to other bands out of the C-band is not straightforward. In fact, in the literature, it was first mentioned that L- and X-bands were not suitable for oil slick observation [16]. In this paper, for the first time, CPD is exploited over X-band SAR measurements, and this has a paramount operational relevance because of the new X-band SAR constellations, namely, TerraSAR-X and Cosmo-SkyMed.

Furthermore, in this paper, in order to best apply the physical CPD approach, a detailed analysis on the estimation of the interchannel correlation is first accomplished. Two operational attractive estimation procedures are theoretically analyzed, and their comparative performances on real data are evaluated.

Experiments undertaken over TerraSAR-X Single-look Slant range Complex (SSC) dual-polarized StripMap data, in which both certified oils and LA are present, show the robustness of the polarimetric model in describing X-band polarimetric scattering with and without surface slicks and the superiority of the CPD standard deviation approach for polarimetric sea oil slick observation purposes. Results demonstrate the important role of dual-polarimetric TerraSAR-X product for such application.

The remainder of this paper is organized as follows. Section II describes the polarimetric model, experimental

Manuscript received October 26, 2010; revised February 4, 2011, May 3, 2011, and June 6, 2011; accepted June 27, 2011. Date of publication August 31, 2011; date of current version November 23, 2011.

D. Velotto and S. Lehner are with the Remote Sensing Technology Institute, German Aerospace Center, 82234 Wessling, Germany (e-mail: domenico.velotto@dlr.de).

M. Migliaccio and F. Nunziata are with the Dipartimento per le Tecnologie, Università degli Studi di Napoli "Parthenope," 80143 Naples, Italy.

Digital Object Identifier 10.1109/TGRS.2011.2162960

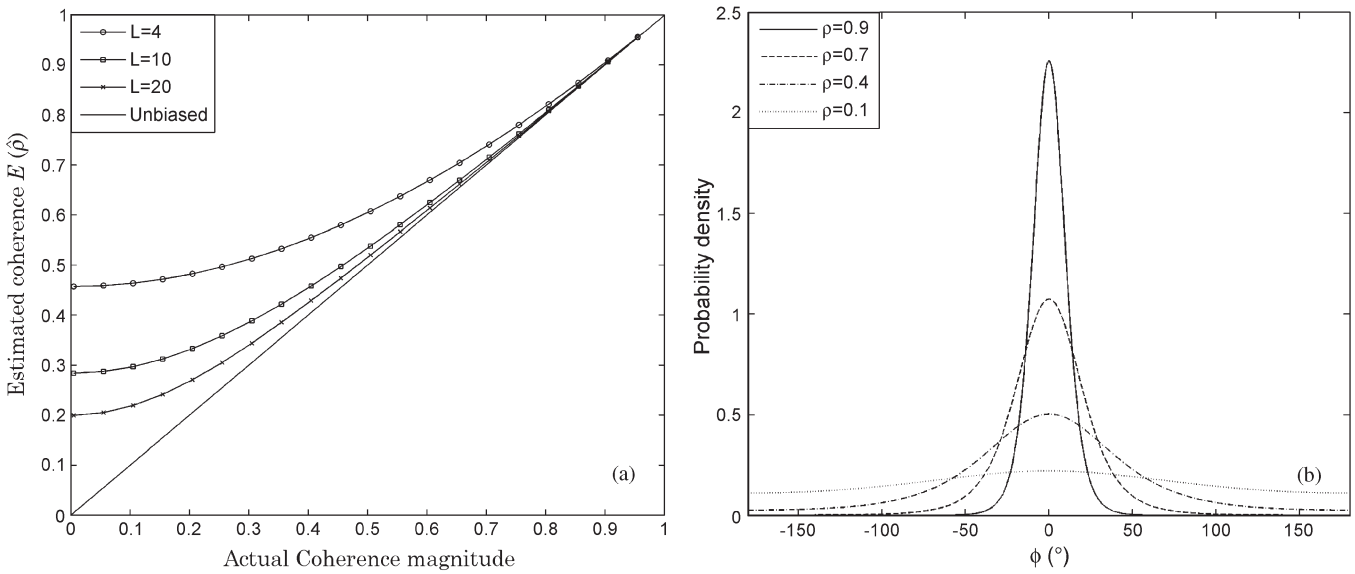

Fig. 1. (a) First moment of coherence amplitude at variance of the look number L equal to 4, 10, and 20. (b) Theoretical CPD pdfs for $\rho = 0.9, 0.7, 0.4, 0.1$, $\overline{\varphi} = 0°$, and $L = 1$.

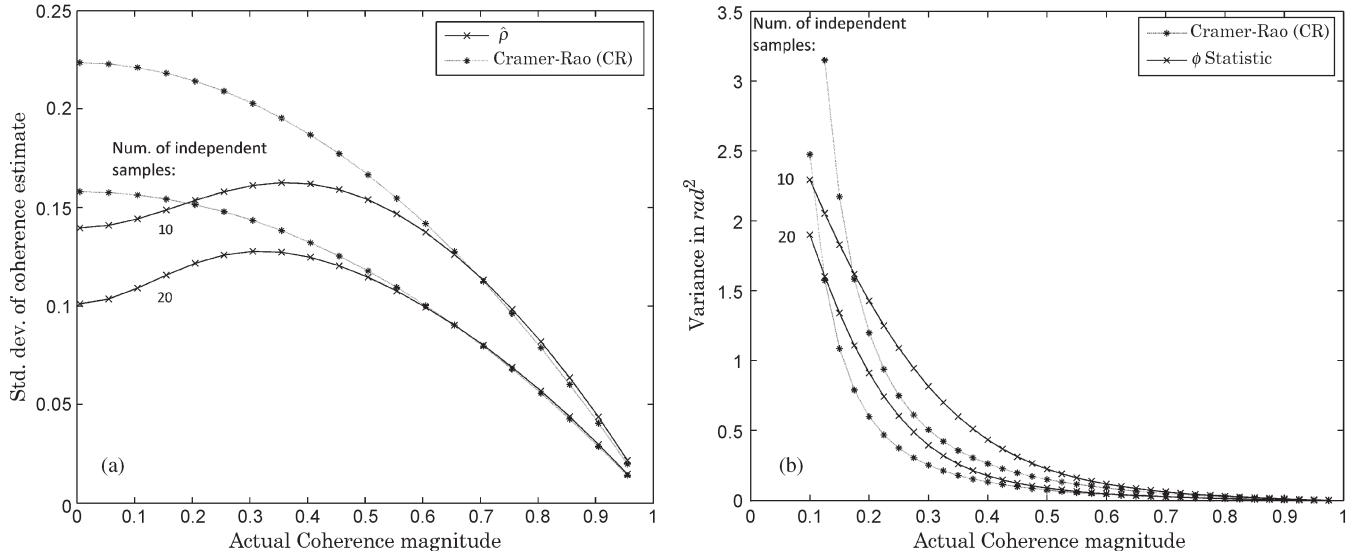

Fig. 2. Standard deviations of the ML estimates of (a) coherence amplitude and (b) CPD are compared with the pertinent CR bound for the numbers of independent samples equal to 10 and 20.

results are shown in Section III, and the conclusions are drawn in Section IV.

II. Polarimetric Model

In this section, the model developed in [5] and [6] is reviewed, and two estimators of the interchannel correlation are introduced and discussed.

The polarimetric electromagnetic model which is the basis of this paper predicts a Bragg (non-Bragg) scattering behavior in accordance with a high (low) interchannel correlation between the copolarized channels [5], [6]. The high interchannel correlation between the copolarized channels is able to observe oils discharged at sea, getting rid of the primary class of LA characterized by weak-damping properties [5], [6].

TABLE I
Expected Behaviour of the Polarimetric Parameters

	$\hat{\sigma}$	$\hat{\rho}$
slick-free/weak-damping	low	high
oil-covered	high	low

In order to implement the model, an estimation of the interchannel correlation between the copolarized channels must be implemented. In this paper, two different estimators are analyzed and compared for the first time.

The estimation of the interchannel correlation between the copolarized channels is a nontrivial problem, and various methods have been developed [17]. It is straightforward that, to take

TABLE II
TERRASAR-X MAJOR SPECIFICATIONS

Imaging Mode	SC		SM				SL				HS			
Polarization Mode	S		S		D		S		D		S		D	
Channels	{HH,VV}		{HH,VV}		{HH/VV, HH/HV, VV/VH}		{HH,VV}		{HH/VV}		{HH,VV}		{HH/VV}	
Data collection range	15°- 60°													
Full performance range	20°-45°		20°-45°				20°-55°				20°-55°			
Range scene size [Km]	100		30		15		10		10		10		10	
Azimuth scene size [Km]	150		50		50		10		10		5		5	
Abs. Radiometric Accuracy [dB]	0.7		0.6		0.6		n.a.		n.a.		n.a.		n.a.	
Relative Radiom. Accuracy [dB]	0.4		0.3		0.3		n.a.		n.a.		n.a.		n.a.	
NESZ [dB]	-26 to -19													
Incidence Angle (°)	20	45	20	45	20	45	20	55	20	55	20	55	20	55
Slant range resolution [m] SSC only			1.2				1.2				0.6		1.2	
Ground range resolution* [m]	19.2	17.0	3.5	3.3	6.6	6.6	3.5	1.7	3.5	3.4	1.8	1.1	3.3	2.2
Azimuth Resolution [m]	19.2	18.5	3.5	3.3	6.6	6.6	3.5	1.7	3.5	3.4	1.8	1.1	3.3	2.2

Notes: S=single-pol, D=dual-pol, * for Spatially Enhanced (SE) resolution mode

full benefit of the model, a viable and robust estimator is a key issue. In fact, it has theoretical and applicative importance for the design of a reliable processing chain.

A first estimator of the interchannel correlation can be provided by HH–VV amplitude coherence ρ often used in SAR interferometry [18]. If we say that $\dot{\rho}$ is the complex coherence of the like-polarized channels

$$\dot{\rho} = \rho e^{j\overline{\varphi}} = \frac{E\left[\dot{S}_{hh}\dot{S}^{*}_{\nu\nu}\right]}{\sqrt{E\left[|\dot{S}_{hh}|^2\right]E\left[|\dot{S}_{\nu\nu}|^2\right]}} \tag{1}$$

where $\overline{\varphi}$ is the mean phase of the complex coherence, $\dot{S}_{hh}$ and $\dot{S}_{\nu\nu}$ are the complex HH and VV scattering amplitudes, respectively, and $E[\cdot]$ is the expectation operator [17].

Once ergodicity is invoked, ρ can be estimated by replacing the expectation operator with an $N \times N$ spatial averaging window to compute the coherence amplitude $\hat{\rho}$. Statistical analysis of $\hat{\rho}$ has been described in [17] and [18], and its first moment $E[\hat{\rho}]$ at variance for looks equal to L is given by

$$E(\hat{\rho}) = \frac{\Gamma(L)\Gamma(1+1/2)}{\Gamma(L+1/2)} \times (1-\rho^2)^L \times {}_3F_2\left([3/2, L, L]; [L+1/2]; [1]; \rho^2\right). \tag{2}$$

A plot of (2) is shown in Fig. 1(a), where it must be noted that $E[\hat{\rho}]$ is biased particularly for low ρ values and this bias decreases with increasing L.

A second estimator of the interchannel correlation can be provided by the standard deviation of the CPD given by

$$\varphi = \angle \dot{S}_{hh}\dot{S}^{*}_{\nu\nu} = \varphi_{hh} - \varphi_{\nu\nu} \tag{3}$$

where φ_{hh} and $\varphi_{\nu\nu}$ are the arguments of the complex HH and VV scattering amplitudes, respectively.

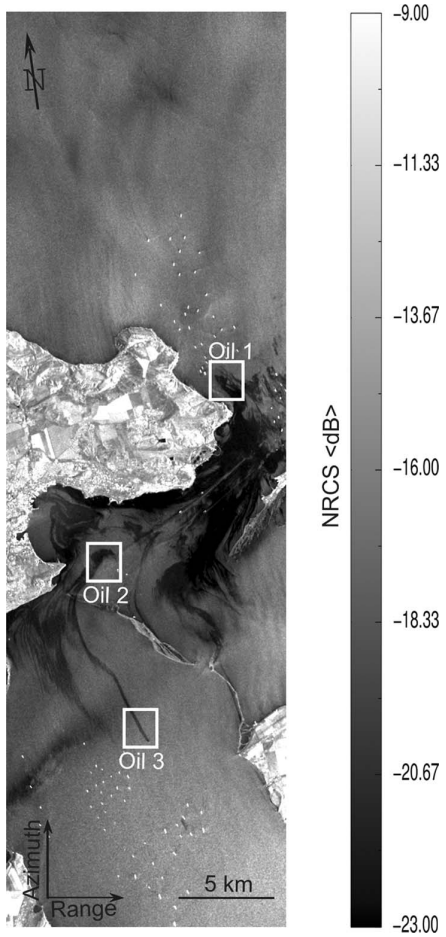

Fig. 3. First data set relevant to the acquisition of November 16, 2007, at 03:52 UTC in Kerch Strait. X-band TerraSAR-X VV SAR image (15 × 50 km) relevant to the acquisition of November 16, 2007, at 03:52 UTC, where three ROIs are emphasized by the white boxes.

Once ergodicity is invoked, the standard deviation of φ can be estimated through a similar $N \times N$ window averaging to get $\hat{\sigma}$. The CPD probability density function (pdf) at variance

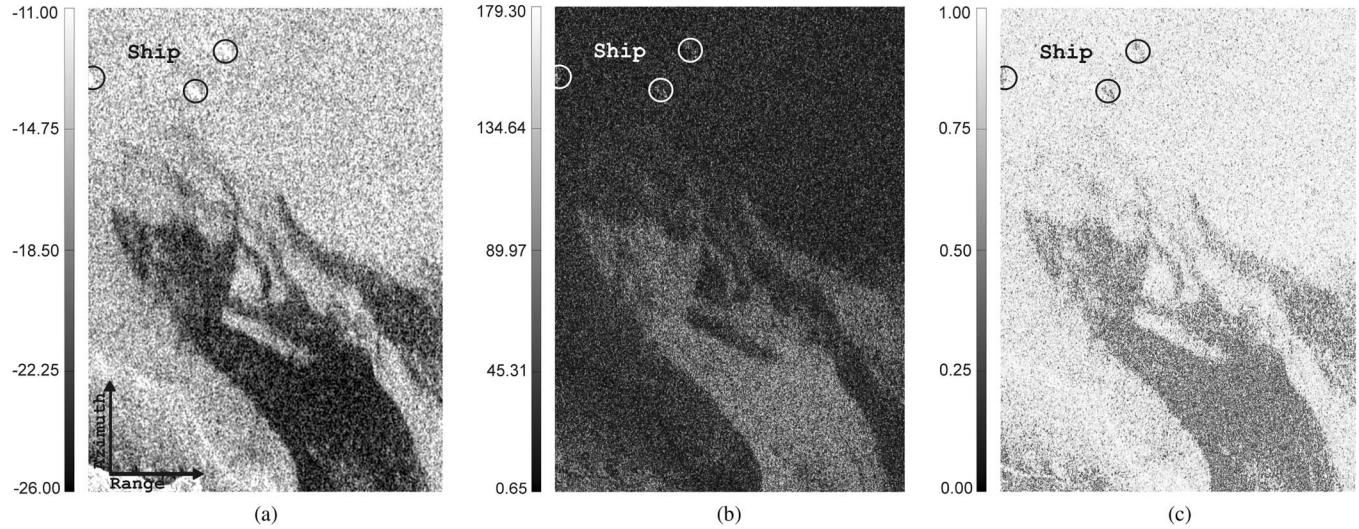

Fig. 4. Excerpt of the SAR data shown in Fig. 3 relevant to the ROI labeled as Oil 1: (a) VV squared modulus image and (b and c) measured $\hat{\sigma}$ and $\hat{\rho}$ maps obtained by using a 3×3 moving window. (a) VV squared modulus image (in decibels). (b) 3×3 $\hat{\sigma}$ map (in degrees). (c) 3×3 $\hat{\rho}$ map.

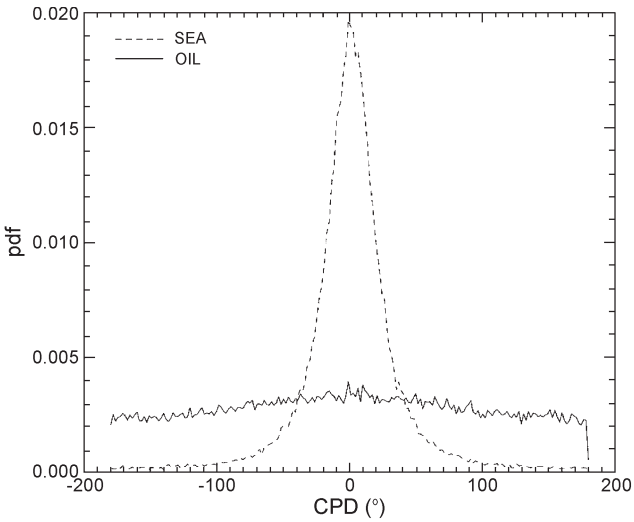

Fig. 5. Measured CPD pdfs for both oil-covered and oil-free sea surfaces.

for looks equal to L has been derived in terms of the complex coherence [19]–[21]

$$p(\hat{\varphi}) = \frac{(1-\rho^2)^L \Gamma(2L)}{2^{L+1/2}\sqrt{\pi}\Gamma(L)} \left(\frac{1}{1-\beta^2}\right)^{(L+1/2)/2} P_{L3/2}^{-L1/2}(-\beta) \quad (4)$$

where $P(\cdot)$ is the Legendre function of the first kind, $\Gamma(\cdot)$ is the Gamma function, and $\beta = \rho\cos(\varphi - \overline{\varphi})$.

A plot of (4), for $L = 1$, $\overline{\varphi} = 0$, and varying ρ, is shown in Fig. 1(b). In general, (4) becomes narrower when either L or ρ increases. The parameter $\overline{\varphi}$ determines the most likely phase (i.e., the location of the mode) which, here, is also the mean phase [5], [20], [21].

When ρ tends to zero (HH and VV channels uncorrelated), the pdf tends to a uniform distribution, while for ρ approaching to one (HH and VV channels fully correlated), the pdf tends to a Dirac delta function. Moreover, for $0 < \rho < 1$, the CPD pdf resembles a Gaussian bell with a mean value $\overline{\varphi}$ and a standard deviation σ inversely related to ρ [19]–[22].

To analyze the effectiveness of the proposed estimators, they are compared with their corresponding Cramer–Rao (CR) bounds. A CR bound gives a lower bound on the variance of any unbiased estimator; hence, an estimator is efficient when it achieves the bound. CR bounds for $\hat{\rho}$ and $\hat{\varphi}$[22]

$$\mathrm{var}(\hat{\rho})_{\mathrm{CR}} = \frac{(1-\rho^2)^2}{2L} \quad (5)$$

$$\mathrm{var}(\hat{\varphi})_{\mathrm{CR}} = \frac{1-\rho^2}{2L\rho^2}. \quad (6)$$

The standard deviations of the ML estimations of ρ and φ are compared with the proper CR bounds in Fig. 2(a) and (b), respectively. It can be noted that, for low coherence values ($\rho < 0.3$), $\hat{\varphi}$ provides an efficient coherence magnitude estimation, while for high actual coherence values ($\rho > 0.5$), the efficient estimator is $\hat{\rho}$.

It is now important to read the previously developed polarimetric model, whose key feature is the interchannel correlation, in terms of $\hat{\sigma}$ and $\hat{\rho}$, focusing on their performances with respect to sea oil slick observation.

A slick-free and weak-damping slick-covered sea surface, calling for a high interchannel correlation between the copolarized channels, is expected to be characterized by the following (see Table I):

1) narrow CPD pdf and, therefore, low $\hat{\sigma}$ values;
2) high $\hat{\rho}$ values.

An oil-covered sea surface, calling for a low HH–VV correlation, is expected to be characterized by the following (see Table I):

1) broaden CPD pdf and, therefore, high $\hat{\sigma}$ values;
2) low $\hat{\rho}$ values.

As a matter of fact, the two proposed estimators are expected to be both able to observe oils and to distinguish them from weak-damping LAs. Since $\hat{\rho}$ has been shown to be biased for low ρ values, the approach based on $\hat{\sigma}$ is expected to perform better.

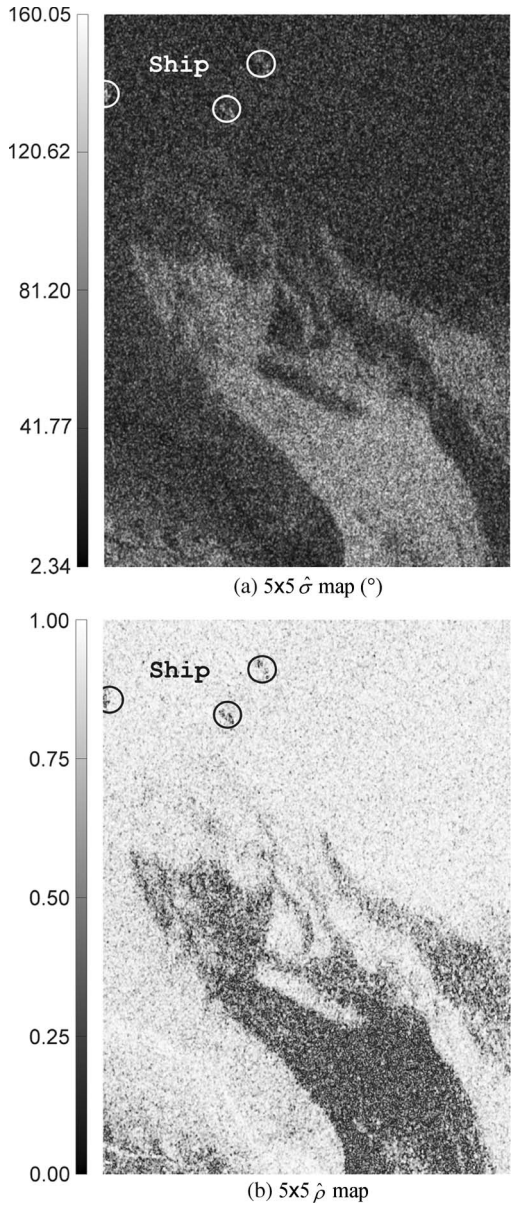

Fig. 6. Filter output for the ROI labeled as Oil 1 using a 5×5 window size: (a) and (b) Measured $\hat{\sigma}$ and $\hat{\rho}$ maps. (a) 5×5 $\hat{\sigma}$ map (in degrees). (b) 5×5 $\hat{\rho}$ map.

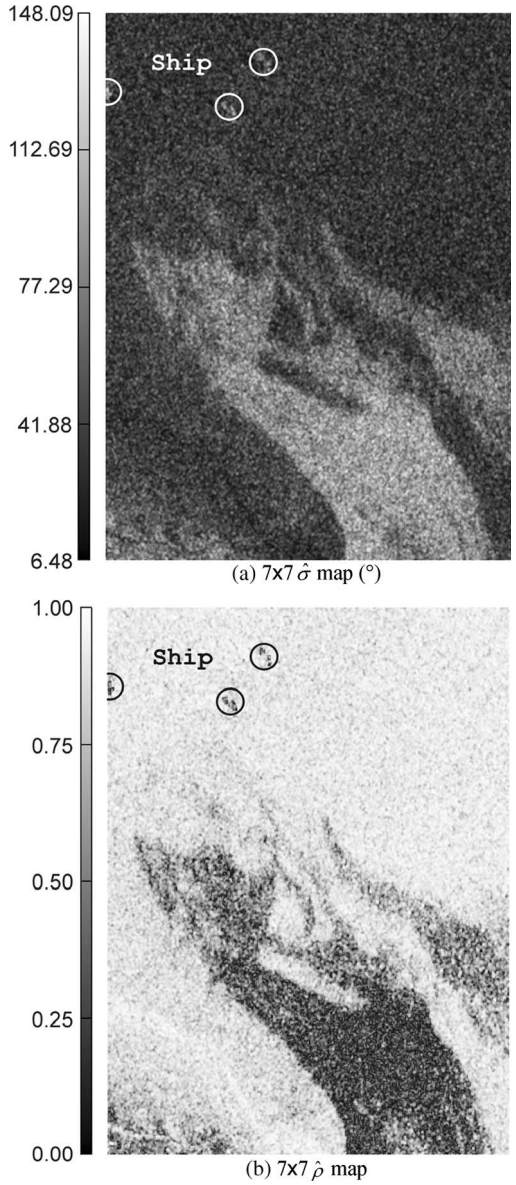

Fig. 7. Filter output for the ROI labeled as Oil 1 using a 7×7 window size: (a) and (b) Measured $\hat{\sigma}$ and $\hat{\rho}$ maps. (a) 7×7 $\hat{\sigma}$ map (in degrees). (b) 7×7 $\hat{\rho}$ map.

III. Experiments

In this section, some thought experiments are presented and discussed to demonstrate the soundness of the proposed model even in X-band and to compare the two interchannel correlation estimators over real data. The data set consist of SSC TerraSAR-X dual-polarization SAR data in which both certified oil slicks and weak-damping LAs are present.

The SAR instrument on board the TerraSAR-X satellite is designed to work in different modes and polarizations (single/dual polarization modes for basic products and quad/twin polarization modes for experimental products) with different swath coverage, incidence angle, and resolution. The TerraSAR-X major specification modes are summarized in Table II.

The Noise Equivalent Sigma Zero (NESZ) for the different TerraSAR-X modes is between -19 and -26 dB, depending mainly on the antenna pattern, the transmitted power, and the receiver noise (see Table II). Another critical parameter with respect to the polarimetric system performance is the channel isolation. The channel isolation on transmit (one way) is better than 34 dB and, thus, 10 dB better than the requirement for the space segment. The cross-polarization isolation (also called crosstalk) of SAR images between all polarization channels is at least 24.9 dB [23].

In all subsequent experiments, both $\hat{\rho}$ and $\hat{\sigma}$ are obtained at variance of the moving averaging window size (3×3, 5×5, and 7×7).

First experiments are relevant to SAR data, where certified oil slicks are present, and then, weak-damping LAs are accounted for.

A. Oil-Spill Observation

The first experiment is relevant to the SSC SAR data gathered on November 16, 2007, 03:52 Coordinated Universal

TABLE III
SUMMARY OF THE OBTAINED RESULTS

DATA SET [NxN]*	Surfactant	Mean $\hat{\sigma}$ slick [°]	Mean $\hat{\sigma}$ sea [°]	Mean $\hat{\rho}$ slick	Mean $\hat{\rho}$ sea	Mean $\overline{\varphi}$ slick [°]	Mean $\overline{\varphi}$ sea [°]	$c_{\hat{\sigma}}$	$c_{\hat{\rho}}$
Kerch Strait [3x3]	Oil 1	85.0	30.2	0.53	0.91	0.17	2.10	2.81	1.72
	Oil 2	61.3	28.9	0.69	0.92	1.53	2.44	2.12	1.33
	Oil 3	45.0	25.0	0.81	0.94	2.22	1.43	1.80	1.16
Kerch Strait [5x5]	Oil 1	93.1	34.5	0.38	0.91	0.18	2.10	2.69	2.39
	Oil 2	67.8	33.2	0.63	0.92	1.51	2.44	2.04	1.46
	Oil 3	50.5	28.8	0.81	0.95	2.21	1.42	1.75	1.17
Kerch Strait [7x7]	Oil 1	95.6	36.1	0.3	0.91	0.20	2.10	2.64	3.03
	Oil 2	70.0	34.7	0.62	0.92	1.50	2.44	2.01	1.48
	Oil 3	52.5	30.4	0.81	0.95	2.21	1.42	1.72	1.17
Black Sea [3x3]	Spill	90.7	60.5	0.50	0.68	3.36	9.21	1.49	1.36
Black Sea [5x5]	Spill	98.5	66.8	0.34	0.62	3.34	9.21	1.47	1.82
Black Sea [7x7]	Spill	100.8	69.0	0.26	0.61	3.30	9.20	1.46	2.34
Kerch Strait [3x3]	LA	38.6	32.3	0.87	0.91	1.08	1.36	1.19	1.05
Kerch Strait [5x5]	LA	43.5	36.8	0.86	0.90	1.07	1.35	1.18	1.05
Kerch Strait [7x7]	LA	45.2	38.4	0.86	0.90	1.04	1.35	1.18	1.05
Ischia wake1 [3x3]	LA	36.0	33.4	0.85	0.90	1.47	1.87	1.08	1.06
Ischia wake1 [5x5]	LA	40.3	37.5	0.88	0.90	1.46	1.86	1.07	1.02
Ischia wake1 [7x7]	LA	41.8	39.0	0.88	0.90	1.45	1.86	1.07	1.02
Ischia wake2 [3x3]	LA	37.6	33.4	0.85	0.88	1.97	1.47	1.12	1.04
Ischia wake2 [5x5]	LA	42.0	37.5	0.86	0.88	1.97	1.47	1.12	1.02
Ischia wake2 [7x7]	LA	43.6	39.0	0.86	0.88	1.98	1.47	1.12	1.02

* N dimension of the moving window

Time (UTC), over Kerch Strait. The TerraSAR-X VV-polarized squared modulus image is shown in gray tones in Fig. 3. A large low backscatter area, due to an accidental oil spill, is clearly visible. On November 11, stormy seas and gale-force winds in the narrow Kerch Strait, which joins the Black Sea and the Sea of Azov, have wrecked a Volganeft-139 Russian oil tanker, spilling at least 2000 metric tons of fuel oil.

Three regions of interest (ROIs) have been selected within the large polluted area (see Fig. 3).

Fig. 4(a) shows the normalized radar cross section (NRCS) in decibels that is relevant to ROI-labeled Oil 1 ($\sim 3 \times 4$ km), where, to better highlight the oil, a parameter scaling procedure, based on the histogram equalization enhancement technique, has been applied. $\hat{\sigma}$ and $\hat{\rho}$ maps, obtained by using a 3×3 moving window, are shown in gray tones in Fig. 4(b)

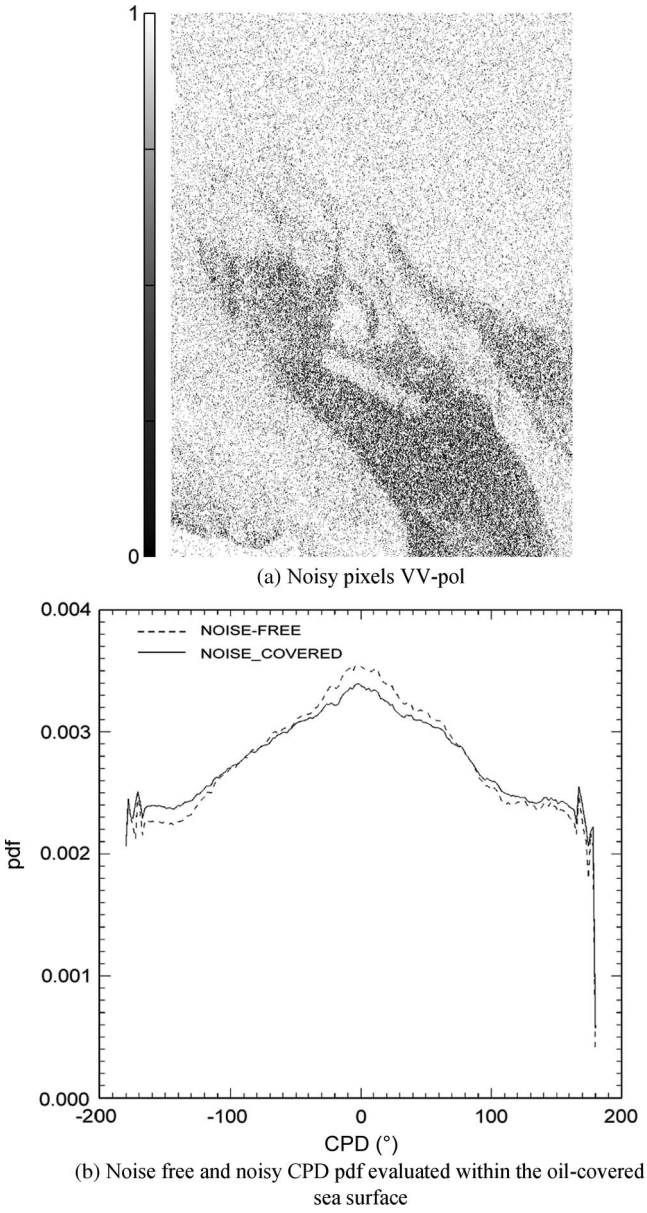

(a) Noisy pixels VV-pol

(b) Noise free and noisy CPD pdf evaluated within the oil-covered sea surface

Fig. 8. Noise effect on the CPD distribution. (a) Pixels above (below) the VV NESZ are in white (black). (b) CPD pdfs evaluated within oil-covered sea surface including and excluding noisy pixels.

and (c), respectively. At this step, no histogram equalization enhancement technique is applied on either image. Fig. 4(b) and (c) shows that $\hat{\sigma}$ ($\hat{\rho}$) is higher (lower) within the oil-covered area. In both cases, the oil slick is clearly distinguishable from the background sea. Results confirm the theoretical model which predicts that the Bragg scattering mechanism dominates everywhere but within the oil-covered sea surface. The CPD standard deviation approach makes the oil brighter than the background, while the sample coherence approach makes it darker. In summary, both $\hat{\sigma}$ and $\hat{\rho}$ filters emphasize the presence of the oil with respect to the background sea.

To quantitatively validate these results, a detailed analysis has been undertaken, measuring the oil-covered and slick-free CPD pdfs (see Fig. 5). It can be noted that their standard deviation values are completely different, i.e., 85° and 30°. The mean $\hat{\rho}$ values, for both slick-free and oil-covered sea surfaces, are more close and equal to 0.53 and 0.91, respectively.

To further compare the performances of $\hat{\sigma}$ and $\hat{\rho}$ with respect to oil slick observation, a contrast parameter is defined and adapted to the different $\hat{\sigma}$ and $\hat{\rho}$ outputs

$$c_{\hat{\sigma}} = \frac{\hat{\sigma}_{\mathrm{OIL}}}{\hat{\sigma}_{\mathrm{SEA}}} \tag{7}$$

$$c_{\hat{\rho}} = \frac{\hat{\rho}_{\mathrm{SEA}}}{\hat{\rho}_{\mathrm{OIL}}}. \tag{8}$$

It can be noted that $c_{\hat{\sigma}}$ and $c_{\hat{\rho}}$ are equal to 2.83 and 1.72, respectively. This witnesses that the CPD-based approach is able to better enhance the presence of oil slicks over the sea.

Filter outputs obtained using a 5×5 (7×7) window size are shown for both $\hat{\sigma}$ and $\hat{\rho}$ in Fig. 6(a) and (b) [Fig. 7(a) and (b)], respectively. The values of $\hat{\sigma}$ and $\hat{\rho}$ measured in these cases are listed in Table III, for both oil-covered and slick-free areas, as well as the corresponding $c_{\hat{\sigma}}$ and $c_{\hat{\rho}}$ values. Note that, although the CPD performances, evaluated in terms of $c_{\hat{\sigma}}$, do not vary too much with respect to window size, a completely different behavior is exhibited by $c_{\hat{\rho}}$, which performs better when larger window sizes are employed. This result is consistent with the theoretical studies undertaken in [17]. Hereinafter, only maps obtained by a 3×3 moving window are shown to save space. Nevertheless, quantitative analyses, accomplished using different window sizes, are summarized in Table III.

It must be noted that no peculiar trend related to the CPD mean value ($\overline{\varphi}$) over the oil-covered and slick-free sea surfaces is revealed in this study even when using different window sizes (see Table III).

Before proceeding further, it is important to discuss the effects of the NESZ on the proposed polarimetric approach. The effect of noise on the CPD distribution is now analyzed.

The average VV NESZ, equal to -25 dB, has been considered to obtain the images shown in Fig. 8(a) and (b), where pixels above (below) the NESZ are marked in white (black). Fig. 8(a) shows that most of the noisy pixels belong to the oil-covered area. Accordingly, to quantify the NESZ effect on the CPD pdf, the latter is evaluated within the oil-covered sea surface, including and excluding pixels below NESZ [see Fig. 8(b)]. The effect of the noise is negligible, as witnessed by the standard deviation values, equal to 82° and 85° for noise-free and noisy pdfs, respectively. These results confirm the physical consistence of the proposed approach. Similar results are obtained for the $\hat{\rho}$-based approach and therefore are not shown to save space.

Fig. 9(a) shows the NRCS image (in decibels) related to the ROI-labeled Oil 2 ($\sim 2.5 \times 3$ km) properly scaled and equalized. The measured $\hat{\sigma}$ and $\hat{\rho}$ maps obtained by using a 3×3 moving window are shown in gray tones in Fig. 9(b) and (c), respectively. Results agree to what formerly experienced and can be quantitatively confirmed analyzing the measured CPD pdfs, Fig. 9(d), relevant to both oil-covered and the surrounding free sea surface. Also, in this case, $\hat{\sigma}$ performs better than $\hat{\rho}$ (Table III).

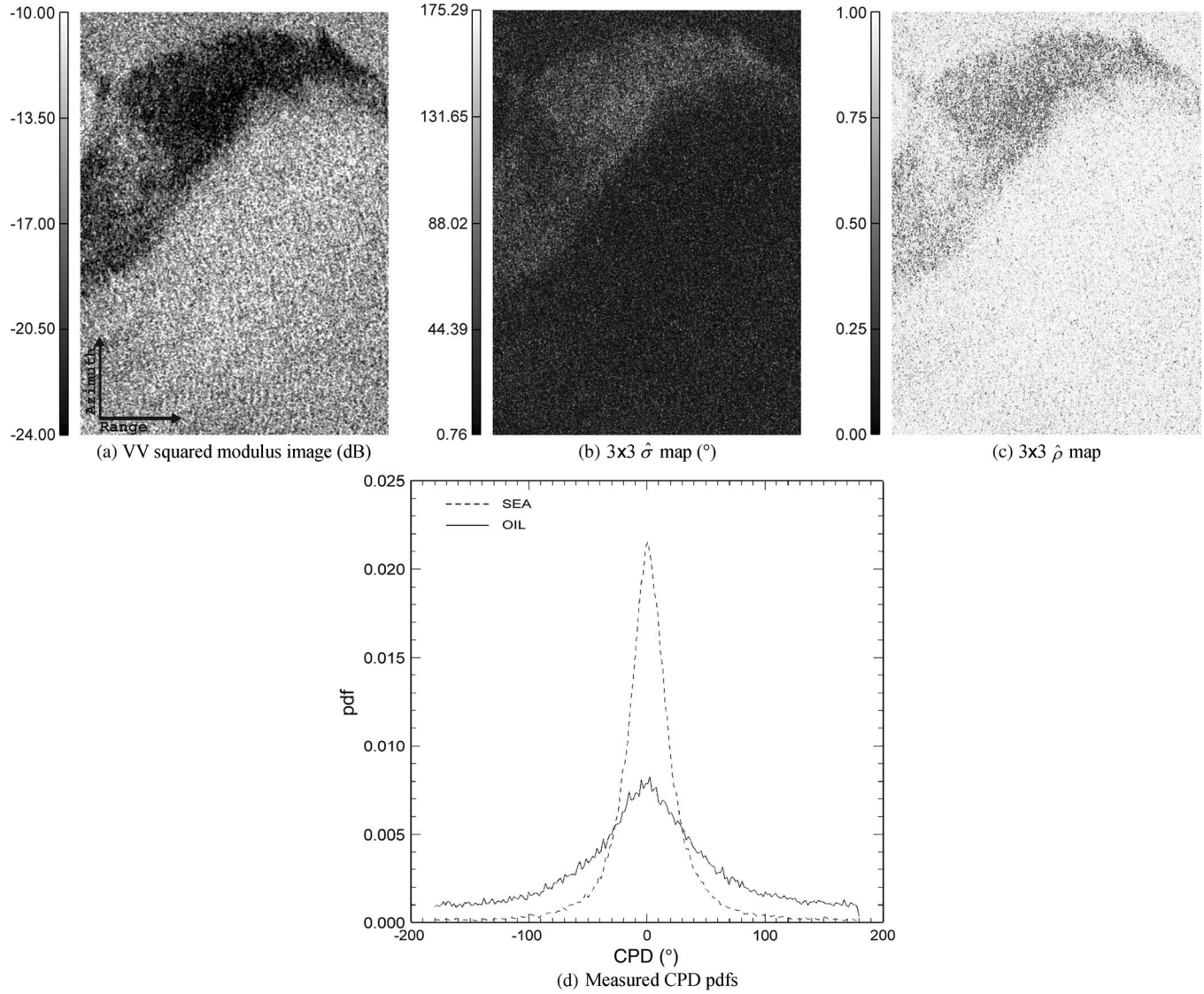

Fig. 9. Excerpt of the SAR data shown in Fig. 3 relevant to the ROI labeled as Oil 2: (a) VV squared modulus image, (b and c) measured $\hat{\sigma}$ and $\hat{\rho}$ maps obtained by using a 3×3 moving window, and (d) measured CPD pdfs for both oil-covered and oil-free sea surfaces. (a) VV squared modulus image (in decibels). (b) 3×3 $\hat{\sigma}$ map (in degrees). (c) 3×3 $\hat{\rho}$ map. (d) Measured CPD pdfs.

Fig. 10(a) shows the NRCS image (in decibels) related to the ROI-labeled Oil 3 (3×3 km) properly scaled and equalized. The measured $\hat{\sigma}$ and $\hat{\rho}$ maps obtained by using a 3×3 moving window are shown in gray tones in Fig. 10(b) and (c). The result agrees with earlier findings (see Fig. 10(d) and Table III).

It must be pointed out that, for all window sizes, the oil-covered $\hat{\sigma}$ ($\hat{\rho}$) values relevant to the ROI Oil 2 and Oil 3 are quite smaller (larger) than the one measured within ROI Oil 1 (see Table III). This is probably due to different environmental conditions along the slick and the weathering processes over the very large polluted area, which affect the oil damping properties.

The second experiment is relevant to the SSC SAR data gathered on July 28, 2009, 04:18 UTC in Black Sea. A VV-polarized NRCS image (in decibels) relevant to an $\sim 2 \times 4$ km subscene, properly scaled and equalized, is shown in gray tones in Fig. 11(a). A low backscatter area, most likely due to an illicit oil discharge since it is very close to a strong scatterer (ship/tanker), is visible.

The measured $\hat{\sigma}$ and $\hat{\rho}$ maps obtained by using a 3×3 moving window are shown in gray tones in Fig. 11(b) and (c), respectively, where features associated to the spillage are clearly visible. The CPD pdfs relevant to the oil-covered sea surface and the surrounding sea are shown in Fig. 11(d). Results agree with the formerly presented (see Table III), witnessing the effectiveness of the approaches to detect also illegal spillages.

B. Weak-Damping LA

The third experiment is relevant to the SSC SAR data gathered on November 16, 2007, 03:52 UTC, over Kerch Strait. A VV-polarized NRCS image (in decibels) relevant to a 3×3 km subscene, properly scaled and equalized, is shown in gray tones in Fig. 12(a). A small low backscatter area, due to marine features, is clearly visible.

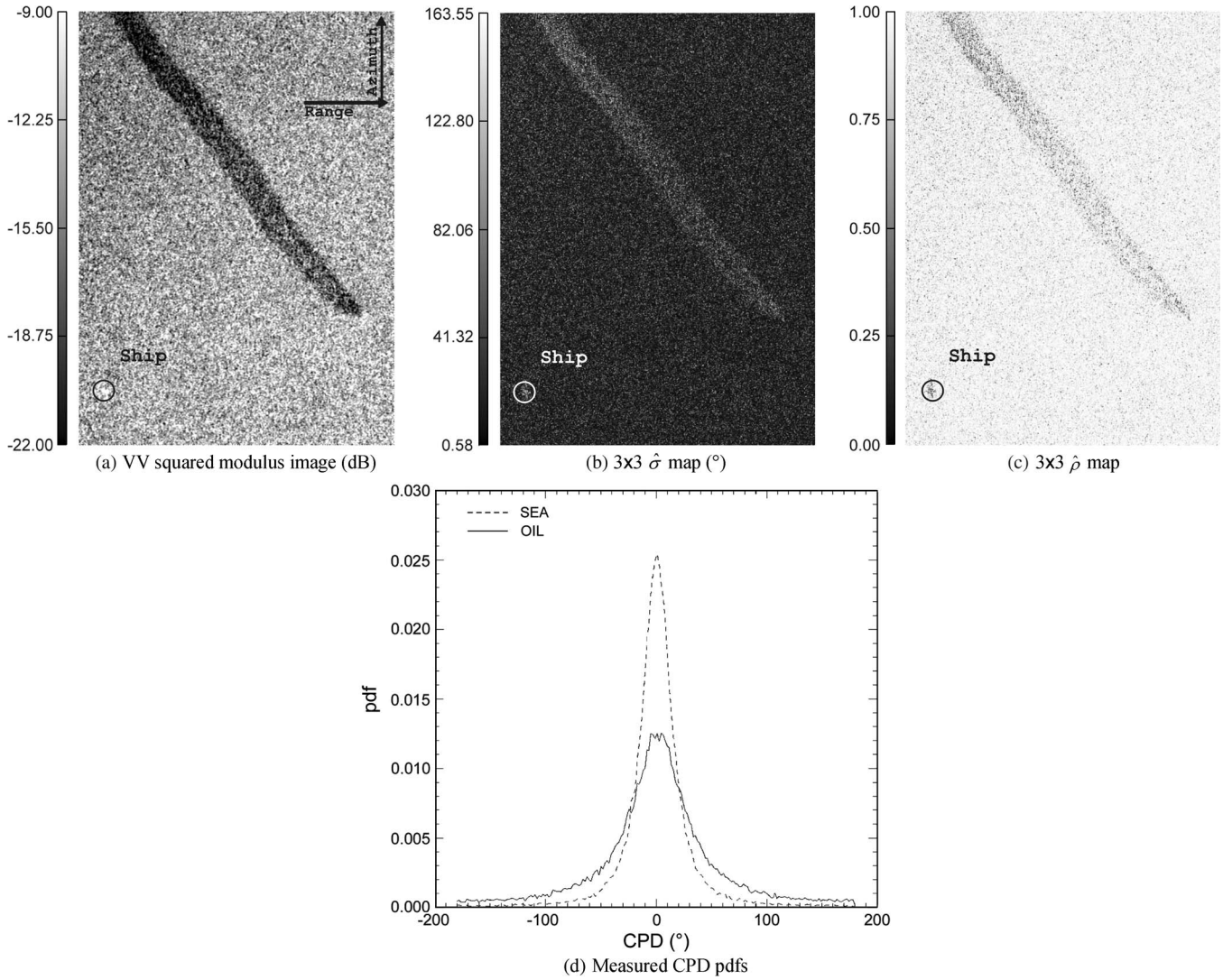

Fig. 10. Excerpt of the SAR data shown in Fig. 3 relevant to the ROI labeled as Oil 3: (a) VV squared modulus, (b and c) estimated $\hat{\sigma}$ and $\hat{\rho}$ maps obtained by using a 3×3 moving window, and (d) measured CPD pdfs for both oil-covered and oil-free sea surfaces. (a) VV squared modulus image (in decibels). (b) 3×3 $\hat{\sigma}$ map (in degrees). (c) 3×3 $\hat{\rho}$ map. (d) Measured CPD pdfs.

The measured $\hat{\sigma}$ and $\hat{\rho}$ maps obtained by using a 3×3 moving window are shown in gray tones in Fig. 12(b) and (c), respectively. The visual (and subjective) analysis of these results shows that such dark area related to the LA is de-emphasized, but this can be much better witnessed by a quantitative analysis. As a matter of fact, to further validate this result, a quantitative analysis has been undertaken measuring the slick-covered and slick-free CPD pdfs [see Fig. 12(d)]. The pdfs are practically overlapped, as also confirmed by their standard deviation values (see Table III). Similar comments apply for $\hat{\rho}$, whose values are 0.87 and 0.91 for slick-covered and slick-free sea surfaces, respectively.

Moreover, Fig. 12(b) and (c) suggests that the both $\hat{\sigma}$ and $\hat{\rho}$ filters act as a de-emphasis filters when applied to data in which weak-damping LAs are present, since the latter are de-emphasized with respect to the surrounding sea. This de-emphasis capability is confirmed by the measured $c_{\hat{\sigma}}$ and $c_{\hat{\rho}}$ close to the unity, independently of the window size used (see Table III).

The fourth experiment is relevant to the SSC SAR data gathered on June 05, 2009, 05:19 UTC, over the Ischia harbor, off the Gulf of Naples, Italy. A VV-polarized NRCS image (in decibels) relevant to a 3×6 km subscene, properly scaled and equalized, is shown in gray tones in Fig. 13(a). Two straight low backscatter areas due to ship wakes, produced by ferries directed to Ischia Island from Naples and verified by local harbor authority, are visible and labeled as Wake 1 and Wake 2. These LAs are of great interest since, due to their elongated shape, they can be erroneously considered as due to illegal discharges.

The measured $\hat{\sigma}$ and $\hat{\rho}$ maps obtained by using a 3×3 moving window are shown in gray tones in Fig. 13(b) and (c), respectively. It can be noted that the features associated to Wake 1 and Wake 2 are de-emphasized in the filtered images. Both approaches are not sensitive to this kind of weak-damping LA. To quantitatively confirm this result, measured slick-free and LA-covered CPD pdfs for both wakes are shown in Fig. 13(d) and (e). The pdfs are practically overlapped, as predicted by the theoretical model (see also Table III).

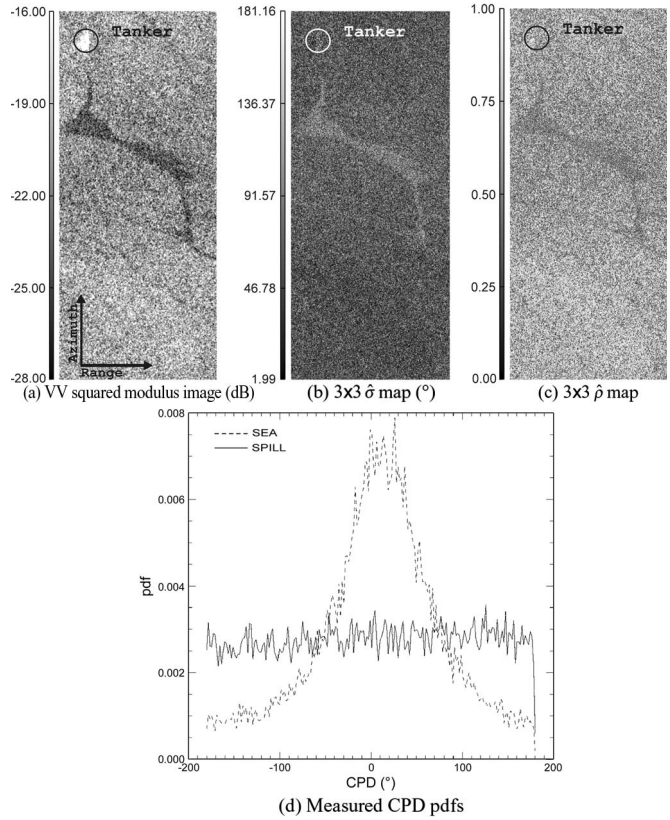

Fig. 11. X-band SAR data relevant to the acquisition of July 28, 2009, at 04:18 UTC: (a) Excerpt of the VV squared modulus image in which a dark area most likely due to illicit oil discharge is present, (b and c) measured $\hat{\sigma}$ and $\hat{\rho}$ maps obtained by using a 3×3 moving window, and (d) measured CPD pdfs for both oil-covered and oil-free sea surfaces. (a) VV squared modulus image (in decibels). (b) 3×3 $\hat{\sigma}$ map (in degrees). (c) 3×3 $\hat{\rho}$ map. (d) Measured CPD pdfs.

IV. Summary and Conclusion

In this paper, a polarimetric model to read the X-band polarimetric sea surface scattering with and without surface slicks has been proposed for the first time. The model exploits the interchannel correlation between copolarized channels. Two approaches are proposed to estimate the HH–VV interchannel correlation, $\hat{\rho}$ and $\hat{\sigma}$: The first is based on the complex coherence and is the estimate of the coherence amplitude, while the second is based on the CPD and is the estimate of the CPD standard deviation. Their performances are discussed for X-band polarimetric SAR oil-spill observation.

Experiments undertaken over SSC TerraSAR-X dual-polarimetric (HH–VV) products confirm the soundness of the model and show the superiority of the CPD approach for oil-spill observation.

In summary, the key results emerging from this study can be listed as follows.

1) X-band dual-polarimetric SAR data are useful for oil-spill observation purposes.
2) Both approaches show a different sensitivity with respect to oil and weak-damping LA.
3) $\hat{\sigma}$ ($\hat{\rho}$) values significantly larger (smaller) than slick-free ones are observed over oil-covered sea surface.

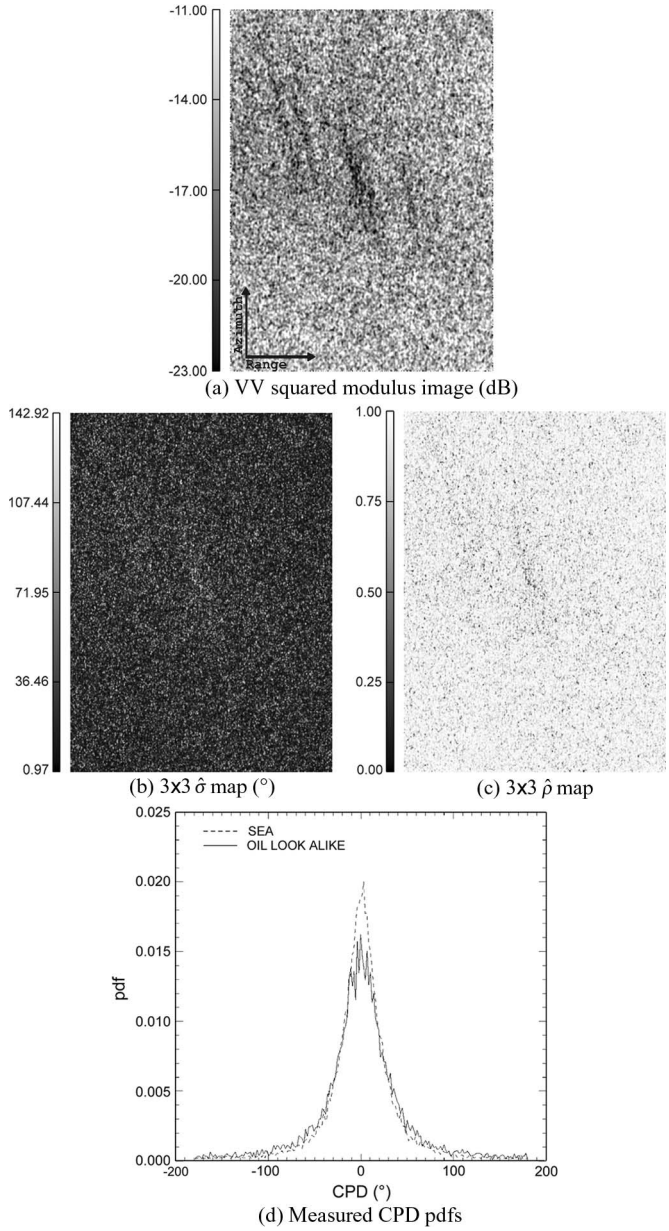

Fig. 12. X-band SAR data relevant to the acquisition of November 16, 2007, at 03:52 UTC: (a) Excerpt of the VV squared modulus image in which a weak-damping oil LA is present, (b and c) measured $\hat{\sigma}$ and $\hat{\rho}$ maps in a 3×3 moving window, and (d) measured CPD pdfs both for slick-covered and slick-free sea surfaces. (a) VV squared modulus image (in decibels). (b) 3×3 $\hat{\sigma}$ map (in degrees). (c) 3×3 $\hat{\rho}$ map. (d) Measured CPD pdfs.

4) $\hat{\sigma}$ and $\hat{\rho}$ values similar to the slick-free ones are observed over areas where a weak-damping LA is present.
5) No sensitivity of $\overline{\varphi}$ with respect to oil slick has been found.
6) CPD standard deviation works better than coherence amplitude when smaller window size is employed. This makes the former approach to be preferred for observing illicit oil spills.

Beyond all scientific aspects, the general value of this study is even more in operational terms since one may think to integrate L-, C-, and X-band SAR measurements ensuring much more dense spatial/temporal coverage and resolution.

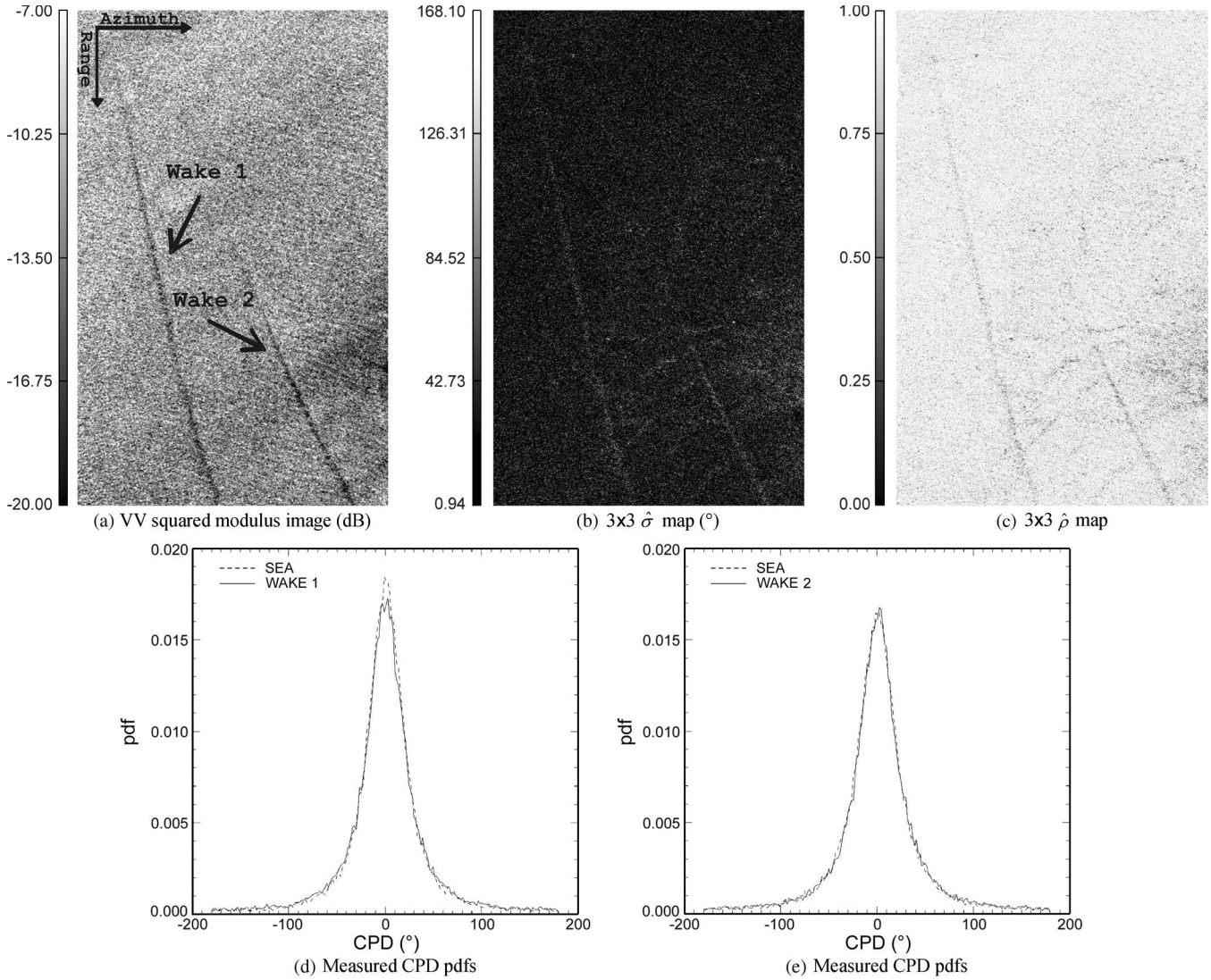

Fig. 13. X-band SAR data relevant to the acquisition of June 05, 2009, at 05:19 UTC: (a) Excerpt of the VV squared modulus image in which two weak-damping oil LAs are present, (b and c) measured $\hat{\sigma}$ and $\hat{\rho}$ maps obtained by using a 3×3 moving window, and (d and e) measured CPD pdfs for both slick-covered and slick-free sea surfaces, Wake 1 (Wake 2). (a) VV squared modulus image (in decibels). (b) 3×3 $\hat{\sigma}$ map (in degrees). (c) 3×3 $\hat{\rho}$ map. (d) Measured CPD pdfs. (e) Measured CPD pdfs.

ACKNOWLEDGMENT

The authors would like to thank the anonymous reviewers and the Associate Editor for the helpful comments and suggestions. The TerraSAR-X data are provided by DLR over the science AO CAL0166 and OCE1045.

REFERENCES

[1] D. A. AL Khudhairy, "Marine oil pollution: Technologies and methodologies for detection and early warning," European Commission, Ispra, Italy, JRC Rep. EUR 20231 EN, 2002.

[2] M. F. Fingas and C. E. Brown, "Review of oil spill remote sensing," *Spill Sci. Technol. Bull.*, vol. 4, no. 4, pp. 199–208, 1997.

[3] C. Brekke and A. H. S. Solberg, "Oil spill detection by satellite remote sensing," *Remote Sens. Environ.*, vol. 95, no. 1, pp. 1–13, Mar. 2005.

[4] C. E. Brown and M. F. Fingas, "Synthetic aperture radar sensors: Viable for marine oil spill response?" in *Proc. 26th AMOP*, Ottawa, ON, Canada, Jun. 10–12, 2003, pp. 299–310.

[5] M. Migliaccio, F. Nunziata, and A. Gambardella, "On the copolarised phase difference for oil spill observation," *Int. J. Remote Sens.*, vol. 30, no. 6, pp. 1587–1602, 2009.

[6] F. Nunziata, A. Gambardella, and M. Migliaccio, "On the use of dual-polarized SAR data for oil spill observation," in *Proc. IGARSS*, Boston, MA, Jul. 6–11, 2008, pp. II-225–II-228.

[7] F. Nunziata, X. Li, M. Migliaccio, A. Montuori, and W. Pichel, "Metallic objects and oil spill detection with multi-polarization SAR," in *Proc IGARSS*, Honolulu, HI, Jul. 25–30, 2010, pp. 2765–2768.

[8] D. Velotto, M. Migliaccio, F. Nunziata, and S. Lehner, "Oil-slick observation using single look complex TerraSAR-X dual-polarized data," in *Proc. IGARSS*, Honolulu, HI, Jul. 25–30, 2010, pp. 3684–3687.

[9] M. Migliaccio, A. Gambardella, F. Nunziata, M. Shimada, and O. Isoguchi, "The PALSAR polarimetric mode for sea oil slick observation," *IEEE Trans. Geosci. Remote Sens.*, vol. 47, no. 12, pp. 4032–4041, Dec. 2009.

[10] M. Migliaccio, A. Gambardella, F. Nunziata, M. Shimada, and O. Isoguchi, "ALOS-PALSAR polarimetric SAR data to observe sea oil slicks," in *Proc. IGARSS*, Cape Town, South Africa, Jul. 12–17, 2009, pp. IV-669–IV-672.

[11] F. Nunziata, A. Gambardella, and M. Migliaccio, "On the Mueller scattering matrix for SAR sea oil slick observation," *IEEE Geosci. Remote Sens. Lett.*, vol. 5, no. 4, pp. 691–695, Oct. 2008.

[12] F. Nunziata, A. Gambardella, and M. Migliaccio, "A unified polarimetric approach for sea oil slick observation," in *Proc. IGARSS*, Cape Town, South Africa, Jul. 12–17, 2009, pp. II-282–II-285.

[13] F. Nunziata, M. Migliaccio, and A. Gambardella, "Pedestal height for oil spill observation," *IET Radar Sonar Navig.*, vol. 5, no. 2, pp. 103–110, Feb. 2011.
[14] M. Migliaccio, F. Nunziata, and A. Gambardella, "Polarimetric signature for oil spill observation," in *Proc. US/EU-Baltic Int. Symp.*, Tallin, Estonia, May 27–29, 2008, pp. 1–5.
[15] A. Gambardella, F. Nunziata, and M. Migliaccio, "A polarimetric sea surface backscattering model," in *Proc. IGARSS*, Cape Town, South Africa, Jul. 12–17, 2009, pp. I-192–I-195.
[16] M. Gade, W. Alpers, H. Huhnerfuss, H. Masuko, and T. Kobayashi, "Imaging of biogenic and anthropogenic ocean surface films by the multifrequency/multipolarization SIR-C/X-SAR," *J. Geophys. Res.*, vol. 103, no. C9, pp. 18 851–18 866, Aug. 1998.
[17] R. Touzi, A. Lopes, J. Bruniquel, and P. W. Vachon, "Coherence estimation for SAR imagery," *IEEE Trans. Geosci. Remote Sens.*, vol. 37, no. 1, pp. 135–149, Jan. 1999.
[18] R. Bamler and P. Hartl, "Synthetic aperture radar interferometry," *Inverse Probl.*, vol. 14, no. 4, pp. R1–R54, Aug. 1998.
[19] K. Sarabandi, "Derivation of phase statistics of distributed targets from the averaged Mueller matrix," *Radio Sci.*, vol. 27, pp. 553–560, 1992.
[20] I. R. Joughin, D. P. Winebrenner, and D. B. Percival, "Probability density function for multilook polarimetric signatures," *IEEE Trans. Geosci. Remote Sens.*, vol. 32, no. 3, pp. 562–574, May 1994.
[21] J.-S. Lee, K. W. Mango, and S. A. Miller, "Intensity and phase statistics of multilook polarimetric and interferometric SAR imagery," *IEEE Trans. Geosci. Remote Sens*, vol. 32, no. 5, pp. 1017–1028, Sep. 1994.
[22] M. S. Seymour and I. G. Cumming, "Maximum likelihood estimation for SAR interferometry," in *IEEE Proc. IGARSS*, Pasadena, CA, 1994, vol. 4, pp. 2272–2275.
[23] M. Schwerdt, D. Schrank, M. Bachmann, C. Schulz, B. J. Döring, and J. H. Gonzalez, "TerraSAR-X re-calibration and dual receive antenna campaigns performed in 2009," in *Proc. EUSAR*, Aachen, Germany, Jun. 7–10, 2010, pp. 218–221.

Domenico Velotto (S'08) was born in Italy on April 30, 1981. He received the M.S. degree (five-year legal course of study) in nautical science (curriculum electronic radio navigation) from the Università degli Studi di Napoli "Parthenope," Naples, Italy, in 2008. In 2009, he joined the Synthetic Aperture Radar (SAR) Oceanography Group, Remote Sensing Technology Institute, German Aerospace Center, Wessling, Germany, where he is currently working toward the Ph.D. degree.

His main research interests deal with electromagnetic modeling, SAR polarimetry, image processing, and Earth observation with emphasis on oil-spill monitoring by means of SAR.

Mr. Velotto was the recipient of the 2008 Best Remote Sensing Thesis Award by the IEEE Geoscience and Remote Sensing South Italy Chapter.

Maurizio Migliaccio (M'91–SM'00) was born in Naples, Italy, in 1962. He received the Laurea degree in electronic engineering from the University of Naples "Federico II," Naples, in 1987.

He was a Visiting Scientist at German Aerospace Center (DLR), Oberpfaffenhofen, Germany. He has also lectured in the U.S., Spain, Germany, and Italy. He is currently a Full Professor of electromagnetics with the Universitá di Napoli "Parthenope," Naples, where he teaches microwave remote sensing. He is a Member of the scientific board of the *Indian Journal of Radio and Space Physics*. He has published more than 150 papers on applied electromagnetics.

Dr. Migliaccio was the recipient of the Geoscience and Remote Sensing (GRS) Chapter Excellence Award in 2007 and was also its Chapter Chair. He was the recipient of the 2009 IEEE GRS Letters Prize Paper Award. He was the IEEE Italy Section Graduate of Last Decade (GOLD) delegate, as well as the General Chairman of the 2008 and 2010 IEEE GOLD Remote Sensing Conferences, both held in Frascati, Italy, at the European Space Agency and at the Italian Naval Academy in Livorno, Italy. He was the European Union Secretary of the COST 243 Action. He is a member of the Italian Space Agency scientific board.

Ferdinando Nunziata (S'03) was born in Italy in 1982. He received the B.S. and M.S. degrees (*summa cum laude*) in telecommunications engineering and the Ph.D. degree (curriculum electromagnetic fields) from the Università degli Studi di Napoli "Parthenope," Naples, Italy, in 2003, 2005, and 2008, respectively.

Since 2010, he has been a Researcher in electromagnetic fields with the Faculty of Engineering "G. Latmiral," Università degli Studi di Napoli "Parthenope." He has been a Lecturer at the National Oceanographic Centre, Southampton, U.K.; Université Catholique de Louvain, Louvain-la-Neuve, Belgium; Helsinki University of Technology, Espoo, Finland; and the City College of New York, New York. He is the author/coauthor of more than 70 papers published in peer-reviewed journals and refereed conferences. His main research interests deal with electromagnetic modeling, single-polarization and multipolarization sea surface scattering, radar polarimetry, and synthetic aperture radar sea oil slick monitoring.

Dr. Nunziata was the recipient of the 2003 IEEE Geoscience and Remote Sensing (GRS) South Italy Chapter Best Remote Sensing Thesis Award and the 2009 Sebetia-Ter International Award for his research activities in remote sensing. He was in the Organizing Committee of the 2008 and 2010 IEEE Graduate of Last Decade (GOLD) Remote Sensing Conferences at the European Space Agency and at the Italian Naval Academy in Livorno, Italy. He served as the Session Chair at the 2008 IEEE International GRS Symposium, Boston, MA. He is the Chairman of the Universitá degli Studi di Napoli "Parthenope" IEEE Student Branch. In 2011, he was selected to serve as GOLD representative to the IEEE GRS Society AdCom.

Susanne Lehner received the M.Sc. degree in applied mathematics from Brunel University, Uxbridge, U.K., in 1979 and the Ph.D. degree in geophysics from the University of Hamburg, Hamburg, Germany, in 1984.

She was a Research Scientist with the Max-Planck Institute for Climatology, Hamburg, and joined the German Aerospace Center (DLR), Wessling, Germany, in 1996. She is currently a Research Scientist in marine remote sensing with the Remote Sensing Technology Institute (IMF), DLR, working on the development of algorithms determining marine parameters from synthetic aperture radars.

A.2. Lehner, S., Pleskachevsky, A., Velotto, D., Jacobsen, S., 2013a. Meteo-marine parameters and their variability observed by high resolution satellite radar images. Oceanography 26 (2): 80–91

THE OFFICIAL MAGAZINE OF THE OCEANOGRAPHY SOCIETY

Oceanography

CITATION

Lehner, S., A. Pleskachevsky, D. Velotto, and S. Jacobsen. 2013. Meteo-marine parameters and their variability observed by high resolution satellite radar images. Oceanography 26(2):80–91, http://dx.doi.org/10.5670/oceanog.2013.36.

DOI

http://dx.doi.org/10.5670/oceanog.2013.36

Meteo-Marine Parameters and Their Variability

Observed by High-Resolution Satellite Radar Images

BY SUSANNE LEHNER, ANDREY PLESKACHEVSKY, DOMENICO VELOTTO, AND SVEN JACOBSEN

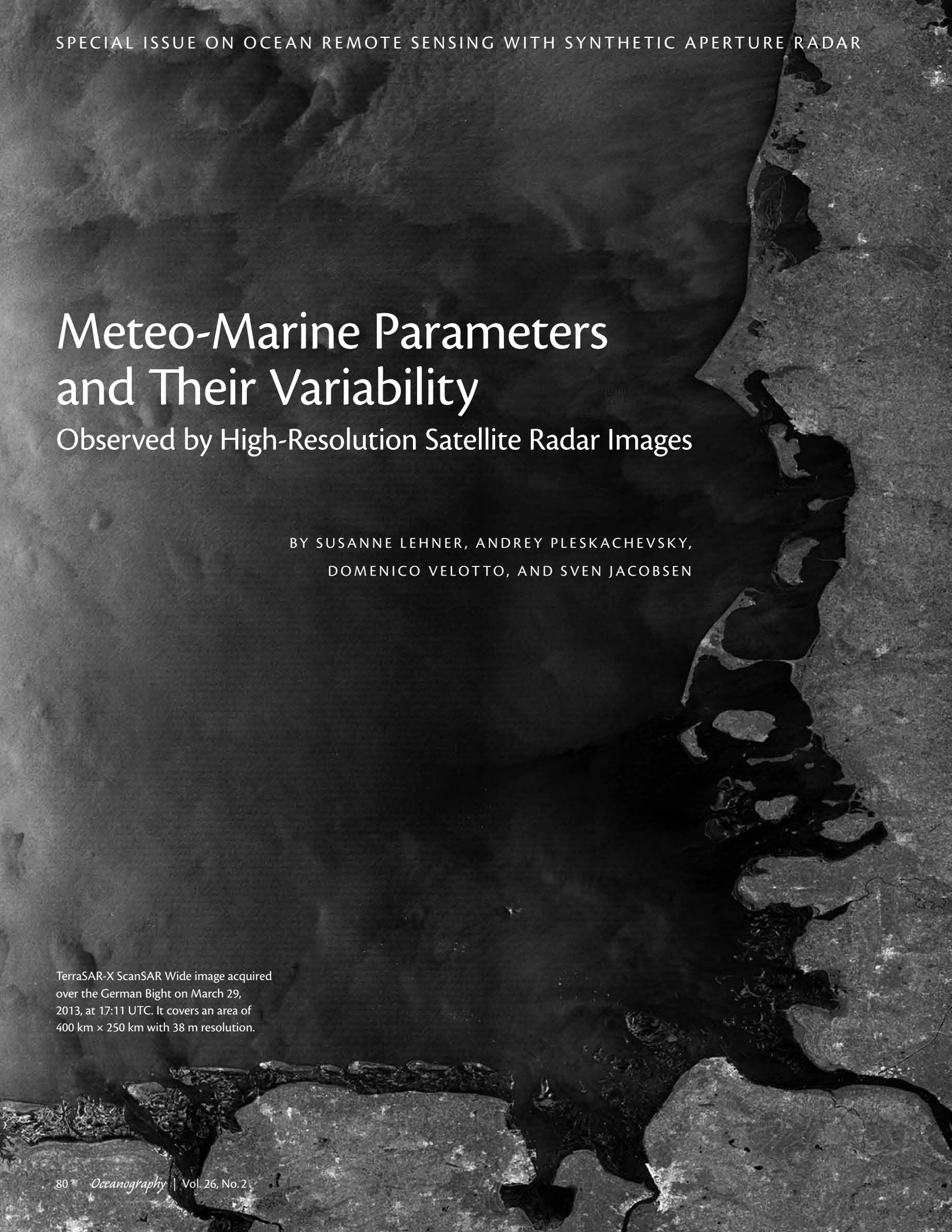

TerraSAR-X ScanSAR Wide image acquired over the German Bight on March 29, 2013, at 17:11 UTC. It covers an area of 400 km × 250 km with 38 m resolution.

ABSTRACT. New radar satellites image the sea surface with resolutions as high as 1 m. A large spectrum of ocean processes can be estimated using such Earth observation data. These data have been applied to investigations of geophysical processes as well as to forecast model validations and near-real-time services. The numerous processes, parameters, and features observed in high-resolution synthetic aperture radar images include winds, waves (with wavelengths as small as 30 m), oil slicks, waterline changes, changes in seabed morphology in shallow waters, wakes and bow waves of ships, underwater topography, wave energy flux along wave tracks from deep water to the coast, and breaking waves. New algorithms have been developed that are capable of taking into account fine-scale effects in coastal areas.

NEW SAR MISSIONS FOR OCEANOGRAPHIC APPLICATIONS

Knowledge of marine and meteorological parameters is important for operational oceanographic services. In situ measurements and global, regional, and fine-resolution forecast models provide information on wind, sea state, and related processes. Spaceborne sensors are especially useful because of their global coverage and their independence from additional input data as compared to in situ methods and mathematical simulations. Remote-sensing data, in particular those acquired from spaceborne synthetic aperture radar (SAR), are an unparalleled source for model validation and verification in the open sea and in coastal zones because these data can also be collected independent of sunlight and cloud coverage.

Spaceborne SAR is a unique sensor that provides two-dimensional information about the ocean surface. The latest-generation of high-resolution SARs is particularly suitable for many ocean and coastal applications. In the last few years, a number of high-resolution X-band radar satellites have been launched, for example, TerraSAR-X, TanDEM-X, and COSMO-SkyMed. Their data provide new perspectives on sea state and related processes in coastal areas, where sea surface variability plays a significant role. A wide range of features and signatures can be observed in these data, including surface winds and gusts, individual waves and their refraction, and effects of breaking waves. Knowledge of such background geophysical processes and an understanding of how they are imaged by SAR are important to successful SAR data processing and use of the results in terms of safety and security issues. Figure 1 shows an example of the effect of improved resolution on imaging coastal features such as breaking waves.

The X-band TerraSAR-X satellite was launched in June 2007 (http://www.dlr.de/TerraSAR-X) and its twin, TanDEM-X, in June 2010. TerraSAR-X and TanDEM-X operate from an altitude of 514 km in sun-synchronous orbits, with ground speeds of 7 km s^{-1} (15 orbits per day). The two satellites orbit in close formation with typical distances between them of 250 to 500 m. They operate with a wavelength of 31 mm and frequency of 9.6 GHz. The repeat cycle is 11 days, but the same region can be imaged with different incidence angles after three days, depending on image latitude. Typical incidence angles range between 20° and 55°. Coverage and resolution depend on satellite mode: stripmap covers 30 km × 50 km with a resolution of about 3 m, while spotlight covers 10 km × 10 km with resolution of about 1 m (Breit et al., 2010).

As is known, targets that are moving to the SAR sensor will not be imaged in their real positions; they are shifted in flight direction. This Doppler effect, also called "train off the rails," plays a special role in the SAR imaging of moving waves. Compared to earlier SAR missions like Envisat Advanced SAR (ASAR), TerraSAR-X offers a number of advantages in addition to its higher resolution. In particular, the Doppler shift of scatterers, moving with velocity u_r toward the sensor (radial velocity) at distance R_o (slant range) is reduced. For example, for the same incidence angle of 22° and u_r = 1 m s^{-1}, the target's displacement in azimuth direction $D_x = (u_r / V_{sar}) \cdot R_o$ (Lyzenga et al., 1985) is ~ 73 m for TerraSAR-X but almost twice as large, ~ 115 m, for Envisat due to different platform velocity V_{sar} and slant range R_o (Envisat altitude was 800 km). Thus, the smoothing of moving wave crests (also called the bunching effect; Alpers and Rufenach, 1979) is noticeably reduced. As a result, imaging of the ocean surface is more stable, and the shortest waves imaged have wavelengths of ~ 25 to 30 m.

Susanne Lehner *(susanne.lehner@dlr.de),* **Andrey Pleskachevsky, Domenico Velotto,** *and* **Sven Jacobsen** *are all on the staff of the German Aerospace Center (DLR), Remote Sensing Technology Institute, Bremen, Germany.*

PROCESSES AND FEATURES OBSERVED IN SAR HIGH-RESOLUTION IMAGES

Knowledge of basic geophysical processes and what remote-sensing mechanism was used to collect the data is necessary for successful processing of images and for use in near-real-time services. The images contain information on wind and on sea state-related processes that must be properly extracted and assessed.

Morphodynamic Developments in Coastal Areas

Changes in seabed morphology in shallow waters can be mapped using SAR images. Wave action in coastal areas, where storms can change the soft seabed relatively rapidly, plays a key role in erosion and transformation of the seabed and the shoreline. For example, in Figure 2, a TerraSAR-X stripmap scene acquired at low tide over Elbe Estuary in the North Sea on November 11, 2008, showing sandbanks that have been partially eroded and split near tidal inlets is compared with smoother bathymetry in the same area processed by BAW (German Federal Waterways Engineering and Research Institute) in 2006. These bathymetry changes can be observed in the SAR image as a result of the way waves propagate and disperse in the estuary, as well as in the flow of local currents.

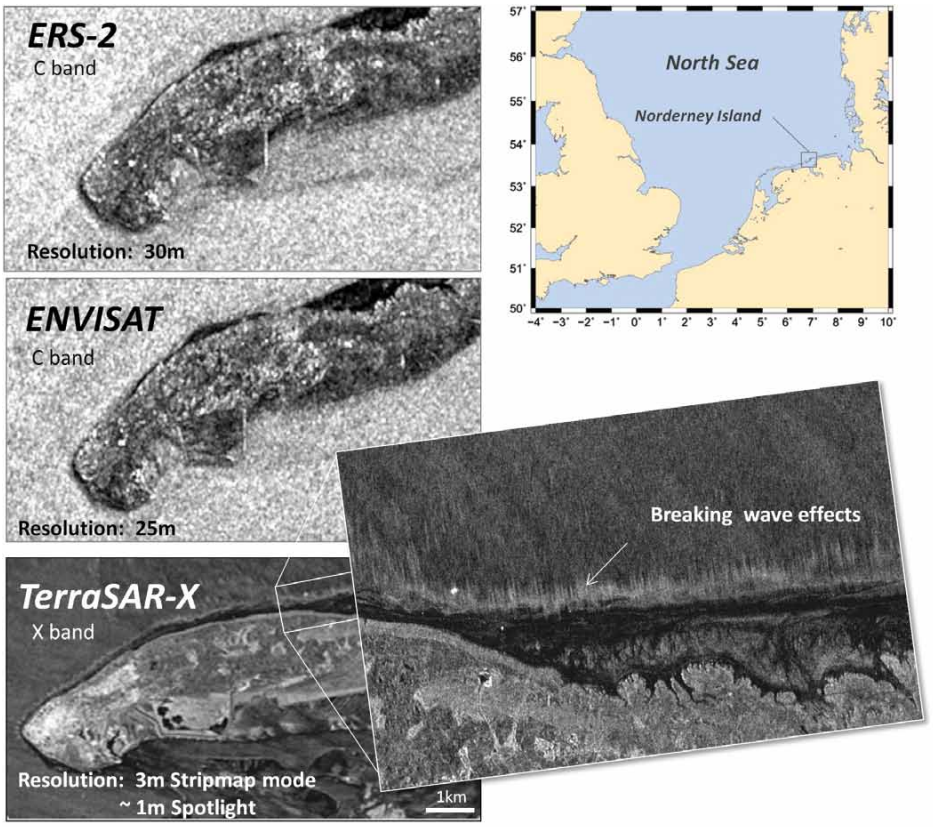

Figure 1. Effect of the improved resolution of the new synthetic aperture radar (SAR) satellites. Details of images from ERS-2 (1995–2011), Envisat ASAR (2002–2012), and TerraSAR-X (launched in 2007) acquired over Norderney Island in the North Sea.

Sea State: Individual Long Wave Refraction and Underwater Topography

In coastal areas, underwater topography influences the refraction of long-period swells at water depths shallower than 70 to 50 m. Ocean surface wave properties change when water depths become less than about half of their wavelength. When a long-period ocean swell propagates toward shore, its wavelength shortens and its wave height increases due to conservation of energy.

The algorithm used to obtain swell wavelength and direction from TerraSAR-X images is based on FFT (Fast Fourier Transform) analysis of subscenes with dimensions of 800 m × 800 m. By computing the FFT for the selected subimage, a two-dimensional image spectrum in wave number space is retrieved. The peak in the two-dimensional spectrum determines peak wavelength and peak wave direction of all waves in the subimage. The retrieved wave directions have an ambiguity of 180° due to the static nature of a SAR image. In coastal areas where wave shoaling and refraction are recognized, propagation direction toward the coast is unambiguous. Starting in the open sea, the box for the FFT is moved along with the wave, and a new FFT is computed. This procedure is repeated until the corners of the FFT box reach the shoreline. In this way, a wave can be tracked from the open sea to the shoreline, and changes in its wavelength and direction can be measured. Wind streaks and ocean wind patterns are removed from the spectra by filtering for analyzed wavelengths between about 50 m and 300 m (background values must be checked for every scene). The

translation of the FFT box to the next point in the swell propagation direction varies in range by ± 15° in order to avoid switching to another wave system in the case of cross seas.

Figure 3 (left) shows a TerraSAR-X spotlight image acquired over Rottenest Island, Australia, on October 20, 2009, with one wave ray. The island is situated ~ 50 km off the coast of Perth, Western Australia (115°30'E, 32°00'S). The long-swell waves induced in the Indian Ocean (storm peak about 1,500 km southwest of the area three days before) and propagating toward the island are visible in the image, and the refraction is well pronounced. This SAR image was special ordered so that long waves could be acquired for bathymetry estimation. The wave forecast by the US National Oceanic and Atmospheric Administration (NOAA) WAVEWATCH III model (http://polar.ncep.noaa.gov/waves) was used to determine the appropriate acquisition time, and it was applied one week before the TerraSAR-X image acquisition. Figure 3 (middle) shows the TerraSAR-X image with 40 wave rays identified. Using 200 wave rays, the wavelength field was obtained for a uniform grid of 150 m resolution. The depths d (Figure 3, right) were derived using the dispersion relation:

$$d(L_p,\omega_p) = \frac{L_p}{2\pi}\,\mathrm{atanh}\,\frac{\omega_p^2 L_p}{2\pi g}, \qquad (1)$$

where g is gravitational acceleration and ω_p is the angular wave peak frequency ($\omega_p = 2\pi/T_p$; T_p is the peak period). The peak period needed in equation 1 is obtained using a combination of first guess and analysis of the tracks (T_p = 13.25 sec). The longest observed wave in the image is L_{max} = 245 m, and a threshold for minimal peak period for this wavelength is obtained from the deepwater relation $T_p min = (2\pi L_{max}/g)^{0.5}$ = 12.25 s.

The estimated underwater topography was compared to sonar measurements on the same grid. About 50% of the compared area had an error range of about ± 10% of the local depth. The obtained bathymetry has an accuracy on the order of 15% for depths of 60 to 20 m. Application of the SAR-based method described here is generally dependent on sea state (swell availability) and data acquisition quality. The latter is influenced

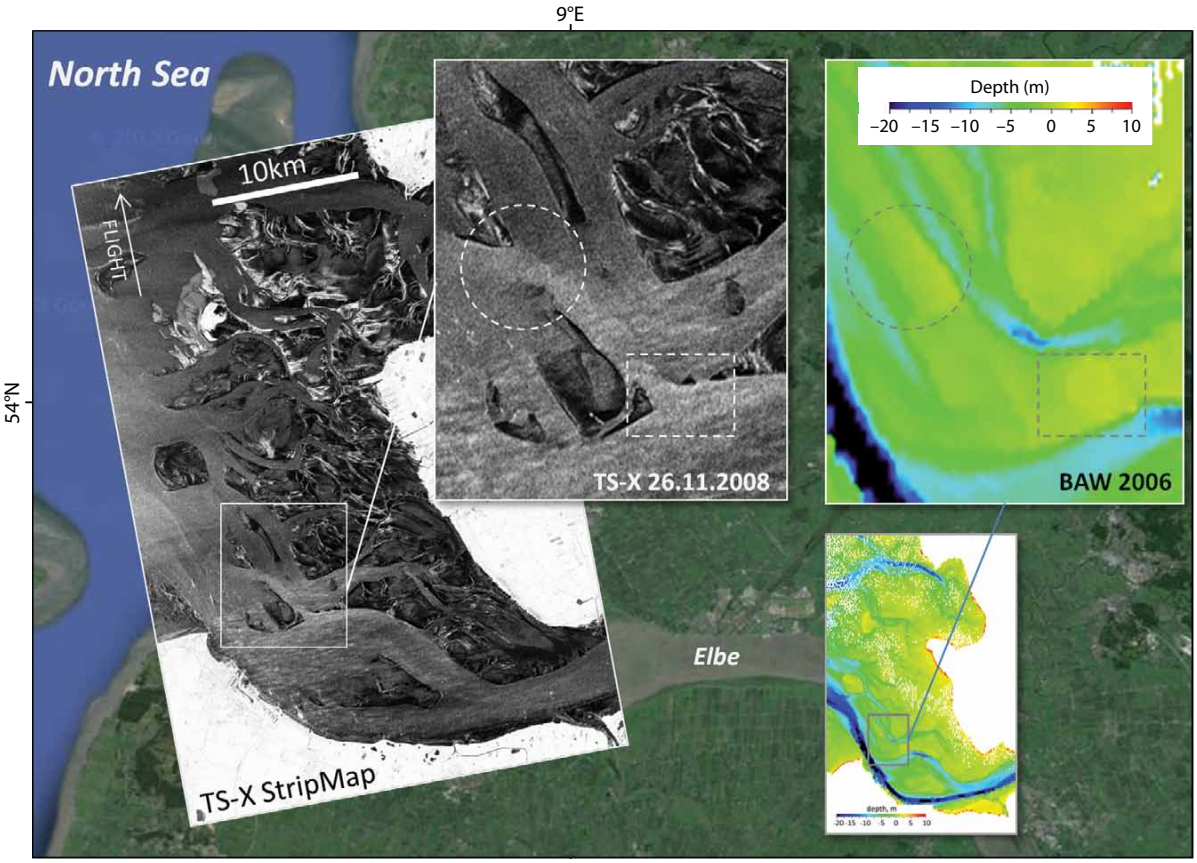

Figure 2. TerraSAR-X stripmap scene (left) with a coverage of 30 km × 50 km and resolution of 3 m, acquired over Elbe Estuary, German Bight, North Sea, on November 26, 2008, 17:10 UTC (low tide). The inset shows the change in Elbe Estuary bathymetry since 2006 when the BAW (German Federal Waterways Engineering and Research Institute) bathymetry map (right) was completed: a long bank was partially eroded and split by inlets (compare areas in dashed circles and squares). *Background image © Google Maps*

by artifacts, nonlinear SAR imaging effects (e.g., availability of local wind sea smearing in the image, breaking waves, ships with wakes), and the complexity of the topography itself (e.g., reef belts can destroy swell waves long before they reach the coast being investigated; Pleskachevsky et al., 2011). The method was successfully tested for different areas and sea states—the Duck Research Pier (North Carolina, USA, range traveling waves), Port Phillip (Melbourne, Australia, azimuth traveling waves), and around Helgoland Island (German Bight, North Sea) (Brusch et al., 2011).

To complete the bathymetric maps, QuickBird optical satellite data were used to map extreme shallow waters (< 10 m depth) near the coast. The algorithms for bathymetry estimation from optical and SAR data were combined and integrated in order to cover different depth domains. The two techniques make use of different physical phenomena and mathematical treatments. Optical methods are based on sunlight reflection analysis and provide depths up to 20 m in calm weather conditions. Depth estimation from SAR is based on the observation of long waves and covers water depths between 70 m and 10 m. Water depths from 20 m to 10 m are where synergy of data from both sources arises. This new technique provides a platform for coastal bathymetric mapping over a broad area on a scale that is relevant to marine planners, managers, and the offshore industry.

In addition to depth estimation, the SAR-based methodology allows detection of shoals such as underwater mountains, reefs, and sand bars with depths < 30 m, even if the quality of sea state information is insufficient for accurately obtaining bathymetry. The remotely sensed information on shoals (e.g., reefs) can be integrated into maritime ship safety and warning systems.

Surface Wind and Integrated Sea State Parameters

Synthetic aperture radar can provide wind information over the ocean by measuring sea surface roughness. A new algorithm XMOD-2 has been developed for TerraSAR-X data that takes the full nonlinear physical model function into account. At the same time, the corresponding sea state parameters can be estimated from the same image. A new empirical model function XWAVE-2 for obtaining significant wave height has been developed for X-band data. The algorithm is based on analysis of image spectra and uses parameters fitted with co-located buoy data and information

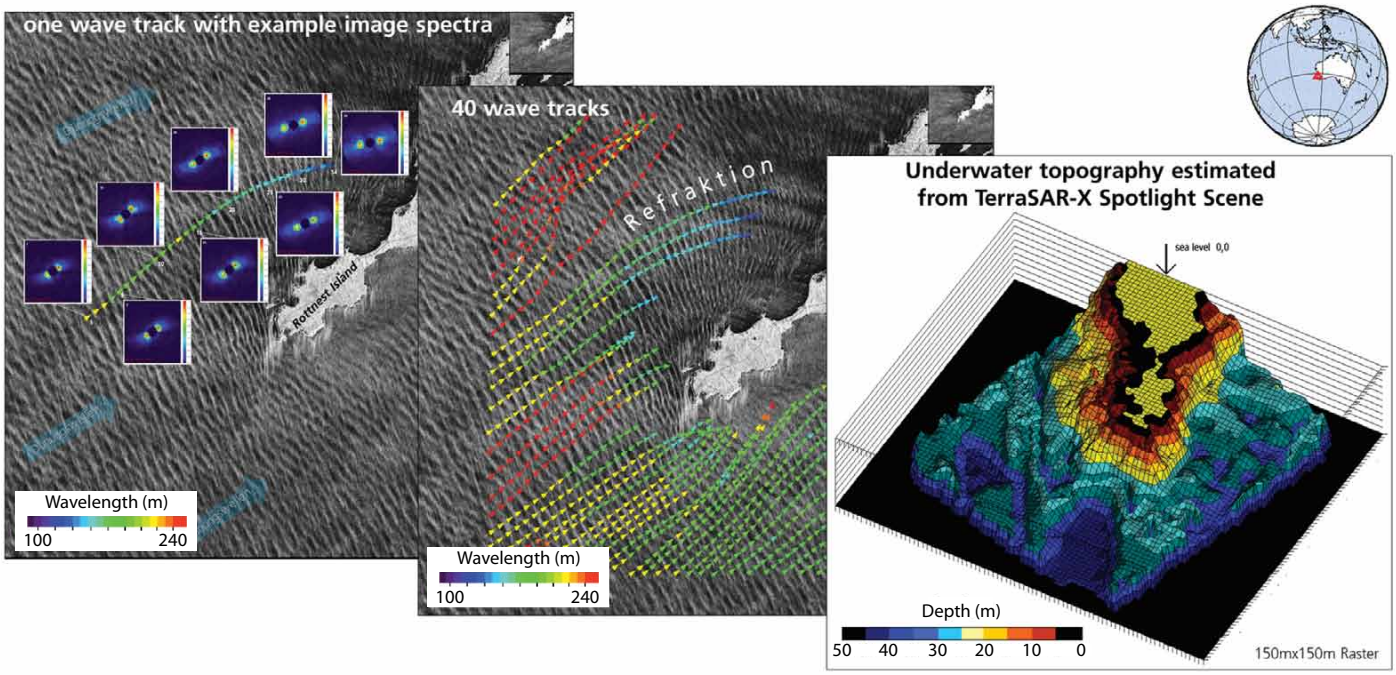

Figure 3. TerraSAR-X spotlight image (left) with dimensions of 10 km × 10 km and resolution of 1 m acquired over Rottenest Island, Australia, on October 20, 2009. (left) Normalized radar cross section (NRCS) and one wave track with example image spectra. (center) Forty wave rays (colored lines) tracked on the image. (right) Bathymetry (uniform raster, 150 m resolution) estimated from the TerraSAR-X image data. To complete the bathymetric maps in the shallowest areas (< 10 m water depth) near the coastline, optical data from the QuickBird satellite were used.

on spectra peak direction and incidence angle. The newly developed empirical algorithm estimates significant wave height H_s directly from TerraSAR-X image spectra without using a priori information and without temporal transferring into wave spectra.

Wind Estimation Algorithm XWAVE-2

The SAR wind field retrieval approach was first developed for C-band SAR provided by, for example, ERS-2 and Envisat ASAR. These approaches used empirically derived Geophysical Model Functions (GMF) that related local wind conditions and sensor geometry to radar cross-section values (e.g., CMOD4 or CMOD5). To utilize the new SAR systems, an X-band linear algorithm XMOD-1 and later a nonlinear XMOD-2 were established for VV- and HH-polarized data to obtain wind fields (Ren et al., 2012; Li and Lehner, in press). The relationship between X-band radar cross section and wind speed, wind direction, and incidence angle in XMOD-2 is given by:

$$\sigma_o(U,\theta,\varphi) = B_0^p(U_{10},\theta)(1 + B_1(U_{10},\theta)\cos(\varphi) + B_2(U_{10},\theta)\cos(2\varphi)), \quad (2)$$

where σ_o is the normalized radar cross section (NRCS), U is the wind speed, and φ is the relative wind direction. This is applicable for an incidence angle θ between 20° and 60° and wind speeds from 2 m s^{-1} to 25 m s^{-1}. The parameters B_i i = 0,2 are tuned using the measurement data sets. To determine wind direction, streak structures on the sea surface of the image are used. These are produced by airflow turbulent eddies at the boundary layer (Etling and Brown, 1993; Sikora and Ufermann, 2000). Shadows behind the coast also provide evidence of wind blowing from the coast.

Data from the Spaceborne Imaging Radar-C/X (SIR-C/X) mission in 1994 and from the European Center for Medium-Range Weather Forecasts (ECMWF) reanalyzed wind fields ERA-40 (*E*CMWF *Re-A*nalysis of the global atmosphere and surface conditions for 45 years) were used to tune the algorithm. The results were validated using in situ measurements from co-located buoys and modeled data with different resolution (HIRLAM model and DWD COSMO). The wind field can be retrieved practically to 20 m resolution by the XMOD algorithm for TerraSAR-X images. In contrast to the previously developed XMOD-1, XMOD-2 consists of a set of nonlinear GMFs and thus depicts the difference between upwind and downwind of the sea surface backscatter in X-band SAR imagery. By exploiting 371 co-locations with in situ buoy measurements that are used as the tuning data set, together with analysis wind model results, the retrieved TerraSAR-X / TanDEM-X sea surface wind speed using XMOD-2 shows close agreement with buoy measurements with a bias of –0.32 m s^{-1}, a root mean square error (RMSE) of 1.44 m s^{-1}, and a scatter index (SI) of 16.0%. Further validation using an independent data set of 52 cases shows a bias of –0.17 m s^{-1}, an RMSE of 1.48 m s^{-1}, and an SI of 17.0% compared to buoy measurements (Li and Lehner, in press).

XWAVE-2 Empirical Algorithm to Derive Sea State Parameters

An empirical X-WAVE-1 model for obtaining integrated wave parameters has been developed for X-band data (Bruck et al., 2011). The algorithm was based on analysis of image spectra and uses parameters fitted with co-located buoy data and information on spectra peak direction and incidence angle. The equation for the newly developed XWAVE-2 algorithm for deriving significant wave height directly from TerraSAR-X SAR image spectra is

$$H_s = a_1 \cdot \sqrt{(E \cdot sin\theta)(1.0 + a_2\cos(\alpha))} + a_3, \quad (3)$$

where α is the wave peak direction related to the azimuth direction ($0° \le \alpha \le 90°$). The cosine function in the formula describes the dependence of wave peak direction in the image relative to satellite flight direction, and E is the integrated value of the directional wave number spectrum. Parameters a_1, a_2, and a_3 are the coefficients tuned to various data sets and are dependent on incidence angle θ. They are determined from a fit between E and the co-located significant wave height, computed by the DWD wave model, co-located buoy measurements, WaMoS-II (Wave Monitoring System), and radar altimeter data (Bruck and Lehner, 2010; Pontes et al., 2010). The peak period T_p corresponds to the wave period with maximum energy in the two-dimensional spectrum in the frequency domain. E is the integrated value of the image spectrum obtained by standard Fourier analysis done on a subscene of a radiometrically calibrated TerraSAR-X intensity image. The integration domain chosen is limited by minimal and maximal wavelength in order to avoid the effects of wind streaks in the turbulent boundary layer and the cut-off effect of SAR imaging of short sea surface waves. The values are set to L_{min} = 30 m and L_{max} = 600 m,

which corresponds to k_{max} = 0.2 and k_{min} = 0.01 in deep water.

Comparison of TerraSAR-X derived H_s with the significant wave height obtained by the buoy located at the Ekofisk oil platform in the North Sea (56°10'03"N, 3°32'32"E) shows a correlation of 0.83. TerraSAR-X derived peak wave length for National Data Buoy Center (NDBC) buoy 44066 (39°34'59"N, 72°36'2"W) and from the buoy located near the Ekofisk oil platform have a correlation of 0.95, an SI of 0.19 m, and an RMSE of 0.89 m, thus showing good agreement with in situ data. Comparison with NDBC buoys results in SI = 13% for peak wavelength measurement and SI = 21% for significant wave height.

Figure 4 shows wind and significant wave height fields estimated from a TerraSAR-X stripmap scene acquired over the Bay of Kiel in the Baltic Sea on December 10, 2012, and scatterplots for both algorithms. The number of entries is 371 for XMOD and 200 for XWAVE algorithms.

Remote-Sensing Data for Coastal Numerical Modeling

One area where spaceborne SAR systems have a significant impact is in the validation of wave forecast models. The forecast modeling services, for example, of the German Weather Service (DWD; http://www.dwd.de) are part of the global marine weather and warning system that provides wave forecasting in transocean shipping routes, storm prediction, and wave- and wind-related information for coastal protection and sport boats, all of which are important services for public safety. Third-generation wave models are now used for sea state prediction, including WAVEWATCH III used by NOAA and UKMET (United Kingdom Meteorological Office) and the WAM model used by European forecast services such as ECMWF, DWD, and the Danish Meteorological Institute (DMI, http://www.dmi.dk). The forecasts are also accessible to public users through Meteo France (MF, http://marine.meteofrance.com/marine).

In the open sea, these wave models are already capable of producing high-quality forecasts, as long as the wind

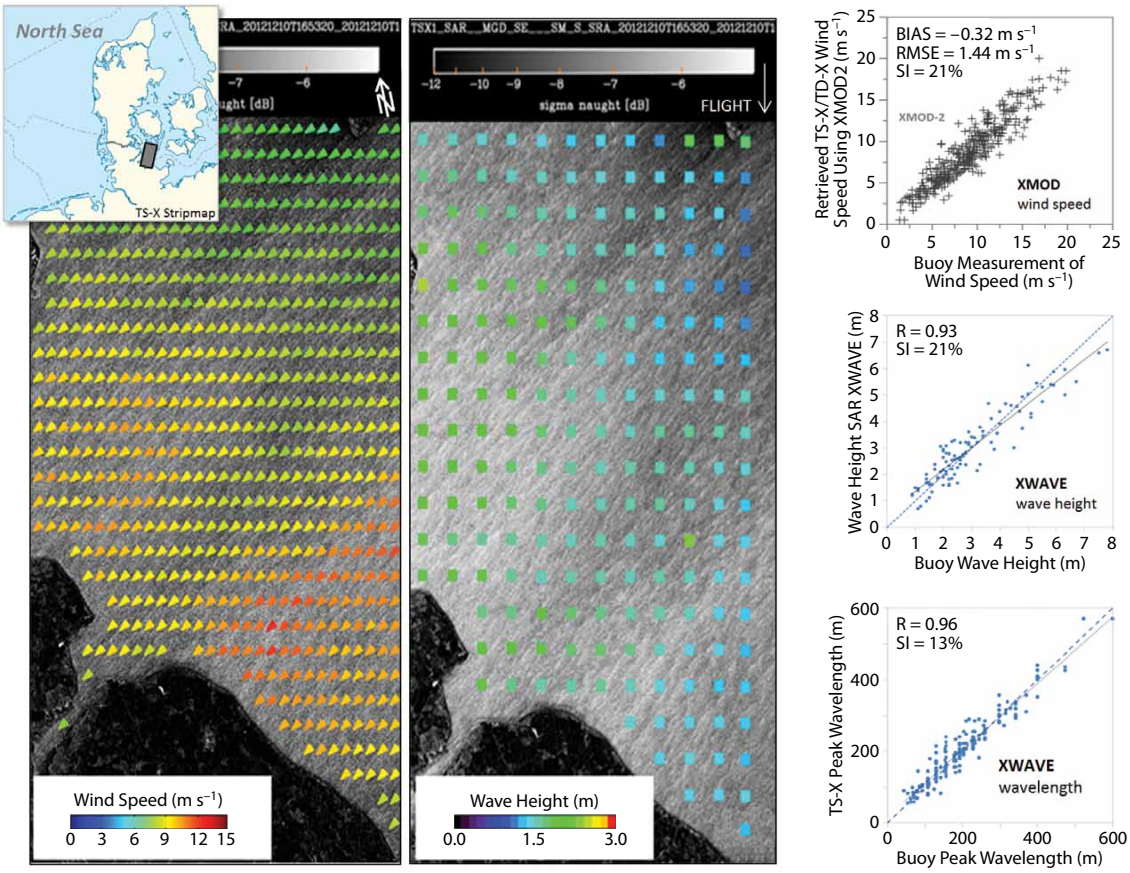

Figure 4. TerraSAR-X stripmap acquired over Kiel Bight in the Baltic Sea on December 10, 2012, at 16:53 UTC, and wind field derived using nonlinear XMOD-2 algorithms (left), significant wave height field derived using XWAVE-2 empirical algorithm (middle), and scatterplots for both algorithms (right). The number of entries is 371 for XMOD and 200 for XWAVE.

input from atmospheric forecast models and boundary conditions for sea state are correct. Uncertainties occur when dealing with numerical modeling and forecasting in coastal areas where physical processes in shallow water, caused by interactions among waves, currents, and the seafloor, become important. Wave properties can change greatly in coastal areas. Significant effort is required to include shallow water interactions in numerical schemes by coupling wave and circulation models through radiation stress and by tuning of the model functions and parameters for coastal processes like dissipation and wave breaking. Such coupled model forecast systems have been developed by several organizations (e.g., DWD, Deltares, Helmholtz-Zentrum Geesthacht [GHZ]), and SAR data from high-resolution TerraSAR-X images have been particularly useful for validating these models.

In the course of an experimental investigation (Lehner et al., 2012), wind and sea state information retrieved from SAR were applied as input to a wave numerical spectral model (wind forcing and boundary condition) running at fine spatial horizontal resolution of 100 m. As boundary conditions, the wave spectra included swell obtained from the XWAVE algorithm and wind sea from JONSWAP spectra based on wind information derived using the XMOD algorithm from the same TerraSAR-X image. Results were compared to co-located buoy measurements. Sensitivity tests for the German Bight in the North Sea (area around Helgoland Island and Hörnum Bight in the North Sea) were carried out for varying local wind speeds (with wind shadowing and gusts visible in TerraSAR-X images but not present in coarser wind data). The results showed sensitivity of local waves to wind variation and the importance of local wind effects on wave behavior. The varying retrieved TerraSAR-X wind speeds (increased and decreased by 3 m s^{-1} in Hörnum Bight) result in a large deviation of about ± 25% of modeled local wave height (Figure 5). Changing sea state properties strongly influence wave coupled processes: turbulent mixing in the water column and processes

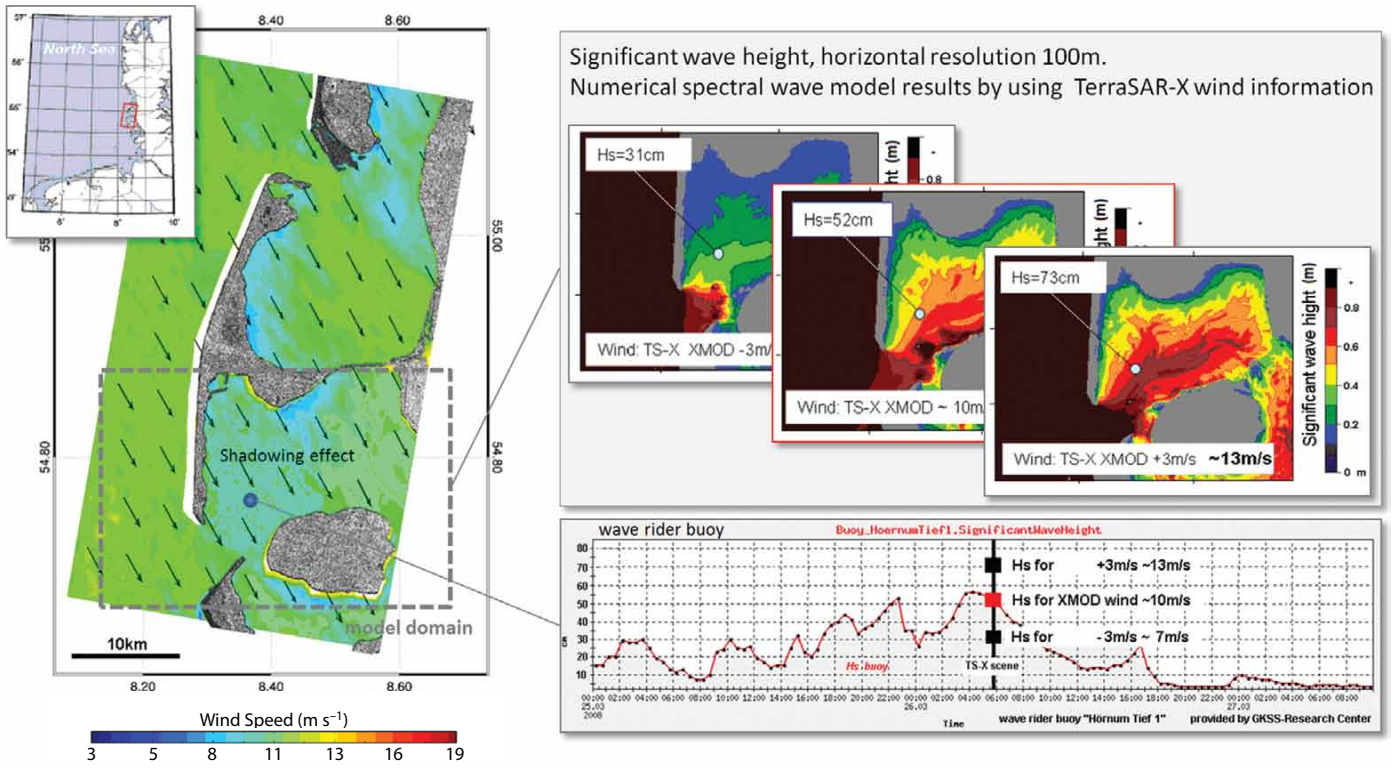

Figure 5. (left) Wind field retrieved using XMOD algorithm from a TerraSAR-X stripmap scene acquired over Sylt Island, North Sea, on March 26, 2008 (wind speed errors due to insufficient information are masked in white). (right) Sensitivity tests: wave height simulated by a numerical model on 100 m resolution mesh using TerraSAR-X derived wind speed (~ 10 m s^{-1}) at buoy position 54°46'2"N, 8°22'8"E corresponds well with buoy measurements (bottom right, in red). Varying the wind speed (increased and decreased at 3 m s^{-1}) results in strong deviations of about ~ 25% of wave height.

at the water-seabed boundary layer change significantly in shallow areas of the Wadden Sea.

Wave Breaking

Another process observed in TerraSAR-X imagery is wave breaking. Knowledge about the spatial distribution of wave heights along the shoreline, especially during storms, is an important issue and crucial for coastal protection. Furthermore, the predominant wave heights in the surf zone can prevent pirates from landing their boats along certain sections of the shore. Thus, information on surf height is of interest for protecting shipping lanes, preventing future attacks by pirates, and for coordinating international anti-piracy forces.

As a wave shoals, its height increases, leading to greater orbital velocity of water particles within the wave. Shoaling occurs until the wave's steepness exceeds a certain threshold, and it breaks. This occurs when orbital velocities in the wave exceed the wave's phase speed. When a wave breaks, water particles and bubbles fly into the air, and the water surface becomes very rough due to intense turbulence. All of this creates a strong echo in the radar signal. Smearing of the scatterers by Doppler shift due to high velocities results in streak-like structures at wave-breaking locations (Wackerman and Clemente-Colón, 2000). These signatures were investigated and their lengths used to estimate the radial speed of the scatterers, providing information about the propagation speed at the crest of the breaking wave and its possible amplitude before breaking (Brusch et al., 2011). Figure 6 shows a TerraSAR-X stripmap image acquired on November 21, 2008, at 17:00 UTC with incidence angle $\theta = 31°$. The white box at upper left highlights a small island located near Trischen Island in Elbe Estuary, and estimated mean breaking wave height adjacent to the island is indicated in red at bottom right.

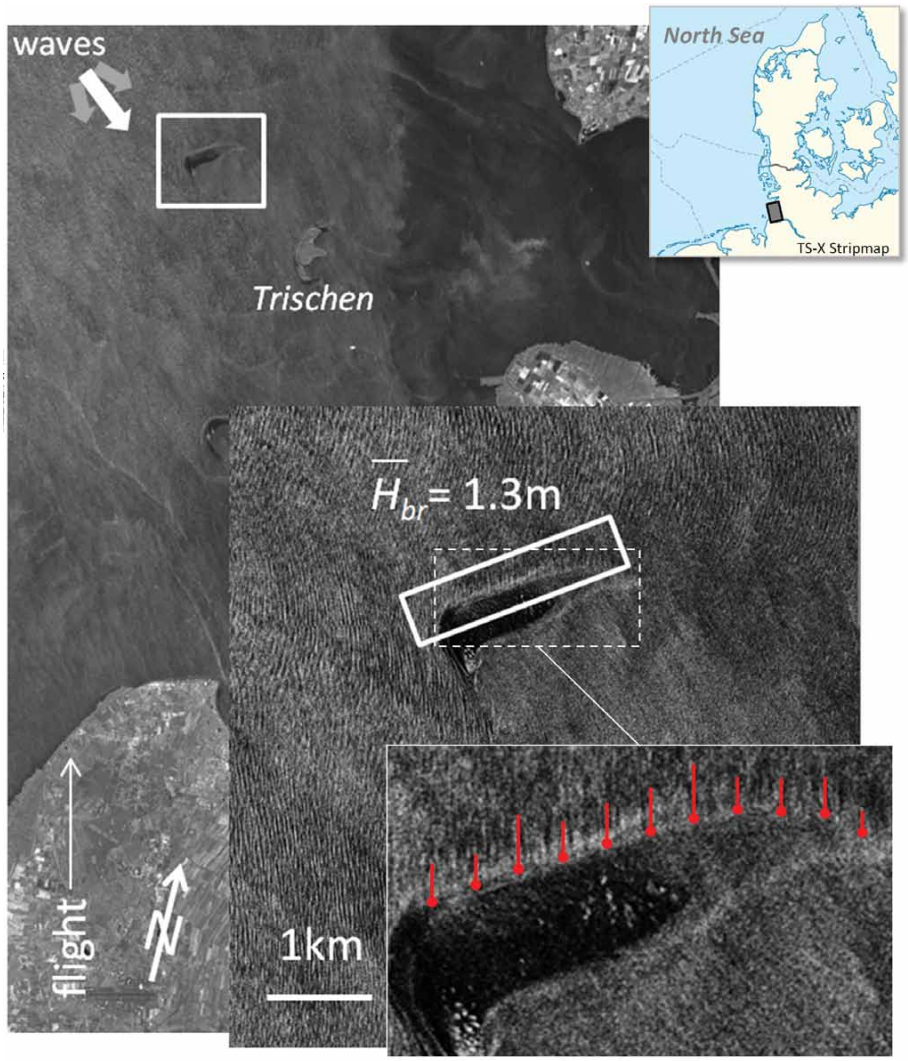

Figure 6. TerraSAR-X stripmap image acquired on November 21, 2008, at 17:00 UTC with $\theta = 31°$. The white box at top left surrounds an island located near Trischen Island in Elbe Estuary. Breaking-wave signatures adjacent to the island are shown in red (bottom right). Estimated mean breaking wave height is $\bar{H}_{br}$ = 1.3 m (1.6 m for spilling breaking and 0.9 m for plunging breaking). The forecast significant wave height outside the bight is H_s = 2.4 m (DWD [German Weather Service] Global Spectral Model with 0.75° resolution) and 1.8 m using a nested model with 1 nm (1.8 km) resolution near the island.

Wave Groups

Detection of wave groups in the ocean using TerraSAR-X data is among the first direct observations of such phenomena at high resolution. Wave groups were studied using data from earlier SAR missions by applying, for example, wavelet techniques (Niedermeier et al., 2005). Due to improved TerraSAR-X and TanDEM-X SAR properties, wave group parameters can be estimated directly using the XWAVE empirical algorithm.

Figure 7 shows an example of wave

groups observed near the Somalia coast. In the stripmap image acquired on November 18, 2010, at 14:56 UTC, the cross seas effect of two wave systems with about 1.8 m significant wave height is observed. Three wave groups are clearly visible; the wave height inside the groups is about 3 m. The origin of the wave groups in this location can be explained in different ways. The first possibility is local shoaling by underwater obstacles. According to the NOAA ETOPO 1-minute global relief, the local depth is about 2,000 m. This means that, in this case, local shoaling should be excluded from consideration. However, it is possible that a local flat-topped mountain exists there but was not imaged by NOAA's coarse data. The second possibility is the impact of local organized wind gusts. Moving convective cells in the atmosphere can produce a localized organized wind gust traveling with a speed close that of the swell system. Strong wind energy that feeds the same wave group for a longer time period can cause enormous growth of individual wave heights within the group (Rosenthal et al., 2011). The third explanation is a combination of phases of both wave systems, traveling with about a 50° phase difference from each other.

North Sea investigations show that abnormal height in wave groups is related to atmospheric effects. Pleskachevsky et al. (2012) found that such abnormal heights are caused by mesoscale wind gusts induced by open atmospheric cells that occur during cold air outbreaks and move across the sea as an organized system, "dragging" the growing waves. These results show local significant wave height increase on the order of meters within the cell, especially in a narrow area of about 2.5 km at the footprint center of a cell. A group of cells under real storm conditions produces a local increase in significant wave height of more than 6 m during a short time window of 10 to 20 minutes (passing the cell). Wave groups, including extreme individual waves with wavelengths of more than 370 m beneath the cell's footprint, are estimated. This corresponds well with measurements of a rogue wave group with wavelengths of about 400 m recorded during the 2006 storm "Britta" that damaged the deck of research platform FiNO-1 located 18 m above mean sea level.

Ship Detection and Oil Spills

Scanning the ocean surface using remote-sensing instruments like SAR provides an opportunity not only to observe surrounding environmental processes but also to detect and monitor ships and turbulent ship wakes and waves (Lehner et al., 2013). With day and night coverage, weather independency, and global coverage, radar sensors onboard TerraSAR-X and its twin TanDEM-X are suitable for practical support of ship security and safety (Lehner et al., in press). Ship position, length, and speed can be identified, compared to Automatic Identification System

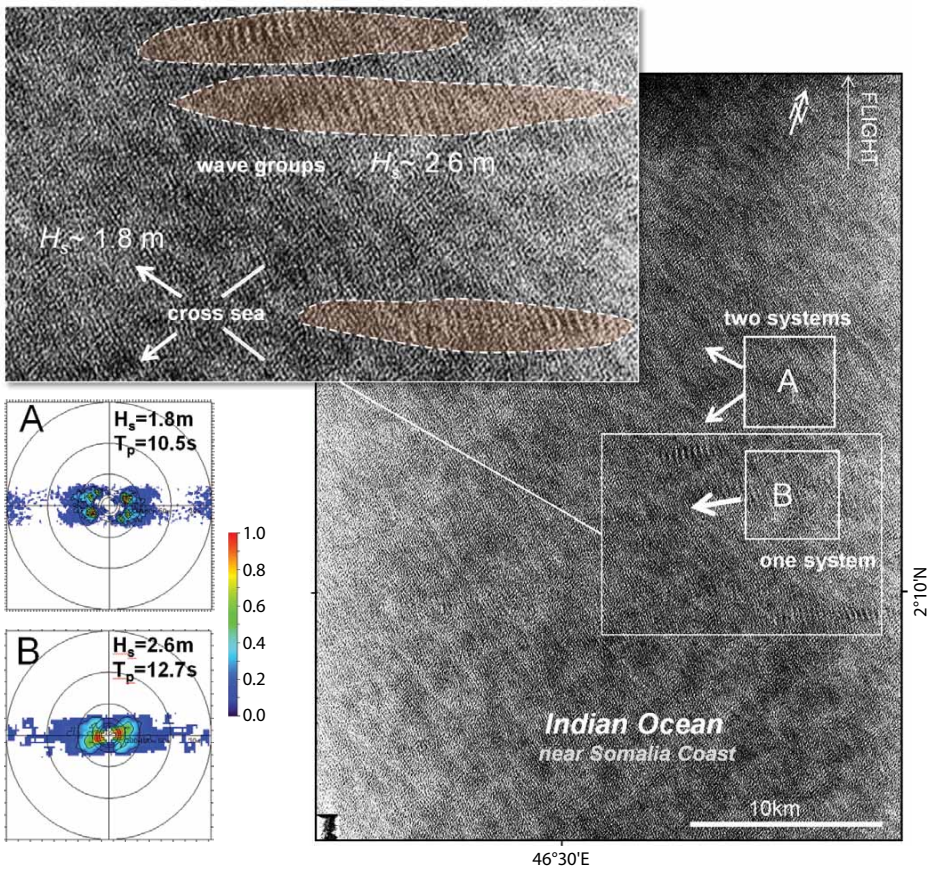

Figure 7. TerraSAR-X VV-polarized image acquired on November 18, 2010, at 14:56 UTC near the Somalia coast. For subscenes A (two-wave system observed) and B (a wave group), the spectra and estimated parameters are shown. According to National Oceanic and Atmospheric Administration 1 nm (1.8 km) bathymetry, the local depth is ~ 2,000 m.

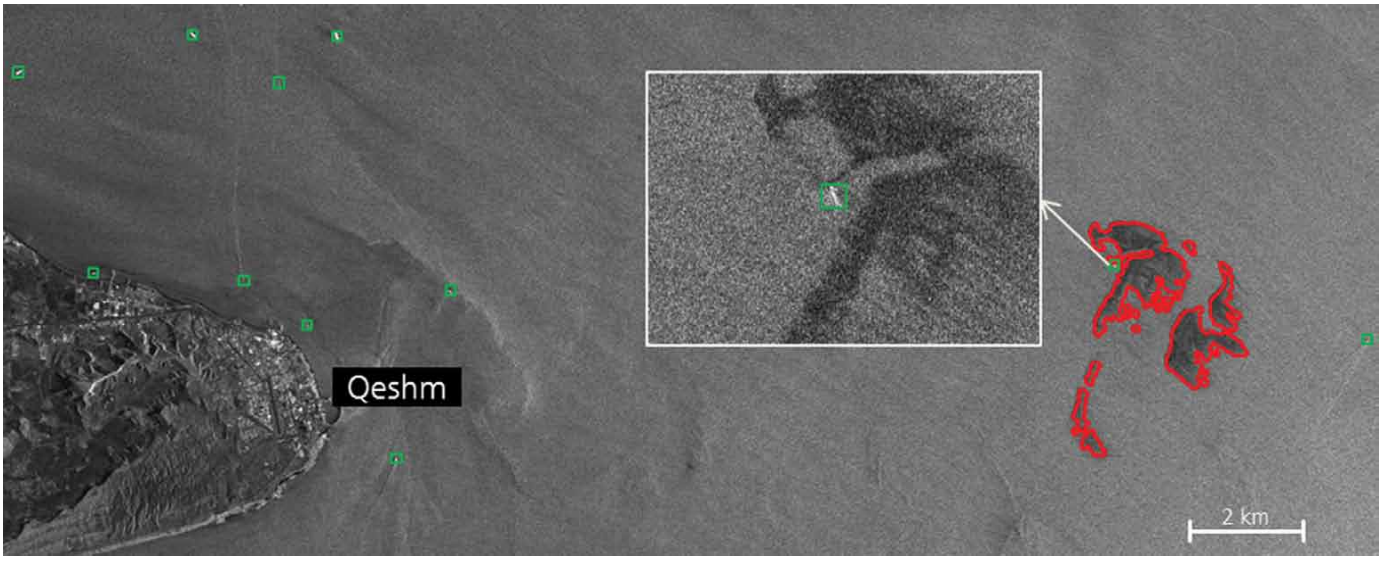

Figure 8. TerraSAR-X image acquired over the Strait of Hormuz, Iran, on July 24, 2009, at 02:22 UTC in stripmap mode, HH-polarization. This is a portion of the full image collected off the coast of Bandar Abbas, near Qeshm Island. Green rectangles show the results of ship detection using SAINT (© DLR), and the red outline was made using an oil spill detection algorithm. The white box is an enlargement of the polluted area showing the detected ship that was probably washing its tanks.

messages, and provided to integrated services. Instances of oil discharge from ships and platforms can also be detected (Velotto et al., 2011) and reported in near-real time. In addition to ship detection, surrounding marine and meteorological parameters can be estimated for operational oceanographic services (e.g., Schwarz et al., 2010).

The presence of surface slicks over the ocean surface attenuates short gravity-capillary waves. These waves, as well as long ocean waves, are the main sources of radar backscatter received by active microwave sensors. Reduction of the radar echo measured over a slick-covered area can be observed visually in an 8-bit scaled SAR image as a dark patch. However, detection of dark patches in SAR images of the ocean surface is only a preliminary step in the SAR oil spill detection algorithm; a detected dark region may not always be related to the presence of an oil spill because other oceanographic phenomena—such as low wind areas, ship wakes, biogenic and natural slicks—have similar signatures (see Caruso et al., 2013, in this issue). Therefore, a classification procedure, based on probabilistic methods (i.e., Bayes classifier), machine learning techniques (i.e., Neural Network, Support Vector Machine), or a physical approach (either using amplitude image or polarimetric SAR data), is needed.

In addition, ships and man-made metallic objects present in the ocean environment (e.g., wind farms, platforms) call for all the three physical scattering models: (1) single-bounce returns caused by direct backscattering from surfaces perpendicular to the radar beam, (2) double-bounce returns due to the dihedral formed by a ship's vertical conducting plates and the sea surface, and (3) multiple-bounce returns caused by a ship's structural elements (e.g., deck and cables). Therefore, ships cause coherent scattering (i.e., measured NRCS by SAR) greater than that from the surrounding sea surface. Figure 8 shows an example of combined oil and ship detection results obtained using high-resolution SAR data.

OUTLOOK

New high-resolution Earth observation data from SAR satellites allow estimation of ocean wave parameters and wind with high spatial resolution and quality. The SAR data can be used to validate spectral numerical wave models and to show and explain the interaction mechanisms among wind, waves, and seafloor. Analysis of TerraSAR-X images shows that it is possible to detect individual waves with wavelengths up to 30 m, their refraction, and wave shoaling. Underwater structures, such as banks, bars, and reefs, can be detected by long wave refraction. Wave energy flux can be estimated for purposes of protecting coastal equipment using SAR information. It is now possible to explore and obtain

underwater topography worldwide by remote-sensing data and by merging optical and SAR data. Although Envisat ASAR has not been available since 2012, its tasks will soon be assumed by a new mode of the TerraSAR-X satellite. The first page of this article shows the new ScanSAR Wide mode that covers an area 400 km × 250 km with 38 m resolution (standard ScanSAR covers about 100 km in the direction of flight with 18 m resolution). Although the image resolution is considerably lower than Envisat ASAR, the broad spatial coverage allows observation of processes such as tidal waves, atmospheric fronts, and wind gusts.

ACKNOWLEDGEMENTS

This study is supported by DLR Space Agency.

REFERENCES

Alpers, W.R., and C.L. Rufenach. 1979. The effect of orbital motions on synthetic aperture radar imagery of ocean waves. *IEEE Transactions on Antennas and Propagation* 27:685–690, http://dx.doi.org/10.1109/TAP.1979.1142163.

Breit, H., T. Fritz, U. Balss, M. Lachaise, A. Niedermeier, and M. Vonavka. 2010. TerraSAR-X SAR processing and products. *IEEE Transactions On Geoscience and Remote Sensing* 48:727–740, http://dx.doi.org/10.1109/TGRS.2009.2035497.

Bruck, M., M.T. Pontes, E. Azevedo, and S. Lehner. 2011. Study of sea-state variability and wave groupiness using TerraSAR-X synthetic aperture radar data. Pp. 1–7 in *Proceedings of the 9th EWTEC 2011*, 5–9 September 2011, Southampton, UK.

Bruck, M., and S. Lehner. 2010. Extraction of wave field from TerraSAR-X data. Paper presented at SEASAR 2010, Advances in SAR Oceanography from ENVISAT, ERS and ESA Third Party Missions, ESA ESRIN, Frascati/Rome, Italy, January 25–29, 2010.

Brusch, S., P. Held, S. Lehner, W. Rosenthal, and A. Pleskachevsky. 2011. Underwater bottom-topography in coastal areas from TerraSAR-X data. *International Journal of Remote Sensing* 32:4,527–4,543, http://dx.doi.org/10.1080/01431161.2010.489063.

Caruso, M.J., M. Migliaccio, J.T. Hargrove, O. Garcia-Pineda, and H.C. Graber. 2013. Oil spills and slicks imaged by synthetic aperture radar. *Oceanography* 26(2):112–123, http://dx.doi.org/10.5670/oceanog.2013.34.

Etling, D., and R.A. Brown. 1993. Roll vortices in the planetary boundary layer: A review. *Boundary-Layer Meteorology* 65:215–248, http://dx.doi.org/10.1007/BF00705527.

Lehner, S., A. Pleskachevsky, and M. Bruck. 2012. High resolution satellite measurements of coastal wind field and sea state. *International Journal of Remote Sensing* 33:7,337–7,360, http://dx.doi.org/10.1080/01431161.2012.685975.

Lehner, S., S. Brusch, and A. Pleskachevsky. 2013. Schiffsdetektion und Beobachtung des Kielwassers in hochaufgelösten TerraSAR-X Satellitenbildern und Sonarmessungen. Paper presented at a workshop held at the Maritime Technologie und Forschung, Forschungsbereich für Wasserschall und Geophysik (FWG).

Lehner, S., A. Pleskachevsky, S. Brusch, M. Bruck, M. Soccorsi, and D. Velotto. In press. Remote sensing of African waters using the high resolution TerraSAR-X satellite. In *Remote Sensing of the African Seas*. V. Barale and M. Gade, eds, Springer.

Li, X.-M., and S. Lehner. In press. Algorithm for sea surface wind retrieval from TerraSAR-X and TanDEM-X data. *IEEE Transactions on Geoscience and Remote Sensing*, http://dx.doi.org/10.1109/TGRS.2013.2267780.

Lyzenga, D.R., R.A. Shuchman, and J.D. Lyden. 1985. SAR imaging of waves in water and ice: Evidence for velocity bunching. *Journal of Geophysical Research* 90:1,031–1,036, http://dx.doi.org/10.1029/JC090iC01p01031.

Niedermeier, A., J.C. Nieto Borge, and S. Lehner. 2005. A wavelet-based algorithm to estimate ocean wave group parameters from radar images. *IEEE Transactions on Geoscience and Remote Sensing* 43:327–336, http://dx.doi.org/10.1109/TGRS.2004.836873.

Pontes, M., M. Bruck, S. Lehner, and A. Kabuth. 2010. Using satellite spectral wave data for wave energy resource characterization. Paper presented at the 3rd International Conference and Exhibition on Ocean Energy, October 6, 2010, Bilbao, Spain.

Pleskachevsky, A., S. Lehner, T. Heege, and C. Mott. 2011. Synergy and fusion of optical and synthetic aperture radar satellite data for underwater topography estimation in coastal areas. *Ocean Dynamics* 61:2,099–2,120, http://dx.doi.org/10.1007/s10236-011-0460-1.

Pleskachevsky, A., S. Lehner, and W. Rosenthal. 2012. Storm observations by remote sensing and influences of gustiness on ocean waves and on generation of rogue waves. *Ocean Dynamics* 62:1,335–1,351, http://dx.doi.org/10.1007/s10236-012-0567-z.

Ren, Y.-Z., S. Lehner, S. Brusch, X. Li, and M. He. 2012. An algorithm for the retrieval of sea surface wind fields using X-band TerraSAR-X data. *International Journal of Remote Sensing* 33:7,310–7,336, http://dx.doi.org/10.1080/01431161.2012.685977.

Rosenthal, W., A.L. Pleskachevsky, S. Lehner, and S. Brusch. 2011. Observation and modeling of high individual ocean waves and wave groups caused by a variable wind field. *Proceedings of the 12th International Workshop on Wave Hindcasting and Forecasting*, October 30–November 4, 2011, Kohala Coast, Big Island, Hawaii. Available online at: http://jcomm.info/images/stories/2011/12thWaves/Papers/2011_workshop-wavehind-and-forecasting__rosenthal_pleskachevsky_lehner_brusch.pdf (accessed September 20, 2013).

Schwarz, E., S. Lehner, and S. Brusch. 2010. Ship detection service. Pp. 115–118 in *Proceedings of the Geoforum MV 2010 Vernetzte Geodaten: Vom Sensor zum WEB*, April 26–27, 2010, Rostock-Warnemünde.

Sikora, T., and S. Ufermann. 2000. Marine atmospheric boundary layer. Cellular convection and longitudinal roll vortices. Pp. 321–330 (Chapter 14) in *Synthetic Aperture Radar Marine User's Manual*. C.R. Jackson and J.R. Apel, eds, NOAA NESDIS Office of Research and Applications, Washington, DC. Available online at: http://www.sarusersmanual.com (accessed September 20, 2013).

Velotto, D., M. Migliaccio, F. Nunziata, and S. Lehner, 2011. Dual-polarized TerraSAR-X data for oil-spill observation. *IEEE Transactions on Geoscience and Remote Sensing* 49:4,751–4,762, http://dx.doi.org/10.1109/TGRS.2011.2162960.

Wackerman, C.W., and P. Clemente-Colón. 2000. Wave refraction, breaking and other near-shore processes. Pp. 171–189 (Chapter 6) in *Synthetic Aperture Radar Marine User's Manual*. C.R. Jackson and J.R. Apel, eds, NOAA NESDIS Office of Research and Applications, Washington, DC. Available online at: http://www.sarusersmanual.com (accessed September 20, 2013).

A.3. Velotto, D., Migliaccio, M., Nunziata, F., Lehner, S., 2013b. Dual-polarimetric TerraSAR-X SAR data for target at sea observation. IEEE Geoscience and Remote Sensing Letters 10 (5): 1114-1118

Dual-Polarimetric TerraSAR-X SAR Data for Target at Sea Observation

Domenico Velotto, *Student Member, IEEE*, Ferdinando Nunziata, *Member, IEEE*, Maurizio Migliaccio, *Senior Member, IEEE*, and Susanne Lehner, *Member, IEEE*

***Abstract*—A physical dual-polarimetric model to observe man–made metallic targets at sea in dual-polarimetric coherent X-band synthetic aperture radar (SAR) data is proposed. The model exploits the intrinsic different symmetry properties of man-made targets and sea surface and is tested over actual StripMap TerraSAR-X HH–HV and VV–VH dual-polarimetric SAR data and colocated ground truth measurements. Then, an operational physically based filter to observe targets at sea is proposed. The filter is very attractive in terms of both detection performances and processing time. A typical SAR scene is processed in seconds by a conventional PC processor.**

***Index Terms*—PolSAR, ship detection, symmetry.**

I. Introduction

SHIP-AT-SEA observation is a key application in the field of global monitoring of environment and security. Synthetic aperture radar (SAR) imagery gives the possibility to overcome the limits of conventional techniques, e.g. Automatic Identification System (AIS), etc., allowing non-cooperative all-day ship surveillance, over wide regions and under almost all weather conditions. SAR-based observation of targets at sea, i.e. ships, oil rigs and wind turbines, is a very non-trivial task due to both speckle, that hampers SAR image interpretation, and the presence of natural phenomena, e.g. atmospheric fronts, changes in ocean backscattering, that may result in false positives [1]–[4]. In [5]–[11] some innovative physically-based approaches have been developed to perform ship detection using polarimetric SAR data exploiting the extra-information provided by these measurements.

Recently, an approach to observe man-made metallic targets using coherent dual-polarimetric L- and C-band SAR data has been proposed in [12]–[14]. The approach, it is based on the fact that sea surface, being reflection symmetric, calls for a negligible correlation between the like- and cross-polarized channels; whereas the reflection symmetry no longer applies for man-made metallic targets that, hence, results in a larger correlation between like- and cross-polarized channels [14]. Accordingly, HH-HV dual-polarimetric SAR data acquired in L- and C-band have been used to test the proposed methodology showing to be an effective and operational-oriented method to observe metallic targets at sea.

Manuscript received September 24, 2012; revised October 29, 2012; accepted November 17, 2012.

D. Velotto and S. Lehner are with the Remote Sensing Technology Institute, German Aerospace Center (DLR), 82234 Wessling, Germany (e-mail: Domenico.Velotto@dlr.de; Susanne.Lehner@dlr.de).

F. Nunziata and M. Migliaccio are with the Dipartimento per le Tecnologie, Università degli Studi di Napoli Parthenope, 80143 Napoli, Italy (e-mail: ferdinando.nunziata@uniparthenope.it; maurizio.migliaccio@uniparthenope.it).

Digital Object Identifier 10.1109/LGRS.2012.2231048

In this study, the physical rationale proposed in [14] is extended to X-band. It must be noted that X-band SAR observation of man-made metallic targets at sea is much more complex than in C- and L-band. At X-band the probability of occurrence of high coherent returns (and, therefore, false-positives) is very high, also at intermediate incidence angles, and it depends on sea state conditions [4]. Therefore, the interest to test this new physically based approach is of particular relevance. In this study, the sensitivity of the model to metallic targets at sea at X-band is investigated; then, a simple and effective technique to observe ships at sea is proposed and verified against actual X-band Single look Slant range Complex (SSC) full-resolution TerraSAR-X SAR data. The technique, that is tested over both HH-HV and VV-VH dual-polarimetric combinations and verified through ground truth information provided by AIS reports, nautical charts and oil rig maps, is shown to be both effective and accurate. Furthermore, the proposed physical-processing, being able to exploit L-, C- and X-band dual-polarimetric full-resolution SAR measurements, can take full benefit of all the operational polarimetric SAR missions and, therefore, it allows enhancing the revisit time and coverage which are very critical issues in target at sea observation.

II. Theoretical Analysis

The most logical way to deal with polarimetric scattering from a distributed and depolarizing target is by using the second-order products of the scattering matrix [15]–[17]. Here the covariance matrix is introduced under the backscatter alignment (BSA) convention and reciprocity assumption:

$$\mathbf{C} = \begin{pmatrix} \langle |S_{hh}|^2 \rangle & \sqrt{2}\langle S_{hh}S_{hv}^* \rangle & \langle S_{hh}S_{vv}^* \rangle \\ \sqrt{2}\langle S_{hv}S_{hh}^* \rangle & \langle |S_{hv}|^2 \rangle & \sqrt{2}\langle S_{hv}S_{vv}^* \rangle \\ \langle S_{vv}S_{hh}^* \rangle & \sqrt{2}\langle S_{vv}S_{hv}^* \rangle & \langle |S_{vv}|^2 \rangle \end{pmatrix}. \quad (1)$$

$\langle\cdot\rangle$, $|\cdot|$, and $*$ stand for the ensemble average, modulus, and complex conjugate, respectively. S_{pq} is the generic scattering matrix complex element with $\{p, q\} = \{h, v\}$. $\mathbf{C}$ is a 3×3 Hermitian semidefinite positive matrix which consists of nine independent parameters and has real and nonnegative eigenvalues and orthogonal eigenvectors.

Since only the linearity and the reciprocity are assumed, (1) represents the most general polarimetric scattering mechanism. When dealing with a naturally distributed scenario, reflection symmetry is generally satisfied. Hence, the correlation between like- and cross-polarized scattering amplitudes vanishes [18], [19], i.e. $\langle S_{hh}S_{hh}^* \rangle = \langle S_{hh}S_{hh}^* \rangle = 0$. The modulus of the correlation between like- and cross-polarized scattering amplitudes r is

$$r = \left| \langle S_{xx}S_{xy}^* \rangle \right| \quad (2)$$

TABLE I
TERRASAR-X DUAL-POLARIMETRIC DATA SET

ID	Data & time (UTC)	Location	Polarization	Inc.angle (°)	Wind speed (m/s)	Wind dir.
IMG-1	2009-07-11; 18:14	Gibraltar	HH-HV	34.73	2.7	SE
IMG-2	2011-08-30; 14:15	San Francisco	VV-VH	39.69	2.2	SE
IMG-3	2009-07-15; 06:29	Gibraltar	HH-HV	30.51	5.1	SW
IMG-4	2009-09-21; 18:06	Spain	VV-VH	20.00	5.5	SE
IMG-5	2012-03-29; 23:57	Gulf of Mexico	VV-VH	43.00	5.0	SE
IMG-6	2012-04-12; 16:49	Naples	HH-HV	28.16	3-5	SW
IMG-7	2011-10-06; 09:28	South Korea	VV-VH	39.68	10-12	NW

where $x, y \in \{h, v\}$ is the natural norm to measure the departure from the reflection symmetry case. When r tends to 0, the observed scene is characterized by the symmetry property; while for r values larger than 0 departure from reflection symmetry is achieved.

To specialize reflection symmetry to the observation of metallic targets at sea in X-band dual-polarization SAR measurements, two scenarios must be distinguished: sea surface with and without metallic targets. Sea surface is a natural distributed target and, hence, is reflection symmetric. This implies that $r \approx 0$ is expected, as demonstrated in [14]. It must be noted that the slight departure from zero mainly depends on the misalignment between radar coordinates and the scene symmetry axis [14]. When dealing with metallic targets, since they are man-made complex targets whose shape consists of plane, dihedral, and trihedral structures, as well as dihedral corner reflectors and thin wires, reflection symmetry is not expected to be still satisfied; therefore, r values significantly larger than the free sea surface one are expected, as demonstrated in [14].

III. EXPERIMENTAL RESULTS

In this section, the effectiveness of the proposed rationale is verified using actual TerraSAR-X SAR data and ground truth information provided by AIS messages, oil rig maps, and nautical charts. TerraSAR-X is a high-resolution SAR designed to work in different modes and polarizations [20]. Single- and dual-polarization products are operationally available on request to the end users, while twin- and quad-polarization products, which are acquired using the experimental dual receive antenna mode, are not standard products. The dual-polarimetric products can be collected in both StripMap (SM) mode, with a polarization combination selectable among HH-HV, VV-VH, and HH-VV, and SpotLight (SL) mode, with only one polarization combination: HH-VV. SM and SL imaging modes are characterized by nominal swath widths of 15 and 10 km, respectively [20].

In this study, StripMap (SM) SSC dual polarization HH-HV and VV-VH products [20] are used. The data set is described in Table I, where ancillary external wind information, extracted from model data, buoys, and scatterometer data, is also provided.

The first experiment is related to the HH-HV SAR data gathered off the Gibraltar coasts on July 11, 2009, at 18:14 Coordinated Universal Time (UTC) (see Table I). The incidence angle at the center image is 34.7°, and a low-to-moderate wind blowing from southeast is present. An excerpt of the HH-polarized amplitude image where land is masked in purple is shown in Fig. 1. Nineteen targets, labeled as $T1-T19$, are

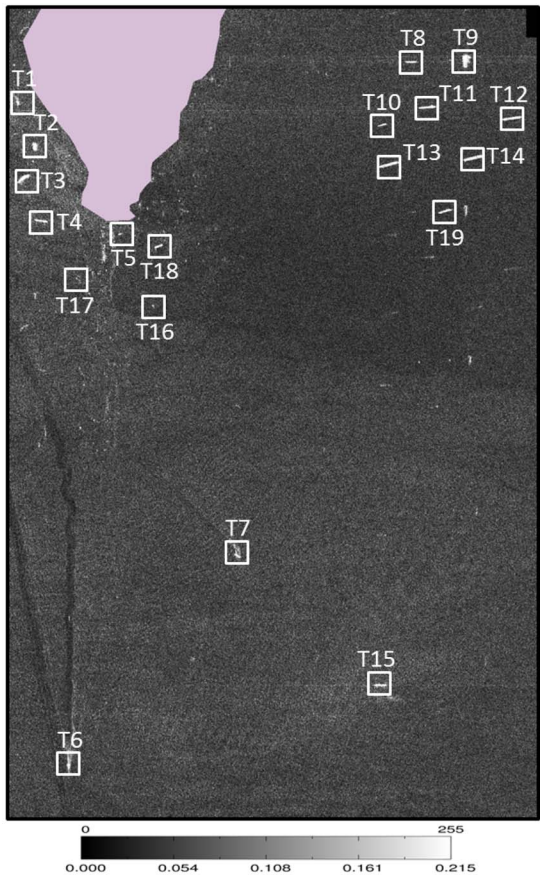

Fig. 1. TerraSAR-X SAR data collected off the coast of Gibraltar on July 11, 2009, at 18:14 UTC. Excerpt of the HH-polarized amplitude image where 19 targets are present: $T1-T16$ are AIS-confirmed ships, and $T17-T19$ are visually inspected targets.

present. According to the AIS information, the targets $T1-T16$ are ships whose sizes range from 40 up to 300 m. No ground truth is available for targets $T17-T19$ which have been visually inspected by trained SAR image analysts by using an enlarged version of both the HH and HV amplitude images. To analyze the sensitivity of the proposed approach, r is evaluated over equal-sized region of interests (ROIs) belonging to targets. Moreover, aside from each ROI, an equal-sized sea area is considered for reference purposes. Mean r values, evaluated within the ROIs in Fig. 1, are listed in Table II. It can be noted that sea surface r values are significantly lower (at least two orders of magnitude) than the correspondent target ones. This confirms the rationale described in Section II, which predicts different symmetry properties for sea surface with and without metallic targets. r values close to 0 are measured over the sea surface; while non-negligible r values apply over target ROIs. To discuss the capability of the r-based approach in observing metallic targets at sea with respect to conventional single-polarization ones, mean values of the HH and HV amplitude channels are evaluated for both targets and sea areas (see Table II). By comparing mean r values with the HH and HV ones, one can note the following (see Table II): 1) r, HH, and HV call for similar values when evaluated within targets, and 2) HH and HV call for similar values when evaluated over sea areas, while significantly lower values (one order of magnitude) are provided by r. This result suggests that the r-based approach

TABLE II
MEAN r, HH, AND HV VALUES AND TCR MEASURED WITHIN THE TARGET AND SEA ROIS IN FIG. 1

	r			HH			HV		
ROIs	target	sea	TCR	target	sea	TCR	target	sea	TCR
T1	0.930	0.003	273.5	1.988	0.084	23.66	0.364	0.043	8.465
T2	1.336	0.003	386.0	3.026	0.077	39.30	0.308	0.044	7.000
T3	1.935	0.003	627.6	2.094	0.074	28.30	0.671	0.042	17.98
T4	0.852	0.002	309.9	1.602	0.067	23.91	0.430	0.041	10.49
T5	0.22	0.002	93.61	1.699	0.055	12.71	0.223	0.042	5.309
T6	0.481	0.002	218.0	1.864	0.056	33.29	0.197	0.039	5.051
T7	1.048	0.002	383.7	1.413	0.065	21.74	0.585	0.042	13.93
T8	1.171	0.002	428.1	1.909	0.057	33.49	0.274	0.048	5.708
T9	3.140	0.002	1122	3.929	0.057	68.93	0.331	0.049	6.755
T10	0.418	0.002	169.4	0.854	0.052	16.42	0.337	0.047	7.170
T11	0.589	0.002	238.6	1.412	0.052	27.15	0.310	0.047	6.596
T12	0.794	0.002	304.2	1.191	0.053	22.47	0.405	0.049	8.265
T13	0.527	0.002	226.0	0.847	0.050	16.94	0.422	0.046	9.174
T14	0.528	0.002	216.5	0.873	0.051	17.12	0.350	0.048	7.292
T15	1.458	0.002	490.4	2.996	0.069	43.42	0.297	0.043	6.907
T16	0.117	0.002	50.09	0.491	0.056	8.768	0.183	0.042	4.357
T17	0.172	0.002	72.51	0.643	0.059	10.89	0.217	0.040	5.425
T18	0.301	0.002	131.1	0.795	0.054	14.72	0.322	0.042	7.667
T19	0.710	0.002	311.7	1.089	0.048	22.69	0.339	0.047	7.213

acts as a clutter suppression technique while enhancing targets. This behavior can be visually recognized by looking at the normalized HH, HV, and r values shown in Fig. 2(a)–(c) and related to a 200×200 pixel sea area that includes the ship $T16$, which is the smallest ship in Fig. 1. It can be noted that the ship calls for similar HH, HV, and r values, while a different behavior is experienced over sea surface where r provides the lowest value. As a matter of fact, the r-based approach allows de-emphasizing the sea surface clutter if compared to single-polarization channels. To quantitatively analyze this de-emphasis capability, a target-to-clutter ratio (TCR) is evaluated for r, HH, and HV. TCR values, listed in Table II, confirm that the r approach performs best in discriminating targets from the surrounding sea, resulting in TCR values at least one order of magnitude larger than the single-polarization ones.

This sensitivity study confirms the behavior predicted for r that exhibits a different sensitivity with respect to targets and sea surface even at X-band. These encouraging results suggest evaluating r over the whole SAR data in Fig. 1. The r image, obtained by replacing the ensemble average in (4) with an $N \times N$ average moving window, is shown in gray tones in Fig. 3(a). In this study, $N = 3$ is adopted to minimize the unavoidable decreasing of the spatial resolution. The r image confirms that reflection symmetry is everywhere in place but over targets. Accordingly, since the following statements are true, a fixed threshold T can be adopted to conceive an unsupervised filter both robust and effective: 1) r values related to targets and sea surface are very well separated (at least two orders of magnitude), and 2) sea surface r values do not exhibit a significant variability. In this study, a fixed threshold $T = 0.1$ is chosen. The r-filter output is shown in Fig. 3(b), where it can be noted that all the targets are correctly observed. Red and blue boxes are used in Fig. 3(b) to distinguish AIS-confirmed ships and visually inspected targets, respectively.

Results obtained by processing the whole TerraSAR-X dual-polarization SAR data ($11\,488 \times 21\,908$ pixels) are summarized in Table III. The scene includes 70 targets: 57 verified against ground truth and 13 visually inspected. All the ground-truth-verified targets are correctly observed by the r-based filter that fails in observing two small targets whose sizes, estimated by the SAR image, range between 10 and 15 m. Note that a filter to remove false positives due to azimuth ambiguities has been also applied [2].

The second experiment is related to the VV-VH SAR data gathered over the San Francisco Bay on August 30, 2011, at 14:15 UTC (see Table I). The incidence angle at the center image is 39.7°, and a low-to-moderate wind blowing from east southeast is present. An excerpt of the VV-polarized amplitude image is shown in gray tones in Fig. 4, where land is masked in purple. The subscene in Fig. 4 includes the San Francisco–Oakland Bay Bridge (upper center), the Treasure Island and Yerba Buena Island (left side), and the Oakland Naval Supply Depot and the Alameda Point (right side). This scene is very challenging to test the proposed technique since very small targets (in the order of the radar resolution) are present. The subscene is characterized by 32 targets (see the white boxes in Fig. 4). According to the AIS message, 3 targets are ships, whose sizes range from 115 up to 195 m, while nautical charts allow classifying 11 targets as lighted buoys, whose sizes are about 2 m. The remaining 18 targets have been visually inspected from the VV and VH images. The gray-tone r image [see Fig. 5(a)] again witnesses that reflection symmetry is everywhere in place but over targets. The output of the r filter is shown in Fig. 5(b). It can be noted that 30 out of the 32 targets are correctly observed. In particular, 9 out of the 11 ground-truth-verified lighted buoys, whose sizes are around 2 m, are detected, while 2 buoys are missed. Results obtained processing the whole SAR scene are summarized in Table III. The scene is characterized by 50 targets: 21 verified against ground truth and 29 visually inspected. All but 2 targets are correctly observed by the r filter; no false positive is present.

The third experiment is related to the HH-HV SAR data gathered off the east coast of Gibraltar on July 15, 2009, at 6:29 UTC (see Table I). The incidence angle at the center image is 30.51°, and a moderate wind blowing from southwest is present. An excerpt of the HH-polarized amplitude image is shown in gray tones in Fig. 6(a), where atmospheric-related phenomena (see bottom side of the image) and a pronounced wavelike pattern (see upper-left side of the image) are visible. These phenomena make this scene very challenging for conventional SAR-based target detectors [1], [3]. The subscene is characterized by six targets, highlighted by white boxes in Fig. 6(a). According to the AIS message, these targets are cargo ships and tankers, whose sizes range from 49–274 m. Due to the fluctuation in the backscatter caused by the atmospheric and wave processes, some targets are hardly visually distinguishable in the HH amplitude image (e.g., the 49-m ship in the middle right of the image). The gray-tone r image (not shown) witnesses that, even in this challenging case, the r-based approach acts as a clutter suppression technique, while enhancing targets. The output of the r filter is shown in Fig. 6(b), where all the targets are correctly observed and no false positive is present. Results obtained processing the whole scene are summarized in Table III. The scene consists of eight

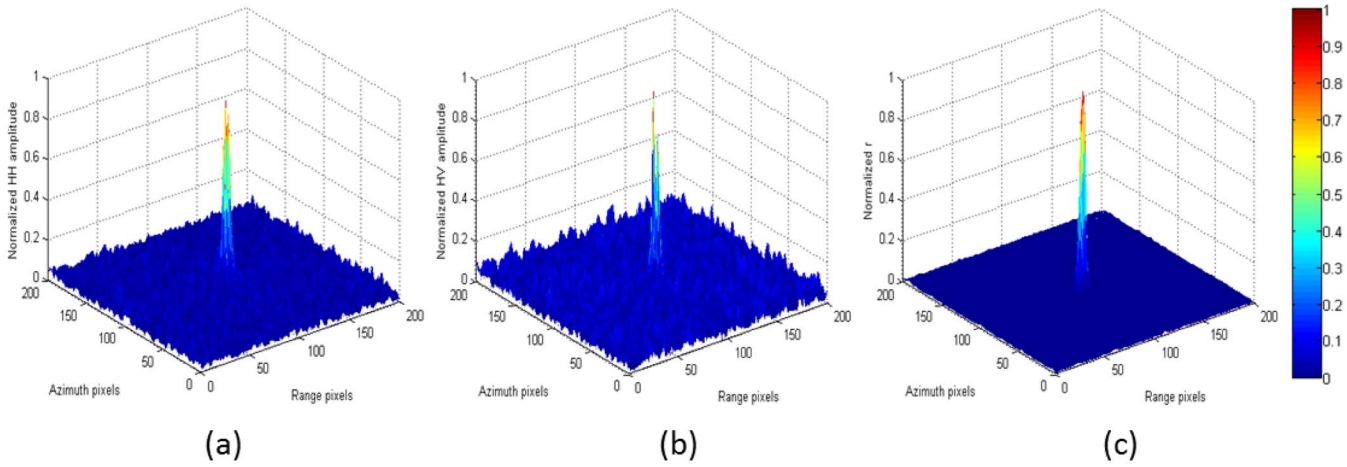

Fig. 2. (a) and (b) Normalized HH and HV amplitudes and (c) r parameter, measured over a sea surface area that includes the ship labeled as $T16$ in Fig. 1.

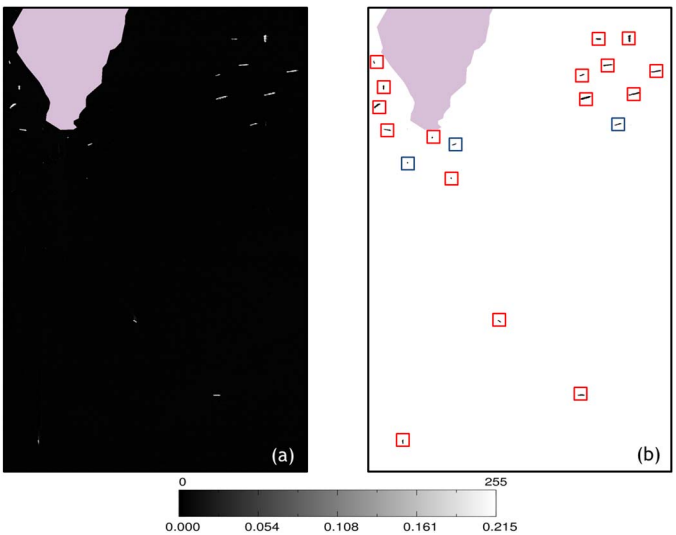

Fig. 3. (a) Gray-tone r image and (b) r-based logical true (sea) and false (ship) outputs where ships validated by AIS message and visually inspected targets are marked in red and blue, respectively.

TABLE III
SUMMARY OF THE RESULTS OBTAINED BY PROCESSING THE SAR DATA IN TABLE I THROUGH THE r FILTER

ID	Targets	Ground truth	Detected targets	False negatives	False positives
IMG-1	70	57	68	2	0
IMG-2	50	21	48	2	0
IMG-3	8	7	8	0	0
IMG-4	7	5	5	2	0
IMG-5	14	7	12	2	0
IMG-6	13	0	12	1	0
IMG-7	29	4	22	7	0

targets: seven verified against ground truth and one visually inspected. All targets are correctly observed by the r filter that results in zero false negatives (after azimuth ambiguity filtering) and zero false positives.

Results obtained by processing the data set detailed in Table I through the r filter are summarized in Table III. The data set consists of seven TerraSAR-X scenes that include 191 targets. The proposed r filter correctly observes 175 targets with 16 false negatives. The latter are always related to small targets

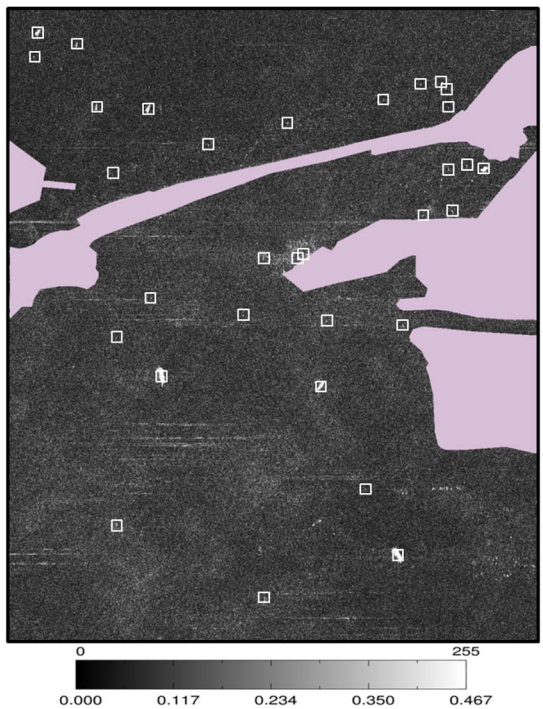

Fig. 4. TerraSAR-X SAR data collected over San Francisco Bay on August 30, 2011, at 14:15 UTC. Excerpt of the HH-polarized amplitude image where 32 targets are present: 18 visually inspected targets and 14 ground-truth-verified targets via AIS and nautical charts.

whose sizes are less than 10 m. No false positive is present. The minimum sizes of the detected AIS-confirmed and visually inspected targets are 20 and 10 m, respectively. Nine lighted buoys, whose sizes are around 2 m, are also detected. Note that, even in high-wind conditions (see IMG-7 in Table III), no false positive is present, while the seven false negatives are due to visually inspected targets whose sizes, estimated by the SAR image, are less than 5 m.

IV. CONCLUSION

A dual-polarimetric model to observe metallic targets at sea in dual-polarimetric coherent HH-HV/VV-VH full-resolution X-band SAR data has been proposed here and verified against actual TerraSAR-X SAR data and ground truth information. The approach exploits the different symmetry properties that

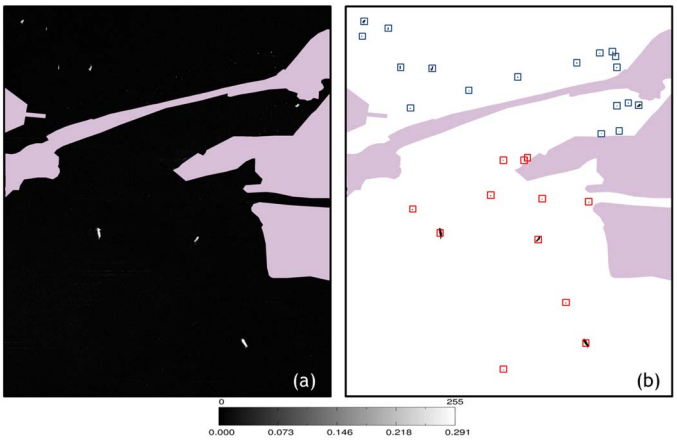

Fig. 5. (a) Gray-tone r image and (b) r-based logical binary output where ground-truth-verified and visually inspected targets are marked in red and blue, respectively.

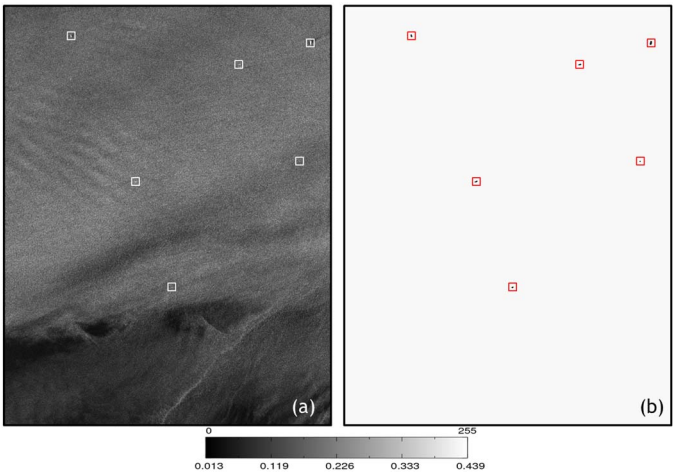

Fig. 6. TerraSAR-X SAR data collected off the east coast of Gibraltar on July 15, 2009, at 6:29 UTC. (a) Excerpt of the HH-polarized amplitude image where six ground-truth-verified targets are present. (b) r-based logical binary output where all the observed targets are marked in red.

characterize sea surface with and without metallic targets. Following this rationale, an operational filter has been proposed to observe targets at sea in a reliable and effective way. A typical TerraSAR-X high-resolution scene is processed in seconds by a standard PC processor. The obtained results are

1) Metallic targets can be distinguished from the surrounding sea using X-band dual-polarimetric SAR data.
2) Both the HH–HV and the VV–VH polarimetric combinations can be used.
3) The r filter allows obtaining binary outputs using a fixed threshold.
4) The r filter works correctly over a broad range of incidence angles and sea state conditions, including high wind.
5) According to the selected threshold, no false positive is obtained, while false negatives are always due to small targets (< 15 m). The minimum size of the detected ground-truth-verified (visually inspected) target is 2 m (8–10 m).
6) The proposed approach, being able to work on L-, C-, and X-band dual-polarimetric SAR data, allows to interoperate all the operational/planned dual-polarimetric SAR missions.

ACKNOWLEDGMENT

TerraSAR-X data are provided by the German Aerospace Center (DLR) via the scientific announcement of opportunity proposal OCE1045. The authors would like to thank NOAA and the Bureau of Ocean Energy Management, Regulation and Enforcement for making oil platform location and nautical charts freely available.

REFERENCES

[1] D. J. Crisp, The state-of-the-art in ship detection in synthetic aperture radar imagery, Defence Sci. Technol. Org., Majura, Australia, Res. Rep. DSTO-RR-0272. [Online]. Available: http://www.dsto.defence.gov.au/corporate/reports/
[2] S. Brush, S. Lehner, T. Fritz, and M. Soccorsi, "Ship surveillance with TerraSAR-X," *IEEE Trans. Geosci. Remote Sens.*, vol. 49, no. 3, pp. 1092–1103, Mar. 2011.
[3] A. Gambardella, F. Nunziata, and M. Migliaccio, "A physical full-resolution SAR ship detection filter," *IEEE Geosci. Remote Sens. Lett.*, vol. 5, no. 4, pp. 760–763, Oct. 2008.
[4] M. Migliaccio, F. Nunziata, A. Montuori, and R. L. Paes, "Single look complex COSMO-SkyMed SAR data to observe metallic targets at sea," *IEEE J. Sel. Topics Appl. Earth Observ. Remote Sens.*, vol. 5, no. 3, pp. 893–901, Jun. 2012.
[5] H. Zhaoying and C. Jinsong, "A review of ship detection algorithms in polarimetric SAR images," in *Proc. Signal Proces.*, 2004, vol. 3, pp. 2155–2158.
[6] C. Liu, P. W. Vachon, and G. W. Geling, "Improved ship detection with airborne polarimetric SAR data," *Can. J. Remote Sens.*, vol. 31, no. 1, pp. 122–131, Feb. 2005.
[7] M. Yeremy, J. W. M. Campbell, K. Mattar, and T. Potter, "Ocean surveillance with polarimetric SAR," *Can. J. Remote Sens.*, vol. 27, no. 4, pp. 328–344, 2001.
[8] R. Touzi and F. Charbonneau, "Characterization of target symmetric scattering using polarimetric SARs," *IEEE Trans. Geosci. Remote Sens.*, vol. 40, no. 11, pp. 2507–2516, Nov. 2002.
[9] J. Chen, Y. Chen, and J. Yang, "Ship detection using polarization cross-entropy," *IEEE Geosci. Remote Sens. Lett.*, vol. 6, no. 4, pp. 723–727, Oct. 2009.
[10] G. Ferrara, M. Migliaccio, F. Nunziata, and A. Sorrentino, "GK-based observation of metallic targets at sea in full-resolution SAR data: A multipolarization study," *IEEE J. Ocean. Eng.*, vol. 36, no. 2, pp. 195–204, Apr. 2011.
[11] A. Marino, N. Walker, and I. Woodhouse, "Ship detection with RADARSAT-2 quad-pol SAR data using a notch filter based on perturbation analysis," in *Proc. IEEE IGARSS*, Honolulu, HI, Jul. 25–30, 2010, pp. 3704–3707.
[12] M. Migliaccio, F. Nunziata, A. Montuori, X. Li, and W. Pichel, "A multifrequency polarimetric SAR processing chain to observe oil fields in the Gulf of Mexico," *IEEE Trans. Geosci. Remote Sens.*, vol. 49, no. 12, pp. 4729–4737, Dec. 2011.
[13] M. Migliaccio, F. Nunziata, A. Montuori, and C. E. Brown, "Marine added-value products by RADARSAT-2 fine quad-polarization mode," *Can. J. Remote Sens.*, vol. 37, no. 5, pp. 441–450, Oct. 2011.
[14] F. Nunziata, M. Migliaccio, and C. E. Brown, "Reflection symmetry for polarimetric observation of man-made metallic targets at sea," *IEEE J. Ocean. Eng.*, vol. 37, no. 3, pp. 384–394, Jul. 2012.
[15] J. J. van Zyl, C. H. Papas, and C. Elachi, "On the optimum polarization of incoherently reflected waves," *IEEE Trans. Antennas Propag.*, vol. AP-35, no. 7, pp. 818–825, Jul. 1987.
[16] I. Hajnsek, E. Pottier, and S. R. Cloude, "Inversion of surface parameters from polarimetric SAR," *IEEE Trans. Geosci. Remote Sens.*, vol. 41, no. 4, pp. 727–744, Apr. 2003.
[17] S. R. Cloude, *Polarisation: Applications in Remote Sensing*. London, U.K.: Oxford Univ. Press, 2009.
[18] S. V. Nghiem, S. H. Yueh, R. Kwok, and F. K. Li, "Symmetry properties in polarimetric remote sensing," *Radio Sci.*, vol. 27, no. 5, pp. 693–711, Jan. 1992.
[19] S. V. Nghiem, S. H. Yueh, R. Kwok, and D. T. Nguyen, "Polarimetric remote sensing of geophysical medium structures," *Radio Sci.*, vol. 28, no. 6, pp. 1111–1130, Jan. 1993.
[20] H. Breit, T. Fritz, U. Balss, M. Lachaise, A. Niedermeier, and M. Vonavka, "TerraSAR-X SAR processing and products," *IEEE Trans. Geosci. Remote Sens.*, vol. 48, no. 2, pp. 727–740, Feb. 2010.

A.4. Velotto, D., Soccorsi, M., Lehner, S., 2014. Azimuth ambiguities removal for ship detection using full polarimetric X-Band SAR data. IEEE Transactions on Geoscience and Remote Sensing 52 (1): 76-88

Azimuth Ambiguities Removal for Ship Detection Using Full Polarimetric X-Band SAR Data

Domenico Velotto, *Student Member, IEEE*, Matteo Soccorsi, *Member, IEEE*, and Susanne Lehner

***Abstract*—Synthetic aperture radar (SAR) ship detection is an important application in the field of maritime security. Azimuth ambiguities caused by the aliasing of the Doppler phase history of each point are often visible in SAR images particularly in ocean areas of low wind speed condition, e.g., in coastal areas, in harbors, etc. The main sources of azimuth ambiguities are man-made metallic structures over the ocean, e.g., ships, oil platforms etc., and over land near the coast, e.g., big tanks, bridges' pylons etc., that have a high SAR backscatter responses. Although the ambiguities' backscatter is generally low, in many situations, it is above the surrounding ocean clutter and are mistaken by classic detection techniques, like constant false alarm rate, as real targets causing false positives. This paper addresses both the discrimination of real targets from non-trivial false positives, namely those due to azimuth ambiguities and the detection itself using a Generalized-K distribution approach. The methodology is firstly proposed and demonstrated over a significant data set of full polarimetric X-band SAR data, which have been acquired by the German satellite TerraSAR-X during the experimental dual receive antenna campaign in April and May 2010. It is based on the intrinsic configuration of monostatic two-channel PolSAR systems and relies on the different signature of azimuth ambiguities in cross-polarized channels. Automatic Identification System messages collected and collocated with the data set analyzed are used as ground truth to evaluate and validate the proposed methodology.**

***Index Terms*—Azimuth ambiguity, dual receive antenna, PolSAR, ship detection, TerraSAR-X.**

I. Introduction

SYNTHETIC APERTURE Radar (SAR) is an imaging system operated on satellite-based platform which provides images of the Earth surface with different spatial resolution, electromagnetic waves polarization, and ground coverage. Moreover, being a non-cooperative Earth monitoring tool, its use in the field of maritime security and safety has increased during the past decade. In fact, SAR images have been used by law enforcement agencies for coastal and fishery monitoring, ship traffic monitoring, and oil spill detection [1], [2].

Ships or, more in general, man-made objects (e.g., oil rigs) over the ocean surface, being complex metallic structures, call for all the three physical scattering models: single-bounce returns, due to direct backscattering from surfaces perpendicular to the radar beam; double-bounce returns, due to the dihedral formed by the vertical ship's conducting plates and the sea surface; multiple-bounce returns, caused by ship's structure (e.g., deck and cables) [3]. Therefore, ships show a larger coherent scattering, i.e., the measured normalized radar cross section (NRCS) by SAR is generally higher than the one measured from the surrounding sea surface, where the wind-driven ocean waves (waves with wavelength range 1–3 cm, also known as Bragg waves) are responsible for a smaller coherent scattering. Single polarization SAR ship detection algorithms exploit this physical behavior by adaptively setting an appropriate NRCS threshold able to separate the ship from the surrounding sea. However, this can be a challenging task due to the speckle, when the distributions of the features characterizing the two responses are mixed and the two modes are not well separated.

Single and multi-polarization SAR images are affected by the presence of range and azimuth (or Doppler) ambiguities which arise due to the fact that the data are sampled with the pulse repetition frequency (PRF). The system is usually designed in order to avoid range ambiguities by selecting the correct swath: the higher the PRF, the smaller the swath. On the other hand, if the PRF is set too low, the Doppler history of returns at different azimuth positions is the same, causing aliasing. These "false" targets become visible particularly in low backscatter area, i.e., over the ocean surface in low wind speed regime. Oceanographic processes like internal waves, breaking waves, sea currents, and so on, together with azimuth ambiguities, are sources of false positives in SAR ship detection algorithms that seek for bright spots in the image. In literature, several methods have been investigated to reduce the intensity or to resolve azimuth ambiguities in single polarization SAR images [4]–[7].

Nowadays, the number of SAR missions equipped with high-resolution X-band sensors is in progressive development (e.g., TerraSAR-X (TS-X), Tandem-X, COSMO-SkyMed). As far as ship detection and target classification are concerned, high-resolution SAR images are preferred to medium- or low-resolution SAR images, where particularly in coastal areas, small vessels are of interest. Numerous methods to detect ships automatically from single polarization SAR images have been developed [8], [9]. One of the best known and applied method is the constant false alarm rate (CFAR) in which the threshold is locally calculated for a pre-defined probability of false alarm. In a very simple CFAR approach, a block of image samples around the pixel under investigation (called background window) is used to estimate the average level of the sea clutter backscatter [10]. The pixel under investigation is assigned to

Manuscript received March 13, 2012; revised August 8, 2012; accepted December 7, 2012. Date of publication February 1, 2013; date of current version November 26, 2013.

D. Velotto and S. Lehner are with Remote Sensing Technology Institute, German Aerospace Center (DLR), 82234 Wessling, Germany (e-mail: Domenico.Velotto@dlr.de; Susanne.Lehner@dlr.de).

M. Soccorsi was with Remote Sensing Technology Institute, German Aerospace Center (DLR), 82234 Wessling, Germany. He is now with Thales Alenia Space–Italy (e-mail: Matteo.Soccorsi@dlr.de).

Digital Object Identifier 10.1109/TGRS.2012.2236337

TABLE I
DATA DESCRIPTION

Product[a] *Name*	**Data ID** *Time*	**Resolution**[b] **(m)** *Rg × Az*	**Inc. Angle**[c] **(°)** *Nr - Fr*	**Size**[b] **(km)** *Rg × Az*	**Wind speed** *m/s*	**Wind direction**
SSC_SM_Q *NS_1*	2010/04/18 *05:50* UTC	2.11 × 6.60	33.04 – 34.54	17.02 × 56.44	3-5	SW
SSC_SM_Q *NS_2*	2010/04/29 *05:50* UTC	2.11 × 6.60	33.04 – 34.54	17.02 × 56.44	1-3	S
SSC_SM_Q *FI*	2010/05/04 *05:59* UTC	2.48 × 6.60	27.39 – 29.10	17.58 × 56.56	8-10	NW
SSC_SM_Q *SF*	2010/04/11 *14:15* UTC	1.84 × 6.60	39.02 – 40.37	17.44 × 56.53	5-7	SO
SSC_SM_Q *SI*	2010/05/01 *22:53* UTC	1.96 × 6.60	36.09 – 37.47	16.85 × 56.85	0-2	NO

[a]SSC = Single look complex Slant Range; SM = StripMap; Q = quad-polarization;[b]*Rg* = Ground Range; *Az* = Azimuth;[c]*Nr* = Near Range; *Fr* = Far Range

a target if its value is larger than the estimated threshold. More complex CFAR algorithms use a parametric distribution model to take into account the statistics of the sea clutter [10]. Even though, CFAR is known to be very efficient, computationally non expensive and therefore widely used for near real time ship detection services [11], its detection efficiency depends on how well the parametric distribution fits the sea clutter characteristics.

For SAR with low spatial resolution and look angle smaller than about 70°, the sea clutter can be modeled as speckle, and hence the amplitude is assumed to be a Rayleigh-type distribution. However, a non-Rayleigh distribution of the sea clutter is observed in high-resolution SAR images where large amplitude values are measured leading to a longer tail in the distribution. According to the related research, many distributions have been proposed to model the amplitude of high-resolution sea echo, i.e., the β, lognormal, Weibull, K and generalized-K (GK) [12]–[15]. Recently, in [16], [17], the three parameter GK distribution is used to describe low backscattering areas and small dominant scatterers (i.e metallic objects) in marine single-look complex (SLC) SAR images. In [17], as outcome of the sensitivity study conducted on the different polarization for C-band RADARSAT-2 fine quad-pol SAR data, a simple index has been defined, and its value has been related to the sea clutter and metallic objects.

In this paper, we propose a method to resolve azimuth ambiguities for ship detection purposes that take the complete benefit of full polarimetric SAR (PolSAR) data combined with the high-resolution capability of X-band sensors into account. The main novelties introduced in this study can be summarized as follows:

- The underpinning rationale that allows solving azimuth ambiguities in full PolSAR images is first described by pointing out the different signature of azimuth ambiguities in cross-polarized channels caused by the acquisition mode and processing of two channel PolSAR system raw data.
- The proposed theoretical rationale is verified against a truly unique data set, consisting of actual full polarimetric X-band satellite SAR data, which have been acquired by the German satellite TS-X during the experimental dual receive antenna (DRA) campaign in April and May 2010, by showing that azimuth ambiguities break the reciprocity law.
- A new complete processing chain of single-look slant range complex (SSC) quad-pol TS-X product has been developed, allowing both discrimination and detection of real targets.
- The discrimination problem takes into account different kinds of non-trivial false positives, namely azimuth ambiguities caused by metallic man-made structures over the ocean (ships, oil rigs, etc.) and over land in coastal areas (buildings, harbor facilities, etc.).
- The GK-based index, proposed in [17] for C-band quad-pol RADARSAT-2 data for metallic object observation at sea, has been first proposed and tested for X-band quad-pol TS-X data. Following a brief sensitivity study, the index has been used to perform the detection of real targets.
- Collected and collocated Automatic Identification System (AIS) messages are used as ground truth to show the effectiveness of the proposed method in solving azimuth ambiguities and to validate the whole detection chain.

The paper is organized as follows: Section II gives a short introduction to the TS-X DRA campaign in 2010 and a data description. Section III addresses three points:—the problem of azimuth ambiguities and their formation in PolSAR data;—analytical description of the GK distribution and the proposed index to observe targets at sea;—summary of the proposed methodology and the processing chain. Experimental results are presented in Section IV, while summary and conclusions are drawn in Section V.

II. DATA DESCRIPTION

TS-X is an operational satellite for scientific and commercial applications equipped with an X-band SAR sensor that provides high-resolution images of the Earth's surface in different modes and polarizations. The SpotLight (SL), StripMap (SM), and ScanSAR are the basic modes with different spatial resolutions and swath coverage [18]. The nominal SAR hardware is designed and optimized for single-channel operation; hence, for SL and SM mode, it offers acquisition in single and dual

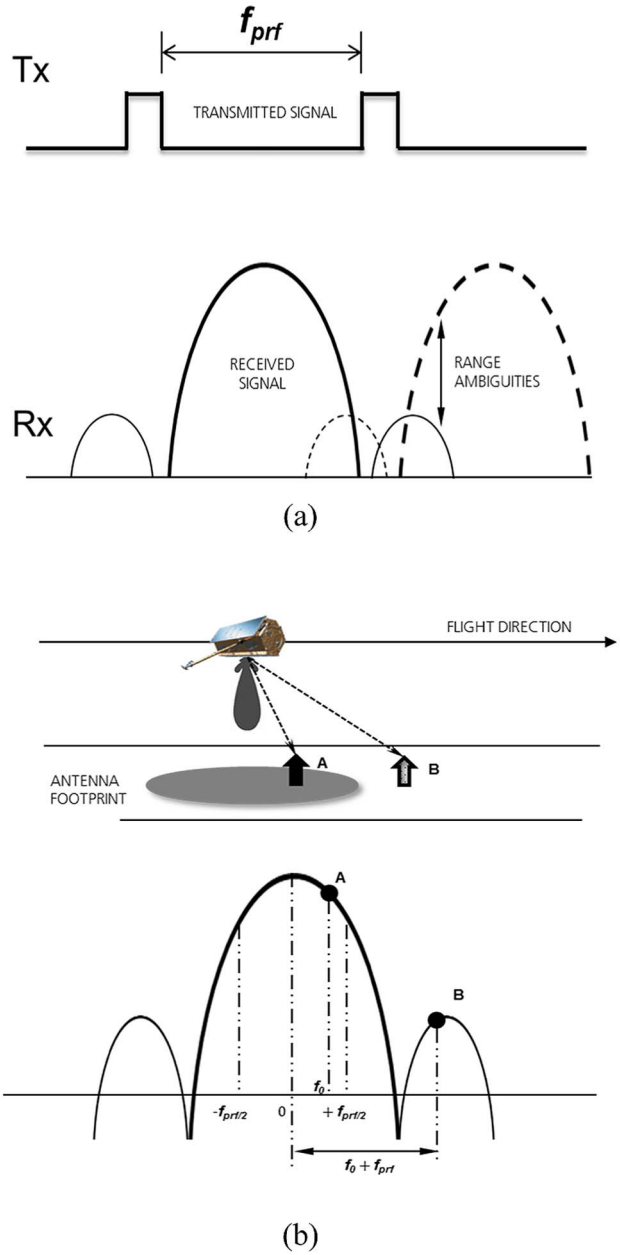

Fig. 1. Illustration of range and azimuth formation in SAR images; (a) portion of the radar return from previous pulse overlap with the return of the present pulse causing range ambiguities; (b) targets A and B have equal Doppler histories due to aliasing; therefore, B appears as if illuminated by a portion of antenna causing azimuth ambiguities.

polarization. Being a design-to-cost system, fully polarimetric capabilities are not foreseen in nominal operation. However, the satellite includes redundant hardware for the critical components. The redundancy concept is such that two receive channels are available when both the nominal and the redundant hardware are used [19]. Carrying a redundant receiver chain, the measurement of the complete scattering matrix (quad-polarization) is achievable creating two receiver channels by splitting the antenna electrically into two halves, and hence the PRF is doubled, leading to half single polarization range extent, as for dual-polarization products. This configuration is called DRA and is operated in the SM mode only [19]. DRA configuration allows also to create two distinct images from the two halves enabling the capability along track interferometry [20].

Full polarimetric X-band SAR data have been acquired by satellite TS-X during the DRA campaign in April and May 2010 over predefined test sites. Among the main objectives of this campaign is the evaluation of quad-polarized X-band high-resolution SAR data in order to improve existing or to develop new technologies and applications. A meaningful data set is processed to show the effectiveness of the proposed method. In Table I, a detailed description of the DRA configuration, some basic information on the data set, and weather situations are given for reference.

III. Model and Methodology Description

In this section, the problem of ambiguities is reviewed, and their formation in PolSAR data is introduced analytically. The description of the GK distribution is given, and a short sensitivity analysis of its parameters regarding the sea surface and targets at sea is conducted. As a result of the two previous steps, a complete processing chain, which performs both discrimination and detection, is proposed and described.

A. Azimuth Ambiguities

The ambiguities are caused by sampling of the Doppler spectrum at finite intervals of the PRF (Fig. 1). From the system design point of view, a too high PRF may produce the overlap of two successive returns causing range ambiguities [Fig. 1(a)]. On the other hand, a too low PRF may cause the effect that Doppler frequencies higher than the PRF are folded into the azimuth spectrum causing aliasing [Fig. 1(b)]. Ambiguities in SAR images are spatially displaced in range and azimuth directions at approximate locations [4]–[7]

$$\Delta x_{\mathrm{AZ}} = \frac{n f_{prf} V_{\mathrm{a}}}{f_{\mathrm{DR}}} \tag{1}$$

$$\Delta x_{\mathrm{RG}} = \frac{n \lambda f_{prf}}{f_{\mathrm{DR}}} \left(f_{\mathrm{DC}} + \frac{n f_{prf}}{2} \right) \tag{2}$$

where n is the ambiguity index, f_{prf} is the PRF, V_{a} is the relative velocity between the SAR's platform and the target, f_{DR} is the Doppler rate, and f_{DC} is the Doppler centroid.

Although the TS-X system is designed to avoid and reduce range ambiguities by setting the correct swath, the azimuth ambiguities are often observed in single and multi-polarization SAR images, particularly in the maritime environment where the absence or the reduced wind speed leads to a low ocean clutter. From the SAR ship detection point of view, it is of high importance to have a low false alarms rate; therefore, (1) is commonly used in CFAR-based ship detection algorithms as a post-processing step to distinguish targets and azimuth ambiguities. In practice, once by CFAR all possible bright anomalies in the image are detected, only the ones that do not follow at distance of $\pm\Delta x_{\mathrm{AZ}}$ from each other are retained as true targets [2]. The drawbacks of this approach are mainly the following: 1) it raises the possibility of missed targets, i.e.,

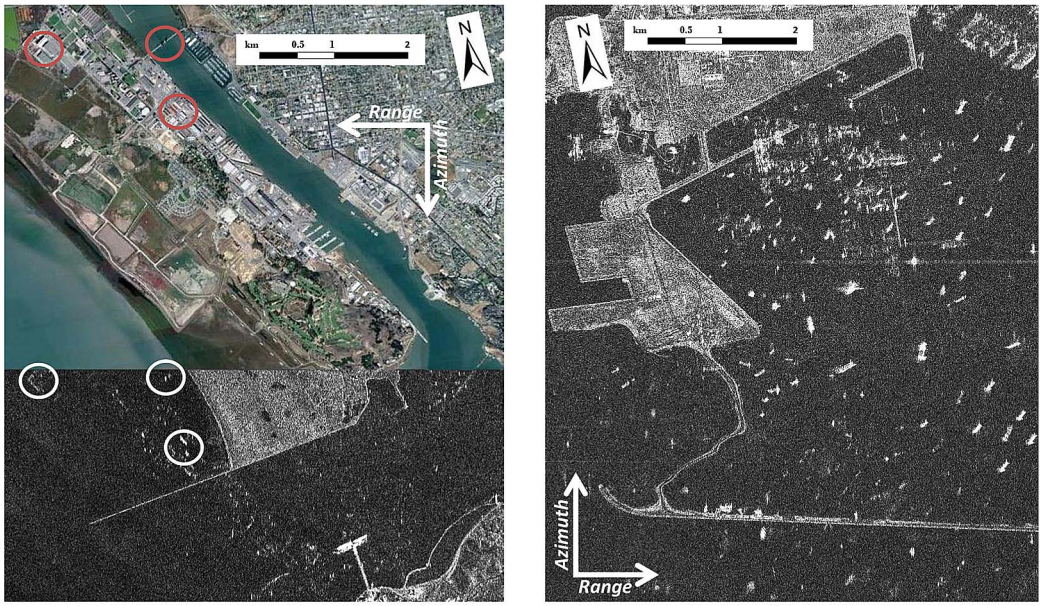

Fig. 2. Examples of challenging SAR azimuth ambiguities problem solving. (a) The grayscale HH polarization amplitude sub-image of the data set named SF is overlapped on Google Earth© background showing the area surrounding the former Mare Island Naval Shipyard (MINSY). White circles indicate azimuth ambiguities caused by man-made structures over land (indicated with red circles). (b) The grayscale HH polarization amplitude sub-image of the data set named SI showing a very complex ship detection scenario over the industrial zone of Tuas, located in the western part of Singapore.

a true target is discarded because at position $\pm\Delta x_{\mathrm{AZ}}$ from another one (this scenario might happen in harbors area with intense ship traffic); 2) it fails to discard azimuth ambiguities caused by man-made metallic structures over land. Examples of challenging azimuth ambiguity problem-solving are shown in Fig. 2. In Fig. 2(a) the HH amplitude sub-scene of the northern corner of the TS-X data set SF (see Table I) is shown in grayscale over a Google Earth© background and oriented along the azimuth direction. Several bright anomalies, some of which shaped like a ship (pointed in Fig. 2(a) with white circles), are clearly visible over the sea surface. A closer look to Fig. 2(a) reveals that these bright anomalies are replicas of man-made structure (pointed with red circles) of the former Mare Island Naval Shipyard (MINSY) located in the upper-left corner of Fig. 2(a). The exact distance between white and red circles is ∼3.6 km and is equal to Δx_{AZ} evaluated using (1), further validating the nature of these bright anomalies. In Fig. 2(b), the grayscale HH polarization amplitude sub-image of the data set named SI (see Table I) shows a very complex ship detection scenario (mixture of true targets and azimuth ambiguities over sea surface) in a harbor area over the industrial zone of Tuas, located in the western part of Singapore. It is easy to recognize that the use of the standard approach to discard azimuth ambiguities can lead to wrong detection results.

In the next section, a brief theoretical polarimetric analysis of the azimuth ambiguities and their formation in SAR images is given.

The TS-X DRA configuration can be seen as a classic two-channel PolSAR system where the horizontally (H) and vertically (V) polarized waves are transmitted pulse to pulse, while the scattered waves are received simultaneously by the two electrically created antennas polarized in H and V. In this way, assuming that the first pulse is H-polarized, the HH and HV components are measured at the same time and formed first, whereas the VH and VV are measured at the same time and formed with a delay of $\Delta\tau/2$, where $\Delta\tau = 1/f_{prf}$ and τ is referred to as slow time. Knowing that the azimuth sample position is given by the direct relationship between V_{a} and τ, the HV samples have azimuth positions $x_n = V_{\mathrm{a}}(n/f_{prf})$, while VH samples have azimuth positions $x_n + (\Delta x/2)$ where $\Delta x = V_{\mathrm{a}}/f_{prf}$. To shift the VH samples at positions x_{n}, a linear interpolation approach is commonly used. Therefore, without loss of information, it can be shown that the HV and VH raw signal after range compression (RC) are related as [4]:

$$VH_{\mathrm{RC}}(x_{\mathrm{n}}, t_{\mathrm{m}}) \cong HV_{\mathrm{RC}}(x_{\mathrm{n}}, t_{\mathrm{m}})F(x_{\mathrm{n}}) \tag{3}$$

where t_{m} is the fast time. $F(x_{\mathrm{n}})$ is the term that includes the interpolation processes [4]:

$$F(x_{\mathrm{n}}) = \sum_{l} 2k_l \cos\left[\frac{2\pi}{\lambda} r'(x_{\mathrm{n}}) l \Delta x\right] \tag{4}$$

where the index l are integer odd numbers, k_l are the correspondent interpolation coefficients, and r' is the first derivative term in the Taylor series of the target range function $r(x)$. For each polarimetric channel, the signal obtained after RC is convolved with the azimuth matched filter to perform the azimuth compression (AC) and to obtain the final image [4]:

$$XY_{\mathrm{AC}}(x_{\mathrm{n}}, t_{\mathrm{m}}) = XY_{\mathrm{RC}}(x_{\mathrm{n}}, t_{\mathrm{m}}) * h(x_{\mathrm{n}}) \tag{5}$$

where X represents the transmitted and Y the received polarization, $h(x_{\mathrm{n}})$ is the azimuth matched filter, and $*$ denotes the convolution operator.

From (3)–(5), it follows that to make $VH_{\mathrm{AC}} \cong HV_{\mathrm{AC}}$, the interpolation coefficient k_l are chosen in order to have

$F(x_{\rm n}) \cong 1$. Assuming that the target position is $x_{\rm T}$, such that $r'(x_{\rm T}) = 0$, and the first ambiguities index positions are $x_{\rm A}^{\pm}$, such that the phase shift between adjacent samples is $\pm 2\pi$, i.e., the Doppler frequency is $\pm f_{prf}$, the following formula is obtained:

$$\frac{4\pi}{\lambda} r'(x_{\rm A}) \Delta x = \pm 2\pi \quad \text{or} \quad \frac{2\pi}{\lambda} r'\left(x_{\rm A}^{\pm}\right) \Delta x = \pm \pi \tag{6}$$

where due to the cosine function symmetry, it is easy to recognize that after the AC:

$$\begin{array}{l} VH_{\rm AC}(x_{\rm n}, t_{\rm m}) \cong HV_{\rm AC}(x_{\rm n}, t_{\rm m}) \\ VH_{\rm AC}(x_{\rm n}, t_{\rm m}) \cong -HV_{\rm AC}(x_{\rm n}, t_{\rm m}) \end{array} \quad \text{for} \quad \begin{array}{l} x_{\rm n} = x_{\rm T} \\ x_{\rm n} = x_{\rm A}^{\pm} \end{array} \tag{7}$$

leading to the following theoretical conclusions:

- HV and VH channels are approximately equal in magnitude and phase for targets' pixels.
- HV and VH channels are each other's complex conjugate for azimuth ambiguity pixels.

In other words, due to the acquisition mode of two channels PolSAR systems and the processing of the measured raw signals, (7) shows that, even though reciprocity applies for targets, azimuth ambiguities break the reciprocity being each other its complex conjugate. This outcome suggests that a proper combination of the two cross-polarized channels is an efficient way to cancel out azimuth ambiguities. The proposed combination will be introduced and discussed in the methodology sub-section. It is pointed out that (7) is valid as well for the n-th index of azimuth ambiguities.

B. GK Distribution

In [16], the GK distribution has been proposed to characterize the speckle of full-resolution SLC single-polarization SAR marine scenes, showing a physically consistent transition among different scattering scenarios present over the ocean surface. Being a suitable parametric distribution model of the sea clutter for C-band full-resolution data [12], [16], [17], it is here first tested on SSC X-band SAR data and used in the detection step of the proposed approach. This sub-section addresses the mathematical description of the GK distribution and the relationship between its parameters and targets at sea, while a focused sensitivity study is addressed in the methodology subsection.

The three parameters GK distribution is an extension of the well-known two parameters K-distribution in the case of weak scattering regime in which a non-uniform distribution of the phase is considered. The GK expression is given by [12]–[16]

$$P(I) = \frac{2\alpha}{\Gamma(\alpha)\eta^{\alpha+1}} \left(\frac{\alpha}{1+a}\right)^{\frac{\alpha-1}{2}} I^{\frac{\alpha-1}{2}} I_o\left(\frac{\nu}{\eta}\sqrt{I}\right) \times K_{\alpha-1}\left\{\frac{2}{\eta}\left[(1+a)\alpha I\right]\frac{1}{2}\right\} \tag{8}$$

where I is the intensity of the backscattered field, $\Gamma(\bullet)$ is the gamma function, $I_0(\cdot)$ is the first kind zero-order modified Bessel function, $K_{\alpha-1}(\cdot)$ is the second kind $\alpha - 1$ order modified Bessel function, and $a = (\nu^2/4\alpha)$. The parameters α, η, and ν are: the shape, slope, and departure from the uniform distribution of the phase parameters [12]–[16]. It is worth to note that for $\nu = 0$ (strong scattering regime) (8) becomes the two parameters K-distribution [21]. Equation (8) for $\alpha \to \infty$ becomes

$$P(I) = \frac{1}{\eta^2} \exp\left(-\frac{\nu^2}{4}\right) \exp\left(-\frac{I}{\eta^2}\right) I_o\left(\frac{\nu}{\eta}\sqrt{I}\right) \tag{9}$$

known as von Laue-Rice pdf and used for characterization of reverberating chambers [18]. In [16] (9) has been rewritten in terms of the Rice factor, i.e., the coherent to incoherent mean intensity field ratio $R = \overline{I}c/\overline{I}i$,

$$P(I) = \frac{1+R}{\overline{I}} \exp(-R) \exp\left(-\frac{I}{\overline{I}}(1+R)\right) I_o\left(2\sqrt{\frac{I}{\overline{I}}R(1+R)}\right) \tag{10}$$

leading to the following expression of η and ν by direct comparison of (9) and (10)

$$\eta = \sqrt{\frac{\overline{I}}{R+1}} \tag{11}$$

$$\nu = 2\sqrt{R}. \tag{12}$$

In [17], a sensitivity analysis of the parameter η and ν, using C-band fine quad-pol SLC SAR data, regarding metallic objects observation has been conducted, taking into account the three possible combinations, e.g., HH, VV and HV. As outcome of this study, a simple combination of GK parameters is proposed to observe targets at sea in full-resolution co-polarized and cross-polarized C-band SAR images:

$$\gamma = (\nu/\eta)^2 \tag{13}$$

showing that γ is a great improvement in terms of contrast for the HV channel.

C. Methodology

The complete processing chain, proposed in this paper to perform both detection and discrimination of targets from azimuth ambiguities at sea, is summarized with the flowchart in Fig. 3.

The pre-processing step (see Fig. 3) consists in the calibration and incidence angle correction of the SSC full polarimetric X-band SAR data. Both cross-polarized channels, i.e., HV and VH, are then used to create an ambiguity free image, hereafter called HV_{free}. To perform the discrimination step (see Fig. 3), according to (7) in the previous theoretical sub-section, the following combination of the cross-polarized channels is proposed:

$$\text{HV}_{free} = \frac{1}{2}\left[(S_{HV} + S_{VH})(S_{HV} + S_{VH})^*\right] \tag{14}$$

where S_{HV} and S_{VH} are the two calibrated SLC cross-polarized channels. The effectiveness of (14) in cancelling out azimuth ambiguities is shown in Fig. 4. It must be pointed out that (14) is a pixel-based method to resolve azimuth ambiguities, therefore good for small targets because the original resolution is kept.

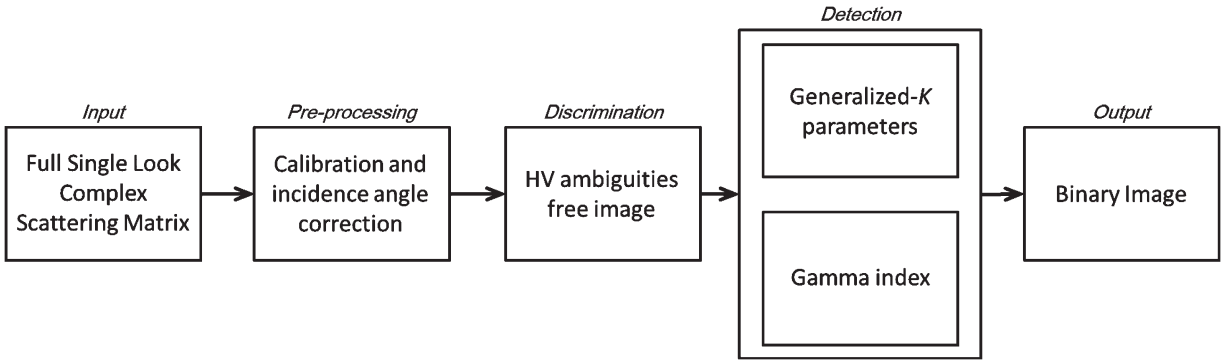

Fig. 3. Sketch of the proposed methodology.

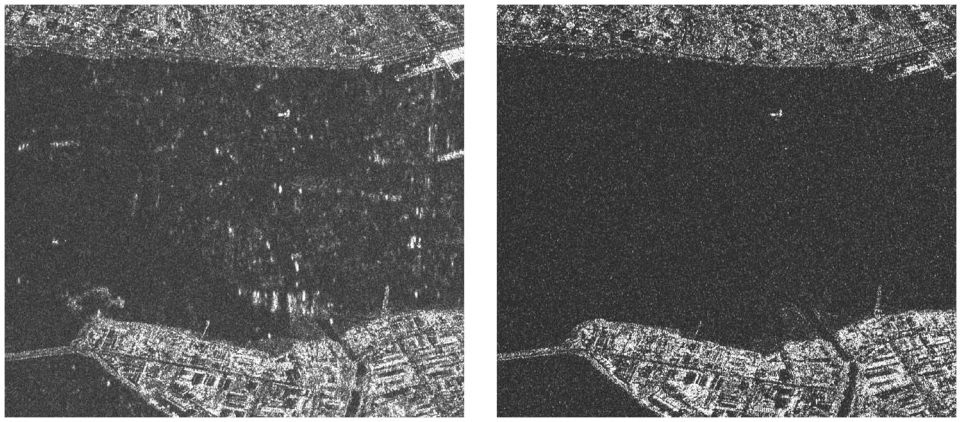

Fig. 4. Excerpt of the data set SI listed in Table I showing a patch of the navigable water of Strait of Johor (between Singapore and Malaysia); (Left) single-look HH power image in slant range projection. The azimuth ambiguities are quite visible making the detection of possible targets very hard. (Right) Single-look HV_{free} power image in slant range projection. Ambiguities have been efficiently canceled out.

TABLE II
GK PARAMETERS AND DERIVATIVES ESTIMATED FROM TERRASAR-X SAR DATA OF FIG. 5

	T1	S1	T2	S2	T3	S3	T4	S4	T5	S5	T6	S6	T7	S7	T8	S8
η_{HV}	0.513	0.070	0.752	0.087	0.816	0.073	0.575	0.073	0.908	0.074	0.489	0.071	0.532	0.079	0.78	0.072
ν_{HV}	1.697	2.060	1.590	2.050	1.812	2.053	1.899	2.074	1.803	2.066	1.752	2.070	1.849	2.074	1.897	2.070
$\eta_{\mathrm{HV}free}$	0.632	0.079	1.045	0.090	1.107	0.077	0.825	0.076	1.308	0.078	0.666	0.075	0.742	0.083	1.113	0.074
$\nu_{\mathrm{HV}free}$	1.657	2.071	1.584	2.052	1.795	2.085	1.899	2.054	1.807	2.072	1.712	2.079	1.804	2.076	1.868	2.053
γ_{HV}	10.94	866.0	4.470	555.2	4.931	790.9	10.91	807.2	3.943	779.4	12.83	850.0	12.08	689.2	5.914	826.5
$\gamma_{\mathrm{HV}free}$	6.874	687.2	2.297	519.8	2.629	733.2	5.298	730.4	1.908	705.6	6.607	768.4	5.911	625.6	2.817	769.7
C_{HV}	79.14		124.2		160.4		74.01		197.7		66.22		57.05		139.7	
$\mathrm{C}_{\mathrm{HV}free}$	99.98		226.3		278.9		137.9		369.8		116.3		105.8		273.2	

In the detection step (see Fig. 3), the estimated GK parameters, given by (11) and (12), are used to evaluate the γ index, given by (13), over the HV_{free} image. It must be pointed out that (11) and (12) are related to the Rice factor R. Here, R is valued employing a suboptimal Rice factor estimator suggested in [16], [17], [22] for metallic objects observation in full-resolution SAR data and here applied over the ambiguities free image:

$$\widehat{\boldsymbol{R}} = \frac{\left[mean(\mathrm{HV}_{free})\right]^2}{2\left[var(\mathrm{HV}_{free})\right]} \tag{15}$$

where mean and variance are estimated in a $m \times m$ moving window. Here, the window's dimension is set to $m = 3$ in order to detect ships having size comparable to the sensor resolution, while minimizing the decrease of the image resolution. Before proceeding further, a focused sensitivity study of the GK parameters (11) and (12) is conducted on both HV and HV_{free} data. All targets in Fig. 5 have been labeled as T1 to T8, while the reference to the surrounding sea is S1 to S8. Table II summarizes η and ν measurements and lists the γ values obtained on both HV and HV_{free} images. For direct comparison, the contrast parameters $\mathbf{C_{HV}}$ and $\mathbf{C_{HV}}_{\boldsymbol{free}}$, defined as the ratio of

TABLE III
OVERVIEW OF THE RESULTS OBTAINED FOR THE PROCESSED DATA SET

Scene	No. Targets	Targets with AIS (*detected*)	Visually inspected ships[A] (*detected*)	Visually inspected targets[b] (*detected*)	Tot. Missed	Ambiguites	False positive caused by Ambiguities
NS_1	18	8(*8*)	0(*0*)	10(*9*)	1	Land&Targets	0
NS_2	19	5(*5*)	6(*6*)	8(*7*)	1	Land&Targets	0
FI	23	14(*14*)	9(*9*)	0(*0*)	0	Tragets	0
SF	29	7(*7*)	18(*18*)	4(*4*)	0	Land&Targets	0
SI	147	0(*0*)	120(*118*)	27(*24*)	5	Land&Targets	0

[a]Amount of targets without AIS classified as ships because of clear signature of ship wakes or others.
[b]Amount of targets without AIS that are possible targets, i.e. buoys, navigation aids, etc., that could not be classified as ships.

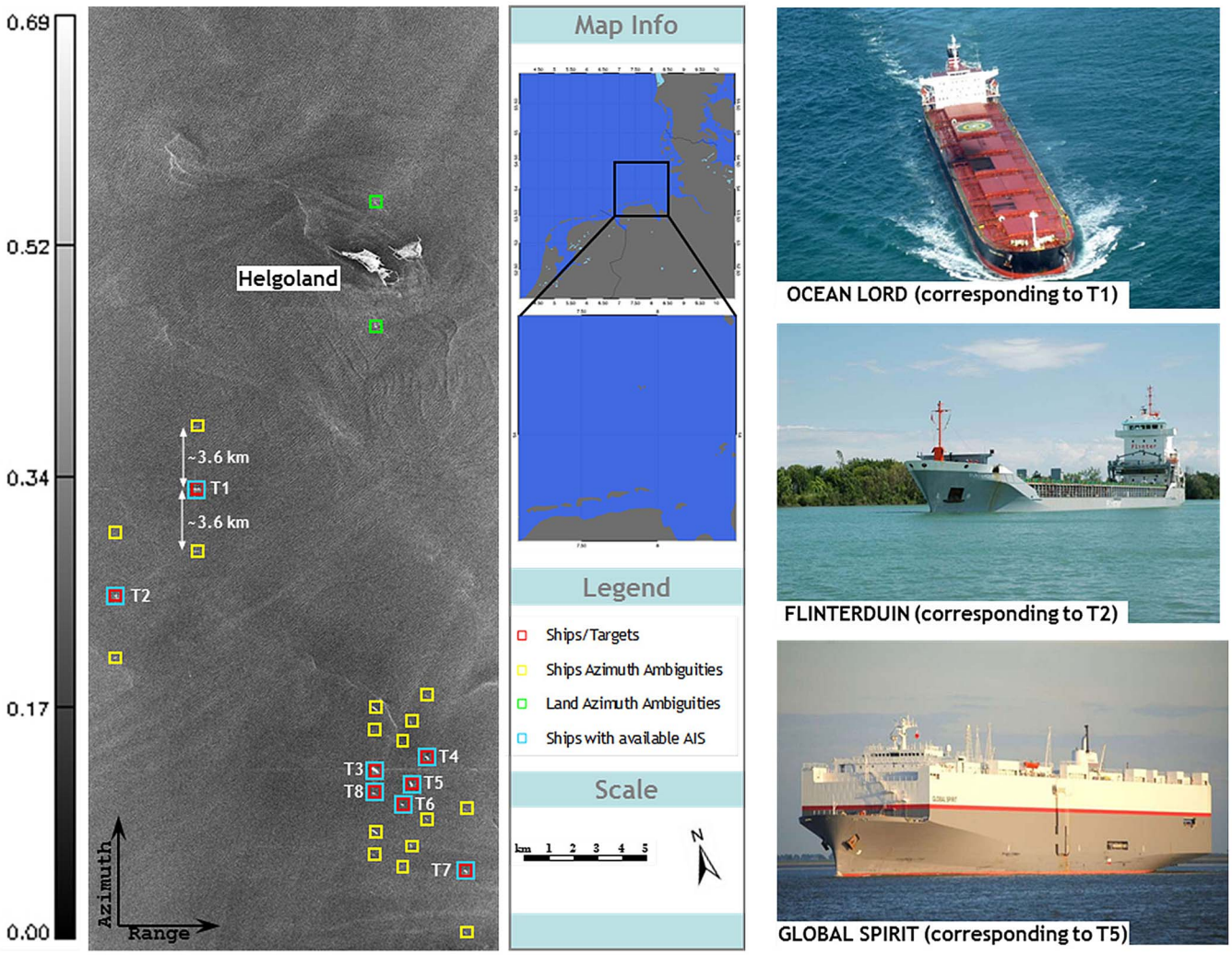

Fig. 5. HH slant range amplitude projection image acquired over Helgoland Island in North Sea, named NS_1 in Table I. Several ships have been imaged and labeled as T1 to T8. The image shows also several azimuth ambiguities caused by targets or strong scatterer over land.

γ obtained for sea and target in HV and HV_{free} images, are included. The following can be noted.

- η and ν valuated within both regions of interest, i.e., targets and sea, for HV_{free} show the same trend of the ones obtained for HV. This shows that the proposed index is congruent.
- η values over targets are one order of magnitude larger than over sea ones, while ν values are comparable. This result shows that the GK parameters are sensible with respect to targets in X-band data, too.
- Targets and sea are well separated in terms of the index γ. Therefore, γ, originally proposed in [13] for C-band

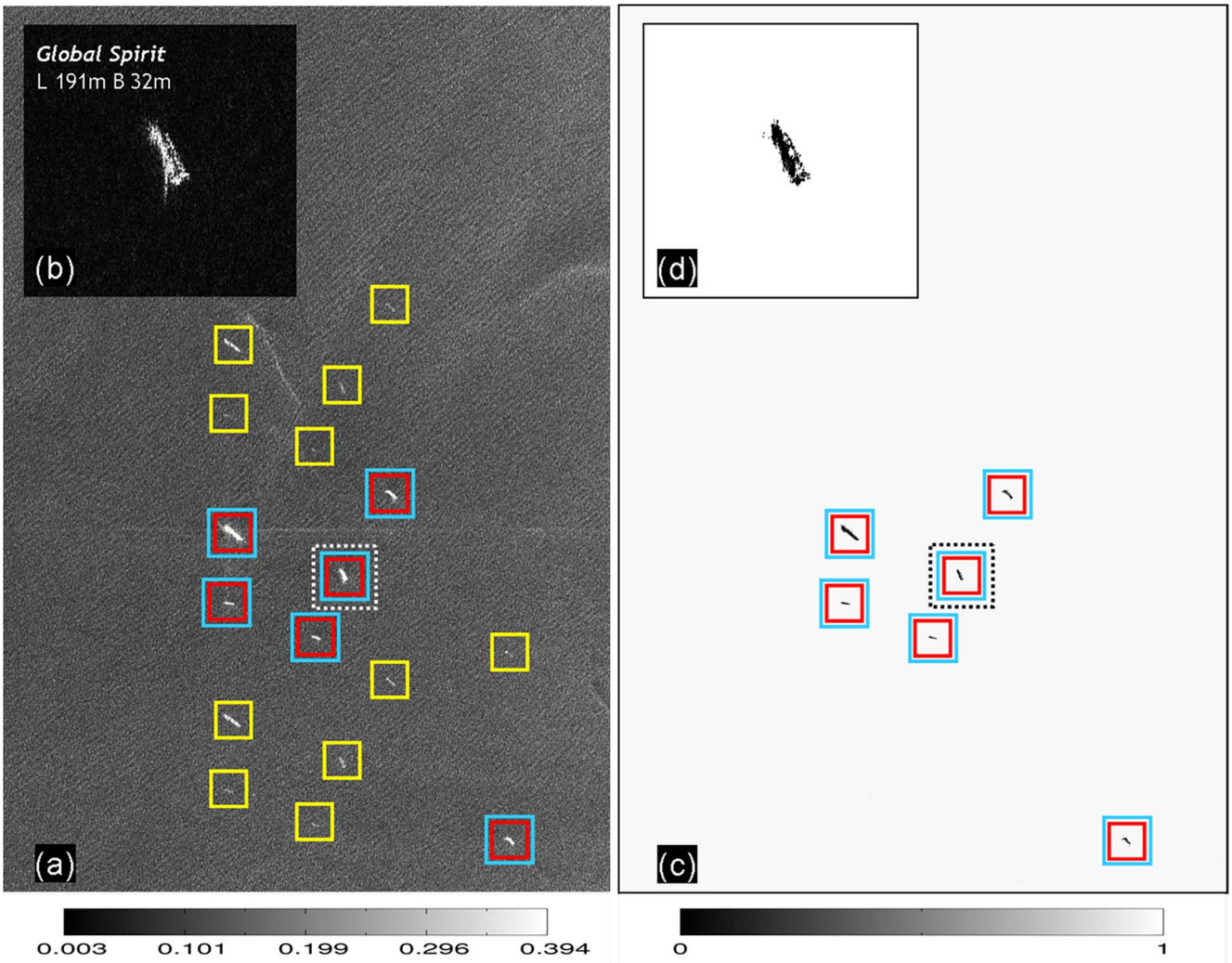

Fig. 6. Excerpt of the data set NS_1 shown in Fig. 5. (a) HH slant range amplitude projection image, (red rectangle) ships/targets, (yellow rectangle) azimuth ambiguities caused by ships/targets, (cyan rectangle) available AIS data; (b) zoom of the white dashed box with the Global Spirit cargo ship and dimension info; (c) comparison of available AIS info and logical true–false output; (d) zoom of the black dashed box correspondent to the cargo ship Global Spirit.

SAR data, can be used to observe targets at sea in full-resolution X-band SAR data.

– γ estimated over the HV_{free} data, shows a gain in terms of contrast of factor ~ 2 compared to the HV one (see $\mathbf{C_{HV}}$ and $\mathbf{C_{HV}}_{free}$ in Table II).

As outcome of the sensitivity study, the following rule is established to perform target detection and to create the binary output image:

$$\begin{cases} \gamma_{\mathbf{HF}free} < \mathbf{10} \Rightarrow \text{target} \\ \gamma_{\mathbf{HF}free} \geq \mathbf{10} \Rightarrow \text{sea} \end{cases}$$

in this way, target and sea pixels are assigned to 0 and 1 in the logical true–false output image, respectively.

IV. Experimental Results

In this section, the experimental results obtained using the proposed processing chain to remove azimuth ambiguities are introduced and discussed.

The processed data set consists of five X-band SSC quad polarization TS-X images acquired in DRA mode, in which both ships/targets and land azimuth ambiguities are present. Basic info on the processed data set are listed in Table I, together with sensor's features and weather conditions for reference. The data set counts different satellite configuration and weather conditions. Available AIS data, collocated with satellite overpasses, are used as ground truth and compared with the detection outputs in order to evaluate the performances of the whole processing chain.

Three experiments are described and presented in detail, while the overall results are summarized in Table III.

The first case is relevant to the acquisition of April 18, 2010 at 05:50 UTC over Helgoland Island situated in North Sea (named NS_1 in Table I). The HH-polarized amplitude image (in slant range projection) is shown in gray tones in Fig. 5. Several bright spots, eight identified as ships (red rectangles) by collocated AIS info (cyan rectangles), are visible together with azimuth ambiguities caused by ships (yellow rectangles) and strong scatterers over land (green rectangles). According

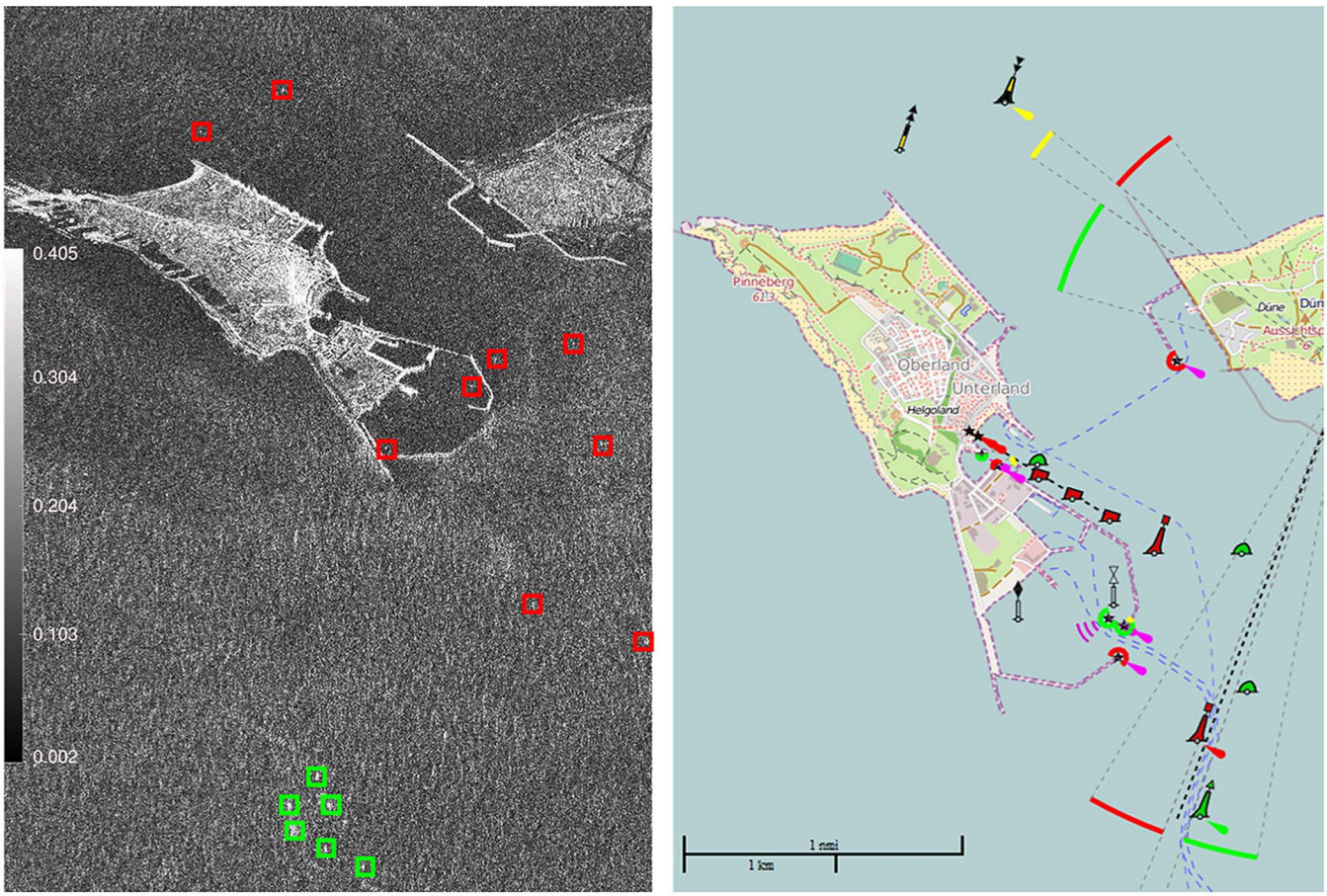

Fig. 7. Excerpt of the data set NS_1 shown in Fig. 5; [Left] HH slant range amplitude projection image, (red rectangle) small targets around Helgoland's harbor area, (green rectangle) azimuth ambiguities caused by strong scatterers over Helgoland's city; [Right] nautical chart of Helgoland Island showing buoys, navigation aids, etc. around the Island.

to (1), and taking into account the specifics of TS-X DRA mode, the azimuth displacement is estimated to be $\sim$3.6 km (indicated with white arrows in Fig. 5 for visual interpretation). Note also the presence of several oceanographic processes along the image (internal waves, breaking waves, and sea currents), which are possible sources of false detection. In the following, a detailed analysis of the two areas of Fig. 5 are discussed.

The first sub-scene of Fig. 5 is shown in Fig. 6. HH-polarized amplitude image in Fig. 6(a) shows SAR signatures of ships and their azimuth ambiguities. Zoom of the white dashed box with the Global Spirit cargo ship and the AIS info is shown in Fig. 6(b). Note that the amplitude values in Fig. 6(b) are stretched in a way that the structure of the imaged target is highlighted. Low backscattering areas inside the cargo ship are due to the low energy received from flat metal regions of the cargo's deck. This effect has been experienced in high-resolution SAR images of cargo ships and is hardly noticeable in low-medium resolution SAR images. Logical true–false image with overlapping available AIS data (cyan rectangle) are shown in Fig. 6(c). The comparison of ground truth data and detection outputs demonstrate the effectiveness of the proposed methodology to discriminate real targets from azimuth ambiguities. In the framework of ship detection applications, all "true" targets are correctly detected, i.e., none of the azimuth ambiguities is mistaken as target. Fig. 6(d) shows how well the ship's structure is preserved in the detection step by visual comparison with Fig. 6(b).

The second sub-scene of Fig. 5, relevant to the surrounding area of Helgoland Island, is shown in Fig. 7. The HH-polarized amplitude image in the left panel of Fig. 7 shows the SAR signature of small targets (red rectangles), azimuth ambiguities caused by strong scatterers from Helgoland city (green rectangles) and breaking waves around the southwest side of Helgoland. It must be noted that these targets are not indicated in Fig. 5 because being very small (few pixels), only a zoom-in highlights their presence. The right panel of Fig. 7 is the nautical chart of Helgoland Island showing buoys, navigation aids, etc. Although, the nautical chart is updated at August, 2011, while the SAR image has been acquired in April, 2010 and is shown in slant range projection, most of the small targets in the SAR image have a correspondence to the nautical chart, e.g., the three targets at the east side of Helgoland harbor. The corresponding logical true–false output is shown in the left panel of Fig. 8 where land has been masked in purple and detected targets are pointed with red rectangles. The result confirms that the proposed methodology works also for ambiguities caused by strong scatterers over land. This is a very interesting outcome because such "false" targets are hardly discarded by post-processing ambiguities removal techniques, i.e., the one

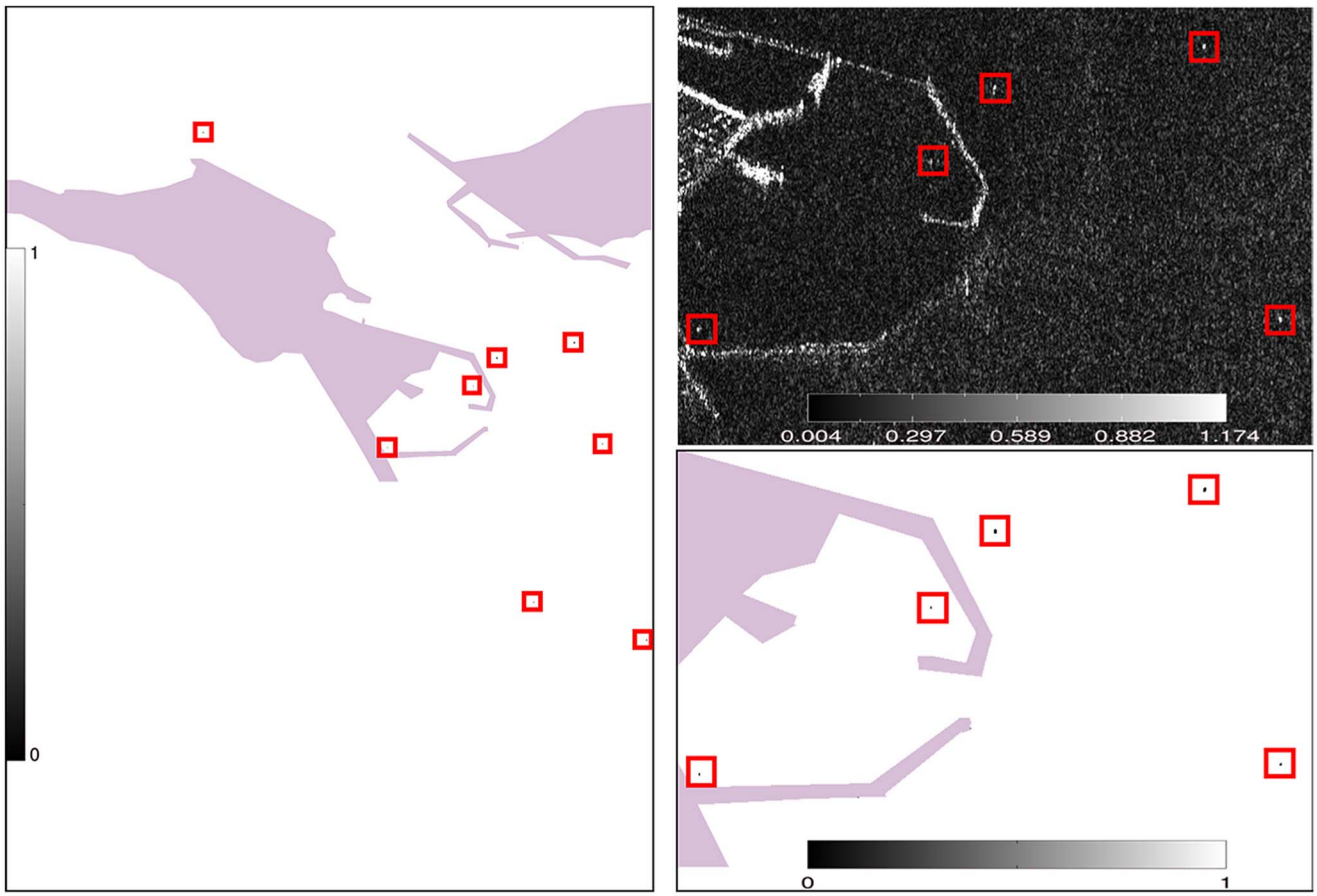

Fig. 8. Excerpt of the data set NS_1 shown in Fig. 5; [Left] logical true–false output obtained for sub-scene shown in Fig. 7, red rectangles indicate detected target, land is masked in purple; [Right] upper panel zoom of Helgoland's harbor, lower panel logical true–false output with detected small targets validated with the use of the nautical chart shown in the right panel of Fig. 7.

that looks at $\pm\Delta x_{\mathrm{AZ}}$ from detected targets. Helgoland's harbor area is shown in full resolution on the upper-right panel of Fig. 8 in order to highlight small targets. The corresponding logical true–false output is shown in the bottom-right panel of Fig. 8, further validating the proposed method in the detection of small targets. It is worth noting that groups of bright pixels caused by breaking waves located far from the harbor entrance are not detected (see left panel Fig. 8).

The second case is relevant to the acquisition of April 29, 2010 at 05:50 UTC over Helgoland Island in North Sea (named NS_2 in Table I).

A large area of the NS_2 data set has been previously selected, and it is shown in Fig. 9. The HH-polarized amplitude sub-scene (left panel of Fig. 9) shows in gray tones several bright spots, six identified as ships (red rectangles), three of which by collocated AIS info (cyan rectangles) and the rest visually by the presence of wakes. Azimuth ambiguities caused by the imaged ships are pointed with yellow rectangles in the left panel of Fig. 9. The OOCL Washington cargo ship in the upper-left side of the Fig. 9 gives the uncommon opportunity to analyze second and third indexes of azimuth ambiguities. The corresponding logical true–false output is shown in the right panel of Fig. 9 where detected targets are pointed by red rectangles and available AIS info with cyan rectangles. Comparison to ground truth data and detected targets confirms consistency to what has been previously shown. Furthermore, it demonstrates that (7) applies for n-th index of azimuth ambiguities as shown mathematically in the Section III-A.

The third case is relevant to the acquisition of April 11, 2010 at 14:15 UTC over San Francisco Bay Area (named SF in Table I).

A challenging area of the SF data set has been previously selected, and it is shown in Fig. 10. The HH-polarized amplitude sub-scene (left panel of Fig. 10) shows in gray tones the coastal zone of Richmond City in the inner East Bay with part of the Richmond-San Rafael Bridge and the Chevron refinery in the upper-right corner of the image. By visual inspection, seven targets have been identified (red rectangles) and classified as: three moored tankers (all fasten to the Chevron tanker terminal), three moving ships, and one moored platform. The SAR sub-scene is characterized by the presence of strong land azimuth ambiguities caused mainly by the Chevron refinery tanks. Bright spots in the middle of the image reproduce clearly the shape of the refinery area. Azimuth ambiguities caused by the imaged targets are also present and pointed with yellow rectangles. The corresponding logical true–false output is shown in the right panel of Fig. 10 where the land is masked in purple and detected targets are pointed by red rectangles. The comparison

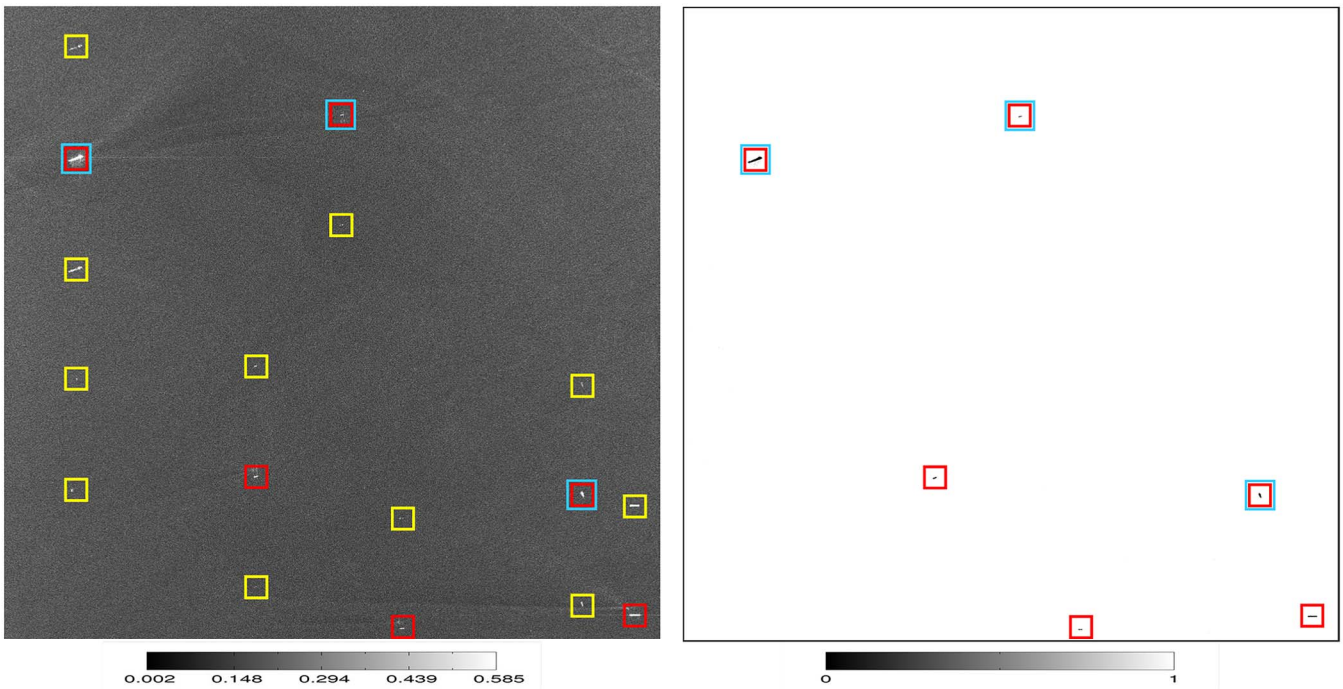

Fig. 9. Excerpt of the data set NS_2 listed in Table I; [Left] HH slant range amplitude projection image, (red rectangle) ships/targets, (yellow rectangle) azimuth ambiguities caused by ships/targets, (cyan rectangle) available AIS data; [Right] comparison of available AIS info and logical true–false output.

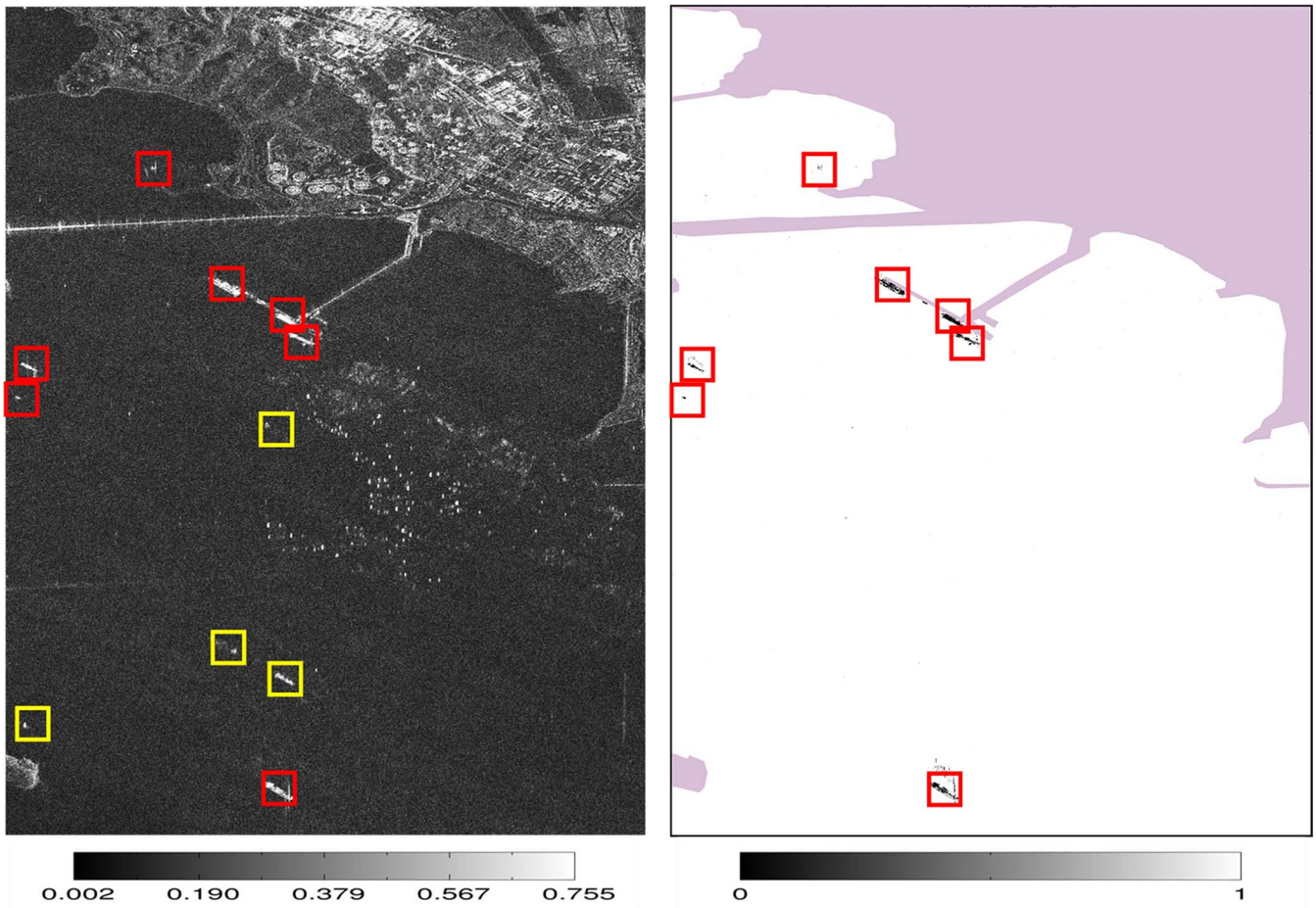

Fig. 10. Excerpt of the data set SF listed in Table I; [Left] HH slant range amplitude projection image, (red rectangle) ships/targets, (yellow rectangle) azimuth ambiguities caused by ships/targets; [Right] logical true–false output, land is masked in purple.

of the detected targets and visually inspected targets reveals a good agreement even for a challenging area as the one under investigation, i.e., none of the azimuth ambiguities is mistaken as a possible target.

An overview of the results obtained for the data set considered is listed in Table III. In Table III, targets without AIS messages have been visually classified in two categories:—ships, in the case, the SAR signature could be associated to this category, e.g., presence of wakes, shape, and so on;—targets if no evidences could be found, e.g., typically small man-made structure (few pixels in the image) like buoys, navigation aids, and so on, with the help of nautical charts where available. The overall results show that, independently from the nature of the azimuth ambiguities and weather conditions, false alarms caused by ambiguities are reduced to zero without any post-processing step. Furthermore, in terms of detection, the performance is quite good with an overall detection of 97%.

V. Summary and Conclusion

In this paper, a new methodology for azimuth ambiguities removal in the framework of SAR ship detection application has been proposed and tested over a meaningful data set of full polarimetric X-band TS-X images acquired during the experimental DRA campaign in April and May 2010. The methodology proposed takes the complete benefit of PolSAR data combined with the high-resolution capability of X-band sensors. In the pre-processing step, both cross-polarization channels are used to generate an ambiguity free image exploiting the fact that, for targets, HV and VH channels are approximately equal in magnitude and phase, i.e., the reciprocity theorem applies, but opposed in phase for azimuth ambiguities. For the detection step, a physical model, based on a combination of GK parameters evaluated over the azimuth ambiguity free image, is applied to observe metallic targets, i.e., ships, buoys and etc., in high-resolution X-band SAR images. AIS data are used as ground truth to evaluate the performances of the proposed methodology to detect "true" targets avoiding false detections caused by targets or land ambiguities over ocean surface.

In summary, the key results emerging from this study can be listed as follow:

- False alarms caused by targets or land azimuth ambiguities over the ocean surface can be reduced to zero exploiting PolSAR data.
- The proposed detection methodology shows a good consistency when compared to ground truth data, i.e., none of the ambiguities is misguided as target.
- Small targets are observed and efficiently detected.

In addition to the aforementioned scientific results, the potential of an existing two-channel X-band PolSAR system has been demonstrated. The results obtained here strongly support the use of X-band PolSAR data for marine target detection purposes, particularly where the problem of ambiguities might be critical, i.e., harbors and coastal areas. Furthermore, it justifies the design of future fully polarimetric high-resolution SAR missions for maritime security applications.

References

[1] H. Greidanus, "Satellite imaging for maritime surveillance of the European seas," in *Remote Sensing of the European Seas*, vol. XXII. New York: Springer-Verlag, 2008, pp. 343–358.

[2] S. Brusch, S. Lehner, T. Fritz, and M. Soccorsi, "Ship surveillance with TerraSAR-X," *IEEE Trans. Geosci. Remote Sens.*, vol. 49, no. 3, pp. 1092–1103, Mar. 2011.

[3] J.-S. Lee, E. Krogager, T. L. Ainsworth, and W.-M. Boerner, "Polarimetric analysis of radar signature of a manmade structure," *IEEE Geosci. Remote Sens. Lett.*, vol. 3, no. 4, pp. 555–559, Oct. 2006.

[4] C. Liu and C. H. Gierull, "A new application for PolSAR imagery in the field of moving target indication/ship detection," *IEEE Trans. Geosci. Remote Sens.*, vol. 45, no. 11, pp. 3426–3436, Nov. 2007.

[5] A. M. Guarnieri, "Adaptive removal of azimuth ambiguities in SAR images," *IEEE Trans. Geosci. Remote Sens.*, vol. 43, no. 3, pp. 625–633, Mar. 2005.

[6] R. Bamler and H. Runge, "PRF-Ambiguity resolving by wavelength diversity," *IEEE Trans. Geosci. Remote Sens.*, vol. 29, no. 6, pp. 997–1003, Nov. 1991.

[7] A. Moreira, "Suppressing the azimuth ambiguities in synthetic aperture radar images," *IEEE Trans. Geosci. Remote Sens.*, vol. 31, no. 4, pp. 885–895, Jul. 1993.

[8] C. C. Wackerman, K. S. Friedman, W. G. Pichel, P. Clemente-Colon, and X. Li, "Automatic detection of ships in RADARSAT-1 SAR imagery," *Can. J. Remote Sens.*, vol. 27, no. 5, pp. 568–577, Oct. 2001.

[9] P. W. Vachon, S. J. Thomas, J. Cranton, H. R. Edel, and D. Henschel, "Validation of ship detection by the RADARSAT synthetic aperture radar and the ocean monitoring workstation," *Can. J. Remote Sens.*, vol. 26, no. 3, pp. 200–212, 2000.

[10] D. J. Crisp, "The State-of the Art in Ship Detection in Synthetic Aperture Radar Imagery," Intell., Surveillance and Reconnaissance Div., Inf. Sci. Lab., Def., Sci. Technol. Org., Edinburgh, Australia, Res. Rep DSTO-RR-0272, May 2004.

[11] S. Brusch, S. Lehner, E. Schwarz, and T. Fritz, "Near real time ship detection experiments," in *Proc. SEASAR Workshop, ESA Commun. Prod. Office*, Frascati, Italy, Jan. 25–29, 2010.

[12] K. D. Ward, R. J. Tough, and S. Watt, *Sea Clutter: Scattering, the K Distribution and Radar Performance*. London, U.K.: The Institution of Engineering and Technology, 2006, ser. IET Radar, Sonar, Navigation and Avionics series 20.

[13] E. Jakeman and P. N. Pusey, "A model for non-Rayleigh sea echo," *IEEE Trans. Antennas Propag.*, vol. AP-24, no. 6, pp. 806–814, Nov. 1976.

[14] E. Jakeman and P. Tough, "Generalized K distribution: A statistical model for weak scattering," *J. Opt. Soc. Amer. A, Opt. Image Sci.*, vol. 4, no. 9, pp. 1764–1772, 1987.

[15] A. L. Maffett and C. C. Wackerman, "The modified beta density function as a model for synthetic aperture radar clutter statistics," *IEEE Trans. Geosci. Remote Sens.*, vol. 29, no. 2, pp. 277–283, Mar. 1991.

[16] M. Migliaccio, G. Ferrara, A. Gambardella, F. Nunziata, and A. Sorrentino, "A physically consistent speckle model for marine SLC SAR images," *IEEE J. Ocean. Eng.*, vol. 32, no. 4, pp. 839–847, Oct. 2007.

[17] G. Ferrara, M. Migliaccio, F. Nunziata, and A. Sorrentino, "Generalized-K (GK)-based observation of metallic objects at sea in full-resolution Synthetic Aperture Radar (SAR) data: A multipolarization study," *IEEE J. Ocean. Eng.*, vol. 36, no. 2, pp. 195–204, Apr. 2011.

[18] H. Breit, T. Fritz, U. Balss, M. Lachaise, A. Niedermeier, and M. Vonavka, "TerraSAR-X SAR processing and products," *IEEE Trans. Geosci. Remote Sens.*, vol. 48, no. 2, pp. 727–740, Feb. 2010.

[19] M. Gabele, B. Bräutigam, D. Schulze, U. Steinbrecher, N. Tous-Ramon, and M. Younis, "Fore and aft channel reconstruction in the TerraSAR-X dual receive antenna mode," *IEEE Trans. Geosci. Remote Sens.*, vol. 48, no. 2, pp. 795–806, Feb. 2010.

[20] J. Mittermayer and H. Runge, "Conceptual studies for exploiting the TerraSAR-X dual receive antenna," in *Proc. IEEE IGARSS*, Toulouse, France, Jul. 2003, pp. 2140–2142.

[21] P. Corona, G. Ferrara, and M. Migliaccio, "Generalized stochastic field model for reverberating chambers," *IEEE Trans. Electromagn. Compat.*, vol. 46, no. 4, pp. 665–660, Nov. 2004.

[22] A. Gambardella, F. Nunziata, and M. Migliaccio, "A physical full-resolution SAR ship detection filter," *IEEE Geosci. Remote Sens. Lett.*, vol. 5, no. 4, pp. 760–763, Oct. 2008.

Domenico Velotto (S'09) was born in Italy, on April 30, 1981. He received the M.S. degree (5-years legal course of study) in nautical science (Curriculum Electronic Radio-Navigation) from the Università degli Studi di Napoli "Parthenope," Napoli, Italy, in 2008.

In 2009, he joined the synthetic aperture radar (SAR) oceanography group at the Remote Sensing Technology Institute, German Aerospace Center (DLR), Wessling, Germany, where he is currently working toward the Ph.D. degree. His M.S. degree thesis was recipient of the 2008 Best Remote Sensing Thesis Award by the IEEE GRS South Italy Chapter. His main research interests deal with electromagnetic modeling, image processing, and Earth observation with SAR polarimetry with emphasis on oil spill and target detection and classification.

Matteo Soccorsi (S'05–M'10) received the M.S. degree in telecommunication engineering from the University of Rome "Tor Vergata," Rome, Italy, in 2005 and the Ph.D. degree in signal and images from Télécom ParisTech, Paris, France, in 2010.

He was with the German Aerospace Center (DLR), Wessling, Germany. He held a postdoctoral position, which is supported by the German Academic Exchange Service (DAAD), in the Marine Remote Sensing Group, Remote Sensing Technology Institute (DLR/IMF). His primary research interests include the development of algorithms for ship detection and ground moving target indicators, with emphasis on the analysis of single-channel complex synthetic aperture radar images.

Susanne Lehner received the M.Sc. degree in applied mathematics from Brunel University, Uxbridge, U.K., in 1979 and the Ph.D. degree in geophysics from the University of Hamburg, Hamburg, Germany, in 1984.

She was a Research Scientist with the Max-Planck Institute for Climatology, Hamburg, and joined the German Aerospace Center (DLR/DFD), Wessling, Germany, in 1996. She is currently a Research Scientist in marine remote sensing with the Remote Sensing Technology Institute (DLR/IMF), German Aerospace Center, working on the development of algorithms determining marine parameters from synthetic aperture radars.

A.5. Velotto, D., Bentes, C., Tings, B., Lehner, S., 2015. First comparison of Sentinel-1 and TerraSAR-X data in the framework of maritime targets detection: South Italy case. IEEE Journal of Oceanic Engineering, *accepted for publication*

First Comparison of Sentinel-1 and TerraSAR-X Data in the Framework of Maritime Targets Detection: South Italy Case

Domenico Velotto, *Member, IEEE*, Carlos Bentes, Björn Tings, and Susanne Lehner

***Abstract*—The Sentinel-1A is the first of two satellites that composes the Sentinel-1 radar mission. Both satellites operate a C-band synthetic aperture radar (SAR) system to give continuity to the European SAR program. SAR is a flexible sensor able to fulfil users/applications requirements in terms of resolution and coverage thanks to different operational modes and polarizations. With the in-orbit availability of very-high-resolution X-band SAR sensors, the Sentinel-1 satellites have been designed to achieve wide coverage at medium to high resolution. The interferometric wide swath (IWS) mode implemented with the terrain observation with progressive scan (TOPS) technique is the standard acquisition mode over European waters and land masses. IWS in dual-polarization (VV/VH) combination offers 250-km swath at 5 m × 20 m (range × azimuth) spatial resolution. These specifications are in line with the needs of the European Maritime and Security Agency (EMSA) for oil spill and ship detection applications included in the CleanSeaNet program. The main goals of this paper are: assessment of medium-to-high-resolution C-band Sentinel-1 data with very-high-resolution X-band TerraSAR-X data for maritime targets detection; synergetic use of multiplatforms satellite SAR data for target features extraction; evaluation of polarimetric target detectors for the available co-polarization and cross-polarization Sentinel-1A IWS VV/VH products. The objectives are achieved by means of real, almost coincident C-band and X-band SAR data acquired by Sentinel-1A and TerraSAR-X satellites over Gulf of Naples and Catania (South Italy). Furthermore, the obtained results are supported by recorded ground truth vessel reports via terrestrial automatic identification system (AIS) stations located in the area.**

***Index Terms*—Multifrequency, multipolarization, synthetic aperture radar (SAR), targets detection.**

I. Introduction

With the launch of Sentinel-1A satellite on April 3, 2014 the European Radar Observatory program became operative in the framework of the Copernicus initiative. Copernicus, previously known as Global Monitoring for Environment and Security (GMES), is a joint initiative of the European Commission (EC) and the European Space Agency (ESA) established with the objective of the implementation of services dealing with environment and security [1]. Thanks to the experience gained by working groups in several European Union (EU) projects, in the Copernicus initiative three priority services have been identified: marine, land, and emergency services.

Sentinel-1 is a long-term constellation mission composed of two C-band radar polar orbiting satellites, i.e., Sentinel-1A and Sentinel-1B (launch of the second is scheduled for 2016), that provides continuous all-weather day/night imagery for the following identified applications [1], [2]:

1) land forests, waters, soil, and agriculture monitoring;
2) natural disasters support via emergency mapping;
3) maritime environment monitoring;
4) sea ice and iceberg observation;
5) high-resolution ice charts production;
6) sea and ice condition forecast;
7) oil spills mapping;
8) sea vessel detection;
9) climate change monitoring.

Each of these particular applications has different needs in terms of coverage, spatial resolution, noise floor, and radar polarization. Nevertheless, synthetic aperture radar (SAR) is a flexible sensor able to fulfil users/applications requirements with a single instrument, thanks to the possibility of implementing different operational modes. Recent SAR missions offer also multipolarization (dual- or full-polarization) acquisition capabilities.

With the availability of commercial very-high-resolution X-band SAR sensors like the German TerraSAR-X/TanDEM-X constellation and the Italian Cosmo-SkyMed 4 satellites constellation, Sentinel-1 satellites have been designed to achieve medium-to-high-resolution imaging capabilities and wide coverage. Despite the aforementioned SAR flexibility, wide coverage and very-high-resolution imagery at the same time are not possible with the actual SAR design technology.

Sentinel-1 is the first satellite built with interferometric wide swath (IWS) mode exploiting the terrain observation with progressive scan (TOPS) technique. IWS is the standard acquisition mode over European waters and land masses for both interferometric applications, e.g., digital elevation model (DEM), and maritime surveillance applications, e.g., pollution and vessel monitoring. IWS in dual-polarization (VV/VH) combination offers 250-km swath at 5 m × 20 m (range × azimuth) spatial resolution in single look. These imagery characteristics are in line with the needs of the satellite SAR-based oil pollution and ship detection European CleanSeaNet service established by the European Maritime and Security Agency (EMSA). As a matter of fact, when a single SAR polarization

Manuscript received January 21, 2015; revised June 03, 2015, September 11, 2015, and December 08, 2015; accepted January 15, 2016.

Associate Editor: R. Romeiser

The authors are with the Maritime Security Lab, Remote Sensing Technology Institute, German Aerospace Center, Bremen 28199, Germany (e-mail: Domenico.Velotto@dlr.de; Carlos.Bentes@dlr.de; Bjoern.Tings@dlr.de; Susanne.Lehner@dlr.de).

Digital Object Identifier 10.1109/JOE.2016.2520216

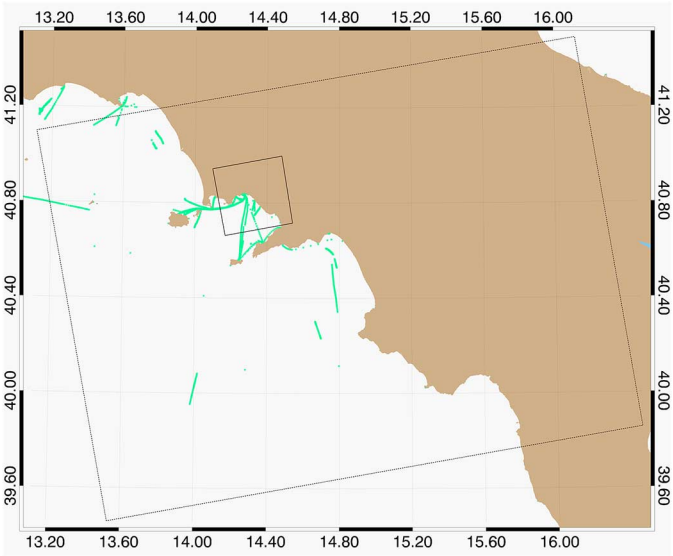

Fig. 1. Collected AIS messages (green dots) inside the boundary box given by the acquired Sentinel-1 (dashed black line) and TerraSAR-X (continuous black line) SAR data over Gulf of Naples, Italy. The time span is approximately 1 h before and 0.5 h after the satellite overpasses.

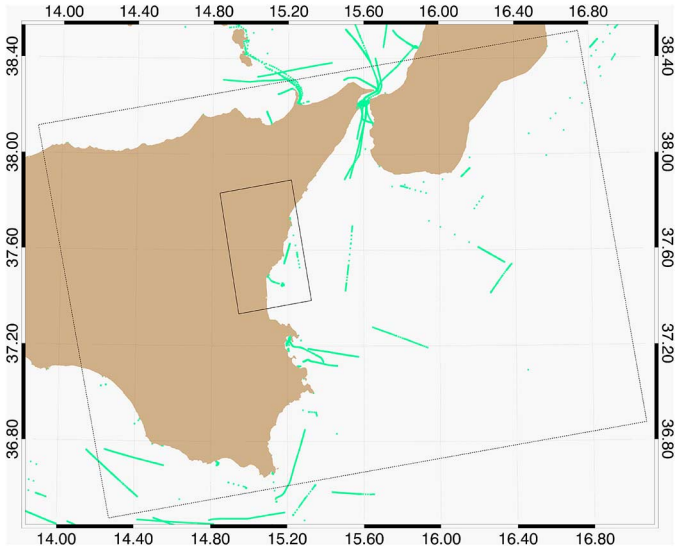

Fig. 2. Collected AIS messages (green dots) inside the boundary box given by the acquired Sentinel-1 (dashed black line) and TerraSAR-X (continuous black line) SAR data over Catania, Italy. The time span is approximately 1 h before and 0.5 h after the satellite overpasses.

is available, VV polarization is the preferred choice for oil spill detection algorithms and HH polarization is preferred for ship detection algorithms [3]. In [4], the potential use of SAR cross-polarization combination (HV or VH) for ship detection is discussed and shown to be useful especially at low incidence angles. On the other hand, while spatial resolution is less important than coverage for SAR oil spill detection, it is a critical parameter for both ship detection (regarding small vessels as fishing boats) and classification. In conclusion, taking into account complementary very-high-resolution X-band satellite SAR data as support for specific application needs, the choice of medium-to-high resolution C-band dual-polarization VV/VH as default product mode over European's water seems a good tradeoff among SAR maritime services prerequisites.

Due to the fact that Sentinel-1A and TerraSAR-X have different orbit characteristics (the first has a mean height of 693 km with a repeat cycle of 12 days; the second has a mean height of 515 km with a repeat cycle of 11 days), an area on Earth can be monitored from space at different times, with different geometries, resolution, and coverage. Despite Sentinel-1A fixed acquisition plan over European waters, TerraSAR-X acquires data on-demand and has a fast satellite commanding (e.g., emergencies cases). Thanks to these properties and the aforementioned complement between the two satellites, Sentinel-1A and TerraSAR-X form an interesting tandem for maritime surveillance applications. Therefore, within this paper, the following objectives have been identified:

1) assessment of the operational IWS C-band Sentinel-1 with StripMap X-band TerraSAR-X data for maritime targets detection;
2) synergetic use of multiplatforms satellite SAR data for targets cross checking and vessel speed estimation;
3) first evaluation of polarimetric target detectors for the available co-polarization and cross-polarization Sentinel-1A IWS products, previously demonstrated for RADARSAT-2 high-resolution quad-pol and very-high-resolution dual-pol TerraSAR-X data [5], [6].

The aims are achieved by means of real, almost coincidental C-band and X-band SAR data acquired by Sentinel-1A and TerraSAR-X satellites. On November 25, 2014, just a few months after Sentinel-1A concluded the commissioning phase, there was an opportunity to command TerraSAR-X acquisitions in the southern part of Italy, very close in time to the planned Sentinel-1A [1], [2]. During these controlled experiments, ground truth data provided by terrestrial automatic identification system (AIS) vessel reports have been recorded approximately 1 h before and 0.5 h after SAR acquisitions. AIS data are used to validate the objectives posed for this paper.

The paper is organized as follows. Section II contains details on the material and data analyzed. Section III is dedicated to the listed purposes 1 and 2. Section IV is dedicated to the listed purpose 3 where the theory and results on polarimetric detectors are presented; discussion and conclusions are sketched in Section V.

II. Material and Data Description

In this section, the material and the data analyzed for the purposes of this paper are introduced and described. Used material consists of satellite SAR data acquired in C- and X-band by two different satellites, and terrestrial AIS reports broadcast by ships in the area given by the satellites footprint on ground. The AIS data set is used to identify most of the maritime targets imaged by SAR and hence represents, for those targets, the ground truth. Therefore, it is worth a short introduction to the terrestrial AIS system before proceeding with SAR data description.

AIS is a messaging system developed for collision avoidance and to support other navigation systems, e.g., marine

TABLE I
SAR DATA DESCRIPTION

Dataset *Name*	**Data ID** *Time*	**Resolution (m)** *Rg × Az*	**Inc. Angle (°)** *Nr - Fr*	**Ground Range Coverage** *km*	**Frequency** *Band*	**Polarization** *T/R*	**Wind** m/s
Gulf of Naples	2014/11/25 *16:50* Z	1.2 × 3.3	27.2 – 30.3	32.1	**X**	**HH**	< 2
	2014/11/25 *16:57* Z	2.7-3.5 × 21.7	30.0 – 46.0	251.8	**C**	**VV/VH**	
Gulf of Catania	2014/11/25 *16:49* Z	1.2 × 3.3	26.9 – 30.3	34.3	**X**	**HH**	3-6
	2014/11/25 *16:56* Z	2.7-3.5 × 21.7	30.0 – 46.0	251.8	**C**	**VV/VH**	

radars, long range identification and tracking (LRIT) systems and vessel traffic service (VTS). Vessels obliged to transmit the message via AIS system are: ships of any type exceeding 300 tons engaged in international voyages, cargo ships exceeding 500 tons, and passenger vessels [7]. Lately, to contrast the large numbers of collisions involving fishing vessels, the EU has amended the Directive 2002/59/EC on the vessel traffic monitoring and information system, proposing that fishing vessels greater than 15 m sailing in European waters be fitted with AIS [8]. Other maritime targets that might be equipped with AIS and broadcast their message are: wind turbines, navigation aids, buoys, etc. Broadcast rate is variable (from seconds to minutes) and depends on the maritime target status, e.g., at anchor, sailing, maneuvering, etc., and AIS message type. Information sent jointly with geographical location are: International Maritime Organization (IMO) number, call sign, maritime mobile service identity (MMSI), speed and course over ground (CoG). Additional vessels' features are: ship name size, type, estimated time of arrival (ETA), and destination. The latter are usually set manually and therefore often unreliable and/or not available. AIS transponder broadcasts in VHF frequency achieving horizontal range of circa 70 km. Satellite reception of AIS signals is possible but here only terrestrial AIS information is exploited. It is evident that not all SAR detected maritime targets could be matched with a valid AIS message. Moreover, due to the fact that SAR is a radar imaging system that takes a snapshot of the observed scene in few seconds, there might be still a time mismatch. For these reasons, the strategy used is to visually confirm automatic colocated AIS data with SAR detections using additional historical AIS data in the time range span of approximately 1 h before and 0.5 h after satellite overpasses. Figs. 1 and 2 show the AIS messages (green dots) collected over the two areas where Sentinel-1A (dashed black line) and TerraSAR-X (continuous black line) data have been acquired. Some shipping route, e.g., between main land and the islands in the Gulf of Naples or in the Strait of Sicily, is clearly visible. Due to the different ground coverage between the Sentinel-1A's IWS mode and the TerraSAR-X's StripMap mode, the multifrequency assessment could be done only in the overlapping area and where targets could be identified with AIS data (see Figs. 1 and 2).

To preserve the original sensors' resolution, both C- and X-band SAR data sets are processed starting from single look complex (SLC) format and slant range geometry. Table I provides a summary of data characteristics corresponding to each acquired data set. It is worth noticing that TerraSAR-X imagery has been planned in HH polarization since it was known that Sentinel-1A would provide the combination VV/VH. Fig. 3 (Fig. 4) shows color-coded ground projection of the SAR data set named in Table I Gulf of Naples (Gulf of Catania). The left panel is the Sentinel-1 IWS VV/VH polarization (RGB color coding is with $\mathrm{R} = \langle|\boldsymbol{VV}|\rangle$, $\mathrm{G} = \langle|\boldsymbol{VH}|\rangle$, and $\mathrm{B} = \langle|\boldsymbol{VV} - \boldsymbol{VH}|\rangle$) acquired on November 25, 2014 at 16:57 Z (November 25, 2014 at 16:56 Z). The right panel is TerraSAR-X HH polarization (RGB color coding is given by $\mathrm{R} = \boldsymbol{std}(|\boldsymbol{HH}|)$, $\mathrm{G} = \boldsymbol{w}_1\langle|\boldsymbol{HH}|\rangle$, and $\mathrm{B} = \boldsymbol{w}_2\langle|\boldsymbol{HH}|\rangle$) acquired on November 25, 2014 at 16:50 Z (November 25, 2014 at 16:49 Z). The weights $\boldsymbol{w}_1$ and $\boldsymbol{w}_2$ are chosen to take into account low and high range variation of the radar amplitude, while $std(\cdot)$, $\langle\cdot\rangle$, and $|\cdot|$ are the standard deviation, average, and absolute value operators, respectively. Acquisitions time differences are about 7 min; both satellite orbits are ascending.

III. C-/X-BAND ANALYSIS AND SYNERGY

Sentinel-1A IWS SLC products are distributed as individually focused complex burst images into three single subswath images (three images for single polarization and six images for dual polarization). Each subswath, namely IW1, IW2, and IW3, has been processed individually (reading, de-bursting, and calibration) and merged at the last stage to produce the map in the left panels of Figs. 3 and 4. The strategy to process subswaths individually is kept also when running target detection algorithms (and additional polarimteric features extraction). This enables the parallelization of algorithms and the achievement of near-real-time (NRT) services, otherwise difficult due to the large amount of data given by IWS SLC products.

Three interesting cases have been chosen for the C-/X-band assessment and synergy with regard to maritime targets detection and surveillance: 1) monitoring of harbor area; 2) analysis of ships and ship wake signatures; and 3) surveillance of small boats without AIS.

A. Monitoring of Harbor Area

Monitoring of harbors from space can be quite a challenging task. Very-high-resolution imageries are usually preferred for

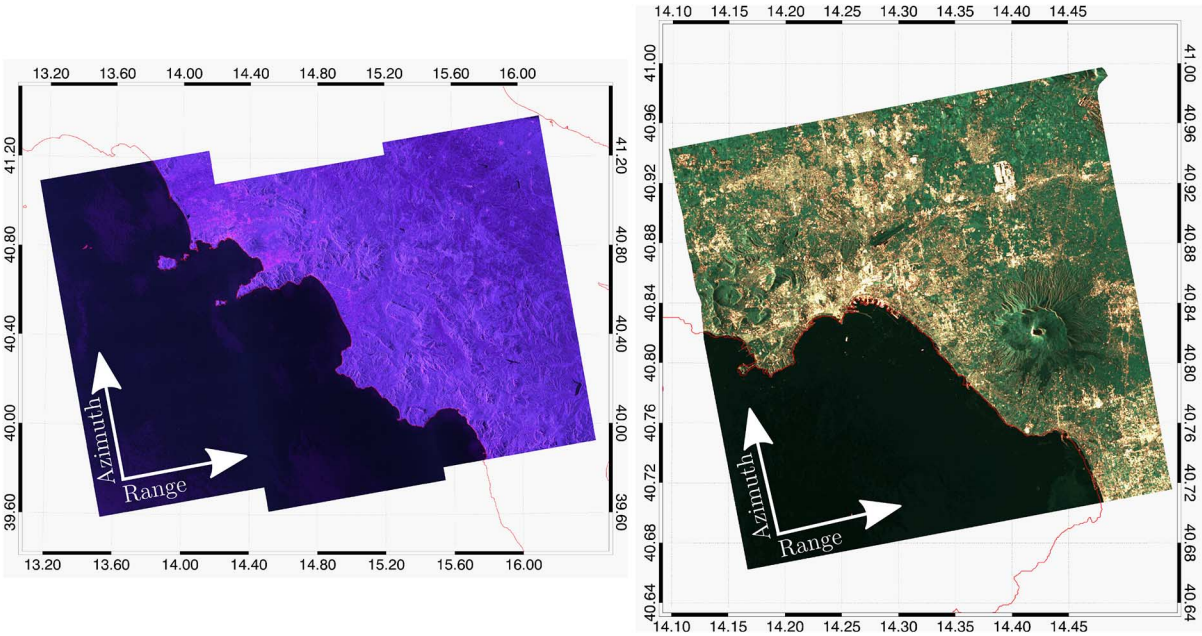

Fig. 3. RGB color-coded representation of the SAR data acquired by Sentinel-1 in IWS dual-polarization VV/VH with $\mathrm{R} = \langle |VV| \rangle$, $\mathrm{G} = \langle |VH| \rangle$, and $\mathrm{B} = \langle |VV - VH| \rangle$ (left) and TerraSAR-X StripMAP single-polarization HH with $\mathrm{R} = std(|HH|)$, $\mathrm{G} = w_1 \langle |HH| \rangle$, and $\mathrm{B} = w_2 \langle |HH| \rangle$ (right) over the Gulf of Naples, Italy.

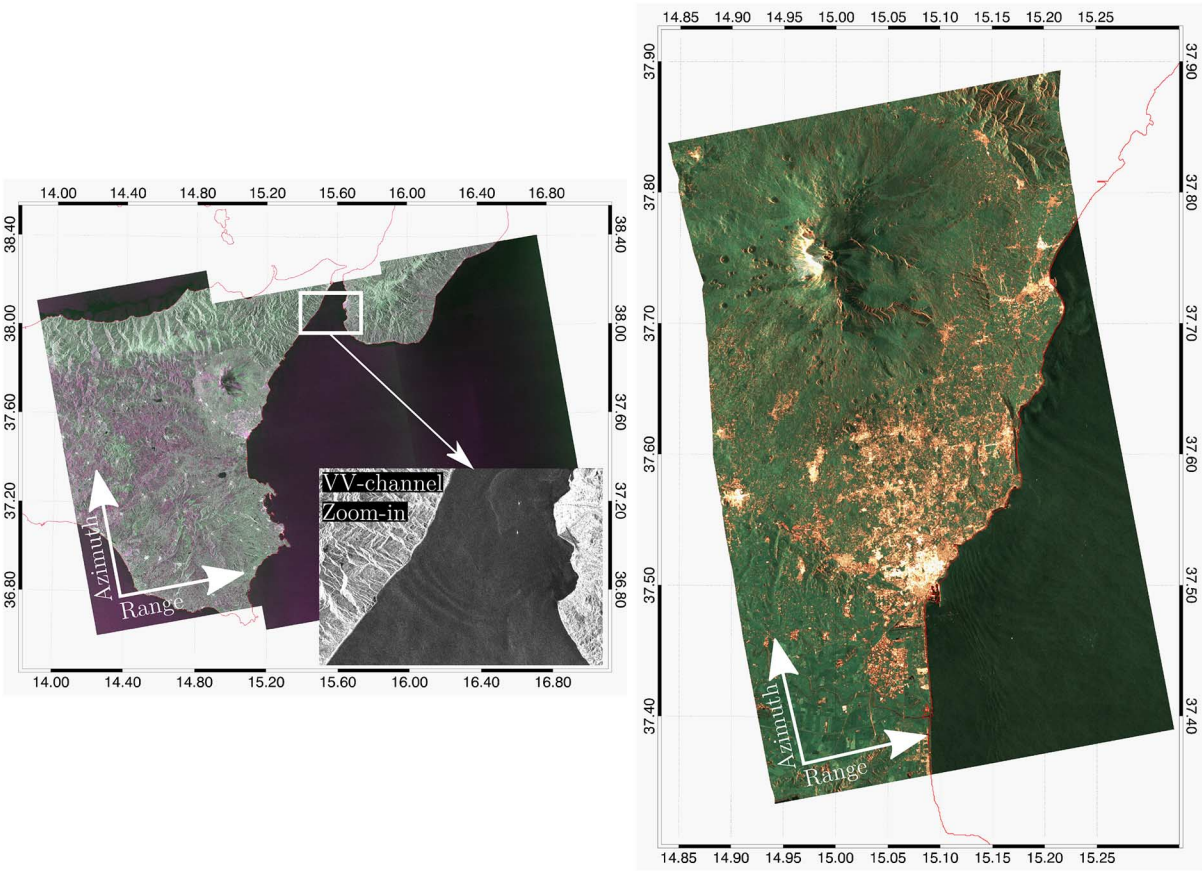

Fig. 4. RGB color-coded representation of the SAR data acquired by Sentinel-1 in IWS dual-polarization VV/VH with $\mathrm{R} = \langle |VV| \rangle$, $\mathrm{G} = \langle |VH| \rangle$, and $\mathrm{B} = \langle |VV - VH| \langle$ (left) and TerraSAR-X StripMAP single-polarization HH with $\mathrm{R} = std(|HH|)$, $\mathrm{G} = w_1 \langle |HH| \rangle$, and $\mathrm{B} = w_2 \langle |HH| \rangle$ (right) over Catania, Italy.

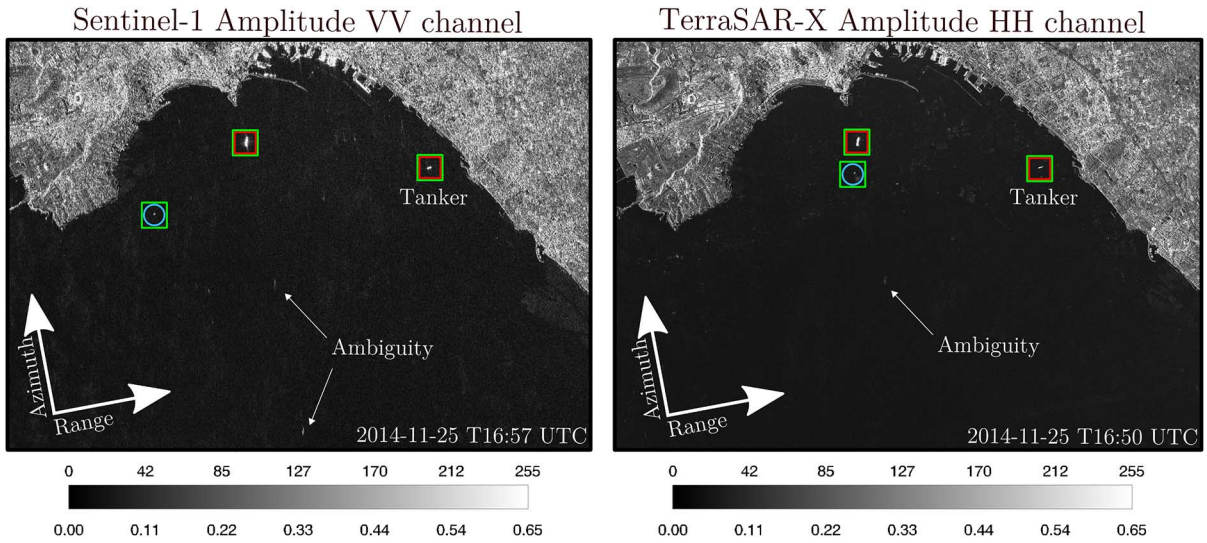

Fig. 5. Closeup of Fig. 3, showing Naples's harbor: Sentinel-1 acquired on November 25, 2014 at 16:57 Z, VV polarization calibrated amplitude (left); TerraSAR-X acquired on November 25, 2014 at 16:50 Z, HH polarization calibrated amplitude (right). Red rectangles are nonmoving marine targets; blue circles are moving marine targets; green rectangles are targets identified by valid AIS message.

this kind of application. Nevertheless, the very-high-resolution SAR data have a limited coverage and the contextual surrounding information is unknown by this means.

Referring to the TerraSAR-X in Fig. 3 (right panel), one can notice a very smooth ocean radar signature in the Gulf of Naples. Having a look at Sentinel-1A imagery acquired after few minutes (Fig. 3, left panel) it is possible to gather that a low meteo-ocean condition is in place all over the bay. This information has been confirmed by auxiliary satellite wind speed measurements and wind speed model data with an average speed below 2 m/s. Similarly, it can be deduced that the internal wave signatures on TerraSAR-X (Fig. 4, right panel) near Catania's harbor are probably originated in the Strait of Messina (where internal wave signatures are also present on Sentinel-1A image in Fig. 4, left panel) and propagating north–south along the coast [9]. In the context of harbor monitoring by means of very-high-resolution satellite SAR imagery, e.g., TerraSAR-X, the possibility to gather large-scale meteo-ocean information by means of complementary wide swath satellite SAR imagery, e.g., Sentinel-1A, is highly desired. In this sense, Sentinel-1 mission will boost such developments thanks to ESA Sentinel-1 mission's free data policy.

In Fig. 5, Naples's harbor, imaged by Sentinel-1 (left panel) and TerraSAR-X (right panel), is shown.

Both subscenes are ground projected and North oriented (satellite orientation is indicated by the arrows range and azimuth). The calibrated amplitude of the respective co-polarization channels (VV for Sentinel-1A and HH for TerraSAR-X) is displayed in Fig. 5. The same histogram scaling is applied in order to have equal visual information content. Speckle is mitigated using a boxcar filter with kernel dimensions adapted to the different resolutions in range and azimuth direction (5×3 in range $\times$ azimuth). These processing steps are used for all cases shown in this section, unless explicitly stated.

Three marine targets are identified as ships by colocated AIS messages (green rectangles); two of them are nonmoving (red rectangles) and one is moving (blue circle). Due to the low ocean clutter both subscenes are affected by azimuth ambiguities. Ships or harbor structures ghosting on the ocean surface is a major problem when dealing with SAR ship detection. These artefacts are often causing false alarms. To mitigate this problem, several methods have been proposed and used in literature for single- and multiple-polarization SAR data [10]–[15]. With both data sets being not fully polarimetric, azimuth ambiguities are removed after ship detection in a postprocessing step which exploits the fixed azimuth and range distance of the ghosts from real targets [10].

The multifrequency analysis of the ship radar signature is conducted taking as example the tanker ship at anchor in the Gulf of Naples in Fig. 5. It is an oil/chemical tanker of dimensions: 144-m length and 23-m breadth. This target has been selected because it is almost perfectly aligned in its length axis with the radar range direction. Furthermore, being the target at anchor, it is assumed that the influence caused by different viewing geometry between the C-/X-band acquisitions is negligible (although with a small difference in incidence angle; see Table I). A pictorial profile of a typical oil/chemical tanker is illustrated in Fig. 6(a), where the main structures are indicated with letters from A to E. Fig. 6(b)–(c) shows the color-coded C-band radar signature acquired by Sentinel-1A in the VV and VH polarizations, respectively. On the other hand, Fig. 6(d) shows the color-coded X-band radar signature acquired by TerraSAR-X in the HH polarization. A common byte scaling is applied to the amplitude measurements across the data set to facilitate the analysis. It is easy to recognize in Fig. 6(b) five strong backscattering points along the tanker length axis, which distribution fits reasonably well with the main structures A–E indicated in Fig. 6(a). These signatures are due to a mixture of direct reflections from the metallic constructions, e.g., crane, bridge, etc., and double-bounce between them and the deck. This is further confirmed by the VH polarization signature in Fig. 6(c) which is more an indication of volume scattering rather than direct or double bounce. The X-band co-polarization

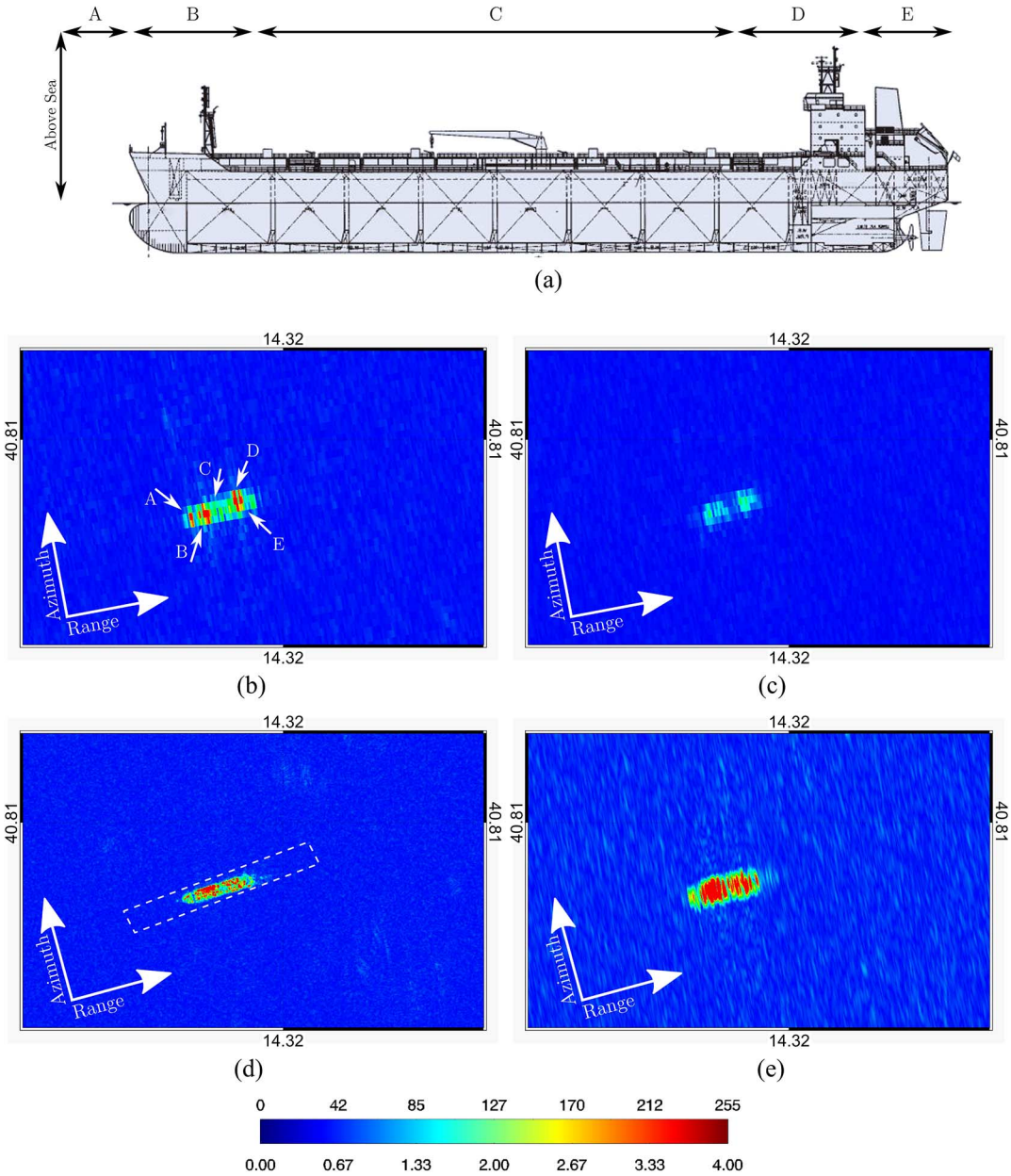

Fig. 6. Multifrequency radar signature of a tanker ship at anchor in Gulf of Naples (see Fig. 5). All SAR images are ground projected with pixel spacing according to the sensor's resolution (see Table I). (a) Typical tanker's profile of the type analyzed here. (b) Sentinel-1A C-band VV-polarization. (c) Sentinel-1A VH-polarization. (d) TerraSAR-X X-band HH-polarization. (e) TerraSAR-X X-band HH-polarization with azimuth resolution reduced to match the one of the Sentinel-1A.

(HH) radar signature in Fig. 6(d) is different from the C-band co-polarization (VV) in Fig. 6(b). Unlike what has been highlighted for C-band VV polarization, a diffuse distribution of strong backscattering points along the tanker length axis is in place at X-band [Fig. 6(d)].

The factors that might produce such behavior in the target signatures at C- and X-bands are: 1) different radar illumination geometry; 2) different polarization; 3) different resolution; and 4) different frequency. The first factor is excluded *a priori* since the target is at anchor (according to the AIS message received) in the harbor area and imaged by the two satellites with similar orbit heading in a short time difference (hence possible target's pitch, roll, and yaw are assumed negligible). Regarding the polarization's influence, having the target at width of 23 m, it is reasonable to assume that the dihedrals responsible for the double bounce (usually the stronger contribution) have a comparable vertical and horizontal size making the radar response quasi polarization independent. In [16], the influence of the factors 1) and 2) have been further analyzed for different types of ships (tanker and cargo), where the Sentinel-1A and TerraSAR-X data have the same polarization and illumination geometry. The conclusions in [16] confirm the assumptions made here. Concerning the resolution influence, being the marine target oriented with the major and minor axes in SAR range–azimuth directions [see Fig. 6(b)–(d)], it can be discussed individually along these directions. The strong azimuth resolution difference between the C- and X-band SAR data (~ 21 m and

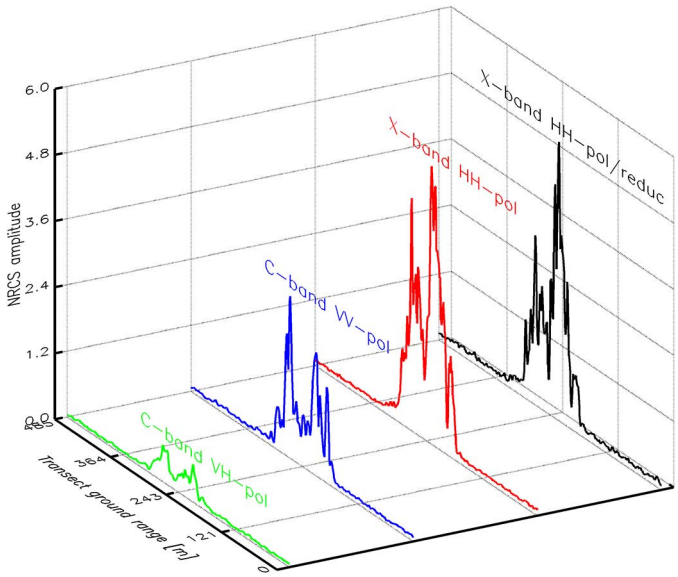

Fig. 7. Tanker ship profiles along the radar viewing direction for different frequency and polarization.

$\sim$ 3 m, respectively) is evident comparing Fig. 6(b) and (d). The tanker's width signature appears in C-band just in few pixels in azimuth direction while in X-band much more details are provided. On the other hand, the comparable resolution in range of the C- and X-band SAR data ($\sim$ 2 m and $\sim$ 1 m, respectively) does not fully justify the different texture in the radar signature along range direction (along the major axis of the tanker). To further investigate this point, an X-band data set with reduced azimuth resolution (down to $\sim$ 21 m as for the C-band data set) has been generated from the original X-band TerraSAR-X product by extracting a sublook with reduced azimuth processed bandwidth, i.e., 1-look with smaller illumination time, via time-frequency analysis. The output of this process is shown in Fig. 6(e), which can be directly compared with Fig. 6(b). Even though range and azimuth resolutions are in this case similar, the different radar signature in range persists. To easily compare the radar range signatures at different frequency and resolution, the data extracted from the region given by the dashed white frame in Fig. 6(d) are plotted (after being averaged in azimuth direction) in Fig. 7 for the case of Fig. 6(b)–(e). Comparing the target range profiles in Fig. 7 it can be observed that resolution does not play a major role. Considering, for example, the main deck of the target under analysis (which corresponds to the area around the 243 m of the transect ground range size in Fig. 7), the radar response in C-band (blue curve in Fig. 7) is quite low with no significant texture, i.e., mostly specular reflection, while both original and reduced resolution X-band data sets (red and black curve in Fig. 7) show noticeable texture in the radar response. As an outcome of this analysis, it is possible to conclude that among the four factors listed, the different working frequencies play the major role in the diverse radar backscatter signatures of the tanker ship observed in Sentinel-1A and TerraSAR-X. Hence, the different information provided by the Sentinel-1A and TerraSAR-X satellite can be exploited to help marine target classification. An applicative example is provided in [16] where a ship located in the coastal zone close to a harbor (non-reporting its status via AIS) could be analyzed at C- and X-band frequency and we conclude that it is probably a cargo at anchor.

It must be noted that previous works in the literature have shown the potential improvements for ship detection application when combining satellite meter-resolution X-band SAR data with optical images [17] or airborne centimeter-resolution X-band data [18]. Monitoring of harbor area making use of multiple SAR satellite operating at different frequencies is therefore here first investigated. The findings in the C-/X-band analysis of the tanker ship are in partial agreement with the multifrequency vessel scattering simulations provided in [19] for two fishing vessels and a passenger ferry. From these simulations, a stable radar backscatter along the frequency span (including C- and X-band) has been observed. Such stability has not been encountered in this study when analyzing the backscatter of a tanker in real C- and X-band SAR data. This is probably due to the fact that oil/chemical tankers usually carry complex metallic structures on their deck, formed by pipelines and cranes, which are normally not present in fishing and ferry vessels. Furthermore, it was observed that the backscatter of a tanker ship in the original and reduced resolution X-band data does not change the fundamental properties characterizing the scattering map of the ship. This observation is in agreement with the outcomes of the downscaling procedure applied at high frequency to the ship's model (which is equivalent to reducing the sensor's resolution) for the simulations of the vessel scattering maps in [19].

B. *Analysis of Ships and Ship's Wake Signatures*

This case has been chosen because ship wake detection is often desired when dealing with SAR marine target detection. In fact, ship wakes might be used to identify moving from non-moving marine targets and to help in detecting small boats for cases where only the wake signature is visible on the ocean surface. In Fig. 8, moving maritime targets (blue circles) identified with AIS (green rectangles) as imaged by Sentinel-1 (left panel) and TerraSAR-X (right panel) are shown. Reported AIS ship types for the two targets in Fig. 8 are: the service vessel (length 61 m) and the fishing vessel (length not reported).

Ship's wake signature on radar imagery is still an open and not fully understood process. The influence of the wind-wave field on the ship wake signature in TerraSAR-X imagery has been carried out in [20] with a pilot experiment that makes use of joint radar and sonar measurements of the wake signature. A multifrequency airborne observation of ship wake has been conducted in [21] using P-, L-, and C-band SAR data taken by NASA/JPL DC-8 Airsar. In [22], it was reported that wakes associated with fishing vessels show different wake opening angles in the P- and L-band images and no wake in the C-band image for wind speed regime $<$ 2 m/s. In the case of Fig. 8, it can be noted that for both Sentinel-1A (left) and TerraSAR-X (right) no wake is clearly visible for the service vessel. This might be due to the low ship speed (AIS reported speed is 3.6 kn) as wind speed is between 3 and 6 m/s. On the other hand, the wake of the fishing vessel shows different signatures between Sentinel-1A (left) and TerraSAR-X (right) imagery as shown in

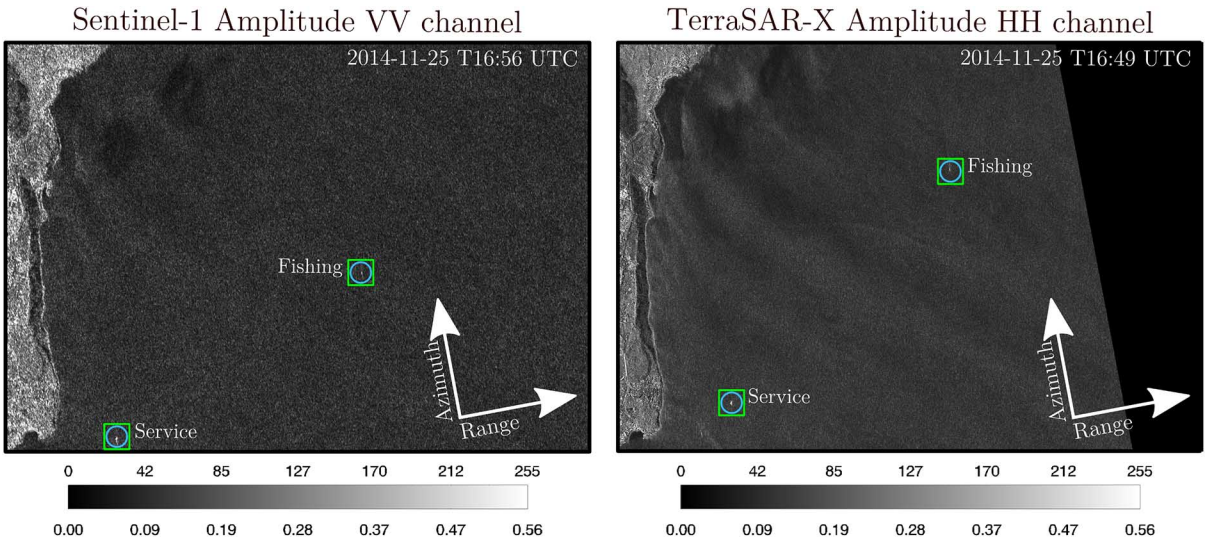

Fig. 8. Closeup of Fig. 4 showing an area North of Catania city with ships and ship's wake signatures: Sentinel-1 acquired on November 25, 2014 at 16:56 Z, calibrated amplitude VV channel representation (left); TerraSAR-X acquired on November 25, 2014 at 16:49 Z, calibrated amplitude HH channel representation (right). Blue circles are moving marine targets; green rectangles are targets identified by valid AIS message.

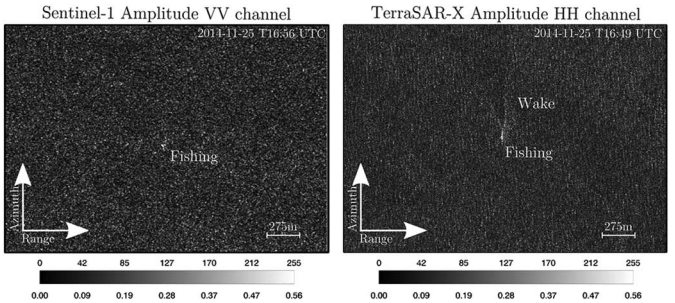

Fig. 9. Full resolution clips showing details of the fishing vessel in Fig. 8 in satellite range–azimuth coordinates; C-band Sentinel-1 (left), X-band TerraSAR-X (right).

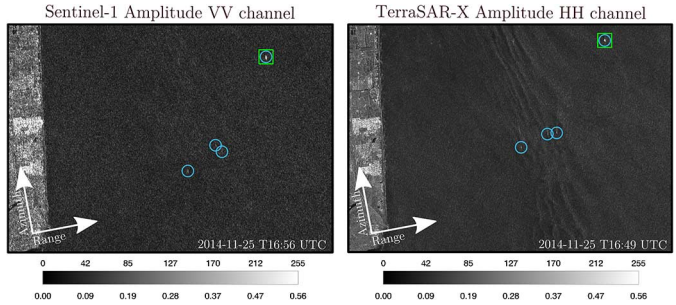

Fig. 10. Closeup of Fig. 4 showing an area south of Catania city with small boats: Sentinel-1 acquired on November 25, 2014 at 16:56 Z, calibrated amplitude VV channel representation (left); TerraSAR-X acquired on November 25, 2014 at 16:49 Z, calibrated amplitude HH channel representation (right). Blue circles are moving marine targets; green rectangles are targets identified by valid AIS message.

details in Fig. 9. The fishing vessel is in the middle of the subscenes and the area around has approximately the same size. The reported AIS speed of the fishing vessel is 9.1 kn and is kept almost constant during the two satellite overpasses. Although the X-band SAR data have been acquired in HH polarization, the fishing vessel wake signature is more pronounced than in C-band (acquired in VV, which is the preferred polarization for SAR wake detection). The lower incidence angle in the X-band band data might play a role in this case.

SAR ship wake detection is usually combined with SAR ship detection to estimate the radial velocity component of moving targets exploiting the Doppler shift effect [22], [23]. This approach cannot be used in the case of SAR imagery with no clear ship wake signature and/or ship moving in direction parallel to the sensor, i.e., azimuth. Such a case is actually given in Fig. 9. Nevertheless, exploiting the availability of multiple images at different acquisition times, classification between moving and nonmoving targets, as well as the estimation of their speed can still be done under certain assumptions. As an example of joint use of Sentinel-1 and TerraSAR-X, the fishing vessel speed has been measured applying a basic change detection algorithm, assuming a linear trajectory at constant speed. The azimuth time difference between the two target positions is about 420 s, while the distance traveled is about 2024 m. This gives an average speed of 9.37 kn that compares well with 9.1 kn reported by the AIS message.

C. Surveillance of Small Boat Without AIS

Because SAR is a synoptic noncooperative surveillance tool, it is mostly useful in the framework of maritime target detection to monitor ships that voluntarily (involved in illegal activity, AIS broadcast not mandatory, fishermen hiding their fishing zone to other fishing vessels, etc.) or involuntarily (not engaged in voyages, AIS, and/or other anticollision system malfunctions, etc.) do not report their positions. Small boats and pleasure crafts often do not use anticollision systems, like AIS, making their position unknown to other ships, especially at nighttime or in foggy conditions.

This is the case of Fig. 10 where three small boats (blue circles) are visually detected in high-resolution C-band VV polarization Sentinel-1A image (left) and very-high-resolution X-band HH polarization TerraSAR-X image (right). It must be pointed out that the visual detection of the three small boats in Sentinel-1A image has been possible thanks to the support of the very-high-resolution TerraSAR-X image acquired

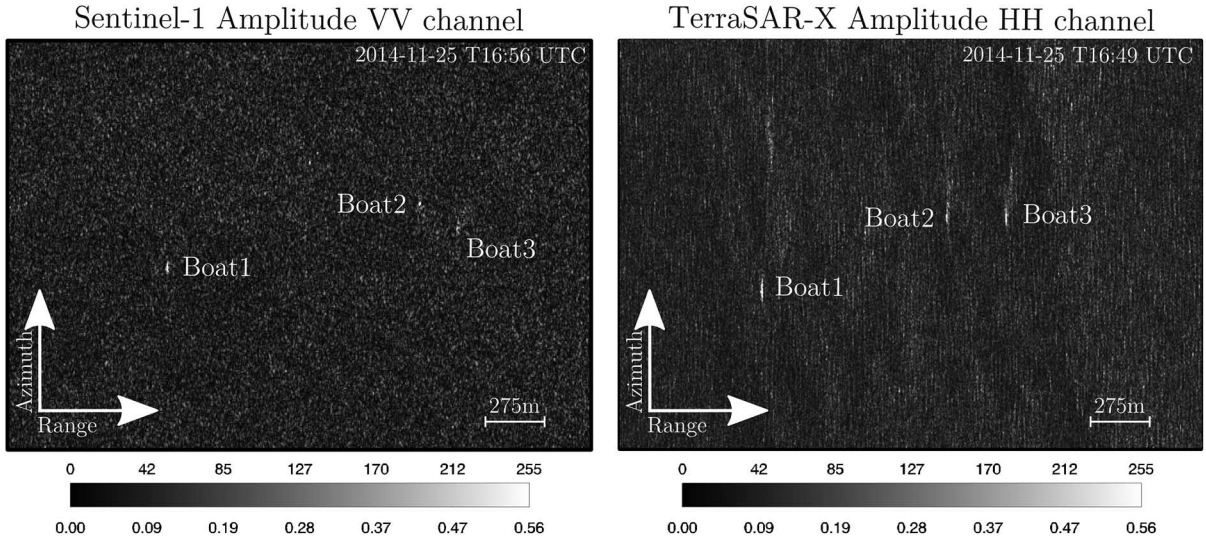

Fig. 11. Full resolution clips showing details of the small boats without AIS in Fig. 10 in satellite range–azimuth coordinates; Sentinel-1 (left), TerraSAR-X (right).

shortly before. This is evident looking at Fig. 11 where full resolution clips of the C-band and X-band data set are shown in the azimuth–range coordinate without interpolation of ground projection processing.

Unfortunately, the size and type of these maritime targets are unknown. To infer the minimum ship size detectable, some work has been done taking into account met-ocean conditions and SAR system design, using C-band data [24] and more recently X-band data [25]. Besides the detection of maritime targets it is often desired to estimate their parameters, e.g., length, width, heading, etc., based on their radar imagery signature. The motion of the small boats in Fig. 11 (as well as for the fishing vessel in Fig. 9) along the satellite azimuth direction produces a SAR imaging artefact, known as the smearing effect, resulting in an elongated shape of the targets. This effect introduces an error when estimating ship parameters [26]. In [26], a methodology has been proposed to reduce this estimation error for different types of SAR products (from medium to very high resolution) using a valuable data set of TerraSAR-X imagery and colocated AIS messages. Applying the same method and assumptions described in the previous section, the speeds of the three targets named Boat1, Boat2, and Boat3 in Fig. 11 have been retrieved. Azimuth time difference for the three targets is about 414 s (they are approximately at the same azimuth line and there are a few milliseconds difference between the three) while the distances traveled are about 750, 377, and 616 m, respectively. These give an average measured speed of about 3.5 kn for Boat1, 1.8 kn for Boat2, and 2.9 kn for Boat3.

IV. Polarimetric Detector: Theory and Results

A first analysis of ship detectability on Sentinel-1 IWS dual-polarimetric products has been carried out in [27] as an extension of the modeling developed in [24] for RADARSAT-1, RADARSAT-2, and Envisat ASAR image data. The model proposed in [27] predicts the minimum ship length considering each polarization available. When comparing model results for co-polarization and cross-polarization IWS products, one of the findings is that ship detection performance at cross-polarization is comparable to the ones at co-polarization [27]. This result is probably due to the IWS incidence angle range as cross-polarization benefits for ship detection are more important at smaller incidence angles [5], [27]. Nevertheless, the promising results obtained by using the polarimetric reflection symmetry properties of maritime targets and ocean clutter for C-band [5] and X-band [6] data suggest evaluating this approach for Sentinel-1A IWS products. In addition, the polarimetric entropy H is extracted from dual-polarimetric covariance matrix and used as a comparison parameter. A ship detector based on the entropy H retrieved from full-polarimetric airborne SAR data was first proposed in [28].

A. Reflection Symmetry Approach

The dual-polarimetric measurements available on Sentinel-1A IWS products can be expressed in terms of the scattering vectors $k_{DH} = (S_{HH}, S_{HV})^T$ or $k_{DV} = (S_{VH}, S_{VV})^T$ depending on the acquired polarization combination. In this paper, Sentinel-1A IWS VV/VH data are analyzed, therefore the 2×2 covariance matrix is defined as

$$\mathrm{C}_2 = \langle k_{DV} \cdot {k_{DV}}^{*T} \rangle = \begin{pmatrix} \langle |S_{VH}| \rangle^2 & \langle S_{VH} S_{VV}^* \rangle \\ \langle S_{VV} S_{VH}^* \rangle & \langle |S_{VV}|^2 \rangle \end{pmatrix}. \quad (1)$$

The reflection symmetry property implies that the unnormalized correlation between co-polarization and cross-polarization channels vanishes for symmetric targets (such as the sea surface) and is different from zero for nonsymmetric targets (such as maritime targets) [5], [6]

$$\begin{cases} \langle S_{VV} S_{VH}^* \rangle = \langle S_{VH} S_{VV}^* \rangle \approx 0, & \text{if target is symmetric} \\ \langle S_{VV} S_{VH}^* \rangle = \langle S_{VH} S_{VV}^* \rangle \neq 0, & \text{if target is not symmetric} \end{cases} \quad (2)$$

Hence, for the following analysis, the modulus of the unnormalized correlation between co-polarization and cross-polarization channels is used as detector:

$$r = |\langle S_{VV} S_{VH}^* \rangle| . \quad (3)$$

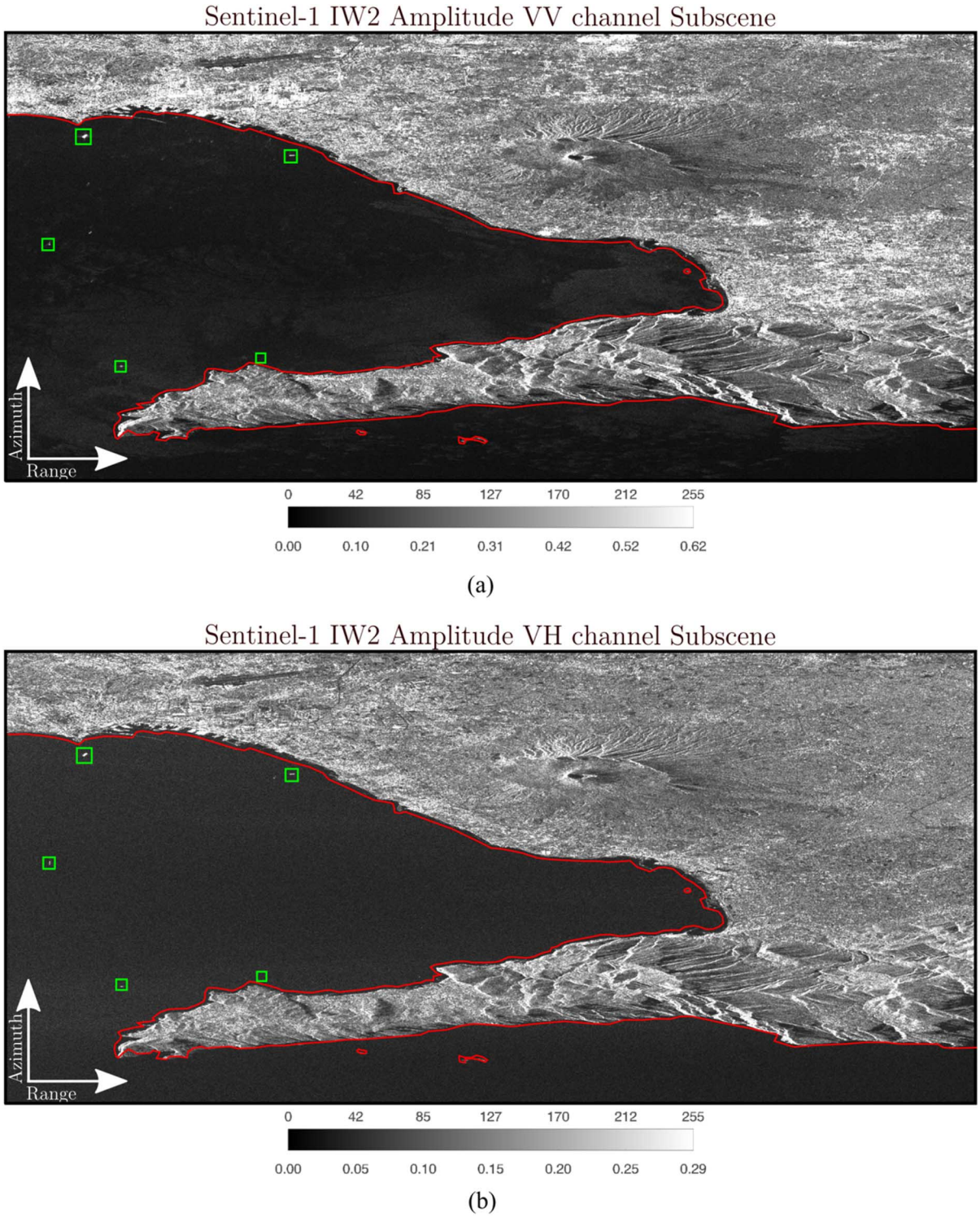

Fig. 12. Gulf of Naples. Subscene extracted from the complex IW2 subswath in range–azimuth coordinates with the coastline in red and ships identified via AIS as green squares. (a) The calibrated amplitude of the co-polarization channel. (b) The calibrated amplitude of the cross-polarization channel.

The estimation window size used to calculate (3) is 5×3 (range $\times$ azimuth) to take into account the higher resolution in range.

In Figs. 12 and 13, the symmetry parameter r image [Fig. 13(a)] is compared with the amplitude of the co-polarization and cross-polarization channel images [Fig. 12(a) and (b), respectively]. Since to retrieve r a window estimation has been used (hence the speckle is also reduced), a boxcar filter of the same size has been applied when processing individually the co-polarization and cross-polarization images.

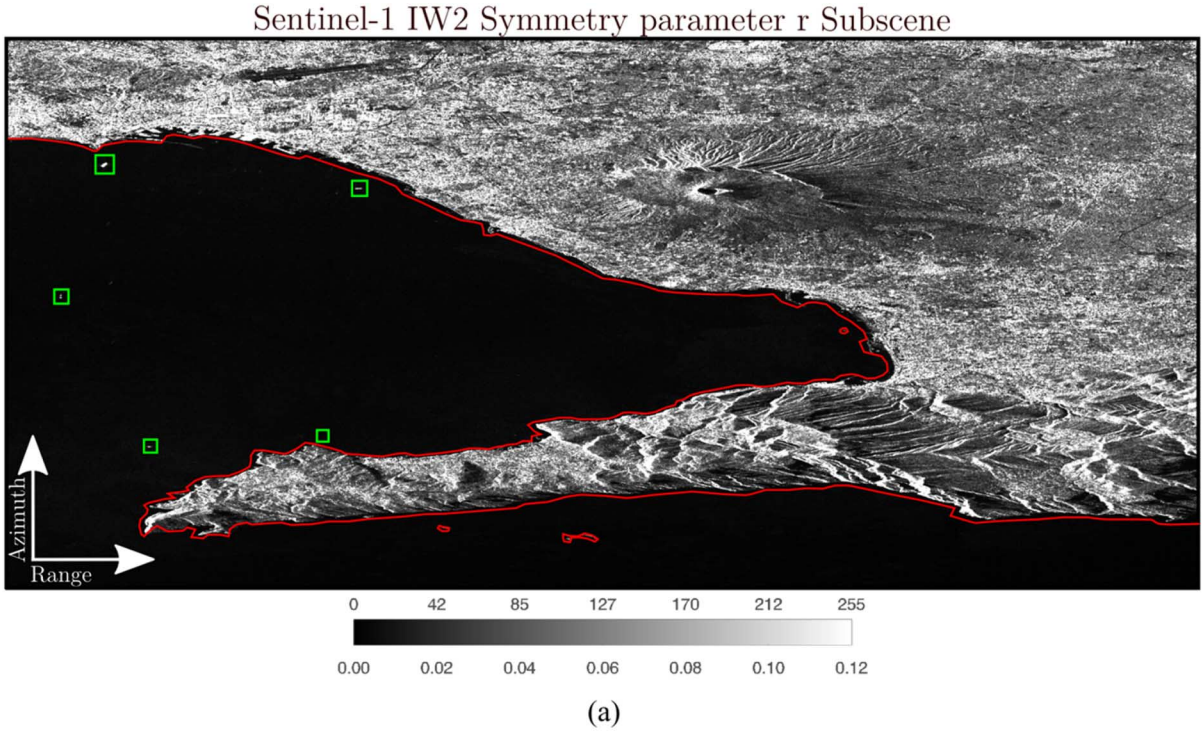

Fig. 13. Gulf of Naples. The coastline is shown in red, and ships identified via AIS are shown as green squares. (a) Estimated symmetry parameter r using 5×3 (range $\times$ azimuth) window. (b) Binary output based on the threshold th.

The binary mask in Fig. 13(b) is obtained by thresholding the r image using the following empirical relation:

$$th = mean\left(r_{\text{ocean}}\right) + 3 * stddev\left(r_{\text{ocean}}\right) \tag{4}$$

where r_{ocean} is an image layer obtained from r after masking out the land, $mean(\cdot)$ and $stddev(\cdot)$ provide the average and standard deviation value of unnormalized correlation r over the ocean, and th is the global threshold. Land masking has been performed with the help of auxiliary data provided by the SRTM water body data set. Equation (4) is reasonable since the amount of ship pixels is negligible compared to the amount of ocean pixels.

B. Entropy Approach

Because (1) is a Hermitian positive–definite matrix, the H2α dual-polarimetric eigenvalues decomposition theorem is applied to retrieve the entropy H [29]

$$H = -\sum_{I=1}^{2} P_i \log_2\left(P_i\right) \tag{5}$$

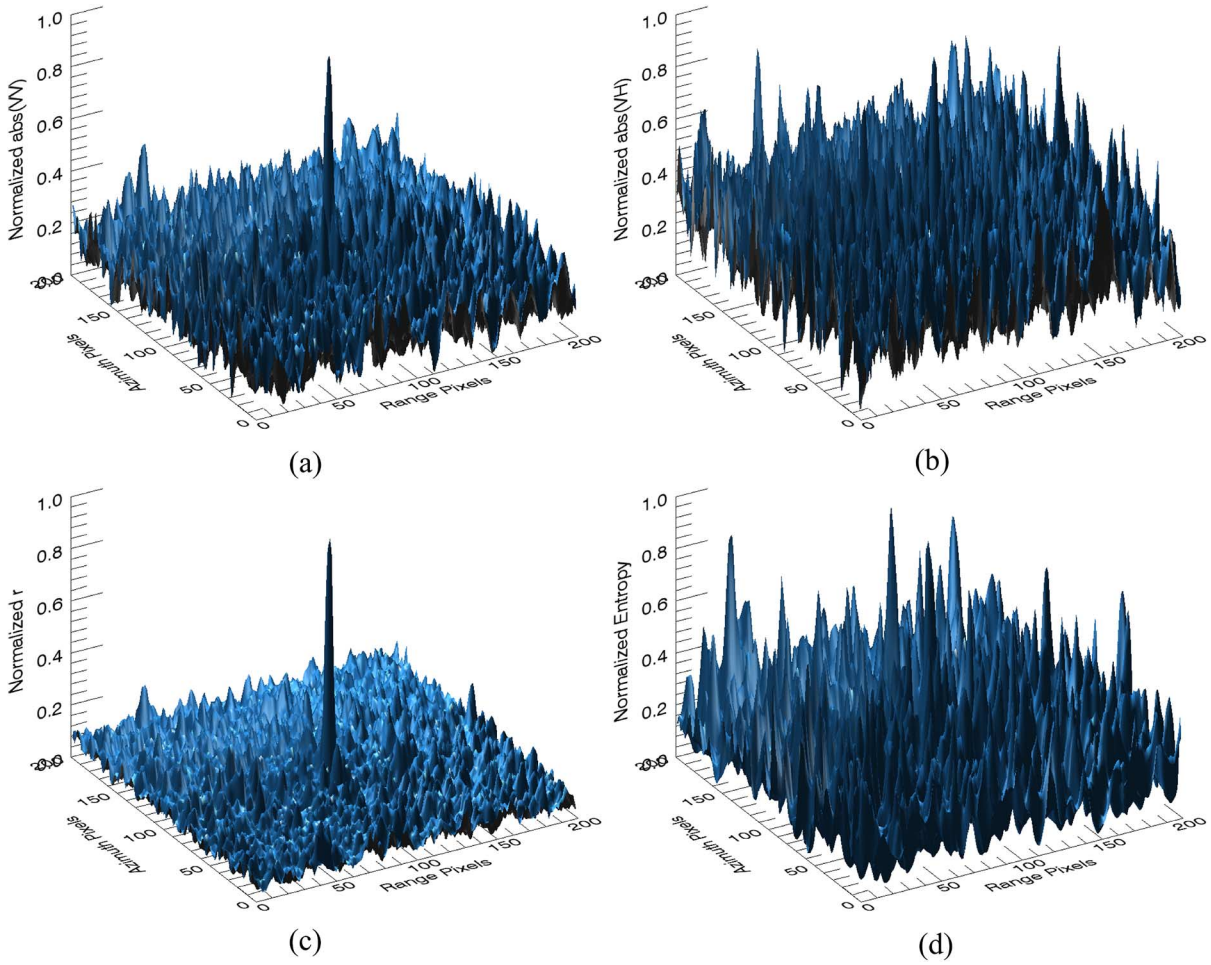

Fig. 14. Three-dimensional representation of the normalized parameters used for comparison: (a) VV polarization; (b) VH polarization; (c) r based; and H based.

where the probabilities P_i are defined as

$$P_i = \frac{\lambda_i}{(\lambda_1 + \lambda_2)}. \tag{6}$$

In (6), λ_1 and λ_2 (with $\lambda_1 > \lambda_2$) are indicating the eigenvalues of the covariance matrix defined in (1).

To show the behavior of the different parameters in case of small maritime targets, the fishing vessel in Fig. 9 is taken as an example. Although this target has been identified with a valid AIS message, the length is not reported.

In Fig. 14, a 200×200 pixels region of interest surrounding the fishing vessel in Fig. 9 is plotted as a surface curve for the normalized VV, VH, r, and H parameters. As a matter of fact, the r-based approach allows de-emphasizing the sea surface clutter while enhancing the maritime target, when compared to single-polarization channels. For the case analyzed, the cross-polarization channel VH and the polarimetric entropy H are not performing well since it is quite difficult to discern the target from the surrounding clutter.

V. Discussions and Conclusion

Synergetic use of multifrequency and multipolarization satellite SAR data in the framework of maritime target detection has been conducted. For this paper, high-resolution C-band dual-polarization VV/VH IWS mode from recently launched Sentinel-1A satellite and very-high-resolution X-band single-polarization HH StripMap mode from TerraSAR-X satellite have been used. Two regions in southern Italy have been imaged by the two satellites almost at the same time and the same orbit path, although placed in two different orbital heights. Maritime targets detected by the SAR imagery have been augmented by ground truth measurements provided by AIS messages collected in the monitored area. Satellite wind speed measurements have been used to get an indication of the met-ocean conditions and motivate some observations.

In the first part of the paper, the assessment of the operational IWS C-band Sentinel-1 with StripMap X-band TerraSAR-X data and their synergetic use were addressed. In particular, three interesting cases have been chosen because these are relevant for maritime surveillance applications: 1) monitoring of harbor area; 2) analysis of ships and ship wake signatures; and 3) surveillance of small boats without AIS. The joint use of the two satellites working at two different frequencies enables applications such as target-type discrimination, moving/nonmoving target differentiation, and moving target speed estimation. It is worth mentioning that only the comparison for the purposes of maritime target observation has been addressed here, although very interesting met-ocean signature differences are also observable between the C- and X-band data sets, e.g.,

the oceanic and atmospheric signature (Fig. 8, top-left corners) and the internal waves signature (Fig. 10, center scenes).

In the second part of the paper, multipolarization analysis of the C-band data set was carried out. Results using the reflection symmetry approach confirmed previous experiences on other C-band and X-band satellite data. From the first analysis conducted here on Sentinel-1A data, the reflection symmetry parameter performed better than single-pol features and dual-polarimetric entropy. A final validation and comparison with other polarimetric detectors is, however, to be done in future work.

ACKNOWLEDGMENT

The authors would like to thank the European Space Agency (ESA) for providing Sentinel-1A data free of charge via Scientific Data Hub (https://scihub.esa.int/). TerraSAR-X data were provided by the German Aerospace Center (DLR) via the scientific announcement of opportunity proposal OCE1045. The views, opinions, and findings contained in this paper are those of the authors and should not be construed as an official DLR's position, policy, or decision.

REFERENCES

[1] ESA Communications "Sentinel-1: ESA's Radar Observatory Mission for GMES Operational Services", 2012.
[2] E. Attema *et al.*, "Sentinel-1—The radar mission for GMES operational land and sea services," *ESA Bull.*, vol. 131, pp. 10–17, 2007.
[3] S. Lehner *et al.*, "Ship surveillance with high resolution Terrasar-X satellite in African waters," *Remote Sensing of the African Seas*, New York, NY, USA: Springer-Verlag, 2014, pp. 285–313.
[4] R. Touzi, P. W. Vachon, and J. Wolfe, "Requirement on antenna cross-polarization isolation for the operational use of C-band SAR constellations in maritime surveillance," *IEEE Geosci. Remote Sens. Lett.*, vol. 7, no. 4, pp. 861–865, Oct. 2010.
[5] F. Nunziata, M. Migliaccio, and C. E. Brown, "Reflection symmetry for polarimetric observation of man-made metallic targets at sea," *IEEE J. Ocean. Eng.*, vol. 37, no. 3, pp. 384–394, Jul. 2012.
[6] D. Velotto, F. Nunziata, M. Migliaccio, and S. Lehner, "Dual-polarimetric terrasar-x SAR data for target at sea observation," *IEEE Geosci. Remote Sens. Lett.*, vol. 10, no. 5, pp. 1114–1118, Sep. 2013.
[7] International Convention for the Safety of Life at Sea (SOLAS), Chapter V: Safety of Navigation, Annex 17 – Automatic Identification Systems (AIS), 2002 [Online]. Available: www.imo.org.
[8] Commission of the European Communities "Common position adopted by the council with a view to the adoption of a directive of the European Parliament and of the council amending directive 2002/59/EC establishing a community vessel traffic monitoring and information system", Jun. 2008.
[9] P. Brandt, A. Rubino, W. Alpers, and J. O. Backhaus, "Internal waves in the strait of messina studied by a numerical model and synthetic aperture radar images from the ERS 1/2 satellites," *J. Phys. Oceanogr.*, vol. 27, no. 5, pp. 648–663, 1997.
[10] S. Brusch *et al.*, "Ship surveillance with TerraSAR-X," *IEEE Trans. Geosci. Remote Sens.*, vol. 49, no. 3, pp. 1092–1103, Mar. 2011.
[11] A. Monti Guarnieri, "Adaptive removal of azimuth ambiguities in SAR images," *IEEE Trans. Geosci. Remote Sens.*, vol. 43, no. 3, pp. 625–633, Mar. 2005.
[12] M. Villano and G. Krieger, "Spectral-based estimation of the local azimuth ambiguity-to-signal ratio in SAR images," *IEEE Trans. Geosci. Remote Sens.*, vol. 52, no. 5, pp. 2304–2313, May 2014.
[13] G. Di Martino, A. Iodice, D. Riccio, and G. Ruello, "Filtering of azimuth ambiguity in stripmap synthetic aperture radar images," *IEEE J. Sel. Top. Appl. Earth Obs. Remote Sens.*, vol. 7, no. 9, pp. 3967–3978, Sep. 2014.
[14] C. Wang, Y. Wang, and M. Liao, "Removal of azimuth ambiguities and detection of a ship: Using polarimetric airborne C-band SAR images," *Int. J. Remote Sens.*, vol. 33, no. 10, pp. 3197–3210, May 2012.
[15] D. Velotto, M. Soccorsi, and S. Lehner, "Azimuth ambiguities removal for ship detection using full polarimetric X-band SAR data," *IEEE Trans. Geosci. Remote Sens.*, vol. 52, no. 1, pp. 76–88, Jan. 2014.
[16] D. Velotto, C. Bentes, B. Tings, and S. Lehner, "Comparison of Sentinel-1 and TerraSAR-X for ship detection," *Proc. IEEE Int. Geosci. Remote Sens. Symp.*, 2015, pp. 3282–3285.
[17] G. Saur *et al.*, "Detection and classification of man-made offshore objects in TerraSAR-X and rapideye imagery: Selected results of the demarine-DEKO project," *Proc. IEEE OCEANS Conf.*, 2011, DOI: 10.1109/Oceans-Spain.2011.6003596.
[18] A. O. Knapskog, S. Brovoll, and B. Torvik, "Characteristics of ships in harbour investigated in simultaneous images from TerraSAR-X and PicoSAR," *Proc. IEEE Radar Conf.*, 2010, pp. 422–427.
[19] G. Margarit, J. J. Mallorqui, J. Fortuny-Guasch, and C. Lopez-Martinez, "Phenomenological vessel scattering study based on simulated inverse SAR imagery," *IEEE Trans. Geosci. Remote Sens.*, vol. 47, no. 4, pp. 1212–1223, Apr. 2009.
[20] A. Soloviev, M. Gilman, K. Young, S. Brusch, and S. Lehner, "Sonar measurements in ship wakes simultaneous with TerraSAR-X overpasses," *IEEE Trans. Geosci. Remote Sens.*, vol. 48, no. 2, pp. 841–851, Feb. 2010.
[21] N. R. Stapleton, "Ship wakes in radar imagery," *Int. J. Remote Sens.*, vol. 18, no. 6, pp. 1381–1386, 1997.
[22] K. Eldhuset, "An automatic ship and ship wake detection system for spaceborne SAR images in coastal regions," *IEEE Trans. Geosci. Remote Sens.*, vol. 34, no. 4, pp. 1010–1019, Apr. 1996.
[23] J. K. Tunaley, "The estimation of ship velocity from SAR imagery," *Proc. IEEE Int. Geosci. Remote Sens. Symp.*, 2003, vol. 1, pp. 191–193.
[24] P. W. Vachon, J. W. M. Campbell, C. A. Bjerkelund, F. W. Dobson, and M. T. Rey, "Ship detection by the RADARSAT SAR: Validation of detection model predictions," *Can. J. Remote Sens.*, vol. 23, no. 1, pp. 48–59, 1997.
[25] C. Bentes, D. Velotto, and S. Lehner, "Analysis of ship size detectability over different TerraSAR-X modes," *Proc. IEEE Int. Geosci. Remote Sens. Symp.*, 2014, pp. 5137–5140.
[26] B. Tings, C. A. B. da Silva, and S. Lehner, "Dynamically adapted ship parameter estimation using TerraSAR-X images," *Int. J. Remote Sens.*, Aug. 2015, DOI:10.1080/01431161.2015.1071898.
[27] P. W. Vachon, J. Wolfe, and H. Greidanus, "Analysis of Sentinel-1 marine applications potential," *Proc. IEEE Int. Geosci. Remote Sens. Symp.*, 2012, pp. 1734–1737.
[28] R. Touzi, "On the use of polarimetric SAR data for ship detection," *Proc. IEEE Int. Geosci. Remote Sens. Symp.*, 1999, vol. 2, pp. 812–814.
[29] S. Cloude, "The dual polarization entropy/alpha decomposition: A PALSAR case study," *ESA Special Publ.*, vol. 644, p. 2, 2007.

Domenico Velotto (M'15) was born in Italy, on April 30, 1981. He received the M.Sc. degree (five-year legal course of study) in nautical science (curriculum electronic radio-navigation and Earth observation systems) from the Università degli Studi di Napoli "Parthenope," Napoli, Italy, in 2008.

In 2009, he joined the Synthetic Aperture Radar (SAR) Oceanography Group, Remote Sensing Technology Institute (MF), German Aerospace Center (DLR), Weßling, Germany, as a Ph.D. student. Since 2013, he has been a Research Assistant at the Maritime Security Lab, DLR, Bremen, Germany. His main research interests deal with electromagnetic models, image processing, and Earth observation with SAR polarimetry with emphasis on oil spill and maritime targets detection and classification.

Carlos Bentes was born in Volta Redonda, Brazil, in 1983. He received the B.S.E.E. and M.S.E.E. degrees from the Instituto Tecnológico de Aeronáutica (ITA), São José dos Campos, Brazil, in 2007 and 2012, respectively.

Since 2013, he has been a Research Assistant at the German Aerospace Center (DLR), Bremen, Germany, in the field of remote sensing. His professional interests and research areas encompass information mining, machine learning, signal processing, and remote sensing applications.

Björn Tings received the B.S. degree in scientific programming and his simultaneous qualification in mathematical-technical software development in 2010 and the M.Sc. degree in artificial intelligence in 2013, both from Aachen University, Aachen, Germany.

During his B.S. studies and during the first year of his M.S. studies he gained practical experience working for the Laboratory for Machine Tools and Production Engineering (WZL), RWTH Aachen University, Aachen, Germany. For his M.S. thesis, he specialized on image processing and pattern recognition in the fields of avionic and defense. Since 2013, he has been a Research Assistant at the Institute for Remote Sensing Technology (IMF), German Aerospace Center (DLR), Bremen, Germany. In IMF's Maritime Safety and Security Lab (FMS) in Bremen, Germany, his research is focused on developing algorithms for detection and classification of ships on synthetic aperture radar (SAR) satellite images. As an interface between the FMS and the satellite data receiving ground station in Neustrelitz, Germany, he is also responsible for the operationalization of research results into NRT-capable SAR data processors.

Susanne Lehner studied mathematics and physics at the University of Hamburg, Hamburg, Germany. She received the M.Sc. in applied mathematics from Brunel University, Uxbridge, U.K., in 1979 and the Ph.D. degree in geophysics from the University of Hamburg, Hamburg, Germany, in 1984.

During the Ph.D., she worked as a Research Scientist at the Max-Planck Institute for Meteorology, Hamburg, Germany. She joined the German Aerospace Center DLR/DFD in 1996. Since 1999, she has been head of the team Radar Oceanography at the Institute for Remote Sensing Technology (IMF), DLR, Oberpfaffenhofen, Germany. In SAR oceanography, her research focused on developing algorithms to extract information on wind fields, sea state, currents, and underwater topography from SAR images. Her recent interest, in addition to global sea state measurements, is in high-resolution coastal SAR oceanography, especially TerraSAR-X oceanography and meteo-marine observations, and maritime traffic surveillance in near real time. She holds a faculty position at the Nova Southeastern University, Port Everglades, FL, USA. She was appointed as Affiliated Faculty Member in 2013. Currently she is head of the Maritime Security Lab, Bremen, Germany, established in July 2013.

List of abbreviations

AAP	azimuth antenna pattern
AASR	azimuth ambiguity to signal ratio
AIS	automatic identification system
ATI	along track interferometry
BMBF	Federal Ministry of education and research
CFAR	constant false alarm rate
CPD	co-polarized phase difference
CSK	COSMO-SkyMed Italian constellation of satellite
DLR	German aerospace agency
DoD	degree of depolarization
DoP	degree of polarization
DRA	dual receive antenna
EM	electromagnetic wave
EMSA	European maritime safety agency
EMSec	Echtzeitdienste für die Maritime Sicherheit
EO	Earth observation
ESA	European space agency
EU	European Union
GLRT	generalized likelihood ratio test
GP-PNF	geometrical perturbation polarimetric notch filter
GUI	graphical user interface
HH	Horizontal-Horizontal transmit-receive polarization
HV	Horizontal-Vertical transmit-receive polarization
IHP	internal Hermitian product
IMO	international maritime organization
IR	infrared
LFS	laser fluoro-sensor
LoS	line of sight
MLE	maximum likelihood estimator

MLP	multi-layer perceptron network
MRW	microwave radiometer
MSA	maritime situational awareness
NEBN	noise equivalent beta naught
NESZ	noise equivalent sigma zero
NN	neural network
NRCS	normalized radar cross section
NRCS	normalized radar cross section
NRT	near real time
PBW	azimuth processed bandwidth
pdf	probability density function
PFA	probability of false alarm
PolSAR	polarimetric SAR
PRF	pulse repetition frequency
PRI	pulse repetition interval
PTD	partial target detector
PTR	point target response
PWF	polarimetric whitening filtering
RADAR	radio detection and Ranging
RAR	real aperture radar
RASR	range ambiguity to signal ratio
RCS	radar cross section
RD-2	RADARSAT-2 Canadian satellite
ROI	region of interest
S1-A	Sentinel-1A ESA satellite
S1-B	Sentinel-1B ESA satellite
SAR	synthetic aperture radar
SC	ScanSAR imaging mode
SL	SpotLight imaging mode
SLC	single look complex
SM	StripMap imaging mode

SNR	signal to noise ratio
SRA	single receive antenna
ST	Staring spotlight imaging mode
TCR	target to clutter ratio
TD-X	TerraSAR-X add-on for digital elevation measurement
TS-X	TerraSAR-X German satellite
UN	United Nations
UV	ultra violet
VH	Vertical-Horizontal transmit-receive polarization
VHR	very high resolution
VV	Vertical-Vertical transmit-receive polarization
WSC	Wide ScanSAR imaging mode
DEM	digital elevation model
IWS	interferometric wide swath
TOPS	terrain observation with progressive scan mode
MTI	moving target indication

List of symbols

$(\cdot)^*$	conjugate operator
$(\cdot)^H$	adjoint operator
$(\cdot)^T$	transpose operator
$\vec{E}_i$, $\vec{E}_s$	incident and scattered electromagnetic field
$\underline{E}_{ij}$	Jones vector
$\dot{S}_{hh}$	complex scattering amplitude for HH polarization
$\dot{S}_{hv}$	complex scattering amplitude for HV polarization
$\dot{S}_{vh}$	complex scattering amplitude for VH polarization
$\dot{S}_{vv}$	complex scattering amplitude for VV polarization
$(\hat{x}, \hat{y}, \hat{z})$	orthogonal basis
$\lvert\cdot\rvert$	absolute value operator
$\langle\cdot\rangle$	expectation operator
C_2	2x2 covariance matrix
C_3, T_3	3x3 covariance and coherency matrix
A_e, ϕ_e, τ_e	amplitude, orientation and ellipsicity of elliptic polarization state
A_w	antenna pattern weight
B_D	Doppler bandwidth
B_g	ground swath width
B_p	total azimuth processed bandwidth
E_{0x}, E_{0y}	amplitudes in $\hat{x}$ and $\hat{y}$ direction of the electric field
L_a	physical antenna size in azimuth direction
L_c	propagation loss and system calibration factor
L_{sa}	synthetic aperture length
P_{R}	received power
P_{T}	transmitted power
W_r	pulse bandwidth in range
f_0	carrier frequency
$\hat{k}$	propagation direction
k_D	generic lexicographic scattering vector for dual-polarization

k_L, k_P	lexicographic and pauli scattering features vectors
k_c	complex wave number
k_r	frequency rate
s_0	closest approach distance
$s_{\mathrm{R_Y}}$	received signal
$s_{\mathrm{T_X}}$	transmitted signal
t_0	closest approach time
v_{S}	satellite speed
v_r	radial velocity of the satellite
$\overline{\alpha}$	polarimetric average alpha angle
β_a	antenna beamwidth in azimuth
β_{sa}	synthetic antenna beamwidth in azimuth
δ_a	resolution in azimuth direction
δ_p	skin depth
δ_r	resolution in slant range direction
λ_B	Bragg wavelength
λ_j, e_j	j-th eigenvalue and eigenvector matrix decomposition
$\dot{\rho}$	complex coherence coefficient
$\widehat{\rho}$	maximum likelihood estimator of the coherence amplitude
$\widehat{\sigma}$	standard deviation of the co-polarized phase difference
σ_0	ocean backscatter coefficient of the first order
τ_p	length of the transmitted pulse
ϕ_x, ϕ_y	phases in $\widehat{x}$ and $\widehat{y}$ direction of the electric field
$\angle(\cdot)$	argument operator
$\det(\cdot)$	determinant operator
h, v	horizontal and vertical polarizations basis
A	polarimetric anisotropy
$E[\cdot]$	first moment of a random variable
G	range antenna pattern
H	polarimetric entropy
L	number of independent samples or looks

S	scattering matrix
Thr	threshold value
$Trace(\cdot)$	trace operator
$W(\cdot)$	two-dimensional wave number spectral density
c	speed of light
$g(\cdot)$	complex envelope of the baseband signal
i	imaginary unit
j	index of the range ambiguity
$mean(\cdot)$	mean value operator
s	slant range or across-track coordinate
$stddev(\cdot)$	standard deviation operator
t	time reference in azimuth or slow time
x	ground range coordinate
y	azimuth or along-track coordinate
β	antenna azimuth angle
γ	co-polarization ratio coefficient
η	normalized radar cross section for VV polarization
θ	antenna elevation angle or incidence angle
λ	wavelength
σ	radar cross section
τ	time reference in range or fast time
$\epsilon(f)$	complex dielectric constant

References

Al-Khudhairy, D., 2002. Technologies and methodologies for Detection and Early Warning.

Alpers, W., Hühnerfuss, H., 1989. The damping of ocean waves by surface films: A new look at an old problem. J. Geophys. Res. Oceans 94, 6251–6265.

Arnaud, A., 1999. Ship detection by SAR interferometry, in: Geoscience and Remote Sensing Symposium, IEEE 1999 International, pp. 2616–2618 vol.5.

Avezzano, R.G., Velotto, D., Soccorsi, M., Del Frate, F., Lehner, S., 2011. Neural networks for oil spill detection using TerraSAR-X data. pp. 817911–817911–7.

Bamler, R., Hartl, P., 1998. Synthetic aperture radar interferometry. Inverse Probl. 14, R1.

Bamler, R., Runge, H., 1991. PRF-ambiguity resolving by wavelength diversity. IEEE Trans. Geosci. Remote Sens. 29, 997–1003.

Baschek, B., Dick, S., Janssen, F., Kübert, C., Massmann, S., Pape, M., Roers, M., 2011. Remote sensing as input and validation tool for oil spill drift modeling, in: Bostater, Jr., C.R., Mertikas, S.P., Neyt, X., Velez-Reyes, M. (Eds.), pp. 81750A–81750A–12.

Baumgartner, S.V., Krieger, G., 2011. Large along-track baseline SAR-GMTI: First results with the TerraSAR-X/TanDEM-X satellite constellation, in: Geoscience and Remote Sensing Symposium, 2011 IEEE International, pp. 1319–1322.

Boerner, W.M., Cram, L.A., Holm, W.A., Stein, D.E., Wiesbeck, W., Keydel, W., Giuli, D., Gjessing, D.T., Molinet, F.A., Brand, H., 1992. Direct and Inverse Methods in Radar Polarimetry - Part 1. Springer Science & Business Media.

Boerner, W.-M., El-Arini, M., Chan, C.-Y., Mastoris, P., 1981. Polarization dependence in electromagnetic inverse problems. IEEE Trans. Antennas Propag. 29, 262–271.

Breit, H., Fischer, M., Balss, U., Fritz, T., 2014. TerraSAR-X Staring Spotlight Processing and Products, in: EUSAR 2014; 10th European Conference on Synthetic Aperture Radar; Proceedings of, pp. 1–4.

Breit, H., Fritz, T., Balss, U., Lachaise, M., Niedermeier, A., Vonavka, M., 2010. TerraSAR-X SAR Processing and Products. IEEE Trans. Geosci. Remote Sens. 48, 727–740.

Brekke, C., Anfinsen, S.N., Larsen, Y., 2013. Subband Extraction Strategies in Ship Detection With the Subaperture Cross-Correlation Magnitude. IEEE Geosci. Remote Sens. Lett. 10, 786–790.

Brekke, C., Solberg, A.H.S., 2005. Oil spill detection by satellite remote sensing. Remote Sens. Environ. 95, 1–13.

Brusch, S., Lehner, S., Fritz, T., Soccorsi, M., Soloviev, A., van Schie, B., 2011. Ship Surveillance With TerraSAR-X. IEEE Trans. Geosci. Remote Sens. 49, 1092–1103.

Buades, A., Coll, B., Morel, J.-M., 2010. Image denoising methods. A new nonlocal principle. SIAM Rev. 52, 113–147.

Cloude, S., 2009. Polarisation: Applications in Remote Sensing. OUP Oxford.

Cloude, S.R., 2007. The dual polarisation entropy/alpha decomposition. Proc. Third ESA Workshop Polarim. Polarim. Interferom. POLInSAR 2007 Frascati Italy.

Cloude, S.R., Pottier, E., 1997. An entropy based classification scheme for land applications of polarimetric SAR. IEEE Trans. Geosci. Remote Sens. 35, 68–78.

Cloude, S.R., Pottier, E., 1996. A review of target decomposition theorems in radar polarimetry. IEEE Trans. Geosci. Remote Sens. 34, 498–518.

Corona, P., Ferrara, G., Migliaccio, M., 2004. Generalized stochastic field model for reverberating chambers. IEEE Trans. Electromagn. Compat. 46, 655–660.

Crisp, D.J., 2004. The state-of-the-art in ship detection in Synthetic Aperture Radar imagery. http://dspace.dsto.defence.gov.au/dspace/handle/1947/3354 (accessed 10.05.2010).

Cumming, I.G., Wong, F.H., 2005. Digital Processing of Synthetic Aperture Radar Data: Algorithms and Implementation. Artech House.

Curlander, J.C., McDonough, R.N., 1991. Synthetic Aperture Radar: Systems and Signal Processing. Wiley.

Di Martino, G., Iodice, A., Riccio, D., Ruello, G., 2014. Filtering of Azimuth Ambiguity in Stripmap Synthetic Aperture Radar Images. IEEE J. Sel. Top. Appl. Earth Obs. Remote Sens. 7, 3967–3978.

Elachi, C., Kuga, Y., McDonald, K., Sarabandi, K., Ulaby, F.T., Whitt, M., Zebker, H., van Zyl, J.J., 1990. Radar polarimetry for geoscience applications.

El-Darymli, K., McGuire, P., Power, D., Moloney, C., 2013. Target detection in synthetic aperture radar imagery: a state-of-the-art survey. J. Appl. Remote Sens. 7, 071598–071598.

Espedal, H.A., Johannessen, O.M., Knulst, J., 1996. Satellite detection of natural films on the ocean surface.

EU -COM(2009)/538, 2009. Towards the integration of maritime surveillance: A common information sharing environment for the EU maritime domain.

European Maritime Safety Agency, 2015. Earth Observation Services - CleanSeaNet. http://emsa.europa.eu/csn-menu.html (accessed 09.7.2013).

Fawcett, T., 2006. An Introduction to ROC Analysis. Pattern Recogn Lett 27, 861–874.

Ferrara, G., Migliaccio, M., Nunziata, F., Sorrentino, A., 2011. Generalized-K (GK)-Based Observation of Metallic Objects at Sea in Full-Resolution Synthetic Aperture Radar (SAR) Data: A Multipolarization Study. IEEE J. Ocean. Eng. 36, 195–204.

Ferraro, G., Baschek, B., de Montpellier, G., Njoten, O., Perkovic, M., Vespe, M., 2010. On the SAR derived alert in the detection of oil spills according to the analysis of the EGEMP. Mar. Pollut. Bull. 60, 91–102.

Ferraro, G., Trieschmann, O., Perkovic, M., Tarchi, D., 2012. Confidence levels in the detection of oil spills from satellite imagery: from research to the operational use. p. 85360G–85360G–11.

Ferro-Famil, L., Reigber, A., Pottier, E., Boerner, W.-M., 2003. Scene characterization using subaperture polarimetric SAR data. IEEE Trans. Geosci. Remote Sens. 41, 2264–2276.

Fingas, M., 2012. The Basics of Oil Spill Cleanup, Third Edition. CRC Press.

Fiscella, B., Giancaspro, A., Nirchio, F., Pavese, P., Trivero, P., 2000. Oil spill detection using marine SAR images. Int. J. Remote Sens. 21, 3561–3566.

Franceschetti, G., Iodice, A., Riccio, D., Ruello, G., Siviero, R., 2002. SAR raw signal simulation of oil slicks in ocean environments. IEEE Trans. Geosci. Remote Sens. 40, 1935–1949.

Franceschetti, G., Lanari, R., 1999. Synthetic Aperture Radar Processing. CRC Press.

Frate, F.D., Petrocchi, A., Lichtenegger, J., Calabresi, G., 2000. Neural networks for oil spill detection using ERS-SAR data. Geosci. Remote Sens. IEEE Trans. On 38, 2282–2287.

Freeman, A., Durden, S.L., 1998. A three-component scattering model for polarimetric SAR data. IEEE Trans. Geosci. Remote Sens. 36, 963–973.

Gade, M., Alpers, W., Hühnerfuss, H., Lange, P.A., 1998a. Wind wave tank measurements of wave damping and radar cross sections in the presence of monomolecular surface films. J. Geophys. Res. 103, 3167–3178.

Gade, M., Alpers, W., Hühnerfuss, H., Wismann, V.R., Lange, P.A., 1998b. On the reduction of the radar backscatter by oceanic surface films: Scatterometer measurements and their theoretical interpretation. Remote Sens. Environ. 66, 52–70.

Gade, M., Scholz, J., von Viebahn, C., 2000. On the detectability of marine oil pollution in European marginal waters by means of ERS SAR imagery, in: Geoscience and Remote Sensing Symposium, IEEE 2000 International, pp. 2510–2512 vol.6.

Gambardella, A., Nunziata, F., Migliaccio, M., 2008. A Physical Full-Resolution SAR Ship Detection Filter. IEEE Geosci. Remote Sens. Lett. 5, 760–763.

Greidanus, H., 2006. Sub-aperture Behavior of SAR Signatures of Ships, in: IEEE International Conference on Geoscience and Remote Sensing Symposium, 2006, pp. 3579–3582.

Grüner, K., Reuter, R., Smid, H., 1991. A new sensor system for airborne measurements of maritime pollution and of hydrographic parameters. GeoJournal 24, 103–117.

Hajnsek, I., Busche, T., Krieger, G., Zink, M., Schulze, D., Moreira, A., 2014. TanDEM-X Ground Segment Announcement of Opportunity: TanDEM-X Science Phase, TD-PD-PL-0032, German Aerospace Center, Microwave and Radar Institute, Germany.

Hippel, A.R.V., 1954. Dielectrics and Waves. Artech House.

Holt, B., 2004. SAR Imaging of the Ocean Surface, in: Synthetic Aperture Radar Marine User's Manual. U.S. Department of Commerce, National Oceanic and Atmospheric Administration, Washington DC, USA, pp. 25–80.

International Maritime Organization, 2015. http://www.imo.org/en/Pages/Default.aspx (accessed 11.03.2014).

ITOPF, 2011. Fate of marine oil spills.

Jakeman, E., Pusey, P.N., 1976. A model for non-Rayleigh sea echo. IEEE Trans. Antennas Propag. 24, 806–814.

Jakeman, E., Tough, R.J.A., 1987. Generalized K distribution: a statistical model for weak scattering. J. Opt. Soc. Am. A 4, 1764–1772.

Jha, M.N., Levy, J., Gao, Y., 2008. Advances in Remote Sensing for Oil Spill Disaster Management: State-of-the-Art Sensors Technology for Oil Spill Surveillance. Sensors 8, 236–255.

Joughin, I.R., Winebrenner, D.P., Percival, D.B., 1994. Probability density functions for multilook polarimetric signatures. Geosci. Remote Sens. IEEE Trans. On 32, 562–574.

Keramitsoglou, I., Cartalis, C., Kiranoudis, C.T., 2006. Automatic identification of oil spills on satellite images. Environ. Model. Softw. 21, 640–652.

Kirscht, M., 1996. Detection and velocity estimation of moving objects in a sequence of single-look SAR images, in: Geoscience and Remote Sensing Symposium, IEEE 1996 International, pp. 333–335 vol.1.

Klemas, V., 2010. Tracking Oil Slicks and Predicting their Trajectories Using Remote Sensors and Models: Case Studies of the Sea Princess and Deepwater Horizon Oil Spills. J. Coast. Res. 789–797.

Knapskog, A.O., Brovoll, S., Torvik, B., 2010. Characteristics of ships in harbour investigated in simultaneous images from TerraSAR-X and PicoSAR, in: 2010 IEEE Radar Conference, pp. 422–427.

Kubat, M., Holte, R.C., Matwin, S., 1998. Machine Learning for the Detection of Oil Spills in Satellite Radar Images. Mach. Learn. 30, 195–215.

Kudryavtsev, V.N., Chapron, B., Myasoedov, A.G., Collard, F., Johannessen, J.A., 2013. On Dual Co-Polarized SAR Measurements of the Ocean Surface. IEEE Geosci. Remote Sens. Lett. 10, 761–765.

Lee, J.-S., Hoppel, K.W., Mango, S., Miller, A.R., others, 1994. Intensity and phase statistics of multilook polarimetric and interferometric SAR imagery. Geosci. Remote Sens. IEEE Trans. On 32, 1017–1028.

Lee, J.-S., Papathanassiou, K.P., Ainsworth, T.L., Grunes, M.R., Reigber, A., 1998. A new technique for noise filtering of SAR interferometric phase images. IEEE Trans. Geosci. Remote Sens. 36, 1456–1465.

Lee, J.-S., Pottier, E., 2009. Polarimetric Radar Imaging: From Basics to Applications. CRC Press.

Lehner, S., Pleskachevsky, A., Brusch, S., Bruck, M., Soccorsi, M., Velotto, D., 2014. Ship Surveillance with High Resolution TerraSAR-X Satellite in African Waters, in: Barale, V., Gade, M. (Eds.), Remote Sensing of the African Seas. Springer Netherlands, pp. 285–313.

Lehner, S., Pleskachevsky, A., Velotto, D., Jacobsen, S., 2013. Meteo-Marine Parameters and Their Variability Observed by High Resolution Satellite Radar Images. Oceanography 26, 80–91. doi:10.5670/oceanog.2013.36

Li, F.K., Johnson, W., 1983b. Ambiguities in Spacebornene Synthetic Aperture Radar Systems. IEEE Trans. Aerosp. Electron. Syst. AES-19, 389–397. doi:10.1109/TAES.1983.309319

Litovchenko, K., Ivanov, A., Ermakov, S., 1999. Detection of oil slicks parameters from ALMAZ-1 and ERS-1 SAR imagery, in: Geoscience and Remote Sensing Symposium, IEEE 1999 International, pp. 1484–1486 vol.3.

Liu, C., Gierull, C.H., 2007. A New Application for PolSAR Imagery in the Field of Moving Target Indication/Ship Detection. IEEE Trans. Geosci. Remote Sens. 45, 3426–3436.

Liu, C., Vachon, P.W., Geling, G.W., 2005. Improved ship detection with airborne polarimetric SAR data. Can. J. Remote Sens. 31, 122–131.

Liu, P., Li, X., Qu, J.J., Wang, W., Zhao, C., Pichel, W., 2011. Oil spill detection with fully polarimetric UAVSAR data. Mar. Pollut. Bull. 62, 2611–2618.

Lombardini, P.P., Fiscella, B., Trivero, P., Cappa, C., Garrett, W.D., 1989. Modulation of the spectra of short gravity waves by sea surface films: slick detection and characterization with a microwave probe. J. Atmospheric Ocean. Technol. 6, 882–890.

Lumsdon, P., Schlund, M., von Poncet, F., Janoth, J., Weihing, D., Petrat, L., 2015. An encounter with pursuit monostatic applications of TanDEM-X mission, in: Geoscience and Remote Sensing Symposium, IEEE 2015 International, pp. 3187–3190.

Maffett, A.L., Wackerman, C.C., 1991. The modified beta density function as a model for synthetic aperture radar clutter statistics. IEEE Trans. Geosci. Remote Sens. 29, 277–283.

Margarit, G., Mallorqui, J.J., Fortuny-Guasch, J., Lopez-Martinez, C., 2009. Phenomenological Vessel Scattering Study Based on Simulated Inverse SAR Imagery. IEEE Trans. Geosci. Remote Sens. 47, 1212–1223.

Marino, A., 2013. A Notch Filter for Ship Detection With Polarimetric SAR Data. IEEE J. Sel. Top. Appl. Earth Obs. Remote Sens. 6, 1219–1232.

Marino, A., Cloude, S.R., Woodhouse, I.H., 2012. Detecting depolarized targets using a new geometrical perturbation filter. Geosci. Remote Sens. IEEE Trans. On 50, 3787–3799.

Marino, A., Sanjuan-Ferrer, M.J., Hajnsek, I., Ouchi, K., 2015. Ship Detection with Spectral Analysis of Synthetic Aperture Radar: A Comparison of New and Well-Known Algorithms. Remote Sens. 7, 5416–5439.

Mehlis, J.G., 1980. Synthetic aperture radar range - Azimuth ambiguity design and constraints. Presented at the International Radar Conference, pp. 143–152.

Mercier, G., Girard-Ardhuin, F., 2005. Oil slick detection by SAR imagery using Support Vector Machines, in: Oceans 2005 - Europe, pp. 90–95 Vol. 1.

Migliaccio, M., Ferrara, G., Gambardella, A., Nunziata, F., Sorrentino, A., 2007a. A Physically Consistent Speckle Model for Marine SLC SAR Images. IEEE J. Ocean. Eng. 32, 839–847.

Migliaccio, M., Gambardella, A., Nunziata, F., Shimada, M., Isoguchi, O., 2009a. The PALSAR polarimetric mode for sea oil slick observation. Geosci. Remote Sens. IEEE Trans. On 47, 4032–4041.

Migliaccio, M., Gambardella, A., Tranfaglia, M., 2007b. SAR Polarimetry to Observe Oil Spills. IEEE Trans. Geosci. Remote Sens. 45, 506–511.

Migliaccio, M., Nunziata, F., Gambardella, A., 2009b. On the co-polarized phase difference for oil spill observation. Int. J. Remote Sens. 30, 1587–1602.

Migliaccio, M., Nunziata, F., Montuori, A., Li, X., Pichel, W.G., 2011. A multifrequency polarimetric SAR processing chain to observe oil fields in the Gulf of Mexico. Geosci. Remote Sens. IEEE Trans. On 49, 4729–4737.

Migliaccio, M., Nunziata, F., Montuori, A., Paes, R.L., 2012. Single-look complex COSMO-SkyMed SAR data to observe metallic targets at sea. Sel. Top. Appl. Earth Obs. Remote Sens. IEEE J. Of 5, 893–901.

Mittermayer, J., Runge, H., 2003. Conceptual studies for exploiting the TerraSAR-X dual receive antenna, in: Geoscience and Remote Sensing Symposium, IEEE 2003 International, pp. 2140–2142.

Mittermayer, J., Schattler, B., Younis, M., 2010. TerraSAR-X Commissioning Phase Execution Summary. IEEE Trans. Geosci. Remote Sens. 48, 649–659.

Monti Guarnieri, A., 2005. Adaptive removal of azimuth ambiguities in SAR images. IEEE Trans. Geosci. Remote Sens. 43, 625–633.

Moreira, A., 1993. Suppressing the azimuth ambiguities in synthetic aperture radar images. IEEE Trans. Geosci. Remote Sens. 31, 885–895.

Moreira, A., Prats-Iraola, P., Younis, M., Krieger, G., Hajnsek, I., Papathanassiou, K.P., 2013. A tutorial on synthetic aperture radar. IEEE Geosci. Remote Sens. Mag. 1, 6–43.

Mott, H., 2006. Remote Sensing with Polarimetric Radar. John Wiley & Sons.

National Research Council, 2003. Oil in the Sea III: Inputs, Fates, and Effects.

Nghiem, S.V., Yueh, S.H., Kwok, R., Li, F.K., 1992. Symmetry properties in polarimetric remote sensing. Radio Sci. 27, 693–711.

Novak, L.M., Burl, M.C., Irving, W.W., 1993. Optimal polarimetric processing for enhanced target detection. IEEE Trans. Aerosp. Electron. Syst. 29, 234–244.

Nunziata, F., Migliaccio, M., Brown, C.E., 2012. Reflection symmetry for polarimetric observation of man-made metallic targets at sea. Ocean. Eng. IEEE J. Of 37, 384–394.

Nunziata, F., Sobieski, P., Migliaccio, M., 2009. The Two-Scale BPM Scattering Model for Sea Biogenic Slicks Contrast. IEEE Trans. Geosci. Remote Sens. 47, 1949–1956.

Oliver, C., Quegan, S., 2004. Understanding Synthetic Aperture Radar Images. SciTech Publishing.

Ouchi, K., Tamaki, S., Yaguchi, H., Iehara, M., 2004. Ship detection based on coherence images derived from cross correlation of multilook SAR images. IEEE Geosci. Remote Sens. Lett. 1, 184–187.

Prats-Iraola, P., Scheiber, R., Rodriguez-Cassola, M., Wollstadt, S., Mittermayer, J., Brautigam, B., Schwerdt, M., Reigber, A., Moreira, A., 2012. High precision SAR focusing of TerraSAR-X experimental staring spotlight data, in: Geoscience and Remote Sensing Symposium, IEEE 2012 International, pp. 3576–3579.

Prats, P., Scheiber, R., Mittermayer, J., Wollstadt, S., Baumgartner, S.V., Lopez-Dekker, P., Schulze, D., Steinbrecher, U., Rodriguez-Cassola, M., Reigber, A., Krieger, G., Zink, M., Moreira, A., 2012. TanDEM-X experiments in pursuit monostatic configuration, in: 9th European Conference on Synthetic Aperture Radar, 2012, pp. 159–162.

Radius, A., Marques, P., 2008. A Novel Methodology for Full Velocity Vector Estimation of Ships Using SAR Data, in: 7th European Conference on Synthetic Aperture Radar (EUSAR), 2008, pp. 1–4.

Raney, R.K., 1988. A `free' 3-dB cross-polarized SAR data. IEEE Trans. Geosci. Remote Sens. 26, 700–702.

Raney, R.K., Runge, H., Bamler, R., Cumming, I.G., Wong, F.H., 1994. Precision SAR processing using chirp scaling. IEEE Trans. Geosci. Remote Sens. 32, 786–799.

Sarabandi, K., 1992. Derivation of phase statistics from the Mueller matrix. Radio Sci. 27, 553–560.

Saur, G., Estable, S., Zielinski, K., Knabe, S., Teutsch, M., Gabel, M., 2011. Detection and classification of man-made offshore objects in TerraSAR-X and RapidEye imagery: Selected results of the DeMarine-DEKO project, in: OCEANS, 2011 IEEE - Spain, pp. 1–10.

Schreier, G., 1993. SAR geocoding: data and systems. Wichmann.

Schwarz, E., Krause, D., Berg, M., Daedelow, H., Maass, H., 2015. Near Real Time Applications for Maritime Situational Awareness. ISPRS - Int. Arch. Photogramm. Remote Sens. Spat. Inf. Sci. XL-7/W3, 999–1003.

Schwerdt, M., Schrank, D., Bachmann, M., Schulz, C., Doering, B., Hueso Gonzales, J., 2010. TerraSAR-X Re-Calibration and Dual Receive Antenna Campaigns performed in 2009, in: 8th European Conference on Synthetic Aperture Radar (EUSAR), 2010, pp. 1–4.

Sciotti, M., Pastina, D., Lombardo, P., 2002. Exploiting the polarimetric information for the detection of ship targets in non-homogeneous SAR images, in: Geoscience and Remote Sensing Symposium, IEEE 2002 International, pp. 1911–1913 vol.3.

Shirvany, R., Chabert, M., Tourneret, J.-Y., 2012. Ship and Oil-Spill Detection Using the Degree of Polarization in Linear and Hybrid/Compact Dual-Pol SAR. IEEE J. Sel. Top. Appl. Earth Obs. Remote Sens. 5, 885–892.

Singha, S., Velotto, D., Lehner, S., 2014. Near real time monitoring of platform sourced pollution using TerraSAR-X over the North Sea. Mar. Pollut. Bull. 86, 379–390.

Skolnik, 2001. Introduction to Radar Systems. Tata McGraw Hill.

Skrunes, S., Brekke, C., Eltoft, T., 2014. Characterization of Marine Surface Slicks by Radarsat-2 Multipolarization Features. IEEE Trans. Geosci. Remote Sens. 52, 5302–5319.

Solberg, A.H.S., Brekke, C., Ove Husoy, P., 2007. Oil Spill Detection in Radarsat and Envisat SAR Images. IEEE Trans. Geosci. Remote Sens. 45, 746–755.

Solberg, A.H.S., Storvik, G., Solberg, R., Volden, E., 1999. Automatic detection of oil spills in ERS SAR images. Geosci. Remote Sens. IEEE Trans. On 37, 1916–1924.

Souyris, J.-C., Henry, C., Adragna, F., 2003. On the use of complex SAR image spectral analysis for target detection: assessment of polarimetry. IEEE Trans. Geosci. Remote Sens. 41, 2725–2734.

Stratton, J.A., 2007. Electromagnetic Theory. John Wiley & Sons.

Suchandt, S., Runge, H., Steinbrecher, U., 2010. Ship detection and measurement using the TerraSAR-X dual-receive antenna mode, in: Geoscience and Remote Sensing Symposium, IEEE 2010 International, pp. 2860–2863.

Tello, M., Lopez-Martinez, C., Mallorqui, J.J., 2005. A novel algorithm for ship detection in SAR imagery based on the wavelet transform. IEEE Geosci. Remote Sens. Lett. 2, 201–205.

Tomiyasu, K., 1978. Tutorial review of synthetic-aperture radar (SAR) with applications to imaging of the ocean surface. Proc. IEEE 66, 563–583.

Topouzelis, K., Karathanassi, V., Pavlakis, P., Rokos, D., 2007. Detection and discrimination between oil spills and look-alike phenomena through neural networks. ISPRS J. Photogramm. Remote Sens. 62, 264–270.

Touzi, R., Lopes, A., Bruniquel, J., Vachon, P.W., 1999. Coherence estimation for SAR imagery. Geosci. Remote Sens. IEEE Trans. On 37, 135–149.

Touzi, R., Vachon, P.W., Wolfe, J., 2010. Requirement on Antenna Cross-Polarization Isolation for the Operational Use of C-Band SAR Constellations in Maritime Surveillance. IEEE Geosci. Remote Sens. Lett. 7, 861–865.

Trivero, P., Fiscella, B., Gomez, F., Pavese, P., 1998. SAR detection and characterization of sea surface slicks. Int. J. Remote Sens. 19, 543–548.

Tunaley, J.K.E., 2003. The estimation of ship velocity from SAR imagery, in: Geoscience and Remote Sensing Symposium, IEEE 2003 International, pp. 191–193 vol.1.

Ulaby, F.T., Moore, R.K., Fung, A.K., 1982. Microwave remote sensing: Active and passive. Volume 2 - Radar remote sensing and surface scattering and emission theory.

Ulaby, F.T., Moore, R.K., Fung, A.K., Ulaby, F.T., 1986. Radar remote sensing and surface scattering and emission theory, Microwave remote sensing. ARTECH House, Norwood, Mass.

Valenzuela, G., 1967. Depolarization of EM waves by slightly rough surfaces. IEEE Trans. Antennas Propag. 15, 552–557.

Valenzuela, G.R., 1978. Theories for the interaction of electromagnetic and oceanic waves — A review. Bound.-Layer Meteorol. 13, 61–85.

Velotto, D., Bentes, C., Tings, B., Lehner, S., 2015a. First comparison of Sentinel-1 and TerraSAR-X data in the framework of maritime targets detection: South Italy case. IEEE J. Ocean. Eng. xx–xx.

Velotto, D., Bentes, C., Tings, B., Lehner, S., 2015b. Comparison of Sentinel-1 and TerraSAR-X for ship detection, in: Geoscience and Remote Sensing Symposium, IEEE 2015 International, pp. 3282–3285.

Velotto, D., Lehner, S., 2014. On the use of full polarimetric SAR data to remove azimuth ambiguity: Application ship detection, in: 10th European Conference on Synthetic Aperture Radar, 2014, pp. 1–4.

Velotto, D., Lehner, S., Soloviev, A., Maingot, C., 2012. Analysis of oceanic features from dual-polarization high resolution X-band SAR imagery for oil spill detection purposes, in: Geoscience and Remote Sensing Symposium, IEEE 2012 International, pp. 2841–2844.

Velotto, D., Migliaccio, M., Nunziata, F., Lehner, S., 2011. Dual-polarized TerraSAR-X data for oil-spill observation. Geosci. Remote Sens. IEEE Trans. On 49, 4751–4762.

Velotto, D., Nunziata, F., Migliaccio, M., Lehner, S., 2013. Dual-polarimetric terrasar-x SAR data for target at sea observation. Geosci. Remote Sens. Lett. IEEE 10, 1114–1118.

Velotto, D., Soccorsi, M., Lehner, S., 2014. Azimuth Ambiguities Removal for Ship Detection Using Full Polarimetric X-Band SAR Data. IEEE Trans. Geosci. Remote Sens. 52, 76–88.

Villano, M., Krieger, G., 2014. Spectral-Based Estimation of the Local Azimuth Ambiguity-to-Signal Ratio in SAR Images. IEEE Trans. Geosci. Remote Sens. 52, 2304–2313.

Wang, C., Wang, Y., Liao, M., 2012. Removal of azimuth ambiguities and detection of a ship: using polarimetric airborne C-band SAR images. Int. J. Remote Sens. 33, 3197–3210.

Ward, K.D., Watts, S., Tough, R.J.A., 2006. Sea Clutter: Scattering, the K Distribution and Radar Performance. IET.

Zhu, X.X., Bamler, R., Lachaise, M., Adam, F., Shi, Y., Eineder, M., 2014. Improving TanDEM-X DEMs by Non-local InSAR Filtering, in: 10th European Conference on Synthetic Aperture Radar, 2014, pp. 1–4.

Ziemke, T., 1996. Radar image segmentation using recurrent artificial neural networks. Pattern Recognit. Lett., Neural Networks for Computer Vision Applications 17, 319–334.